Quantification of Arrhythmogenic Substrate in High-Density Local Activation Maps

---

Cuantificación del Sustrato Arritmogénico en Mapas de Activación Local de Alta Densidad

Doctoral Thesis

Samuel Ruipérez Campillo

December 2024

Supervisors: Prof. Dr. Francisco S. Castells Ramón
Prof. Dr. José Millet Roig

Escuela Técnica Superior de
Ingeniería de Telecomunicación
Instituto ITACA
Universitàt Politècnica de Valéncia

Abstract

Arrhythmias, particularly atrial fibrillation (AF) and ventricular tachycardia (VT), are major contributors to cardiovascular morbidity and mortality. Accurate characterization of the electrical conduction patterns underlying these arrhythmias is essential for diagnosis and treatment, particularly in guiding catheter ablation therapy. Recent advancements in high-density (HD) catheters have improved intracardiac signal acquisition; however, challenges such as signal orientation dependency and insufficient mapping resolution still limit their clinical effectiveness. This doctoral dissertation explores novel signal processing techniques that leverage HD catheters to better characterize arrhythmogenic substrates, with the goal of improving arrhythmia diagnosis and treatment.

The core of this research focuses on two key developments. First, a novel cross-clique configuration for omnipolar electrogram (EGM) reconstruction is introduced, addressing the limitations of traditional triangular-clique configurations, which are sensitive to signal propagation direction. The cross-clique method was validated through both simulations and animal model experiments, demonstrating its ability to provide orientation-independent, accurate EGM reconstructions. Second, this thesis develops an advanced metric for quantifying conduction heterogeneity at a local level: the Vector Field Heterogeneity (VFH) metric. This metric was designed to identify and quantify conduction abnormalities with high-density multiarray catheters, helping clinicians target regions of interest for ablation therapy. Additionally, a metric for global spatio-temporal analysis (REACT) was developed to complement the local understanding of electrical disarray in arrhythmia conduction patterns.

The results of this research highlight the significant potential of these methods. The cross-clique configuration was shown to improve the precision of omnipolar EGM signals compared to existing techniques, providing a robust tool for intracardiac mapping. The VFH metric, validated through simulation and experimental models, was found to be a reliable marker of local conduction disarray, particularly useful for identifying functional isthmuses in VT substrate mapping. Similarly, the REACT metric demonstrated its ability to capture global patterns of disorganization in AF, offering insights into patient-specific responses to ablation therapy and predicting clinical outcomes.

In conclusion, this thesis makes several important contributions to the field of cardiac electrophysiology. The novel signal processing techniques developed here offer enhanced diagnostic accuracy and treatment guidance for both atrial and ventricular arrhythmias. By improving the precision of omnipolar EGMs and introducing new methods for assessing conduction heterogeneity, these findings have the potential to improve ablation strategies and improve clinical outcomes. Future work will focus on further validating these methods in larger clinical trials and integrating them with emerging technologies, such as ECGi, to enhance non-invasive diagnostic capabilities.

Resumen

Las arritmias, en particular la fibrilación auricular (FA) y la taquicardia ventricular (TV), contribuyen en gran medida a la morbilidad y mortalidad cardiovasculares. La caracterización precisa de los patrones de conducción eléctrica subyacentes a estas arritmias es esencial para el diagnóstico y el tratamiento, en particular para guiar la terapia de ablación con catéter. Los recientes avances en los catéteres de alta densidad (HD) han mejorado la adquisición de señales intracardiacas; sin embargo, problemas como la dependencia de la orientación de la señal y la insuficiente resolución del mapeo siguen limitando su eficacia clínica. Esta tesis doctoral explora nuevas técnicas de procesamiento de señales que aprovechan los catéteres de alta densidad para caracterizar mejor los sustratos arritmogénicos, con el objetivo de mejorar el diagnóstico y el tratamiento de las arritmias.

El núcleo de esta investigación se centra en dos desarrollos clave. En primer lugar, se introduce una novedosa configuración en cruz para la reconstrucción de electrogramas (EGM) omnipolares, que aborda las limitaciones de las configuraciones triangulares tradicionales, que son sensibles a la dirección de propagación de la señal. El método cross-clique se validó mediante simulaciones y experimentos con modelos animales, demostrando su capacidad para proporcionar reconstrucciones EGM precisas e independientes de la orientación. En segundo lugar, esta tesis desarrolla una métrica avanzada para cuantificar la heterogeneidad de la conducción a nivel local: la métrica de heterogeneidad del campo vectorial (VFH). Esta métrica se diseñó para identificar y cuantificar las anomalías de la conducción con catéteres multiarray de alta densidad, ayudando a los médicos a seleccionar las regiones de interés para la terapia de ablación. Además, se desarrolló una métrica para el análisis espacio-temporal global (REACT) para complementar la comprensión local de la disarray eléctrica en los patrones de conducción de la arritmia.

Los resultados de esta investigación ponen de relieve el importante potencial de estos métodos. Se demostró que la configuración cross-clique mejora la precisión de las señales EGM omnipolares en comparación con las técnicas existentes, proporcionando una herramienta robusta para el mapeo intracardiaco. La métrica VFH, validada mediante simulación y modelos experimentales, resultó ser un marcador fiable de la desorganización de la conducción local, especialmente útil para identificar istmos funcionales en la cartografía de sustratos de taquicardia ventricular. Del mismo modo, la métrica REACT demostró su capacidad para captar patrones globales de desorganización en la FA, ofreciendo información sobre las respuestas específicas de los pacientes al tratamiento de ablación y prediciendo los resultados clínicos.

En conclusión, esta tesis hace varias contribuciones importantes al campo de la electrofisiología cardiaca. Las novedosas técnicas de procesamiento de señales aquí desarrolladas mejoran la precisión diagnóstica y la orientación terapéutica de las arritmias auriculares y ventriculares. Al mejorar la precisión de las EGM omnipolares e introducir nuevos métodos para evaluar la heterogeneidad de la conducción, estos hallazgos pueden mejorar las estrategias de ablación y los resultados clínicos. El trabajo futuro se centrará en validar aún más estos métodos en ensayos clínicos más amplios e integrarlos con tecnologías emergentes, como ECGi, para mejorar las capacidades de diagnóstico no invasivo.

Resum

Les arrítmies, en particular la fibrilació auricular (FA) i la taquicàrdia ventricular (TV), contribueixen en gran manera a la morbiditat i mortalitat cardiovasculars. La caracterització precisa dels patrons de conducció elèctrica subjacents a aquestes arrítmies és essencial per al diagnòstic i el tractament, en particular per a guiar la teràpia d'ablació amb catèter. Els recents avanços en els catèters d'alta densitat (HD) han millorat l'adquisició de senyals intracardíacs; no obstant això, problemes com la dependència de l'orientació del senyal i la insuficient resolució del mapatge continuen limitant la seua eficàcia clínica. Aquesta tesi doctoral explora noves tècniques de processament de senyals que aprofiten els catèters d'alta densitat per a caracteritzar millor els substrats arritmogènics, amb l'objectiu de millorar el diagnòstic i el tractament de les arrítmies.

El nucli d'aquesta investigació es centra en dos desenvolupaments clau. En primer lloc, s'introdueix una nova configuració en creu per a la reconstrucció d'electrogrames omnipolars (EGM), que aborda les limitacions de les configuracions triangulars tradicionals, que són sensibles a la direcció de propagació del senyal. El mètode en creu s'ha validat mitjançant simulacions i experiments amb models animals, demostrant la seua capacitat per a proporcionar reconstruccions EGM precises i independents de l'orientació. En segon lloc, s'ha desenvolupat una mètrica avançada per a quantificar l'heterogeneïtat de la conducció a nivell local: la mètrica d'heterogeneïtat del camp vectorial (VFH). Aquesta mètrica s'ha dissenyat per a identificar i quantificar les anomalies de la conducció amb catèters multielectrode d'alta densitat, per tal d'ajudar els metges a seleccionar les regions d'interès per a la teràpia d'ablació. A més, s'introdueix una mètrica per a l'anàlisi espaciotemporal global (REACT) per a complementar la comprensió local de la desorganització elèctrica en els patrons de conducció de l'arrítmia.

Els resultats d'aquesta investigació posen en relleu l'important potencial dels mètodes proposats. Així, s'ha demostrat que la configuració en creu millora la precisió dels senyals EGM omnipolars en comparació amb les tècniques existents, proporcionant una ferramenta robusta per al mapatge intracardíac. La mètrica VFH, validada mitjançant simulació i models experimentals, ha resultat ser un marcador fiable de la desorganització de la conducció local, especialment útil per a identificar istmes funcionals en la cartografia de substrats de taquicàrdia ventricular. De la mateixa manera, la mètrica REACT ha demostrat la seua capacitat per a captar patrons globals de desorganització en la FA, oferint informació sobre les respostes específiques dels pacients al tractament d'ablació i predient els resultats clínics.

En conclusió, esta tesi fa diverses contribucions importants al camp de l'electrofisiologia cardíaca. Les noves tècniques de processament de senyals desenvolupats milloren la precisió diagnòstica i l'orientació terapèutica de les arrítmies auriculars i ventriculars. En millorar la precisió dels EGM omnipolars i introduir nous mètodes per a avaluar l'heterogeneïtat de la conducció, aquests avanços poden millorar les estratègies d'ablació i els resultats clínics. El treball futur es centrarà en validar encara més aquestos mètodes en assajos clínics més amplis i integrar-los amb tecnologies emergents, com ECGi, per a millorar les capacitats de diagnòstic no invasiu.

Acknowledgements

I would like to sincerely thank Professors Pepe and Paco for their guidance and for giving me the opportunity to explore the challenges and complexities of electrophysiology from an engineering viewpoint. Despite the physical distance, your continued support made this research possible. The work we have done together has been incredibly rewarding and a truly memorable part of my journey.

I am deeply grateful to Dr. José Luis Merino, Dr. Rubén Casado, Dr. Sanjiv Narayan, and Dr. Johanna Tonko for their invaluable clinical advice and training. Their insights have been instrumental in shaping my understanding of the clinical aspects of my research.

A heartfelt thank you to Elisa and my companions in the lab and institute. Your camaraderie, encouragement, and collaboration have been key to the success of this project.

Finalmente, gracias a mis amigos y familia, en especial a mis padres, mis tíos, Irene y Nico. Vuestro apoyo y cariño han sido indispensables.

Contents

Contents **ix**

List of Figures **xiii**

List of Tables **xvii**

Glossary **xix**

1 Introduction **1**
- 1.1 Motivation . . . 1
- 1.2 Objectives . . . 2
- 1.3 Hypotheses . . . 3
- 1.4 Structure of this dissertation . . . 4

2 State of the Art **5**
- 2.1 The heart: role and anatomy . . . 5
  - 2.1.1 The cardiovascular system in a nutshell . . . 5
  - 2.1.2 Structural anatomy of the heart . . . 6
- 2.2 Electrophysiology behind the pulse . . . 7
  - 2.2.1 Electrophysiology and conduction system . . . 7
  - 2.2.2 Cardiac action potentials . . . 7
  - 2.2.3 Electrophysiological signal propagation: the heartbeat . . . 9
- 2.3 Cardiac arrhythmias . . . 9
  - 2.3.1 Atrial flutter . . . 10
  - 2.3.2 Atrial fibrillation . . . 11
  - 2.3.3 Ventricular tachycardia . . . 11
- 2.4 Non-invasively measuring the cardiac activity . . . 13
  - 2.4.1 Introduction to the electrocardiogram . . . 13
  - 2.4.2 Twelve-lead ECG patterns and features . . . 14
  - 2.4.3 Vectorial analysis of the cardiac cycle . . . 15
  - 2.4.4 The vectorcardiogram . . . 17
- 2.5 Electrical propagation through the cardiac tissue . . . 18
  - 2.5.1 Propagation of the action potential signal . . . 19
  - 2.5.2 Electrogram signals . . . 19

2.5.3 Transmembrane currents 20
2.5.4 Conduction velocity estimation 21
2.6 Characterizing the tissue: intracardiac recordings 26
2.6.1 Electro-anatomic mapping systems in arrhythmias 27
2.6.2 Electrogram recordings in a grid catheter 28
2.6.3 Signal processing for omnipolar electrograms 30

3 Characterization of AFL and Slow Conduction Regions 33
3.1 Introduction 34
3.2 Study design 35
3.3 Materials 36
3.3.1 Synthetic data 36
3.3.2 Clinical data 37
3.4 Methods 39
3.4.1 Preprocessing 39
3.4.2 VCG archetypes 41
3.4.3 Characterisation of VCG loops 41
3.4.4 Statistical analysis 45
3.5 Results 46
3.5.1 Synthetic data 46
3.5.2 Real data 47
3.6 Discussion 50
3.6.1 Study limitations 54
3.7 Conclusions 54

4 Cross-Omnipolar Electrograms in HD Arrays 55
4.1 Introduction 56
4.2 Methods 58
4.2.1 Configurations of bEGMs within a clique 59
4.2.2 Estimation of oEGMs 60
4.2.3 Assessement of oEGM estimation 60
4.2.4 Statistical Analysis 61
4.3 Results 61
4.4 Discussion 66
4.5 Conclusions 68

5 Cross-omnipolar EGMs in HD Catheters: Experimental Animal Study 69
5.1 Introduction 70
5.2 Materials 71
5.3 Methods 71
5.3.1 Clique configurations 71
5.3.2 oEGM estimation 73
5.3.3 Assessment of oEGM reliability 74
5.3.4 Statistical analysis 75
5.4 Results 76
5.5 Discussion 80
5.5.1 Study limitations 83
5.6 Conclusions 84

6 Vector Field Heterogeneity in Cardiac Electrical Propagation Maps 85

6.1 Introduction 86
6.2 Materials 87
  6.2.1 Simulated data 87
  6.2.2 Experimental data 88
6.3 Methods 88
  6.3.1 Creation of propagation maps 88
  6.3.2 Vector Field Heterogeneity 89
  6.3.3 Metric comparison with the widely accepted Spatial Inhomogeneity index 91
  6.3.4 Statistical analysis 92
6.4 Results 93
  6.4.1 Simulations 93
  6.4.2 Experimental data 95
  6.4.3 Metric comparison 96
6.5 Discussion 98
  6.5.1 Limitations and future work 101
6.6 Conclusions 102

7 Identification of Ablation Targets of VT using VFH 103
7.1 Introduction 104
7.2 Materials and methods 104
7.3 Results 107
7.4 Discussion 109
7.5 Conclusions 110

8 Quantifying Clinical Response in Atrial Arrhythmias using REACT 111
8.1 Introduction 112
8.2 Methods 113
  8.2.1 Patient recruitment and clinical electrophysiology study . . . 113
  8.2.2 Electrogram recording and pre-processing 114
  8.2.3 Identification of regions of repetitive activity 114
  8.2.4 Identifying physiological variations underlying repetitive activity values 115
  8.2.5 Unsupervised machine learning of repetitive activity and clinical variables 116
  8.2.6 Statistical analysis 116
8.3 Results 116
  8.3.1 Patient demographics 116
  8.3.2 Islands of electrogram similarity 116
  8.3.3 Islands of electrogram similarity: global and regional 118
  8.3.4 Clinical phenotypes based on islands of electrogram similarity 119
  8.3.5 Calibrating repetitive activity value to physiological electrogram variations 120
  8.3.6 Clinical phenotypes identified by machine learning 120
8.4 Discussion 121
  8.4.1 Metrics of atrial fibrillation organization and disorganization 121
  8.4.2 Mechanisms for synchronized sites 122
  8.4.3 Previous reports of repetitive activations in atrial fibrillation . 122
  8.4.4 Prior studies linking atrial tachycardia and atrial fibrillation . 123

8.4.5 Clinical utility of repetitive activity 123
8.4.6 Limitations 123
8.5 Conclusions 124

9 Discussion 125
9.1 Achievement of thesis objectives 125
9.2 Answering the initial hypotheses 126
9.3 Non-invasive vs intracardiac measurements: can we do without one? 127
9.4 ECGi as a promising bridge 129
9.5 Intracardiac recordings: not all that glitters is gold 129
9.6 Omnipolar technology and the advantage of the cross clique 130
9.7 Validation of the cross-omnipole in animal and clinical studies 131
9.8 Insights on the inter-electrode distance for array catheters 132
9.9 From omnipolar technology to quantifying local electrical disarray in clinical settings 133
9.10 Local and global organization conduction patterns 134
9.11 Overall limitations and future work 135

10 Conclusions 139

A Scientific Impact of this Dissertation 141
A.1 Scientific journal articles 141
A.2 Awards associated with the research for this thesis 142
A.3 International engineering conference publications 142
A.4 International medical conference publications 143
A.5 National engineering conference publications 144

B Appendices to Chapter 3 147
B.1 VCG loop alignment 147

C Appendices to Chapter 5 149
C.1 Statistical analysis 149
C.2 Code 150

D Appendices to Chapter 6 155
D.1 Statistical tests results 155
D.2 Computation of VFH from LATs 155

E Appendices to Chapter 8 159
E.1 Additional description of the data 159
E.2 Dynamics of AF organization quantified by the REACT algorithm . . 159
E.3 REACT pseudocode 162

Bibliography 165

List of Figures

2.1 Heart anatomy and circulation: Sagittal section and detailed view of left atrium . . . 8
2.2 Membrane potential and ion permeability of cardiac cells. . . . 10
2.3 ECG signal from a healthy patient . . . 15
2.4 Mean vector and standard directions of mean potential vectors . . . 16
2.5 Conduction velocity estimation techniques . . . 22

3.1 Simulated VCG example: Frontal, transversal, sagittal planes, 3D representation, and velocity profile . . . 38
3.2 Electroanatomical mapping of perimitral MRAT with activation sequence and slow conduction region . . . 40
3.3 Twelve-lead ECG of CCW AFL with adenosine and superimposed VCGs from atrial cycles . . . 42
3.4 Detection of primary and secondary slow velocity intervals in perimitral CCW MRAT: VCG projections and atrial ECG signal . . . 44
3.5 Box plot of the correlation coefficient of types I to IV with their representative archetypes. . . . 47
3.6 ROC curves for all patients corresponding to each of the groups . . . 48
3.7 VCG archetypes for MRAT groups: Principal slow velocity region and rotation sense . . . 49
3.8 Examples of VCGs for CCW perimitral MRAT with highlighted slow velocity regions . . . 51
3.9 Slow velocity intervals in AFL: Detection from velocity profile and correlation with CTI electrode activation . . . 52

4.1 Geometry of advisor™ HD Grid and electrode configuration approaches 57
4.2 Bidimensional loops from orthogonal bEGMs for triangular, square, and cross configurations at various propagation directions . . . 62
4.3 Omnipolar EGMs and residual signal: Retrieved propagation directions and bipole configurations . . . 63
4.4 Comparison of bipoles, triangular, and square configurations: Boxplots of amplitude, oEGM relation, LAT error, and angle estimation error . . . 64
4.5 Dependence of bipolar morphology on unipolar delay and uEGM morphologies . . . 66

5.1 Multielectrode array: Arrangement, device, and experimental setup . . . 72
5.2 Electrode clique configurations: $C_{◺}$, $C_{◿}$, $C_{◸}$, $C_{◹}$, and $C_{\times}$ 73
5.3 Graphical description of some of the metrics assessed: **A.** NLA; **B.** ORR; **C.** PW 76
5.4 Bipolar loops and propagation directions for triangular and cross configurations at 1-4 mm interelectrode distances 78
5.5 Omnipole reconstruction by triangular and cross configurations with oEGM components at 1-4 mm interelectrode distances 79
5.6 Comparison of triangular and cross configurations for key parameters in the animal model 82
5.7 Morphology analysis of oEGMs for triangular and cross cliques in an animal model 83

6.1 Bipolar loop representation on epicardium of Langendorff rabbit heart at 37°C under 4 Hz stimulation 89
6.2 Illustration of heterogeneity scores and VFH values with propagation and heterogeneity maps under 4 Hz stimulation and basal recording . . 92
6.3 Calculation of SI index for a 6×6 grid: Propagation, LAT, phase maps, and phase differences at 4 Hz stimulation and basal recording 93
6.4 VFH value analysis: Simulated propagation maps, disorganisation, and catheter size effects 94
6.5 VFH values by stimulation type: Box and whisker plots for different catheter sizes 95
6.6 Heterogeneity analysis example for 8×8 catheter grid: Propagation vector and heterogeneity maps with VFH values 97
6.7 SI index values by stimulation type: Box and whisker plots for different catheter sizes 97
6.8 ROC and PR curve comparison between VFH metric and SI index for 4×4 electrode grid 99
6.9 VFH values by stimulation type and catheter size: Omnipolar-derived vs. LAT-derived vector maps 101

7.1 Cross omnipolar reconstruction: Voltage domain illustration and propagation direction estimation with VFH map 106
7.2 Summary statistics and data distribution of local VFH in VT patients: Heterogeneity and vector maps with VT activation maps 108
7.3 VFH and voltage maps for VT patient (male, 64 y.o., ICM, LVEF 25%) . . 109

8.1 Abstract figure of the REACT metric 112
8.2 Quantifying EGM synchronization by REACT mapping: LA mapping with 64-pole catheter and 3D visualization 115
8.3 REACT spectrum in atrial arrhythmias: Treatment response from AT to AF with ablation or cardioversion 117
8.4 Organization and temporal analysis spectrum: Global and regional differences in AT, AF termination, and nontermination, and REACT variations over one minute 118
8.5 ROC curve of REACT organization for predicting AF termination: Five-fold cross-validation and AUC 119
8.6 Physiology nomograph of REACT: Impact of shape and timing variations on pacing EGMs 120

8.7 Unsupervised ML of REACT and clinical variables: Cluster analysis and termination rate prediction . . . 121

C.1 Supplementary statistics cross omnipole: NLA . . . 151
C.2 Supplementary statistics cross omnipole: ORR . . . 152
C.3 Supplementary statistics cross omnipole: PW . . . 153
C.4 Supplementary statistics cross omnipole: MD . . . 154

D.1 Statistical test plots: VFH & SI by stimulation type and catheter size; ROC & PR curve comparison . . . 157
D.2 ROC curves comparison between omnipolar-derived and LAT-derived VFH . . . 158

E.1 Electrograms from 2-by-2 electrode grid . . . 161
E.2 AUROC curves for AF termination prediction in non-paroxysmal and paroxysmal AF . . . 163
E.3 REACT map and EGM patterns in 55 y.o. male with AF termination . . . 164

List of Tables

2.1 Overview of selected CV estimation methods: Advantages and caveats . 27

3.1 Summary of parameters, descriptions, and values in the synthetic model 39
3.2 AUROC for synthetic patients 46
3.3 Results of correlation of archetypes with patients from MRAT groups . . 48
3.4 ”Results of $\mathbf{TF_{LV}}$, $\mathbf{DF_{LV}}$, $\mathbf{TDR_{LV}}$, and $V_{\max}/V_{\min}$ artio 50
3.5 Results of arc parameter for all MRAT groups 50

4.1 Statistical values of results for simulations 65

5.1 Results for the different metrics 80
5.2 Post-hoc test p-values comparing configuration coefficients by metrics and distances 80
5.3 Post-hoc test p-values comparing distance coefficients by metrics and configurations 81

6.1 VFH values for different grid sizes according to the stimulation type . . 95
6.2 P-values of Wilcoxon rank-sum test for comparing VFH values according to stimulation type 96
6.3 P-values of Wilcoxon rank-sum test for comparing VFH values according to catheter size 96
6.4 SI values for different grid sizes according to the stimulation type 98
6.5 Wilcoxon rank-sum test p-values for comparing SI indices by stimulation type 98
6.6 Wilcoxon rank-sum test p-values for comparing SI indices by catheter size 98
6.7 AUC values for the ROC and PR curves 99

7.1 Summary of mean and standard deviation of VFH values across different regions 109

8.1 Baseline characteristics 117

D.1 P-values of Wilcoxon rank-sum test for comparing LAT-derived VFH values according to stimulation type 156
D.2 Wilcoxon test p-values for VFH by catheter size 156

E.1 Propensity matching characteristics 159
E.2 List of clinical variables used in clustering 160

Glossary

AF Atrial Fibrillation. xiv, xv, 1, 2, 4, 6, 9, 11, 20, 21, 27, 35, 53, 56, 70, 86, 110–124, 126–128, 130, 134, 135, 140, 159, 160, 163, 164
AFL Atrial FLutter. xiii, 1, 2, 4, 7, 9–11, 34, 35, 38, 42, 45, 47, 50, 52, 53, 67, 116, 127, 128, 135
AT Atrial Tachycardia. xiv, 70, 111–113, 116–121, 123, 124
AUROC Area Under the Receiving Operating Characteristics Curve. 45, 46, 48, 107, 116, 119, 122

CCW Counterclockwise. xiii, 33, 34, 37–39, 42, 44, 47–53, 128
CV Conduction Velocity. 4, 21–27, 30–32, 55, 56, 58, 61, 65–68, 70, 74, 83, 100, 128, 130, 136
CW Clockwise. 33, 34, 37–39, 47–50, 52, 53, 128

DF Dominant Frequency. 2, 112, 121, 135

ECG Electrocardiogram. 6, 10, 11, 13–15, 17, 18, 34–39, 41, 42, 44, 50, 53, 54, 115, 123, 128, 129, 133, 135, 140
EGM Electrogram. xiii, 1–3, 19, 20, 26–32, 37, 52, 55–71, 73–77, 79–84, 86, 88, 91, 100, 101, 104–106, 110, 111, 113–124, 126, 127, 129–136, 139
EP Electrophysiology/Electrophysiological. 2, 3, 6, 11, 21, 34, 36–38, 40, 54–56, 66, 67, 70, 71, 83, 85, 86, 98, 101, 104, 109, 126–130, 133, 134, 137, 139, 140

IQR Interquartile Range. 61, 75, 93, 95, 96, 98, 109

LAT Local Activation Time. xiii, xiv, xvii, 24, 27, 55, 56, 58, 60, 61, 64, 65, 67, 68, 91, 93, 100, 101, 130, 131, 133, 155, 156, 158
LVA Low Voltage Area. 12, 103, 105, 107–110

MRAT Macroreentrant Atrial Tachyarrhythmia. xiii, 2, 33–38, 40, 41, 43, 44, 47–54, 128

NVA Normal Voltage Area. 12, 103, 105, 107–110

PR Precision-Recall. xvii, 93, 97, 99, 100

QQ Quantile-Quantile. 76, 93, 150–155, 157

REACT Repetitive Activity. xiv, 100, 111–124, 134, 135, 140, 159, 161, 162, 164
RF Radiofrequency. 11, 34, 105
ROC Receiver Operating Characteristics. xv, xvii, 93, 97, 99, 100, 107, 116, 119, 155, 157, 158

SD Standard Deviation. 47, 52, 61, 75, 94, 95, 99, 100, 107, 109, 115, 116, 119
SI Spatial Inhomogeneity. xv, xvii, 85–87, 91–93, 96–102, 133, 134, 155, 157, 158

VCG Vectorcardiogram. xiii, 6, 18, 33, 35–54, 128
VFH Vector Field Heterogeneity. xiv, xv, xvii, 85–87, 89, 91–103, 106–110, 132–134, 136, 137, 139, 140, 155–158
VT Ventricular Tachycardia. xiv, 1, 2, 4, 9, 11, 12, 27, 56, 103–105, 107–110, 126, 127, 129, 134, 136, 139, 140

Chapter 1

Introduction

This chapter introduces the doctoral dissertation, which is presented as a compilation of research articles based on work conducted up to 2023 and published by 2024. It outlines the motivation, hypotheses, main objectives, and sub-objectives of the research, and provides a clear overview of the dissertation's structure.

1.1 Motivation

Arrhythmias affect an estimated 1.5% to 5% of the general population, with atrial fibrillation (AF) being the most common sustained form [1]. These conditions, which may present with or without symptoms, complicate accurate prevalence assessments and are linked to increased morbidity and mortality. Early detection and effective management are essential to mitigate these risks. Arrhythmias occur when there is an irregularity in the electrical signals propagating through the heart, often due to structural or functional abnormalities [2]. Bradycardias, characterized by slower-than-normal heart rates, are typically less harmful, whereas tachycardias, which involve elevated heart rates, pose greater risk and can arise in both the atria and ventricles. AF results from chaotic electrical activity in the atria, leading to uncoordinated heartbeats [3], while atrial flutter (AFL) features more organized but rapid signals. In the ventricles, disorganized electrical signals can lead to ventricular fibrillation, a life-threatening condition that requires immediate intervention [4, 5].

Accurate signal acquisition, processing, and interpretation are crucial for diagnosing and treating arrhythmias, particularly for guiding catheter ablation therapy [6, 7]. Recent advances in cardiac signal acquisition, such as the development of high-density (HD) catheters, have greatly enhanced the ability to diagnose and treat complex arrhythmias like ventricular tachycardia (VT) [8], Brugada syndrome [9], and AF [10]. These technologies provide high-resolution mapping of the heart's electrical activity. However, their effectiveness depends on sophisticated signal processing techniques. Current techniques face limitations: unipolar electrograms (EGMs) often contain noise and artifacts [11, 12], while bipolar signals are sensitive to wave propagation direction and catheter positioning [13, 14]. In response to these challenges, omnipolar reconstruction was recently introduced, particularly with the HD grid catheter (Abbott Laboratories, Illinois, US). This technique addresses some of the limitations of conventional mapping methods [15, 16, 17, 18] and has been clinically applied to detect scar tissue [19], characterize conduction gaps [20], and diagnose arrhythmias such as AF [21], and VT [22]. However, omnipolar reconstruction is not entirely independent of the signal's propagation direction, leaving room for further improvement [23, 12].

AF, the most common and complex arrhythmia, poses a significant societal burden due to its links to stroke, heart failure, and mortality [24, 25]. The mechanisms sustaining AF remain debated, with various theories proposing different ablation targets. Nademanee et al. suggested that low-voltage, fractionated EGMs are crucial in maintaining AF [26, 27, 28], while others argue that focal sources or rotors are responsible. Although rotor-based mapping, like FIRM-guided systems, has shown promise, outcomes are inconsistent, with potential false rotor detection [29, 30, 31, 32]. Dominant frequency (DF) mapping also helps localize arrhythmogenic zones [33, 34], and fibrosis, as shown by Marrouche et al., improves ablation outcomes when targeted via MRI [35].

In addition to atrial fibrillation (AF), macroreentrant atrial tachyarrhythmia (MRAT), often called atrial flutter (AFL), is a common atrial arrhythmia. MRAT is driven by reentrant circuits in the atria, with slow conduction regions that allow the arrhythmia to persist by facilitating repolarization and repeated activation. Catheter ablation, particularly targeting slow conduction zones like the cavotricuspid isthmus, is the primary treatment [36, 37]. Electroanatomical mapping aids ablation but remains time-intensive, especially for atypical MRAT.

VT is another serious arrhythmia, characterized by three or more consecutive QRS complexes at a rate exceeding 100 beats per minute [38]. VT can significantly impair quality of life and is a major risk factor for sudden cardiac death, particularly in patients with structural heart disease [39, 40]. VT often precedes ventricular fibrillation, a lethal condition that requires immediate intervention [41, 38]. Mechanistically, VT can be focal or reentrant, with reentrant VT typically associated with myocardial infarction-induced scar tissue [42, 43]. VT mapping and ablation are complicated by the instability of the arrhythmia during episodes, necessitating advanced mapping strategies to improve treatment outcomes.

In this dissertation, AF, MRAT, and VT will serve as the primary clinical validation scenarios. AF is the most common atrial arrhythmia, atypical MRAT is challenging due to its diverse reentrant circuits and slow conduction regions that make ablation time-intensive, and VT poses significant risks in ventricular pathology. By focusing on these three arrhythmias, this research aims to develop advanced signal processing techniques that optimize the use of high-density catheters, ultimately enhancing diagnostic and therapeutic interventions for these conditions.

1.2 Objectives

This doctoral research aims to explore the potential of high-density catheters, combined with advanced digital signal processing techniques, to deepen our understanding of the electrophysiological (EP) mechanisms underlying arrhythmias. The project will adopt a translational approach, beginning with in-silico simulations to model cardiac electrical activity in a controlled environment. These simulations will be followed by animal studies to validate the proposed methods under predefined experimental conditions. Finally, retrospective clinical experiments will be performed to assess the efficacy of these methods in real world scenarios.

The primary objective is to leverage the capabilities of new high-density catheters for intracavitary signal acquisition and enhance the accuracy of arrhythmia characterization and treatment through advanced signal processing and mapping techniques. Specifically, the following tasks have been outlined:

1. **Study limitations of multielectrode catheters for omnipolar EGM estimation:** Investigate the challenges and constraints associated with using diagnose multielectrode array catheters in the estimation of omnipolar EGM conceived as a virtual bipolar EGM aligned with the direction of propagation.
2. **Develop and validate techniques to improve omnipolar EGM reconstruction:** Propose and test new methods to enhance the reconstruction quality of omnipolar EGMs, aiming for a more precise and reliable representation of the underlying EP activity.
3. **Propose new metrics to quantify local electrical disarray:** Introduce and validate novel metrics for local quantification of inhomogeneous conduction, a key characteristic of impaired EP tissue. These metrics will be developed to better identify arrhythmogenic substrates.
4. **Propose new metrics to quantify global electrical disarray:** Examine the global spatio-temporal heterogeneity of the substrate using global mapping techniques with intra-cardiac catheters.
5. **Translate improved diagnostic techniques to clinical settings:** Assess the applicability of enhanced omnipolar EGM reconstruction techniques and new metrics in a clinical context, investigating their relevance for diagnosing and treating patients with complex arrhythmogenic substrates.

Ultimately, this work aims to develop tools that enhance the diagnosis and treatment of arrhythmias, enabling more accurate mapping and characterization of arrhythmogenic substrates. By addressing both atrial and ventricular arrhythmias, this research will expand our understanding of cardiac EP and provide a foundation for improving clinical outcomes in patients with these complex conditions.

1.3 Hypotheses

We hypothesize that by developing advanced signal analysis methods for high-density catheters, we can more effectively characterize arrhythmogenic tissue, leading to a better understanding of the mechanisms underlying arrhythmia initiation and perpetuation, with a focus on clinical applications.

Specifically, the first hypothesis is that in high-density multi-electrode catheters, the recordings from four electrodes arranged in a 2x2 square can be used to reconstruct omnipolar signals. We further hypothesize that these signals can overcome the limitations of current triangular omnipoles, bipoles, and unipoles, particularly in terms of orientation independence.

Secondly, we hypothesize that using a robust representation of omnipolar signals, we can create accurate propagation maps that serve to design biomarkers to quantify the heterogeneity of electrical propagation patterns in patients with arrhythmias. These biomarkers could be used to identify regions of interest in substrate mapping within clinical settings.

Our third hypothesis is that raw unipolar signals from global mapping catheters can be analyzed to evaluate the spatio-temporal heterogeneity of propagation patterns. These metrics could be used to identify the etiologies or spectra of clinical responses in patients with atrial or ventricular arrhythmias.

1.4 Structure of this dissertation

This dissertation is presented as a compendium of articles and is structured as follows. Chapter 1 introduces the motivation, hypothesis, main objective, and subobjectives of the thesis. This is followed by chapter 2, which provides the necessary background knowledge, covering both physiological aspects (first three sections) and methodological aspects (last three sections). The subsequent six chapters (from chapter 3 to chapter 8) constitute the *compendium of articles* that form the core of this doctoral thesis. These chapters compile the research work conducted up to 2023 and published by 2024.

In a nutshell, chapter 3 explores non-invasive methods to assess intra-cardiac signal propagation, conduction velocity (CV), and patterns, providing a means to non-invasively differentiate between AFL types. Shifting to a more invasive standpoint, Chapter 4 introduces the novel concept of the cross-omnipole in high density multi-electrode catheters, demonstrating its superiority over previous configurations and validating it through simulations. Chapter 5 builds on this by validating the cross-omnipole configuration in an animal model. Expanding on these foundations, chapter 6 presents a local heterogeneity metric for characterizing propagation patterns at a local level in cardiac tissue, while chapter 7 evaluates its clinical potential to identify isthmus regions in VT patients using substrate maps. Lastly, chapter 8 extends the concept by evaluating the global heterogeneity of electrical patterns in the atria and validating the approach in AF patients, assessing a spectrum of clinical responses.

The final chapters include chapter 9, which discusses the thesis as a whole and reflects on the work presented in the various chapters. This section also addresses limitations, future directions, and how the findings align with the initial hypotheses and objectives. Lastly, chapter 10 presents the conclusions and impact of the research conducted in this dissertation.

Chapter 2

State of the Art

This Chapter provides an overview of the state of the art, beginning with a clinically focused exploration of the electrophysiological processes underlying cardiac arrhythmias. The first three sections focus on key aspects of heart anatomy, electrophysiological conduction, and the mechanisms behind different arrhythmias. The third, fourth and fifth sections transition to a more technical perspective, with an emphasis on signal processing methods, including the non-invasive and intracardiac measurement of cardiac activity, electrograms, and advanced techniques in mapping and analyzing electrophysiological signals.

2.1 The heart: role and anatomy

The heart is the central organ in the cardiovascular system, responsible for maintaining the continuous flow of blood to meet the metabolic demands of the body. This section provides an overview of the heart's role in both pulmonary and systemic circulation, highlighting how its anatomical structures and mechanical functions work in concert to sustain life. Additionally, it explores the structural details of the heart, offering insight into how these components contribute to the overall efficiency of the circulatory system.

2.1.1 The cardiovascular system in a nutshell

The heart plays a crucial role in the circulatory system, which takes care of efficiently transporting substances across cells, tissues, and organs to meet the metabolic needs of a multicellular body. Simple diffusion is insufficient for this task, necessitating the heart's function as a powerful pump within the cardiovascular system. This system also includes blood vessels, which act as conduits, and blood, which carries solutes, water, and cells. The heart's pumping action supports two primary circulatory pathways: pulmonary circulation, moving blood from the right ventricle through the lungs to the left atrium, and systemic circulation, transporting blood from the left ventricle to the body's tissues and back to the right atrium. Arteries carry oxygen-rich blood from the heart to tissues, while veins return oxygen-depleted blood to the heart. This coordinated process ensures that oxygen is delivered to organs and tissues through red vessels and that deoxygenated blood is returned through blue vessels [44, 45].

2.1.2 Structural anatomy of the heart

Located in the chest, the heart is protected by the epicardium and the pericardium, a fibrous sac filled with a lubricating fluid. The heart wall, or myocardium, is primarily composed of cardiac muscle cells, while its inner surface is lined with the endothelium [44]. The pericardium and epicardium provide mechanical protection to the heart, with the pericardium serving as a shock absorber against physical impacts and the epicardium providing a smooth, frictionless surface for the heart to move within the chest cavity. The myocardium, being the muscular layer, is responsible for the contractile force needed to pump blood throughout the body. This muscle is unique in its endurance and rhythmic contractions, driven by the heart's intrinsic electrical conduction system.

The human heart consists of four chambers: two atria and two ventricles. Each side of the heart contains an atrium and a ventricle, separated by atrioventricular (AV) valves. The left AV valve, known as the bicuspid or mitral valve, and the right AV valve, known as the tricuspid valve, allow blood flow from the atria to the ventricles. The ventricles are divided by a muscular wall called the interventricular septum. AV valves are passive structures that open and close in response to pressure gradients; they open when the pressure in the atrium exceeds that in the ventricle and close when the pressure gradient reverses. These valves are anchored to the papillary muscles by chordae tendineae to maintain their function [46, 47]. A schematic representation of the human heart is depicted in fig. 2.1.A.

To ensure blood flows into the arteries during ventricular contraction and to prevent backflow into the ventricles during relaxation, the heart contains semilunar valves located in the pulmonary trunk and the aorta. The pulmonary valve, situated in the pulmonary trunk, and the aortic valve, located in the aorta, operate based on pressure gradients between the ventricles and the arteries[44, 47]. These valves are crucial for maintaining unidirectional blood flow through the heart and into the systemic and pulmonary circulations.

Understanding the orientation of the heart within the thorax is essential for interpreting its anatomical planes, and how they may affect the representation of non-invasive recordings such as electrocardiograms (ECGs) and reconstructions of these such as the VCG. While the body is traditionally studied in coronal, axial, and sagittal views, the heart's primary planes are conventionally the long-axis, four-chamber, and short-axis, corresponding to frontal, horizontal, and sagittal views, respectively [48]. These reference systems are not aligned, which must be considered when examining anatomical representations [49].

Left atrial anatomy

Of noticeable importance for this dissertation is the left atrial chamber, given the significance of AF and flutter in the field of EP. The left atrium is the highest and most posterior chamber of the heart, receiving oxygenated blood, which is then pumped into the left ventricle for systemic circulation.

Separated from the right atrium by the obliquely positioned inter-atrial septum, the left atrium has a cuboidal shape and is surrounded by anterior, left lateral, medial, posterior, and superior walls [50]. The anterior wall is situated behind the pericardial sinus and the aortic root, while the posterior wall houses the terminal ends of the pulmonary veins[51]. Notably, the atrial wall behind the aorta is fragile, which is important during catheter ablation treatments for atrial tachyarrhythmias, such as AFL [52]. Compared to the right atrium, the left atrium is smaller and thicker, with three primary openings: the mitral valve distally, the left atrial appendage (LAA) laterally, and the pulmonary veins proximally [51]. The wall narrows near the mitral annulus.

The structure of the left atrium originates from the pulmonary veno-atrial junctions, bordered by fibro-fatty tissue, which transitions into the atrioventricular junction at the mitral orifice [53]. There is an aperture from the body of the left atrium to the LAA, which is smaller, slenderer, and more curved than in the right atrium. Blood enters the left atrium through the inferior and superior pulmonary veins, which also includes the LAA on the lateral side, a septal portion, and an inferior vestibule. The left lateral ridge is a common site for ectopic foci, often treated through ablation procedures [54]. Ectopic foci are abnormal pacemaker sites outside the sinoatrial node that can disrupt the heart's normal rhythm [55]. An overall view of the anatomical structures discussed can be seen in fig. 2.1.B.

2.2 Electrophysiology behind the pulse

The heart's rhythmic contractions are governed by intricate electrophysiological processes, which are essential for maintaining effective blood flow throughout the body. This section begins by examining the heart's conduction system, highlighting how electrical impulses are generated and propagated to control the heartbeat. It then explores the mechanisms behind cardiac action potentials, the electrical signals that trigger muscle contractions. Finally, it discusses how these signals spread across the heart to ensure the coordinated pumping action of the atria and ventricles.

2.2.1 Electrophysiology and conduction system

The heart muscle cells, organized in tightly bound thin layers, form the myocardium and contract approximately once per second, totaling around three billion times over a typical lifespan [44]. Heart cell activation is heavily influenced by innervation. Sympathetic postganglionic fibers from thoracic and spinal nerves innervate both atria and ventricles, releasing norepinephrine onto beta-adrenergic receptors on cardiac muscle cells [57]. In contrast, parasympathetic fibers from the vagus nerve innervate the atria, acting on muscarinic receptors for acetylcholine [58].

2.2.2 Cardiac action potentials

Cardiac contraction signals originate in the autorhythmic cells of the myocardium, which are noncontractile and interconnected via gap junctions that enable the rapid spread of depolarization [59, 60]. An action potential (AP) is triggered when the membrane potential reaches a specific threshold, causing rapid depolarization followed by repolarization. The resting membrane potential of myocardial contractile

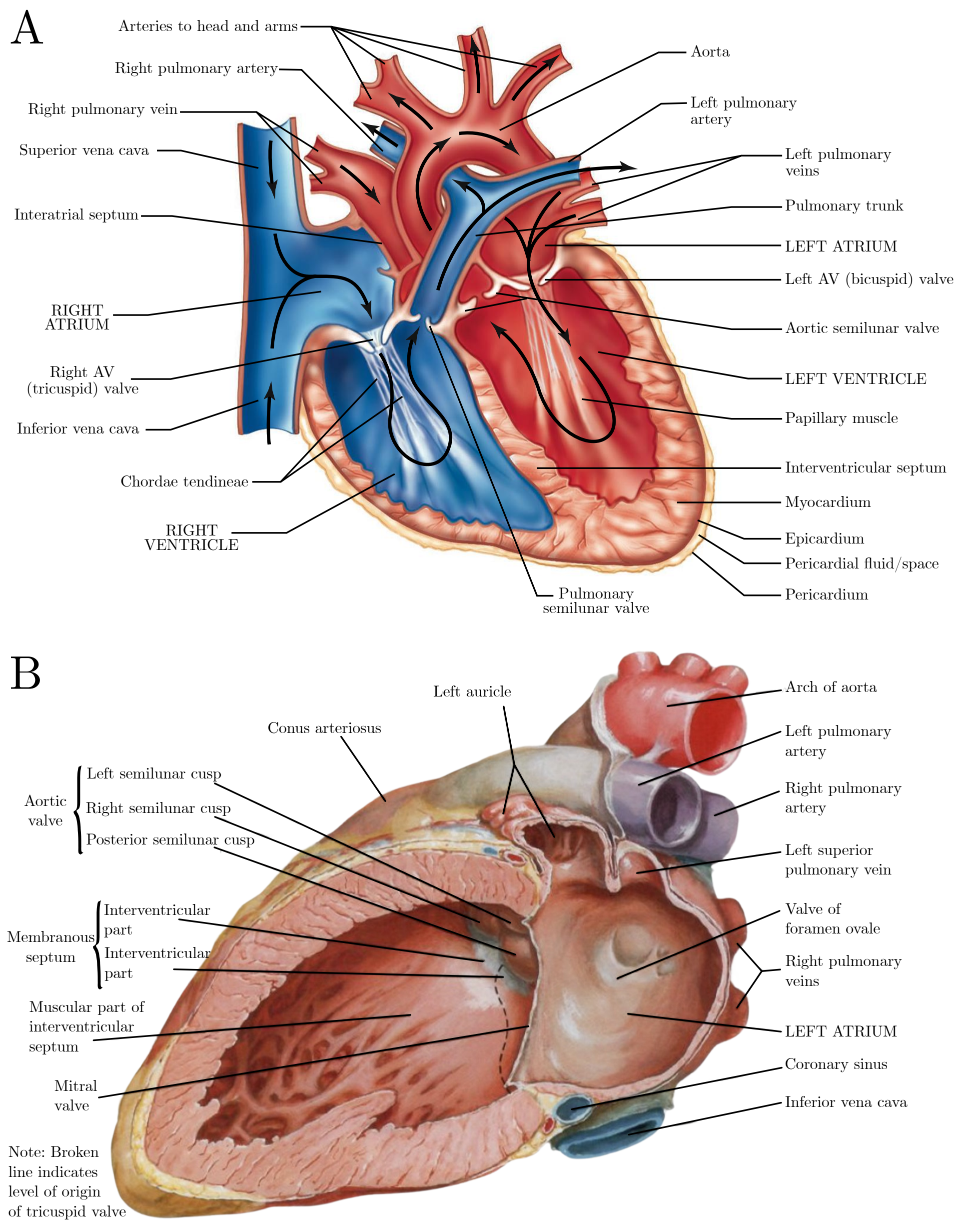

Figure 2.1: **A**: shows the anatomy of the heart in a sagittal section, highlighting the right (blue) and left (red) sides that correspond to the pulmonary and systemic circulations, respectively. The right atrium and right ventricle are part of the pulmonary circulation, depicted in blue, where deoxygenated blood is directed towards the lungs. On the other hand, the left atrium and left ventricle, depicted in red, are part of the systemic circulation, carrying oxygenated blood to the body. Arrows indicate the direction of blood flow through the heart chambers and major vessels. Key anatomical structures such as valves (tricuspid, bicuspid/mitral, aortic, and pulmonary valves), septa (interatrial and interventricular), and key vessels (pulmonary arteries, veins, and aorta) are labeled for clarity. This image was retrieved from [44]. **B**: offers a detailed view of the left atrium, showing a cut through this chamber and the adjacent structures. This diagram highlights important features such as the aortic valve and the structure of the left atrial appendage. The image has been worked over a figure in [56].

cells is closer to the equilibrium potential of potassium ions (-90mV) than that of sodium ions (+60mV), indicating higher potassium permeability [60]. During depolarization, voltage-gated sodium channels open, allowing sodium ions to enter and depolarize the cell. Repolarization involves the transient opening of potassium channels, resulting in a distinctive action potential plateau (Figure 2.2).

Autorhythmic cells exhibit a pacemaker potential, an unstable membrane potential due to the influx of positive charges through funny current (I_f) channels, leading to spontaneous depolarization. Depolarization in myocardial cells triggers the opening of voltage-gated calcium channels (L-type), balancing potassium efflux and creating the action potential plateau. Eventually, these calcium channels close, and potassium efflux through open channels returns the membrane potential to its resting state [61].

The strength of cardiac muscle contraction varies depending on the amount of calcium ions entering the cell, which in turn triggers further calcium release from the sarcoplasmic reticulum [62, 63]. The heart rate is influenced by epinephrine and norepinephrine acting on β_1 receptors, which increase the rate of pacemaker depolarization, while acetylcholine from the vagus nerve reduces the heart rate via muscarinic receptors. Nodal cell APs differ from those of myocardial contractile cells, featuring slow depolarization that ensures a continuous heartbeat without a stable resting potential [61].

2.2.3 Electrophysiological signal propagation: the heartbeat

Effective pumping of blood through the pulmonary and systemic circulations requires atrial contraction to precede ventricular contraction, initiated by muscle cell depolarization spread via gap junctions [65, 66]. The sinoatrial node (SN) serves as the heart's pacemaker, generating APs that trigger myocardial depolarization and contraction [67, 68]. The heart rate is thus determined by the SN's discharge rate [69, 70].

Although located in the right atrium, the SN's rapid conduction ensures simultaneous atrial contraction. The APs then travel to the ventricles via the atrioventricular node (AN), which delays conduction to allow complete atrial contraction before ventricular excitation. Internodal pathways facilitate AP conduction through the atria [66]. Post-AN excitation, the AP propagates through the bundle of His along the interventricular septum, branching into left and right pathways and into Purkinje fibers within the ventricular walls. This rapid conduction ensures synchronous ventricular contraction and coordinated heart function.

2.3 Cardiac arrhythmias

Cardiac arrhythmias encompass a wide range of abnormal heart rhythms that can significantly affect patient outcomes, varying from benign conditions to life-threatening episodes. In this section, we focus on atrial flutter AFL, atrial fibrillation AF, and ventricular tachycardia VT, as these arrhythmias represent key clinical scenarios in which our proposed techniques will be applied. Each of these conditions presents unique pathophysiological mechanisms that provide valuable information to develop targeted diagnostic and therapeutic approaches.

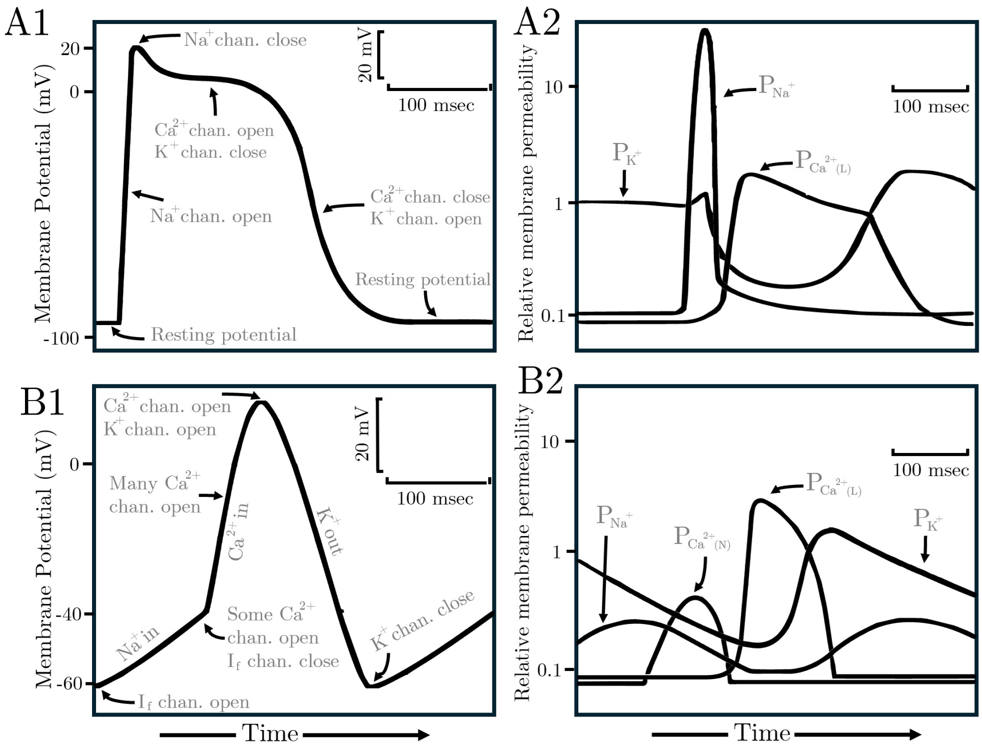

Figure 2.2: Membrane potential and ion permeability of cardiac cells. A1: Depiction of the action potential in myocardial contractile cells, highlighting key ion permeability changes for Ca^{2+}, Na^+, and K^+. **A2**: Temporal changes in ion permeability during the action potential of contractile cells. **B1**: Illustration of the action potential in autorhythmic cells of the myocardium, showing ion permeability changes for Ca^{2+}, Na^+, and K^+, and the activity of funny current (I_f) channels. **B2**: Time course of ion permeability variations in autorhythmic cardiac cells. This figure is inspired on figures from [44, 56, 64].

2.3.1 Atrial flutter

AFL is a type of supraventricular tachycardia, characterized by a distinctive, uniform, and regular ECG waveform. AFL is physiologically defined by a macroreentrant circuit (MC), where the electrical activity circulates around a large anatomical obstacle, often in a circular or elliptical pattern, commonly repetitive. The most common form of AFL occurs in the right atrium (RA) and is referred to as typical or common AFL, where the tricuspid valve acts as the central obstacle around which the reentry circuit revolves [71].

The electrocardiographic signal of AFL is often marked by a characteristic "sawtooth" pattern, most evident in leads II, III, and aVF. In typical AFL, the MC is anatomically constrained by structures such as the venae cavae and crista terminalis, with the cavotricuspid isthmus (CTI) serving as a critical component of the circuit. The electrical signal in common AFL must traverse the CTI, which is crucial for the perpetuation of the arrhythmia. The atrial rate in AFL typically ranges between 150 and 320 beats per minute, depending on the conduction ratio with the ventricles [72].

AFL can be classified into typical and atypical forms. Typical AFL is more common and occurs in the RA. Conversely, atypical AFLs can occur in either the right or left atrium, involving reentrant circuits around various obstacles, such as the mitral valve in the case of perimitral AFL. Atypical AFL is often associated with structural heart disease or post-surgical atrial scarring, which can create electrically silent areas that facilitate reentry [73]. The ECG patterns in atypical AFL are more variable but still exhibit the repetitive atrial activity within the QRS complexes.

The treatment of AFL primarily involves catheter ablation, especially in cases of typical AFL where the target is the CTI. In this case, ablation aims to create a line of conduction block between the tricuspid valve and the inferior vena cava, thereby interrupting the reentrant circuit and preventing the continuation of the arrhythmia. This procedure is guided by EP mapping, which allows for precise localization of the circuit and effective delivery of ablation energy. While radiofrequency (RF) ablation is the most commonly used technique, cryoablation is also employed in certain cases, depending on the specific anatomical and clinical considerations [74]. The success rate of catheter ablation for AFL is high, making it a preferred treatment option for long-term rhythm control.

2.3.2 Atrial fibrillation

AF is the most common sustained cardiac arrhythmia, characterized by rapid and irregular atrial activity. It significantly increases the risk of stroke, thromboembolism, heart failure, and overall mortality [75]. The prevalence of AF escalates with age, particularly in those with underlying conditions such as hypertension, coronary artery disease, and heart failure [76]. Studies, including the Framingham study, have reported that the lifetime risk of developing AF is approximately 25% for men and women aged 40 years and older [77, 78].

AF is typically classified into paroxysmal, persistent, and permanent forms, depending on the duration and frequency of episodes [79, 80]. Electrocardiographically, AF is identified by the absence of discrete P waves and an irregular R-R interval, indicative of disorganized atrial electrical activity. The management of AF involves strategies for either rhythm control, which aims to restore and maintain sinus rhythm, or rate control, which focuses on controlling the ventricular rate while accepting AF as the persistent rhythm. Stroke prevention through anticoagulation is a central aspect of AF management due to the high risk of thromboembolic events associated with this condition [80, 81].

Catheter ablation has become a widely accepted treatment for symptomatic, drug-refractory AF, particularly in younger patients and those without significant structural heart disease. This procedure typically involves the isolation of the pulmonary veins, which are often the source of ectopic foci that trigger AF, thereby preventing the recurrence of the arrhythmia [54, 82, 83].

2.3.3 Ventricular tachycardia

VT is a severe arrhythmia that originates from the ventricles and is defined by three or more consecutive QRS complexes occurring at a rate greater than 100 beats per minute [38]. Episodes of VT can significantly reduce the quality of life and increase the risk of mortality [39, 40]. VT is the most common sustained arrhythmia and is a precursor to ventricular fibrillation, a leading cause of sudden cardiac death [41, 38]. The risk of VT is particularly high in patients with underlying structural heart disease, where it can lead to cardiac arrest or sudden cardiac death. VT can arise from several pathological conditions, including myocardial infarction, structural heart abnormalities, inherited arrhythmia syndromes, and electrolyte imbalances [84].

VT can be classified based on duration, morphology, hemodynamic characteristics, and underlying mechanisms. Hemodynamically, VT may be classified as stable or unstable. Stable VT might present with minimal symptoms, while unstable VT requires immediate medical intervention due to significant impairment of cardiac function. The latter condition often results in unmappable tachycardias, complicating the mapping and treatment of the arrhythmia during episodes [38]. This instability is a key factor in selecting appropriate mapping strategies for ablation.

Mechanistically, VT can be either focal or reentrant. The earlier results from abnormal automaticity or triggered activity from a specific area, spreading activation in all directions. Conversely, reentrant VT, the more common type, is associated with myocardial infarction, where the formation of scar tissue disrupts normal electrical conduction [42, 43].

Scar-related VT

Scar-related VT is the predominant form observed in patients with structural heart disease [85]. It involves reentrant circuits within fibrotic or scarred myocardial regions, where slow and heterogeneous electrical conduction through narrow myocardial channels supports the reentrant activity by re-exciting previously depolarized tissue [86, 87]. This substrate is characterized by regions of slow conduction and unidirectional block, which are crucial for the maintenance of the reentrant circuit [43]. The three-dimensional structure of the reentrant circuit and substrate can vary widely, including subendocardial, intramural, or subepicardial localizations, and may extend across the entire ventricular wall [88, 89].

In the context of scar-related VT, understanding the anatomical and functional sites within the scar tissue that contribute to the arrhythmia is essential for effective mapping and ablation. The critical isthmus (IS) within the scar is a narrow channel of surviving myocardial fibers that allows electrical conduction. This region is marked by slow conduction and is bordered by areas of complete or functional block, sustaining the reentrant circuit [90, 85]. Targeting the isthmus during ablation is crucial for disrupting the reentrant circuit and terminating VT.

In later chapters we will refer to low voltage areas (LVAs) as bystander areas, comprising excitable tissue regions within the scar that are not part of the reentrant circuit but can be passively activated by the propagating wavefront [91]. On the other hand, normal voltage areas (NVAs), or alternatively healthy areas, are regions of the myocardium unaffected by the scar, maintaining normal electrical conduction properties. These regions can connect to the scarred myocardium and serve as the origin or exit point for the reentrant circuit [92]. A further description of these regions is provided in chapter 7.

2.4 Non-invasively measuring the cardiac activity

This section introduces the key principles behind non-invasive methods for measuring cardiac activity, focusing on the electrocardiogram (ECG). Beginning with the historical development of the ECG, it highlights the significant contributions of Willem Einthoven and the creation of Einthoven's Triangle, which laid the foundation for modern cardiac monitoring. It then discusses how the 12-lead ECG system has evolved to provide comprehensive views of the heart's electrical activity from various anatomical perspectives, enhancing diagnostic accuracy and understanding of cardiac function.

2.4.1 Introduction to the electrocardiogram

In the late 19th century, it was discovered that the heart's electrical activity could be detected through surface electrodes placed on the skin. Although the first human ECG was recorded in 1887 [93], substantial technological advancements were necessary before it could be widely used in clinical practice.

Known as the father of the modern ECG, it was Willem Einthoven who significantly advanced this technique by defining the standard components of the ECG signal by formulating the concept of 'Einthoven's Triangle' [94]. This triangle, formed by electrodes positioned on both arms and the left leg allowed to define the first three leads as:

$$\begin{aligned} \text{Lead I}: \quad & V_I = \Phi_L - \Phi_R && \text{(2.1a)} \\ \text{Lead II}: \quad & V_{II} = \Phi_F - \Phi_R && \text{(2.1b)} \\ \text{Lead III}: \quad & V_{III} = \Phi_F - \Phi_L && \text{(2.1c)} \end{aligned}$$

where V_I represents the voltage of Lead I, V_{II} represents the voltage of Lead II, V_{III} represents the voltage of Lead III, Φ_L denotes the potential at the left arm, Φ_R denotes the potential at the right arm, and Φ_F denotes the potential at the left foot [95, 96].

From these leads, referred to as Einthoven's limb leads, the following relationship can be derived following Kirchhoff's second law:

$$V_{II} = V_I + V_{III} \tag{2.2}$$

This framework was expanded by the augmented limb leads (aVR, aVL, and aVF), introduced by Goldberger, whose motivation was to measure the potential difference between a single electrode and a reference point defined as the midpoint of the other two electrodes [97]. These augmented leads can be expressed as combinations of the left arm, left foot, and right arm potentials as:

$$V_{aVR} = \Phi_R - \frac{\Phi_L + \Phi_F}{2} \tag{2.3a}$$

$$V_{aVL} = \Phi_L - \frac{\Phi_R + \Phi_F}{2} \tag{2.3b}$$

$$V_{aVF} = \Phi_F - \frac{\Phi_R + \Phi_L}{2} \tag{2.3c}$$

Using eq. (2.1a), eq. (2.1b), and eq. (2.1c), Goldberger leads can be expressed as a function of Einthoven's leads as follows:

$$V_{aVR} = -V_I + \frac{V_{III}}{2} \tag{2.4a}$$

$$V_{aVL} = V_I - \frac{V_{II}}{2} \tag{2.4b}$$

$$V_{aVF} = V_{III} + \frac{V_I}{2} \tag{2.4c}$$

In 1944, the precordial leads (V_1, V_2, ..., V_6) were introduced by Wilson, with the aim of measuring potentials closer to the heart [98]. This led to the development of the 12-lead ECG system used today, which, despite some leads being derivable from others, enhances pattern recognition by providing different vector projections in orthogonal planes. Particularly, the precordial leads are placed on the chest as follows: V_1 is placed in the fourth intercostal space to the right of the sternum, while V_2 is placed in the fourth intercostal space to the left of the sternum. V_3 is positioned diagonally between V_2 and V_4. V_4 is placed between the fifth and sixth ribs in the midclavicular line. V_5 is on the same level as V_4 but in the anterior axillary line, and V_6 is on the same level as V_4 and V_5 but in the midaxillary line. Additionally, the anatomical aspects of these leads further refine their clinical utility: V_1-V_2, considered the septal leads, primarily observe the ventricular septum but can also display ECG changes originating from the right ventricle. Conversely, V_3-V_4, or anterior leads, allow understanding conduction at the anterior wall of the left ventricle. Lastly, V_5-V_6, or anterolateral leads, represent the lateral wall of the left ventricle. These placements are of interest for capturing the heart's electrical activity from various angles, thereby enhancing the diagnostic accuracy of the ECG [99].

2.4.2 Twelve-lead ECG patterns and features

The standard ECG (see fig. 2.3) captures various aspects of cardiac activity. The primary components are the P wave, the QRS complex, and the T wave.

The P wave reflects atrial depolarization, preceding atrial contraction. The QRS complex, representing ventricular depolarization, follows. Ventricular repolarization is indicated by the T wave.

Depolarization spreads across the atria or ventricles, prompting muscle contraction. Hence, the P wave marks the start of atrial contraction, and the QRS complex marks the beginning of ventricular contraction. The ventricles remain contracted until the

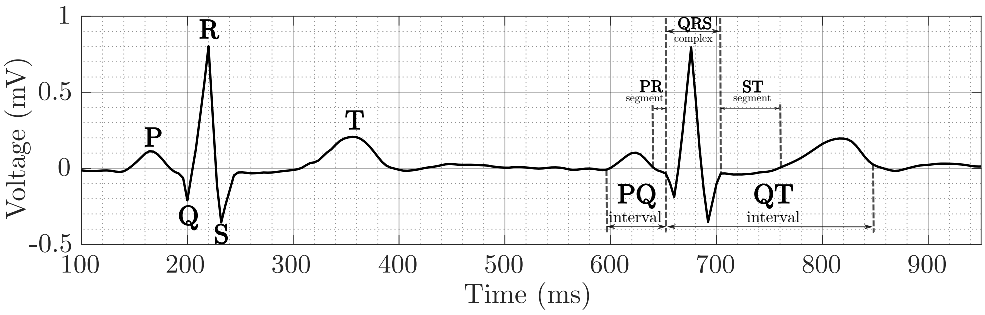

Figure 2.3: ECG Signal from a healthy patient. This processed signal from a healthy patient has been low and high pass filtered. P, Q, R, S, and T waves are shown on the left beat, while PQ and QT intervals, PR and ST segments, and the QRS complex are labeled on the right beat.

end of the T wave. Atrial repolarization overlaps with the QRS complex, rendering the atrial T wave unobservable in a standard ECG.

The ECG signal's voltage depends on electrode placement relative to the heart. For the QRS complex, this voltage ranges from 1 to 1.5 mV, measured from the R wave's lowest to the S wave's highest point. The P wave's amplitude ranges from 0.1 to 0.3 mV, and the T wave ranges from 0.2 to 0.3 mV.

The P-Q or P-R interval spans from the start of the P wave to the onset of the QRS complex, representing the time between atrial and ventricular excitation. It is commonly referred to as the P-R interval due to the frequent absence of the Q wave.

The Q-T interval extends from the beginning of the Q wave to the end of the T wave, covering the duration of ventricular contraction. In cases where the Q wave is absent or poorly defined, the interval is measured from the R wave.

2.4.3 Vectorial analysis of the cardiac cycle

The cardiac electric potential at a specific instant in time can be represented by a vector encoding both direction and magnitude. This can be generated based on the current flow, with a length proportional to the voltage difference of the potential across the heart anatomy.

At the moment of ventricular septum depolarization, current flows from depolarized to non-depolarized areas, primarily toward the apex from the ventricular base. The instantaneous mean vector, summing all vectors generated at that instant, points in this direction, indicating the substantial current and potential (fig. 2.4).

Vectors are labeled by direction, standardized for universal understanding. Leftward is 0 degrees, downward is +90 degrees, and upward is either +270 or -90 degrees (fig. 2.4.B). The mean QRS vector aligns with +59 degrees. Lead directions correspond accordingly to 0°, +60°, and +120° for leads I, II, and III, and +90°, +210°, and +330° (or -30°) for leads aVF, aVR, and aVL, respectively. The mean QRS vector's alignment with lead II makes it preferred for cardiac signal representation. These directions are summarized in fig. 2.4.B

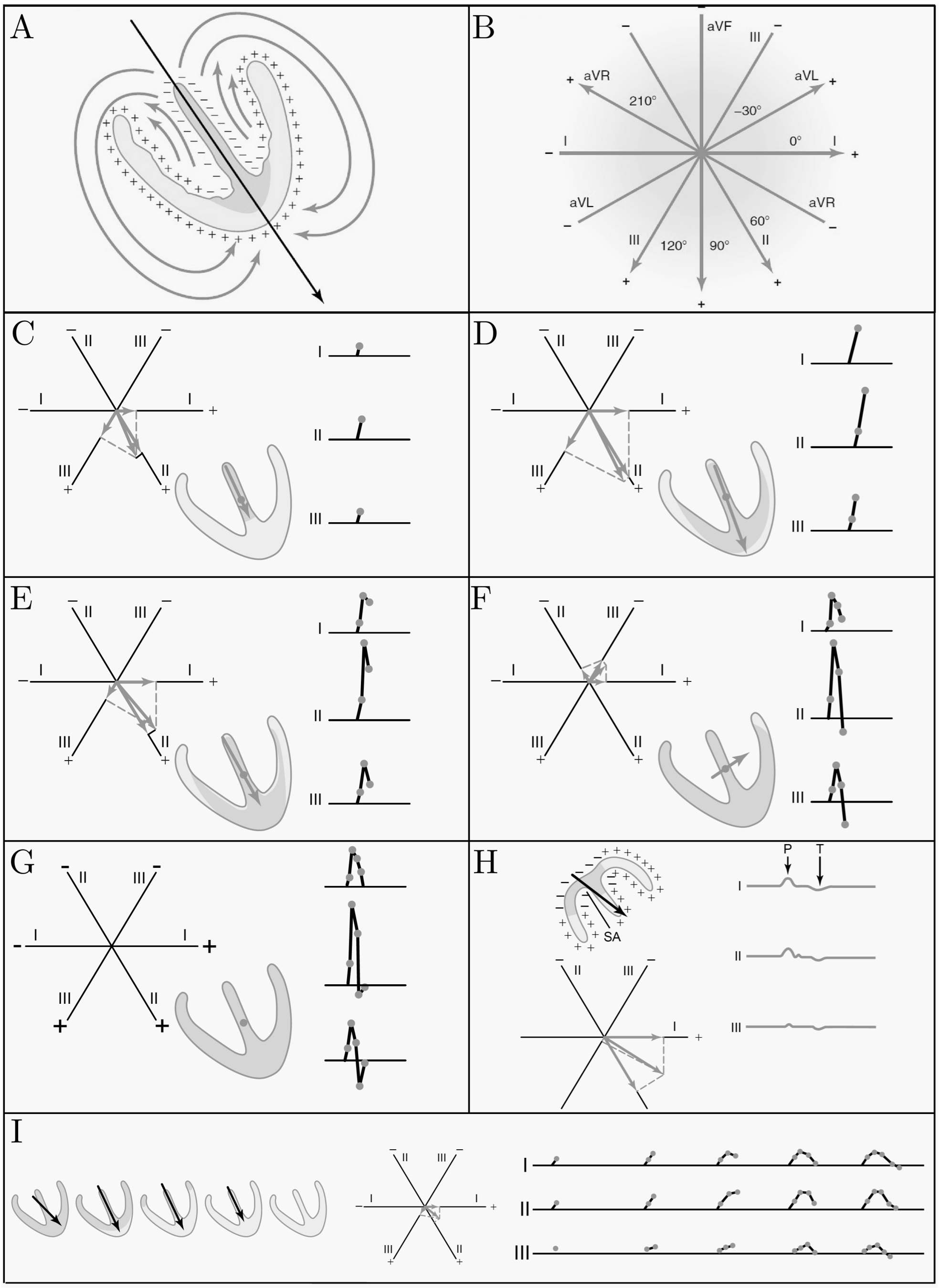

Figure 2.4: Mean vector and standard directions of mean potential vectors. A: Mean vector during ventricular septum depolarization. **B:** Standard directions of mean potential vectors relative to leads I, II, III, aVR, aVL, and aVF. The left side of the chest is at 0º, with anatomical drawings mirrored (figures adapted from [100]).

QRS complex from a vectorial standpoint

The QRS complex marks the initiation of ventricular depolarization, rapidly spreading across the endocardial surfaces of the septum (fig. 2.4.C left). At approximately 0.01 seconds after the onset of depolarization, the vectors are small due to limited depolarization, with lead II showing a significantly larger vector as it aligns with the current flow through the septum. This results in a positive voltage increment in the three leads (fig. 2.4.C right).

Depolarization then extends across the ventricular endocardial surfaces (fig. 2.4.D-E). At around 0.02 seconds (fig. 2.4.D), the vectors lengthen due to increased depolarization, notably in lead II. By 0.035 seconds after the initialization of the signal propagation at the SA node (fig. 2.4.E), the vectors shorten as the now electronegative heart apex, which neutralizing positive charges, shifts the vector axis leftwards, increasing the lead I voltage significantly more than lead III (fig. 2.4.E right).

Finally, the impulse travels through the ventricular muscle (fig. 2.4.F-H). At 0.05 seconds (fig. 2.4.F), the vector is short due to minimal positive charge flow, with a negative direction for leads II and III and positive for lead I, resulting in negative voltages for leads II and III (fig. 2.4.F right). In the last QRS complex step (fig. 2.4.G), the vector becomes zero as depolarization completes, returning all leads to baseline at 0 mV.

T wave from a vectorial standpoint

Following the QRS complex, ventricular repolarization occurs from 0.15 to 0.35 seconds post-depolarization onset (fig. 2.4.I). Repolarization starts at the ventricles' outer surfaces and ends at the endocardial areas due to reduced endocardial blood flow during contraction, causing the vector to point towards the apex (fig. 2.4.I middle). The T wave formation involves five steps (fig. 2.4.I right), with small initial vectors growing larger during mid-repolarization and weakening towards the end.

P wave and atrial T wave from a vectorial standpoint

The P wave results from atrial depolarization, starting at the sinoatrial node (SN) and spreading towards the atrioventricular node (AN) (fig. 2.4.H left). The vector originates at the SN, pointing towards the AN, showing positive voltage variations in leads I, II, and III (fig. 2.4.H right), with the smallest in lead III.

Atrial repolarization begins at the SN and proceeds slowly due to the absence of Purkinje fibers. Consequently, the vector points backwards as the SN becomes positive relative to the atrial muscle, causing negative voltage variations in leads I, II, and III (fig. 2.4.H right). However, this phenomenon is obscured in the ECG by the concurrent QRS complex, requiring specialized techniques to isolate the atrial signal.

2.4.4 The vectorcardiogram

In 1914, Williams first used the term ”vector” to describe the heart vector, representing the instantaneous dipole strength and direction of the heart's electrical activity [101]. The primary aim of electrocardiography is to dynamically measure this heart vector, requiring the use of a vectorcardiogram (VCG). The VCG employs three orthonormal leads (X, Y, and Z) aligned with the body's primary axes and normalized to measure the dynamic x, y, and z components of the heart vector [102].

By analyzing the combined amplitudes in the xy, xz, yz, and xyz planes and amplitudes, the VCG provides two-dimensional or three-dimensional patterns of cardiac movement. Notably, the lead Z amplitude in the sagittal plane peaks before lead Y, explaining why the largest ECG amplitude is often missed, as the heart vector's direction at that instant typically does not align with any lead vectors. Vectorcardiography addresses this by computing a fourth scalar lead, representing the vector magnitude via the Pythagorean theorem (root-sum-squared $x - y - z$ amplitudes).

Over the following decades, various VCG systems with distinct electrode configurations were developed. Prominent among these were systems by Burger et al. [103], McFee et al. [104], Schmitt et al. [105], and Frank [106], with the Frank system becoming the most widely adopted. Key figures in VCG development included Robert P. Grant [107] and J. Willis Hurst [108], who facilitated the routine clinical use of VCGs in the 1960s.

While comparative studies evaluating the performance of different VCG reconstruction methods on various downstream tasks exist [109, 110, 111], this topic lies outside the scope of this dissertation. Instead, we will follow the widely accepted reconstruction using the Inverse Dower Transform in the subsequent chapters. Specifically, we define:

$$\mathbf{VCG}(\tau) = \mathbf{W_{ITD}} \times \mathbf{ECG}(\tau) \tag{2.5}$$

where:

$$\mathbf{VCG}(\tau) = \begin{bmatrix} \mathbf{X_{VCG}}(\tau) & \mathbf{Y_{VCG}}(\tau) & \mathbf{Z_{VCG}}(\tau) \end{bmatrix}^{\mathrm{T}} \tag{2.6}$$

$$\mathbf{ECG}(\tau) = \begin{bmatrix} \ell_{\mathbf{V_1}}(\tau) & \ell_{\mathbf{V_2}}(\tau) & \ell_{\mathbf{V_3}}(\tau) & \ell_{\mathbf{V_4}}(\tau) & \ell_{\mathbf{V_5}}(\tau) & \ell_{\mathbf{V_6}}(\tau) & \ell_{\mathbf{I}}(\tau) & \ell_{\mathbf{II}}(\tau) \end{bmatrix}^{\mathrm{T}} \tag{2.7}$$

with $\ell_{\mathbf{x}}(\tau)$ representing the lead $\mathbf{x}$ over time, and the weight matrix for the Inverse Dower Transform:

$$\mathbf{W_{ITD}} = \begin{bmatrix} -0.172 & -0.074 & 0.122 & 0.231 & 0.239 & 0.194 & 0.156 & -0.010 \\ 0.057 & -0.019 & -0.106 & -0.022 & 0.041 & 0.048 & -0.227 & 0.887 \\ -0.229 & -0.310 & -0.246 & -0.063 & 0.055 & 0.108 & 0.022 & 0.102 \end{bmatrix} \tag{2.8}$$

2.5 Electrical propagation through the cardiac tissue

Although surface ECGs provide valuable insight into the electrical activity of the heart, they are limited by their external nature. To gain a more detailed understanding of the electrophysiological processes of the heart, particularly in the diagnosis and treatment of arrhythmias, we must explore intracardiac signals with focus on

EGMs, which offer a closer view of electrical propagation directly within cardiac tissue. The EGM signal can be understood as the recording of potential changes in the cells adjacent to an electrode, resulting from the propagation of the action potential described in Section section 2.2.2 across the tissue. In this section, we get inspiration from Abdi et al. [112] to describe the propagation of cardiac AP, how EGM signals can be modelled as a sum of transmembrane currents of cells in the vicinity of the recording electrodes, and how transmembrane currents can be estimated by solving an interpolation-deconvolution problem.

2.5.1 Propagation of the action potential signal

Using the reaction-diffusion equation [113] as a reference, the action potential propagation in a two-dimensional framework and the transmembrane current can be expressed as:

$$Q\frac{\partial V(x_c, y_c, \tau_c)}{\partial \tau} = \mathcal{I}(x_c, y_c, \tau_c) + \mathcal{I}_{st}(x_c, y_c, \tau_c) - \mathcal{I}_{ion}(x_c, y_c, \tau_c, V), \tag{2.9}$$

$$\mathcal{I}(x_c, y_c, \tau_c) = S_v^{-1} \nabla \Sigma(x_c, y_c) \nabla V(x_c, y_c, \tau_c). \tag{2.10}$$

where $V(x_c, y_c, \tau_c)$ is the cell potential at time τ_c and location (x_c, y_c), $Q = 1\,\mu\mathrm{F\,cm}^{-2}$ is the total membrane capacitance, $\mathcal{I}_{st}$ is the stimulus current, $\mathcal{I}_{ion}$ is the total ionic current computed according to the Courtemanche model [114], $S_v = 0.24\,\mu\mathrm{m}^{-1}$ is the surface-to-volume ratio at the cellular level, and $\Sigma(x_c, y_c)$ is the intracellular conductivity tensor [112].

2.5.2 Electrogram signals

Conceptualizing a single EGM times series as a weighted sum of transmembrane currents generated by individual cells, we can define these weights are inversely proportional to the distance between each cell and the recording electrode. Given a cell positioned at (x_c, y_c) and an electrode at (x_m, y_m) with a fixed height z_0 above the two-dimensional tissue plane, the distance between them is given by $\sqrt{(x_c - x_m)^2 + (y_c - y_m)^2 + z_0^2}$. Accordingly, the EGM can be modeled as follows:

$$\Phi(x_m, y_m, \tau_c)_{EGM} = \frac{1}{4\pi\sigma_e}\int_S \frac{\mathcal{I}(x_c, y_c, \tau_c)}{\sqrt{(x_c - x_m)^2 + (y_c - y_m)^2 + z_0^2}} dS(x_c, y_c), \tag{2.11}$$

where m ranges from 1 to M, the total number of electrodes, S represents the surface area containing the modeled cells, $S(x_c, y_c)$ is the differential surface area element, and σ_e is the constant extracellular conductivity [113]. This model incorporates the spatial convolution of the transmembrane current $\mathcal{I}(x_c, y_c, \tau_c)$ with a distance-dependent kernel $\kappa_0(x_c, y_c) = \frac{1}{\sqrt{x_c^2 + y_c^2 + z_0^2}}$. The spatial sampling performed by the electrode array is captured by the sampling operator ς_0, which is given by $\varsigma_0(x_c, y_c) = \sum_{m=1}^{M} \delta(x_c - x_m)\delta(y_c - y_m)$, where $\delta(x_c)$ is the Dirac delta function. The EGM, as modeled in eq. (2.11), can thus be reformulated as:

$$\Phi(x_c, y_c, \tau_c)_{EGM} = \frac{1}{4\pi\sigma_e}\left[\varsigma_0(x_c, y_c)\kappa_0(x_c, y_c) \circledast \mathcal{I}(x_c, y_c, \tau_c)\right], \tag{2.12}$$

where $\circledast$ represents a two-dimensional spatial convolution. In this formulation, we assume that the electrode's physical dimensions are small enough to be considered negligible, as proved in this framework by Abdi et al. [112].

To address the inverse problem, eq. (2.12) can be discretized in both spatial and temporal domains. Spatially, this involves replacing blocks of cells within the three-dimensional tissue with modeled *cells* on a uniform 2D grid, where the cell-to-cell spacing is Δx and the grid size is $N = r_c \times c_e$, representing the number of cells along the grid's rows and columns, respectively. Temporal sampling is performed with a sampling period T, resulting in T_s discrete time steps. The resulting discretized convolution model for the EGM is expressed as:

$$\Phi[x, y, \tau] = k\varsigma_0[x, y]\left[\kappa_0[x, y] \circledast \mathcal{I}[x, y, \tau]\right], \tag{2.13}$$

where x, y and τ are integers indexing the sample grid, and $k = \frac{\Delta x^2}{4\pi\sigma_e}$. The sample spacing for the kernel, $\kappa_0[x, y]$, is determined by a limit of $(2n+1) \times (2n+1)$ grid points. To facilitate the convolution process, the modeled kernel is extended by n cells in each direction. The sampling operator $\varsigma_0[x, y]$ ensures that only the M measured spatial locations are considered, with all other locations excluded. This discrete model can then be readily transformed into a matrix-based representation [115].

2.5.3 Transmembrane currents

Estimating the transmembrane currents $\mathcal{I}[x, y, \tau]$ can be achieved by solving a deconvolution-interpolation problem. The deconvolution can be performed by minimizing the least square error between the observed EGM Φ and the estimated value $\varsigma_0(\kappa_0 \circledast \mathcal{I})$ – first term in eq. (2.14). Given the limited number of EGMs compared to modeled cells, and the low-pass filtering effect of the distance kernel, the inverse problem is inherently ill-posed, often leading to unstable solutions [112]. To address this, regularization techniques are introduced to stabilize the solution by incorporating prior knowledge of the expected outcome. A common choice is Tikhonov regularization [116], which imposes spatial constraints but may not provide sufficient interpolation, especially when the expected wave pattern is narrowly defined, as in fractionated EGMs [117, 118, 119]. A more effective approach assumes that sharp deflections in an EGM are indicative of wave propagation and AF. These deflections are captured in the first-order time derivative of the transmembrane current $\mathcal{I}'[x, y, \tau]$.

Assuming that the temporal derivative will have sparse, non-zero elements in fractionated EGMs, effectively capturing these rapid deflections, the first-order derivative of the transmembrane current can be considered sparse. To enforce this sparsity, an ℓ_1-norm constraint in the regularization function can be employed resulting in the optimization problem:

$$\min_{\mathcal{I}} ||\Phi - \varsigma_0(\kappa_0 \circledast \mathcal{I})||_2^2 + \lambda||\mathcal{I}'||_1 \tag{2.14}$$

where

$$||\mathcal{I}||_2^2 \triangleq \sum_x \sum_y \sum_\tau |\mathcal{I}[x, y, \tau]|^2, \tag{2.15}$$

$$||\mathcal{I}'||_1 \triangleq \sum_x \sum_y \sum_\tau |\mathcal{I}'[x, y, \tau]|, \tag{2.16}$$

and λ is the regularization parameter that controls the influence of the regularization term.

To manage the ℓ_1-norm and ℓ_2-norm terms in eq. (2.14), one can utilize the Split Bregman algorithm [120, 121], which decouples these terms by introducing splitting variables $Z_1 = \kappa_0 \circledast \mathcal{I}$ and $Z_2 = \mathcal{I}'$. The modified optimization problem becomes:

$$\min_{\mathcal{I}, Z_1, Z_2, B_1, B_2} ||\Phi - \varsigma_0 Z_1||_2^2 + \mu_1||Z_1 - (\kappa_0 \circledast \mathcal{I}) - B_1||_2^2 + \lambda||Z_2||_1 + \mu_2||Z_2 - \mathcal{I}' - B_2||_2^2 \tag{2.17}$$

where B_1 and B_2 are Bregman iterative parameters, and μ_1 and μ_2 are penalty parameters. This formulation allows the problem in eq. (2.17) to be broken down into five steps, each updating one unknown parameter $\mathcal{I}, Z_1, Z_2, B_1$, or B_2 [122]. Overall, by avoiding performing computations in the Fourier domain and computationally expensive matrix inversions, this algorithm proves fast convergence and a reasonable precision and accuracy in practice [112].

Lastly, it is important to recognize that the modeled cell size Δx in the inverse problem is significantly larger than a real cell size. Each modeled cell represents a cluster of cells in three-dimensional tissue. Consequently, the estimated transmembrane currents are more localized and should be interpreted as such.

2.5.4 Conduction velocity estimation

Conduction velocity (CV) describes the propagation of the wavefront impulse generated by action potentials, characterized by its speed and direction. CV measurements provide crucial information in both electrophysiology (EP) settings, where they help identify patterns and potential arrhythmogenic mechanisms [123, 124, 125, 126], and in laboratory settings, where they offer insights into the tissue's microarchitecture [127, 128]. Regions with slower CV are commonly associated with fibrosis, reduced connectivity, altered cellular coupling [129, 130, 131, 132, 133, 134, 135, 136], and reentry regions, which may correlate with arrhythmia initiation sites [130, 137]. However, due to the non-planar nature of the propagation wavefront [138, 139, 140], structural branching of the tissue [141, 142], the complex 3D structure of the cardiac walls, limited understanding of 3D propagation patterns [143, 144, 145], and the complex propagation patterns in cases of arrhythmias like AF, various methods of differing nature have been proposed to estimate CV [146]. Next, we describe and illustrate some of these methods (fig. 2.5).

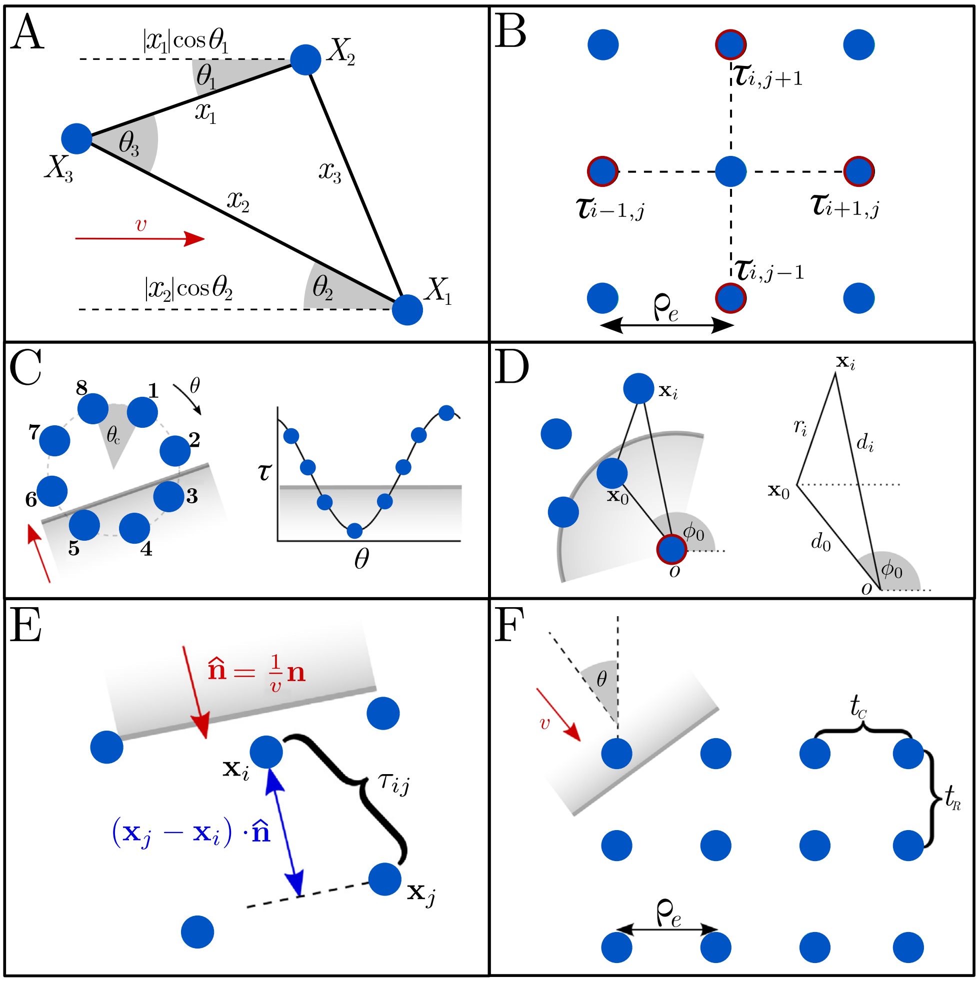

Figure 2.5: Summary of various techniques used for estimating CV. **A:** CV estimation using triangulation. The angle θ_3 is computed using the cosine rule based on known lengths x_1, x_2, and x_3. Angles θ_1 and θ_2 determine the wavefront's angle of incidence with respect to sides x_1 and x_2. **B:** Finite difference technique for CV estimation on a grid with electrode separation ρ_e. Activation gradients are computed horizontally and vertically using activation times from four highlighted electrodes. **C:** Planar wave activation across a circular catheter, estimated with a sinusoidal function fitting technique. Activation times at 8 electrodes fit a translated cos θ function. **D:** Circular wave CV and focal source o estimation using recording points at positions x_i. The distances from the focal source and the earliest activation point x_0 are denoted by d_i and r_i. **E:** Planar wavefront velocity estimation from differences in location and activation time. Inter-electrode distances normal to the wavefront and their time delays are used to estimate wavefront speed v. **F:** Planar wavefront velocity estimation from an equally spaced electrode grid using a MLE approach. Row and column time delays, t_R and t_C, are used to compute velocity through trigonometry. *The panels of this figure are based on figures from* [146].

Local measurement requirements

The spatial resolution is crucial for estimating CV, especially for complex, non-planar wavefront profiles. To achieve higher resolution, the spatial Nyquist criterion requires the inter-electrode distance to be less than half of the smallest relevant spatial wavelength [127]. Thus, when selecting an estimation method, one must consider the trade-off between achieving a high-resolution vector field, which may be susceptible to errors due to increased uncertainty in position and activation time measurements, and obtaining a more accurate lower-resolution estimation, which might miss important propagation patterns in the underlying substrate.

Triangulation

Applied in numerous clinical studies [147, 148, 149, 150], triangulation allows for the estimation of CV from a set of arbitrary points on the selected surface. These points can be appointed by an operator or automatically chosen using methods such as Delaunay triangulation [151] or edge completion [152]. As shown in fig. 2.5.A, there is a relationship between the angle of incidence of the propagating wave and the speed:

$$\cos\theta_2 = \cos(\theta_3 - \theta_1), \tag{2.18}$$

$$\mathbf{v} = \frac{|\mathbf{x}_1|\cos\theta_1}{t_a} = \frac{|\mathbf{x}_2|\cos\theta_2}{t_b}, \tag{2.19}$$

where the CV is represented by $\mathbf{v}$, the angle θ_3 at the earliest activation vertex $\mathbf{X}_3$ can be determined by:

$$\theta_3 = \arccos\left(\frac{|\mathbf{x}_1|^2 + |\mathbf{x}_2|^2 - |\mathbf{x}_3|^2}{2|\mathbf{x}_1||\mathbf{x}_2|}\right), \tag{2.20}$$

and the angles θ_1 and θ_2, originating from vertex $\mathbf{X}_3$, describe the angles between the wavefront and the edges of the triangle converging at such origin. One can then determine the direction of activation by solving for θ_1 as

$$\theta_1 = \arctan\left(\frac{t_b|\mathbf{x}_1| - t_a|\mathbf{x}_2|\cos\theta_3}{t_a|\mathbf{x}_2|\sin\theta_3}\right). \tag{2.21}$$

Finite differences

Well-suited for commonly used multi-electrode array catheters, finite differences between neighboring electrodes, as represented in fig. 2.5.B, have been used in various studies, including optical mapping studies [153, 154]. Using first-order finite differences to compute the vertical and horizontal components of the activation gradient:

$$\frac{\partial\tau}{\partial x} = \frac{1}{2\rho_e}\left(\tau_{i+1,j} - \tau_{i-1,j}\right)\mathbf{i}, \tag{2.22}$$

$$\frac{\partial\tau}{\partial y} = \frac{1}{2\rho_e}\left(\tau_{i,j+1} - \tau_{i,j-1}\right)\mathbf{j}, \tag{2.23}$$

one can estimate the direction of activation $\hat{\xi}$ as:

$$\hat{\xi} = \frac{\mathbf{i}\,\frac{\partial \tau}{\partial x}}{\sqrt{\left(\frac{\partial \tau}{\partial x}\right)^2 + \left(\frac{\partial \tau}{\partial y}\right)^2}} + \frac{\mathbf{j}\,\frac{\partial \tau}{\partial y}}{\sqrt{\left(\frac{\partial \tau}{\partial x}\right)^2 + \left(\frac{\partial \tau}{\partial y}\right)^2}}, \tag{2.24}$$

and the conduction speed $|\mathbf{v}_u|$ and its unit vector as:

$$|\mathbf{v}_u| = \frac{1}{|\nabla \tau|} = \frac{1}{\sqrt{\left(\frac{\partial \tau}{\partial x}\right)^2 + \left(\frac{\partial \tau}{\partial y}\right)^2}}, \tag{2.25}$$

leading to the expression of the CV as:

$$\mathbf{v}_u = |\mathbf{v}_u|\hat{\xi} = \frac{\mathbf{i}\,\frac{\partial \tau}{\partial x}}{\left(\frac{\partial \tau}{\partial x}\right)^2 + \left(\frac{\partial \tau}{\partial y}\right)^2} + \frac{\mathbf{j}\,\frac{\partial \tau}{\partial y}}{\left(\frac{\partial \tau}{\partial x}\right)^2 + \left(\frac{\partial \tau}{\partial y}\right)^2}. \tag{2.26}$$

Due to the susceptibility of this approach to noise when estimating the local activation time (LAT) in neighboring electrodes, a two-dimensional Gaussian smoothing operator can be used in a convolution-trend to smooth the velocity vector field [146].

Polynomial techniques

These involve fitting one or more polynomial surfaces $P(\mathbf{x}) = P_\kappa(\mathbf{x})$ to subsets of the space-time coordinates $(\mathbf{x}, \tau)$, where $\mathbf{x}$ denotes the electrode position, τ represents the wavefront activation time, and κ is the order of the polynomial surface. The surface is fitted to the data using a standard least-squares algorithm. Although this method using quadratic surfaces has been applied to regularly spaced unipolar electrode arrays in the two-dimensional case [127], the arrangement of points can be arbitrary.

To compute a CV vector at an arbitrary point $\mathbf{x}$ using quadratic polynomial surfaces, the data $(\mathbf{x}_i, \tau_i)$ within a fixed neighborhood of $\mathbf{x}$ is fitted to an expression of the form:

$$P(x_1, x_2) = c_1 x_1^2 + c_2 x_2^2 + c_3 x_1 x_2 + c_4 x_1 + c_5 x_2 + c_6. \tag{2.27}$$

The velocity vector is then defined as:

$$\mathbf{v} = \begin{pmatrix} \frac{\partial x_1}{\partial P} \\ \frac{\partial x_2}{\partial P} \end{pmatrix} = \begin{pmatrix} \frac{P_{x_1}}{P_{x_1}^2 + P_{x_2}^2} \\ \frac{P_{x_2}}{P_{x_1}^2 + P_{x_2}^2} \end{pmatrix}. \tag{2.28}$$

Further considerations were described by Cantwell et al. [146], and prior works [127, 128, 154, 155, 156, 157, 158].

Sinusoidal function fitting

Assuming a planar wavefront passing through a circular arrangement of electrodes with θ_c as a constant offset and radius $d/2$ (see fig. 2.5.C), the activation times can be described by:

$$\tau(n) = \tau_c - A\cos\left[\gamma(n-1) - \varphi_0\right], \tag{2.29}$$

where τ_c denotes the central activation time and φ_0 represents the initial phase angle of activation [159]. The initial values for the unknowns τ_c, A, and φ_0 are estimated based on the activation sequence. The parameters can be fitted by using an algorithm such as one of sequential quadratic nature. The CV is subsequently calculated as $d/2A$.

Experiments on simulation data validating this method have been performed [159], followed by studies on circular multipolar catheters in clinical settings [160, 161]. Further, generalizations of this method to other catheter configurations have been proposed [162], with the limitation that two-dimensional projections may distort inter-electrode distances which may introduce errors when estimating a focal source [146], see fig. 2.5.D.

Radial basis functions

LATs can be interpolated across a surface using radial basis functions (RBF). This class of functions, $\varphi(\mathbf{x}) = \varphi(||\mathbf{x}||)$, depends only on the distance from a fixed point. A typical example is the Gaussian function $\varphi(d/2) = e^{-(c(d/2))^2}$. For activation times τ_n at N electrode positions $\mathbf{x}_n$, the activation surface can be modeled as a combination of radial basis functions:

$$P(\mathbf{x}) = \sum_{n=1}^{N} a_n \varphi_n(||\mathbf{x} - \mathbf{x}_n||) + \sum_{m=1}^{M} b_m \Gamma_m(\mathbf{x}), \tag{2.30}$$

The RBFs φ_n are centered at the measurement points $\mathbf{x}_n$, and the second term Γ_m represents the associated polynomial [163]. The constraints $P(\mathbf{x}_n) = \tau_n$ ensure that the surface represents the recorded activation times at the electrode locations. Solving the linear system of N equations allows for the determination of the coefficients a_n. To avoid including additional low-order polynomials Γ_m and constraints to ensure a unique solution to the interpolation problem, the RBF of choice must be positive definite [164].

Isopotential lines

To estimate CV, one can analyze the distance traversed by an isopotential line (IL) over a fixed time interval [165]. This involves constructing an IL at each time instant using a parametric spline fitted through data points at a constant potential. In this manner, the direction of wavefronts can be inferred from the sign of the derivative of voltage over time. Given a fixed time window, the CV at a point on the line is determined by examining the distance travelled in the direction perpendicular to the isopotential line. However, this method may require data with higher resolution than typically available in clinical settings and necessitates absolute measurements of membrane potential, restricting its use primarily to optical mapping. A generalization of this method involves using spatial gradients of any scalar quantity for which a specific isovalue corresponds to the excitation wavefront [166]. This approach is commonly known as arbitrary scalar fields [146].

Time delays

In regions with closely spaced electrodes, time differences can be used to estimate propagation velocity by assuming a planar wavefront [167]. For any given pair of electrodes in the vicinity, the wavefront CV can be expressed as:

$$v = \frac{(\mathbf{x}_j - \mathbf{x}_i) \cdot \mathbf{n}}{\tau_{ij}}, \tag{2.31}$$

where $\mathbf{x}_i$ and $\mathbf{x}_j$ are the positions of the electrodes, $\mathbf{n}$ is the unit vector normal to the planar wavefront, and τ_{ij} is the time difference between them. By defining $\hat{\mathbf{n}} = (1/v)\mathbf{n}$, the following system of equations can be established:

$$(\mathbf{x}_j - \mathbf{x}_i) \cdot \hat{\mathbf{n}} = \tau_{ij}, \tag{2.32}$$

This equation relates the inter-electrode distances in the direction of the wavefront to the corresponding time delays, which can be represented in matrix form as: $\mathbf{X}^\top \hat{\mathbf{n}} = \tau$ (see fig. 2.5.E)

Maximum likelihood estimation

Given that the signal's wavelength is comparable to the electrode grid size, the incident wave can be assumed to be planar with an angle θ and velocity v. Electrodes share the same signal morphology $s(n)$, and can be modeled as a time-shifted version of $s(n)$ based on each electrode's row R and column C:

$$x_{R,C}(n) = s\left(n - (R-1)t_R - (C-1)t_C\right) + \omega_{R,C}(n) \tag{2.33}$$

where $\omega(n)$ is Gaussian white noise with variance σ^2 and n (see fig. 2.5.F). The time delays t_R and t_C between rows and columns can be estimated by maximizing the probability $p(t_R, t_C | x_{R,C}(n), s(n))$.

Using Bayesian inference, the maximum likelihood estimation (MLE) of (t_R, t_C) reduces to minimizing a cost function, incorporating weights based on the SNR, significantly improving estimation accuracy. The conduction speed and angle of incidence are then computed as:

2.6 Characterizing the tissue: intracardiac recordings

In this section, we explore the characterization of cardiac tissue through intracardiac EGMs, focusing on the use of electro-anatomic mapping systems and grid catheters

Table 2.1: Overview of selected CV estimation methods: Advantages and caveats. A comprehensive list and detailed descriptions is provided by Cantwell et al. [146].

Method	Key Refs.	Benefits	Caveats
Triangular	[168, 150, 149, 169]	Local score, examines regional variabilities	Prone to LAT errors, challenging to automate
Finite Diff.	[154, 170]	Local score, assesses regional variabilities	Prone to noise/missing data, fails if times are identical, needs grid
Polynomial	[127, 128, 154, 157, 171]	Flexible point arrangement, robust to noise	May require more points, choice of ΔX, ΔT needed
Sinus-fit	[159, 160, 161, 162]	Curvature measure, distance to focal source	Single macroscopic wavefront only, one vector per catheter
RBF	[163, 172]	Finds LATs anywhere, no assumption on arrangement	Computation-heavy
IL	[165]	Accurate wavefront curvature estimation	Needs membrane potential measurements, high resolution
Time delay	[167]	Uses neighboring location data, handles incorrect LATs	Assumes plane wave locally
MLE	[173]	Tolerant of LAT errors	Needs grid of recording points

for detailed assessment of arrhythmias. We will discuss how these technologies enhance our understanding of local electrical activity, activation patterns, and arrhythmogenic substrates, providing a foundation for subsequent signal processing and omnipolar EGM analysis.

2.6.1 Electro-anatomic mapping systems in arrhythmias

Electroanatomic mapping systems serve for the diagnosis and treatment of arrhythmias, and should be used when indicated by the guidelines [174, 175, 176, 177, 178]. High-density mapping involves the use of a multitude of electrodes to capture detailed electrical activity within the chamber examined, providing a local understanding of the conduction patterns on the surface of the cavity.

High-density mapping systems typically consist of multiple electrodes arranged on a catheter or balloon, which is inserted into the heart chamber of interest. These systems can record numerous EGMs simultaneously, offering a detailed temporal and spatial resolution of the cardiac electrical activity. The recorded data are processed to generate three-dimensional (3D) maps of electrical activation and voltage. These maps help identify abnormal conduction pathways and areas of scar tissue that are critical in guiding ablation procedures [179, 180]. Of particular importance for this dissertation is the HD Grid Mapping Catheter from Abbott. This catheter features a multi-electrode grid design that enables high-density mapping.

In AF, mapping systems are used to delineate the complex and often diffuse electrical activity within the atria. This helps in pinpointing focal triggers, commonly located near the pulmonary veins, facilitating targeted ablation to isolate these areas from the rest of the atrium [54, 181]. For VT, particularly in patients with structural heart disease, high-density mapping aids in identifying re-entrant circuits and regions of low voltage indicative of scar tissue. These insights are crucial for deploying linear ablation lesions to interrupt these circuits and prevent arrhythmia recurrence [182, 183].

Advancements in high-density mapping technology include the integration of imaging modalities such as computed tomography (CT) and magnetic resonance imaging (MRI) with electroanatomic mapping systems [184]. This fusion of imaging data enhances the anatomical accuracy of the electroanatomic maps, providing a more detailed and precise framework for guiding catheter ablation [185, 186]. Non-fluoroscopic catheter navigation systems have further reduced radiation exposure during procedures, enhancing the safety profile of these interventions [187, 188].

Clinical studies have demonstrated that high-density mapping improves the success rates of complex ablation procedures by providing detailed anatomical and electrical information that is not available through conventional mapping techniques [189]. Future advancements may focus on the development of real-time MRI-compatible catheters, which could allow for real-time visualization of both anatomical and electrical data without the use of ionizing radiation. Additionally, improvements in 3D ultrasound imaging could provide a non-invasive alternative for detailed intracardiac imaging [190, 191].

2.6.2 Electrogram recordings in a grid catheter

In this and next sections, we examine the four adjacent electrodes from a grid-array catheter. This analysis sets the groundwork for the subsequent chapters of this thesis, specifically chapter 4 and chapter 5. The electrodes are labeled as follows: on the lower most abscissa, the I on the left and II on the right. Analogously, at the uppermost abscissa, III on the left (on top of I on the same ordinate), and IV on the right, aligned with II on the ordinate. Considering a planar wave, let τ_o denote the reference time at which the wave passes through the center of the square grid. Assuming a constant velocity v within the grid and a distance ρ_e between adjacent electrodes (with $\sqrt{2}\rho_e$ between diagonally opposite electrodes), the activation times at the four electrodes are given by:

$$\tau_{\mathrm{I}} = \tau_o - \frac{\rho_e}{2v}\sin\gamma - \frac{\rho_e}{2v}\cos\gamma; \tag{2.34}$$

$$\tau_{\mathrm{II}} = \tau_o + \frac{\rho_e}{2v}\sin\gamma - \frac{\rho_e}{2v}\cos\gamma; \tag{2.35}$$

$$\tau_{\mathrm{III}} = \tau_o - \frac{\rho_e}{2v}\sin\gamma + \frac{\rho_e}{2v}\cos\gamma; \tag{2.36}$$

$$\tau_{\mathrm{IV}} = \tau_o + \frac{\rho_e}{2v}\sin\gamma + \frac{\rho_e}{2v}\cos\gamma. \tag{2.37}$$

Let $\psi(\tau)$ represent the unipolar voltage waveform created as a plane wave passes a specific point at $\tau = 0$. When one or more electrodes within the square register $\psi(\tau)$, the resulting unipolar and bipolar EGMs (u-EGMs and b-EGMs) can be described as follows:

$$u_i(\tau) = \psi(\tau - \tau_i), \qquad i \in \{\mathrm{I}, \mathrm{II}, \mathrm{III}, \mathrm{IV}\} \tag{2.38}$$

$$\begin{aligned} b_{i,j}(\tau) &= u_j(\tau) - u_i(\tau) \\ &= \psi(\tau - \tau_j) - \psi(\tau - \tau_i), \quad i, j \qquad \neq i \in \{\mathrm{I}, \mathrm{II}, \mathrm{III}, \mathrm{IV}\}. \end{aligned} \tag{2.39}$$

Bipolar signals can be derived along different directions within the square: horizontally ($b_{\mathrm{I,II}}(\tau)$ and $b_{\mathrm{III,IV}}(\tau)$), vertically ($b_{\mathrm{I,III}}(\tau)$ and $b_{\mathrm{II,IV}}(\tau)$), and along the diagonals ($b_{\mathrm{I,IV}}(\tau)$ and $b_{\mathrm{II,III}}(\tau)$). The activation time of each b-EGM $b_{i,j}(\tau)$ is related to the wave's passage through the midpoint between electrodes i and j. Consequently, relative delays may occur between different $b_{i,j}(\tau)$. Using the Taylor series expansion for $u_i(\tau) = \psi(\tau - \tau_i)$ around $\tau_i = \tau_o$, we approximate:

$$u_i(\tau) \approx \psi(\tau - \tau_o) - \Delta\tau_i \psi'(\tau - \tau_o) + \frac{1}{2}(\Delta\tau_i)^2 \psi''(\tau - \tau_o) \tag{2.40}$$

$$b_{i,j}(\tau) \approx -\Delta\tau_{i,j}\psi'(\tau - \tau_o) + \frac{1}{2}\left((\Delta\tau_j)^2 - (\Delta\tau_i)^2\right)\psi''(\tau - \tau_o). \tag{2.41}$$

where $\Delta\tau_{i,j} = \tau_j - \tau_i$ represents the time differences between activation at electrodes i and j, with $i, j \in \{\mathrm{I}, \mathrm{II}, \mathrm{III}, \mathrm{IV}\}$, and $\Delta\tau_i = \tau_i - \tau_o$ denotes the time difference between activation at electrode i and the reference activation time at the center of the square. Combining eq. (2.34) eq. (2.35) eq. (2.36), eq. (2.37) and eq. (2.41), we express the bipoles as:

$$b_{\mathrm{I,II}}(\tau) \approx -\frac{\rho_e}{v}\sin\gamma\,\psi'(\tau - \tau_o) - \frac{\rho_e^2}{4v^2}\sin(2\gamma)\,\psi''(\tau - \tau_o) \tag{2.42}$$

$$b_{\mathrm{III,IV}}(\tau) \approx -\frac{\rho_e}{v}\sin\gamma\,\psi'(\tau - \tau_o + \tau) \tag{2.43}$$

$$b_{\mathrm{I,III}}(\tau) \approx -\frac{\rho_e}{v}\cos\gamma\,\psi'(\tau - \tau_o) - \frac{\rho_e^2}{4v^2}\sin(2\gamma)\,\psi''(\tau - \tau_o) \tag{2.44}$$

$$b_{\mathrm{II,IV}}(\tau) \approx -\frac{\rho_e}{v}\cos\gamma\,\psi'(\tau - \tau_o) + \frac{\rho_e^2}{4v^2}\sin(2\gamma)\,\psi''(\tau - \tau_o) \tag{2.45}$$

$$b_{\mathrm{I,IV}}(\tau) \approx -\left(\frac{\rho_e}{v}\sin\gamma + \frac{\rho_e}{v}\cos\gamma\right)\psi'(\tau - \tau_o) \tag{2.46}$$

$$b_{\mathrm{II,III}}(\tau) \approx -\left(\frac{\rho_e}{v}\sin\gamma - \frac{\rho_e}{v}\cos\gamma\right)\psi'(\tau - \tau_o) \tag{2.47}$$

which we further simplify to:

$$b_{\mathrm{I,II}}(\tau) \approx -\frac{\rho_e}{v}\sin\gamma\,\psi'\left(\tau - \tau_o + \frac{\rho_e}{2v}\cos(\gamma)\right) \tag{2.48}$$

$$b_{\mathrm{III,IV}}(\tau) \approx -\frac{\rho_e}{v}\sin\gamma\,\psi'\left(\tau - \tau_o + \frac{\rho_e}{2v}\cos(\gamma)\right) \tag{2.49}$$

$$b_{\mathrm{I,III}}(\tau) \approx -\frac{\rho_e}{v}\cos\gamma\,\psi'\left(\tau - \tau_o + \frac{\rho_e}{2v}\sin(\gamma)\right) \tag{2.50}$$

$$b_{\mathrm{II,IV}}(\tau) \approx -\frac{\rho_e}{v}\cos\gamma\,\psi'\left(\tau - \tau_o - \frac{\rho_e}{2v}\sin(\gamma)\right) \tag{2.51}$$

$$b_{\mathrm{I,IV}}(\tau) \approx -\frac{\sqrt{2}\rho_e}{v}\cos\!\left(\gamma - \frac{\pi}{4}\right)\psi'(\tau - \tau_o) \tag{2.52}$$

$$b_{\mathrm{II,III}}(\tau) \approx -\frac{\sqrt{2}\rho_e}{v}\sin\!\left(\gamma - \frac{\pi}{4}\right)\psi'(\tau - \tau_o) \tag{2.53}$$

From these approximations, the second-order expressions for the various b-EGMs $b_{i,j}(\tau)$ reveal the relative delays between them. The relationship between $b_{\mathrm{I,II}}(\tau)$ and

$b_{\mathrm{I,III}}(\tau)$, measured in different directions (x and y), is expressed as:

$$\begin{aligned} b_{\mathrm{I,III}}(\tau) &\approx -\frac{\rho_e}{v}\cos\gamma\,\psi'(\tau-\tau_o) - \frac{\rho_e^2}{4v^2}\sin(2\gamma)\,\psi''(\tau-\tau_o) \\ &\approx \frac{\cos\gamma}{\sin\gamma} b_{\mathrm{I,II}}\left(\tau - \frac{\rho_e\sin\left(\frac{\pi}{4}-\gamma\right)}{\sqrt{2}v}\right). \end{aligned} \tag{2.54}$$

Equation (2.54) poves that the b-EGM along the y-axis (I-III) is a scaled version of the b-EGM along the x-axis (I-II) by a factor of $\frac{\cos\gamma}{\sin\gamma}$ and is delayed by $\varepsilon = \frac{\rho_e\sin\left(\frac{\pi}{4}-\gamma\right)}{v\sqrt{2}}$. This represents the delay for the wave to pass between the midpoints of each electrode pair, which are separated by $\rho_e/\sqrt{2}$. As foreseen, for $\gamma = \frac{\pi}{2}$ (propagation along the abscissa), $b_{\mathrm{I,III}}(\tau) = 0$, whereas for $\gamma = \frac{\pi}{4}$, the delay $\varepsilon = 0$, indicating simultaneous activation of both bipolar EGMs in the abscissa and ordinate directions. Similarly, the relationship between $b_{\mathrm{I,II}}(\tau)$ and $b_{\mathrm{III,IV}}(\tau)$, both along the horizontal coordinate, is described by:

$$\begin{aligned} b_{\mathrm{III,IV}}(\tau) &\approx -\frac{\rho_e}{v}\sin\gamma\,\psi'(\tau-\tau_o) + \frac{\rho_e^2}{4v^2}\sin(2\gamma)\,\psi''(\tau-\tau_o) \\ &\approx b_{\mathrm{I,II}}\left(\tau - \frac{\rho_e}{v}\cos\gamma\right). \end{aligned} \tag{2.55}$$

Equation (2.55) indicates that b-EGMs along parallel directions exhibit identical amplitudes, as expected. The delay $\varepsilon = \frac{\rho_e}{v}\cos\gamma$ varies from 0, when propagation is aligned with the electrode pairs ($\gamma = \frac{\pi}{2}$), to $\frac{\rho_e}{v}$, when propagation is perpendicular to the direction of the electrode pairs ($\gamma = 0$).

2.6.3 Signal processing for omnipolar electrograms

Local unipoles are commonly used to measure propagation speed and local cellular activation from a group of four closely spaced electrodes, which we refer as a clique, originating from an array with equispaced electrodes. In literature proposing triads of electrodes from the clique to reconstruct the omnipolar signal, the CV vector and other omnipolar signal features are assumed to be located at the center of the clique [18, 192]. Yet, the real center of these triangular configurations may differ from that location as the 'center' of a triangle of electrodes in a clique does not coincide with the center of the clique.

Assuming that the four electrodes of a clique lie on a tight planar myocardial surface, we can define a 2D coordinate system and show the distance (*d*) between the electrodes. The clique then forms a square, and a wave could traverse the clique, for instance, from left to right along the x axis. Commonly, a spatial derivative is applied to unipolar signals recorded by the electrodes to better reveal local information—this derivative is known as bipolar EGMs. In this example, the largest amplitude would be observed in bipolar the bipolars along the wave's direction, while the bipole perpendicular to the wave would be the smallest. This spatial derivative is expressed mathematically as follows: Let $\Phi(\tau)$ represent a collection of unipolar EGMs $\varphi(\tau)$ from a 4-electrode clique organized as:

$$\Phi(\tau) = \begin{bmatrix} \varphi_1(\tau) \\ \varphi_2(\tau) \\ \varphi_3(\tau) \\ \varphi_4(\tau) \end{bmatrix} = \begin{bmatrix} \varphi_1(\tau_1) & \varphi_1(\tau_2) & \cdots & \varphi_1(\tau_{n-1}) & \varphi_1(\tau_n) \\ \varphi_2(\tau_1) & \varphi_2(\tau_2) & \cdots & \varphi_2(\tau_{n-1}) & \varphi_2(\tau_n) \\ \varphi_3(\tau_1) & \varphi_3(\tau_2) & \cdots & \varphi_3(\tau_{n-1}) & \varphi_3(\tau_n) \\ \varphi_4(\tau_1) & \varphi_4(\tau_2) & \cdots & \varphi_4(\tau_{n-1}) & \varphi_4(\tau_n) \end{bmatrix} \tag{2.56}$$

Here, n is the number of samples taken at different time points τ_0, τ_1, τ_2, etc.

The corresponding vertical, diagonal and horizontal bipoles are defined from the lower-left electrode of the clique as a reference as:

$$d\Phi(\tau) = \begin{bmatrix} \varphi_1(\tau) - \varphi_2(\tau) \\ \varphi_1(\tau) - \varphi_3(\tau) \\ \varphi_1(\tau) - \varphi_4(\tau) \end{bmatrix} \tag{2.57}$$

with the following distance matrix:

$$dX = -\begin{bmatrix} 0 & d & d \\ d & 0 & d \end{bmatrix} \tag{2.58}$$

where each column contains the abscissa and ordinate distance for each bipole in $d\Phi(\tau)$. Assuming the electrode coordinates do not change over time, the distance matrix shall remain constant.

Additionally, unipolar EGMs are known to relate to the electric field at the extracellular-myocardial interface. Therefore, the relationship between this E field and unipolar voltages is known to be:

$$E = -\bigtriangledown\varphi \tag{2.59}$$

The relationship between E, $\bigtriangledown\varphi$, and $d\Phi$ is detailed in the work of Deno et al. [15]. We introduce now the omnipole concept as a least squares solution for E.

Revisiting the example where the omnipole is produced by a travelling wave almost parallel to the $\hat{x}$ axis, one can prove that (1) for an observer moving with the wave, voltage changes should be zero, and (2) voltage changes perpendicular to the planar wave propagation should also be zero, for a sufficiently small interelectrode distance d. In this bi-dimensional context with a wave travelling along the $\hat{x}$ axis:

$$\frac{D\varphi}{Dt} = \dot{\varphi} + \frac{\partial\varphi}{\partial x}v_x = 0 \tag{2.60}$$

where $D\varphi/Dt$ is the total time derivative (zero for an observer moving with the wave); $\dot{\varphi}$ is the partial time derivative of $\varphi; \partial\varphi/\partial x$ is the spatial derivative along the wave propagation; and v_x is the wave's velocity. One could further simplify to $\dot{\varphi} = v_x E_x$, where E_x is the component of E oriented along the travelling wave's direction, in this case, along the $\hat{x}$ axis.

A CV vector (ν) comprises a magnitude (CV) and an activation direction. At a fixed location, as the travelling wave passes, CV can be determined from definition above for $\dot{\varphi}$, using phase velocity, which is the ratio of temporal and spatial derivatives of φ.

$$v_x(\tau) = -\frac{\dot{\varphi}(\tau)}{E_x(\tau)} \tag{2.61}$$

Assuming the waveform propagates locally with a nearly constant CV, the signals $\dot{\varphi}(\tau)$ and $E_x(\tau)$ must be similar. The term omnipole originates from searching for a spatial derivative in every possible direction around the electrode clique to maximize the correlation with the temporal derivative. Thus, omnipolarity yields the wavefront direction. Their ratio is a multiplicative constant describing the wave's CV. This allows us to select an activation direction (in this example, $\hat{x}$) to maximize the correlation of $\dot{\varphi}(\tau)$ and $E_x(\tau)$. Figure 1E visually represents how the CV of the propagating wave is calculated. Here, the closest match to the time derivative is a close approximation of vertical and horizontal bipoles as the wave propagates along the $\hat{x}$ axis.

The acquisition and processing of omnipolar EGMs from cliques to calculate omnipolar EGM signals $\varphi(\tau)$, activation direction, and CV, are repeated throughout the field of view within a selected medium using consecutive electrode cliques to obtain a vector field from a set of adjacent velocity vectors, ν. This concept, applicable to any travelling wave, can also be used for fluorescence signals obtained using voltage or calcium fluorophores.

Chapter 3

Non-invasive Characterisation of Macroreentrant Atrial Tachycardia Types from a Vectorcardiographic Approach with the Slow Conduction Region as a Cornerstone

Abstract

Background and Objectives: Macroreentrant atrial tachyarrhythmias (MRATs) can be caused by different reentrant circuits. The treatment for each MRAT type may require the ablation at different sites, either at the right or left atria. Unfortunately, the reentrant circuit that drives the arrhythmia is unknown previous to the electrophysiologic intervention. **Methods:** A noninvasive approach based on the comparison of atrial VCG loops is proposed. An archetype for each group was created, which served as reference to measure the similarity between loops. Methods were tested in a variety of simulations and real data obtained from the most common right (peritricuspid) and left (perimitral) macroreentrant circuits, each divided into CW and CCW subgroups. Adenosine was administered to patients to induce transient AV block patients allowing the recording of the atrial signal without the interference of ventricular signals. From the vectorcardiogram, we measured intrapatient loop consistence, similarity of the pathway to archetypes, characterisation of slow velocity regions and pathway complexity. **Results:** Results show a considerably higher similarity with the loop of its corresponding archetype, in both simulations and real data. We found the capacity of the vectorcardiogram to reflect a slow velocity region, consistently with the mechanisms of MRAT, and the role that it plays in the characterisation of the reentrant circuit. The intra-patient loop consistence was over 0.85 for all clinical cases, similarity of the pathway to archetypes was found to be 0.85±0.03, 0.95±0.03, 0.87±0.04 and 0.91±0.02 for the different MRAT types (and $p < 0.02$ for 3 of the 4 groups), and pathway complexity (with $p < 0.05$ to discriminate among cases). **Conclusions:** We conclude that the presented methodology allows us to differentiate between the most common forms of right and left MRATs and predict the existence and location of a slow conduction zone. This approach may be useful to plan the ablation procedure in advance.

This chapter is based on the publication: S. Ruipérez-Campillo et al. (2021). Non-invasive characterisation of macroreentrant atrial tachycardia types from a vectorcardiographic approach with the slow conduction region as a cornerstone. *Computer Methods and Programs in Biomedicine*, 200, 105932. [193]

3.1 Introduction

MRAT, also commonly named AFL, is the second most common atrial tachyarrhythmia with an increasing prevalence [36, 194]. Catheter ablation is the most common treatment [195]. However MRAT is physiologically caused by a macroreentrant EP circuit at the atria, which usually follows a path surrounding one or more anatomic obstacles [37]. The most frequent MRAT type, also known as typical AFL, follows a common pattern located at the right atrium, where the activation path surrounds the tricuspid valve [196], in any of the two possible directions, either clockwise (CW) or counterclockwise (CCW) [197]. Atrial activation in typical AFL passes through an isthmus with slow conduction as a distinctive feature, which favours perpetuation of the macroreentry, as it allows the full repolarisation of the atrial myocytes once the refractory period is over. Being ready for a new activation, subsequent cycles are repeated steadily and periodically [198, 199]. Ablation of the cavotricuspid isthmus creates a line of conduction block which terminates typical AFL and makes it no longer inducible [200]. Although some other options have been proposed in recent history [201], the RF ablation of the cavotricuspid isthmus is a well defined treatment [202].

Beyond typical AFL, other circuits may also cause sustained atrial macro reentries, which otherwise will require different ablation interventions. Hence, MRAT can be classified into different MRAT types [203], where typical AFL is the most prevalent (90%), whereas the other cases are usually denoted as atypical AFL. In recent times the use of electroanatomical mapping systems allows integration of electrical activation data of the atrial on computerised 3d anatomical models of the atria. This has facilitated mapping and ablation of these arrhythmia but still is a time consuming procedure which requires expertise and training. Although ECG Imaging (ECGI) is a promising noninvasive mapping technique, it is not widely employed in clinical settings yet and its results are controversial [204, 205].

Therefore, a method to distinguish different atypical flutter types and identify the most probable reentrant circuit from the ECG would be valuable in order to obtain key information prior to the EP study. Identifying whether the MRAT is from the left or right atrium is of great help as it facilitates to plan the procedure: either maintain the patient with medicines or refer them to the appropriate facility in case of ongoing MRAT. The other essential advantage would be simplifying the electroantomical mapping by directing the physician to the interest area - avoiding starting from the scratch.

Though first described more than a century ago [206], the mechanisms and techniques used for its diagnosis have seen little more than minor changes in practice. Traditionally, the diagnosis relied heavily on the twelve-lead ECG analysis and the distinctive atrial waves in leads II, III, aVF, aVL, V1,V2, characterised by continuous and regular saw-tooth waveforms with cycle lengths of around 250ms [196]. In 2001, more than three decades after the first classification of AFL, the European Society of Cardiology and the North American Society of Pacing and EP developed the current classification of the arrhythmia [207]. Although the analysis of ECG is used to detect flutter cases [208], waveform variants, such as positive or biphasic waves, that have been proven to exist, are not easily associated with different MRAT types [209]. Thus, ECG is just orientative even for typical AFL cases as false positives and negatives are commonly registered.

A major hindrance for MRAT diagnosis is that most patients present a 2:1 atrioventricular conduction ratio. Consequently, the atrial wave is overlapped by the ventricular components (either the QRS complex or the T-wave). In those cases, the atrial wave is no longer visible unless there is a longer RR interval (e.g. with a 4:1 conduction ratio). Although several methods to cancel the ventricular activity in AF signals have been proposed in the literature [210, 211], these are not applicable to MRAT signals, as atrial and ventricular components are coupled. Therefore, in the attempt to remove the QRS-T, the atrial signal is likely to be subtracted as well. Moreover, the strategy based on Blind Source Separation [212, 213], which provides one atrial source free from ventricular components –also in MRAT– is insufficient for this purpose, as three independent atrial components would be required to reconstruct the VCG loop. As a result, the unequivocal retrieval of the atrial signal in MRAT recordings still remains a technical challenge [214]. This limitation, however, can be overcome by blocking the AV node during a short period of time, e.g. by administrating adenosine [215].

Apart from ECG interpretation, the vectorcardiographic approach [216], sustained on the dipolar nature of the heart, was defined for the representation of 3 dimensional surface loops. Quantitative measurements, such as planarity, plane orientation, loop roundness or the vector with maximum amplitude, among others, have been defined to assess the morphology of the QRS loop [217, 218]. Moreover, the QRS-T angle has been associated with the risk of sudden cardiac death [219]. With respect to MRAT, VCGs have also been described [220, 221], but no clear correlation has been demonstrated for proven mechanisms. Unlike P, QRS or T waves, which are caused by synchronised depolarisation/repolarisation of the myocytes following a rest period with isoelectric potential, in MRAT, the atrial signal is a result of a continuous activation. Accordingly, atrial VCGs lack coordinates for the origin of activation. Hence, as MRAT loops differ in their generation mechanisms from P loops, novel features, specifically conceived for MRAT, should be explored to extract clinically meaningful information.

In this study we hypothesise that there is a correlation between the atrial VCG loops and the type of AFL that the patient suffers. This correlation is thought to be strongly related to the distribution of slow conduction areas at the left atrium. Thus, differences in the VCG loop patterns will be studied to characterise the MRAT archetype defined for each group.

3.2 Study design

In order to prove our hypothesis, we developed a method based on a new perspective of the VCG signal, where the evolution of the dipole direction and the slow conduction regions play a significant role. This method was tested from different standpoints. On the one hand, we evaluated the properties of the methods using simulations. Several simulation strategies have been employed to test methods for the processing of cardiac signals, including geometrical models [222], signal synthesis from the combination of periodic components [223], semi-synthetic signals from the manipulation and combination of real signals [213] and computational methods based on physiological properties, as used in [224]. In this study, we used a geometrical model, which allows for a full control and parametrisation of the 3D loop described by the vector and the location of the slow conduction regions.

A synthetic VCG generator was designed, based on a mathematical model to support the methods used for the analysis and the posited hypothesis. On the other hand, a prospective study was designed to test the methods on MRAT patients. Patients were recruited at the Robotic Cardiac EP and Arrhythmia Unit, at the Hospital Universitario La Paz (Madrid, Spain) according to a protocol approved by the hospital's ethics committee. The recruitment protocol was compliant with the Declaration of Helsinki and all patients involved signed consent forms. The classification of the MRAT type was determined after the EP procedure. Clinical data (ECG measurements) are transformed to VCG signals before feature extraction.

The proposed methodology involved the creation of VCG archetypes for each group and VCG feature extraction parameters to quantify its similarity to an archetype, intra-patient consistence of the atrial VCG loop, the velocity profile of the trajectory and the complexity (i.e. the sinuosity) of the VCG trace. Statistical tests were finally carried out to evaluate the performace of the methods.

3.3 Materials

3.3.1 Synthetic data

A geometrical model aiming to generate loops based on distinctive features of atrial VCGs was created. This model highlights the non-uniform velocity of the trajectory and the presence of a slow velocity region. The purpose of the simulations is to contrast the information exploited from the methods with a full control of the geometrical properties of the loops.

Bearing in mind that diverse reentry circuits with different plane orientation, location of the slow region and rotation sense may exist, 8 archetypes defined according to those characteristics were defined. The variability of loops belonging to the same group was considered by introducing a wide range of randomized variables, such as shape, plane rotation, spatial shifts of the slow velocity region and complex curvatures in the pathway.The model follows a geometrical approach with random parameters following a uniform distribution between ranges empirically found in VCGs from MRAT patients.

The generation of the VCG loops starts with the definition of an ellipse. From the Euler expression, the relationship between major and minor semi-axes are randomised within a range of values. It is worth mentioning here that, when discretising the XYZ projections or signals according to the constant sampling period, the spatial discretisation of the elliptical figures entail a higher density of points near the minor semi-axis, so that the spatial velocity of the trajectory described by the loop is not constant along the entire path. However, this should not be regarded as a limitation, but rather an asset of the model, as variations of the velocity profile also appear in real MRAT VCG loops.

Taking a deeper look at the idea of forcing a more pronounced slow velocity region as a characteristic feature, a non-uniform discretisation of the angle is obtained from:

$$\Delta\theta_n = \alpha \left|\cos\left(n\frac{\pi}{N} + \varphi\right)\right| + \Delta\theta_{\min}, \tag{3.1}$$

where $\Delta\theta_n$ is the angular increment at each n sample, N the total number of samples of the loop, $\Delta\theta_{\min}$ the minimum angle increment, which sets up the minimum velocity, $\alpha + \Delta\theta_{\min}$ is maximum angle variation, which stands for high velocity regions, and the phase argument φ determines the location of rapid and slow regions. The parameters in Eq. (3.1) must fulfill the constraint that the accumulated angle increment throughout the entire loop equals 2π. Accordingly, if a lower $\Delta\theta_{\min}$ is desired, α must be increased to fulfill that condition, as one parameter relies on the other. Overall, choosing one of them will directly fix the velocity balance between rapid and slow regions.

To create a wide variety of loop shapes with meanders, curvature variations and avoiding strict confinement within a plane, the vector modulus (radius of the projections), which depends on the angle and the semi-axes, is varied by means of weighted (Q_1, Q_2 and Q_3) frequency modulating functions (C_1, C_2 and C_3), so that:

$$r(\theta) = \frac{a \cdot b}{\sqrt{(a \cdot \cos(\theta) + Q_1C_1)^2 + (b \cdot \sin(\theta) + Q_2C_2)^2 + Q_3C_3}} \tag{3.2}$$

This allowed a wide range of combinations of large arc deviations and small but rapid oscillations. A similar modulation vector is also defined in the perpendicular plane of the ellipse, thereby allowing the path to run out of the main plane. As a result, a curvature throughout all 3 dimensions is generated.

In order to avoid possible sharp peaks in the velocity profile (which may occasionally appear) a low-pass filter is applied over the 3-dimensional path. An adaptation of the Savitzky–Golay filter over the three axes was implemented [225] to make the trajectory smoother and avoid these possible peaks. Finally, the spatial orientation of the loop is set by means of a geometric rotation of the three axes. An example of a synthetic VCG loop is represented in figure 3.1.

With this model, 4 different groups were defined, according to the location of the slow region and with different loop orientations. On average, the location of the slow region was set at every 90º for the different groups. With regard to plane orientation, the loops were rotated with ±40º per coordinate, with some overlapping between groups. Moreover, each group was then divided into two, according to the direction of the trajectory, either CW or CW. Both versions were considered as independent groups for VCG analysis, so that loops classified into 8 groups were generated (groups 1 to 4 and 5 to 8 corresponding to either CW or CCW versions, respectively). A summary of the parameters and degrees of freedom from the model is depicted in table 3.1.

3.3.2 Clinical data

After the protocol approval, 30 consecutive MRAT patients submitted to an EP intervention were included in the study. ECG and EGM data was registered by a polygraph (Labsystem pro, Bard, Boston Scientific) with sampling frequency of 1KHz. Data generated by the electro-navigator during the intervention were recorded and synchronised with the polygraph for the latter analysis and description of the gold standard. During ECG registration, adenosine was administered in order to temporally block the atrio-ventricular conduction and hence, obtain pure

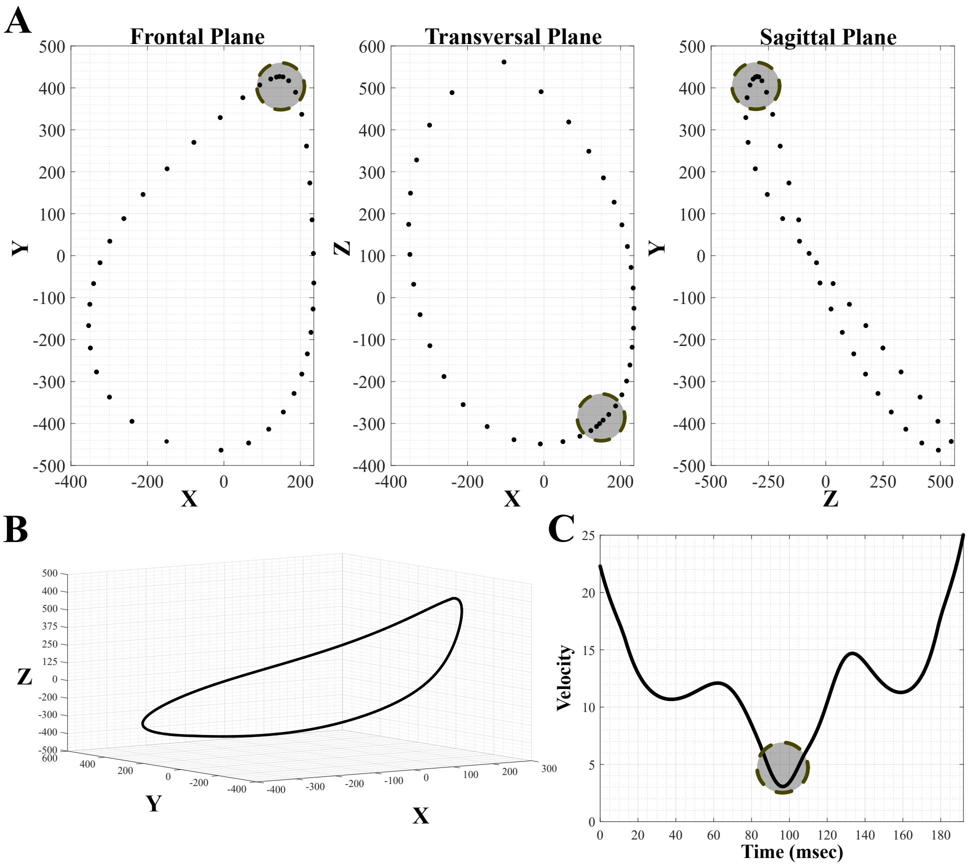

Figure 3.1: Example of a simulated VCG. **A**. Frontal, Transversal and Sagittal planes. **B**. 3D representation. **C**. Velocity Profile.

atrial signals free from any ventricular component. From the outcomes of the EP intervention, patients were grouped in the following groups: CW typical AFL (5), CCW typical AFL (6), CW perimitral MRAT (3) and CCW perimitral MRAT (8). The remaining 8 patients were identified as periveins (either pulmonar or cavae) or other MRAT forms, and were included in a miscellaneous MRAT group. In this study, data from patients with anatomical problems or a long history of cardiac disease were disregarded for the statistical analysis. In addition to the ECG data, the results of the EP studies were available for all patients and considered as the gold standard that identified the macroreentrant circuit —and thus, the MRAT type. An example of an electroanatomic mapping with the activation sequence of a perimitral MRAT is shown in figure 3.2.

Table 3.1: Summary of the parameters, description, and values in the synthetic model.

Category	Param.	Description	Range
Ellipse geometry	P	Perimeter	[2000, 2500]
	c	Constant maintaining semi-axes (a and b) relation within a range to keep an elliptical shape.	$\left[\frac{1}{\sqrt{10}\pi}, \frac{\sqrt{2}}{\sqrt{13}\pi}\right]$
	b	Minor semi-axis. Note that this parameter is not independent.	$b = c \cdot P$
	a	Major semi-axis. Note that this parameter is not independent.	[1.5b, 2b]
Configuration of the low velocity region	α	Maximum angular displacement (constrains maximum velocity).	[0.3, 0.7]
	$\Delta\theta_{\text{min}}$	Minimum angular displacement (constrains minimum velocity).	$\left[10^{-2}, 10^{-4}\right]$
	θ_0	Location of the low velocity region	Types 1,2,5 and 6: 0° Types 3,4,7 and 8: 180°
Creating winding pathway	C_1Q_1	Variation over the major semi-axis	[0, 150]
	C_2Q_2	Variation over the minor semi-axis	[0, 150]
	C_3Q_3	Overall variation (over the radius)	[0, 15]
Plane rotations	X axis	Types 1 and 5: [40°, 80°]	
		Types 2 and 6: [10°, 50°]	
		Types 3 and 7: [10°, 50°]	
		Types 4 and 8: [40°, 80°]	
	Y axis	Types 1 and 5: [70°, 110°]	
		Types 2 and 6: [40°, 80°]	
		Types 3 and 7: [40°, 80°]	
		Types 4 and 8: [70°, 110°]	
	Z axis	Types 1 and 5: [20°, 60°]	
		Types 2 and 6: [-10°, 30°]	
		Types 3 and 7: [-10°, 30°]	
		Types 4 and 8: [20°, 60°]	
Sense of rotation	CW	Types 1-4	
	CCW	Types 5-8	

3.4 Methods

3.4.1 Preprocessing

Atrial VCG loops computing

From the ECG recordings, only the segments under the effects of adenosine depicting a saw-tooth waveform with no ventricular contractions were selected. These signals were bandpass filtered between 1Hz and 30Hz to reduce thermal noise and remove the baseline wandering whilst preserving the atrial content intact. Signals were filtered bidirectionally to minimise transient distortion. The atrial cycle length was computed from the first maximum of the atrial signal's autocorrelation function. Having estimated this period, an excerpt with 10 cycles was delimited (Figure 3.3.A). Subsequently, the signal was split into 10 segments, each of them lasting one exact atrial cycle length.

The VCG was then obtained according to the Inverse Dower's Transform [226] to estimate Frank's leads from the standard ECG system, as this is the most commonly

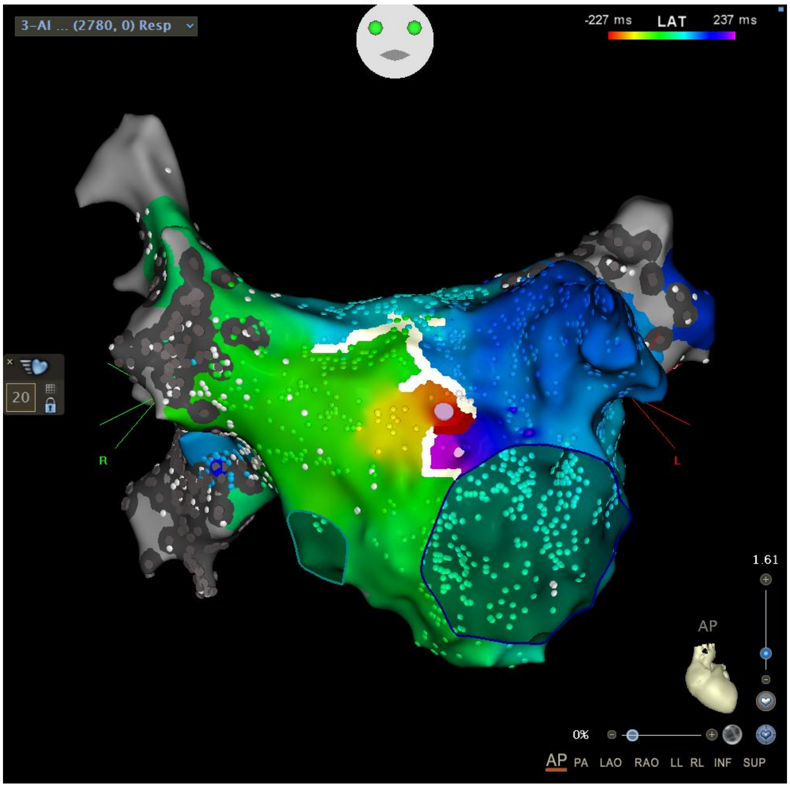

Figure 3.2: Electroanatomical mapping with the activation sequence of a perimitral MRAT. The area in red corresponds to the slow conduction region (see the video in the supplemental material to reproduce the activation sequence). The EP study was used as the gold standard to identify the reentrant circuit and hence the MRAT type. This figure was generated by CARTO®3, Biosense Webster.

used transformation, although other vectorcardiographic transformations have also been proposed [227].

VCG loop consistence

The consistence assesses the similarity amongst intrapatient atrial VCG loops. Thus, it allows us to determine their repeatibility, which could be impaired due to either the variability of the macroreentrant circuit, the quality of the signal (i.e. signal-to-noise ratio) or respiration [220].

Taking 10 VCG loops for each patient, the consistence is computed from the Eigen Value Decomposition [228], which outputs 10 orthogonal vectors with decreasing representation in terms of variance to the input data. Consistence is then defined as the percentage of variance explained by the most representative component. As macroreentrant circuits in MRAT are repeatible events, consistence values close to 1 are expected in practically all cases, unless a corrupted signal or an unstable circuit is present. Outliers with clearly low consistence values were excluded from the analysis.

Averaged VCG loops

The VCGs from all cycles were averaged to create a representative single-loop VCG signal for a patient (see figure 3.3). As the atrial cycle length will be different for each patient, and with the aim of allowing interpatient VCG loop comparison, XYZ components were resampled so that the averaged VCG had the same number of samples in all patients (in this study we considered 500 samples, although this number is not a critical point).

3.4.2 VCG archetypes

In order to identify the MRAT type for a given patient, a representative VCG for each group would be required, so that the similarity to each VCG pattern could be obtained and therefore determine the greater similarity of MRAT to an unknown VCG. To this end, the VCGs were divided into different groups (both in simulations and real data), VCG archetypes are created from the average of time aligned VCGs. In order to prevent excessive amplitudes of ECG signals, all VCGs were previously normalised so that their respective vectors had the same averaged modulus along the entire loop. The ensemble of VCG loops belonging to the same MRAT group was jointly aligned according to a least squares minimisation approach described in Appendix appendix B.

3.4.3 Characterisation of VCG loops

Vectorcardiographic signals have been previously characterised [229]. The new approach described below was applied to both simulated and real data. Before any feature extraction and for every VCG, the mean value was firstly removed from all three Cartesian axes, so that the loop was spatially repositioned towards its centre of gravity –notice that it will be closer to the low-velocity region, as it has a higher density of samples.

Similarity between VCG loop pairs

In order to assess the similarity between VCG loop pairs, the 3-dimensional VCG vectors were correlated sample-by-sample until all N vectors that make up each loop were compared. The similarity between two loops is hence defined as:

$$S = \frac{1}{N} \sum_{i=1}^{N} \frac{\mathbf{x}_i^T \mathbf{y}_i}{||\mathbf{x}_i|| \, ||\mathbf{y}_i||}, \tag{3.3}$$

where $\mathbf{x}_i$ and $\mathbf{y}_i$ are the 3-dimensional vectors of each VCG loop, respectively, at the i-th sample and N is the total number of samples, which is the same in both loops since they were previously resampled as previously mentioned. Notice that, in this definition, the similarity is not affected by differences in the amplitude of the vectors, but relies solely on the direction the vectors are pointing to. As the slow regions have a higher spatial density of samples, they will be over-weighted with respect to other regions and thus, play a key role in this parameter. In other words, two VCGs decribing exactly the same path but with different locations of the slow region will not have a similarity of 100%. Otherwise, two VCGs describing different paths but

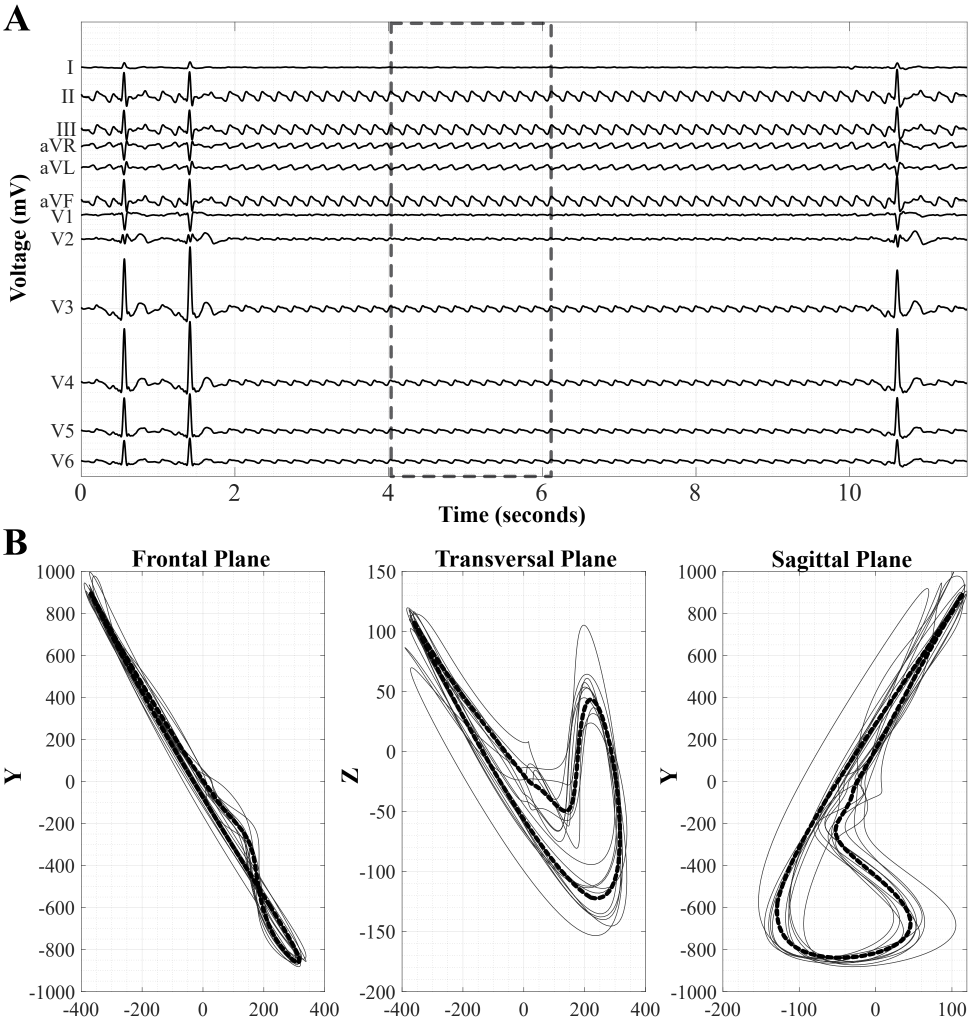

Figure 3.3: **A**. 12-lead ECG signal from a typical CCW AFL under the effects of adenosine. Notice large RR segments due to AV blockage. **B**. VCGs reconstructed from 10 consecutive atrial cycles are superimposed (see region in the dashed box in A), with the averaged VCG in thick dashed trace.

with roughly the same location of slow regions may have a higher similarity than visually expected.

It is worth mentioning that special care must be taken in the alignment of the loops, as misaligned loops would erroneously provide low correlation values. Therefore, the similarity parameter S is in fact a cost function $S(k)$, which depends on the loop alignment, where k is the number of samples by which the second loop is shifted, taking N possibilities, from 0 to $N-1$. Due to the variability of MRAT loops, particularly if they come from different MRAT types, we cannot a priori estimate the shape of the cost function. The possible existence of local maxima at which a maximisation function could get anchored is unknown. For this reason, anywhere that the similarity between loops is computed in this study, all N possible shifts will be considered, taking the absolute maximum S_{max}. As subsequently reported in the results section on the cost function shape, in later studies a maximisation function could be applied with the aim of carrying out less iterations and hence saving computational load.

Identification of the most alike archetype

For each VCG, the similarity to each archetype was computed as described in sections 3.4.3 and 3.4.3. The highest coefficient will determine which group it is closest to. In the case of real data, due to the low number of patients in each group and, in order to ensure a fair comparison, the VCG being tested were excluded for the generation of the archetypes following a Leave One Out strategy.

Slow conduction velocity regions

The velocity profile along the loop is computed from the spatial distance between consecutive loop samples. As the units of the VCG leads are given in volts and the temporal scale is expressed in atrial cycles, the resulting units are [V/cycle]. A threshold fixed to a quarter of the maximum velocity was set to identify the VCG sites and the temporal instants associated to slow conduction (see figure 3.4). From this, the following parameters were defined: (1) **T**ime **F**raction during which the trajectory advances with low velocity (TF_{LV}); (2) **D**istance **F**raction outlined during the low velocity period DF_{LV} and (3) the ratio between these two parameters, i.e. **T**ime fraction over **D**istance fraction (as a **R**atio) under low velocity conditions (TDR_{LV}).

As MRAT VCGs are closed loops, the angular velocity profile was also computed, in order to enrich and supplement the information provided by the velocity profile. At the i-th sample, the angular velocity ω, which is expressed in [rad/s] units, is defined as:

$$\omega_i = \frac{1}{T_s} \arccos\left(\frac{\mathbf{v}_i^T \mathbf{v}_{i+1}}{||\mathbf{v}_i||\ ||\mathbf{v}_{i+1}||}\right), \tag{3.4}$$

where $\mathbf{v}_i$ is the 3-dimensional vector at the i-th sample and T_s is the sampling period (with required corrections after resampling). To illustrate the interpretation of this parameter, let us consider an MRAT loop with no meanders and a cycle length of 250ms. In this case, the expected angular velocity, on average, would be 8π rad/s, as

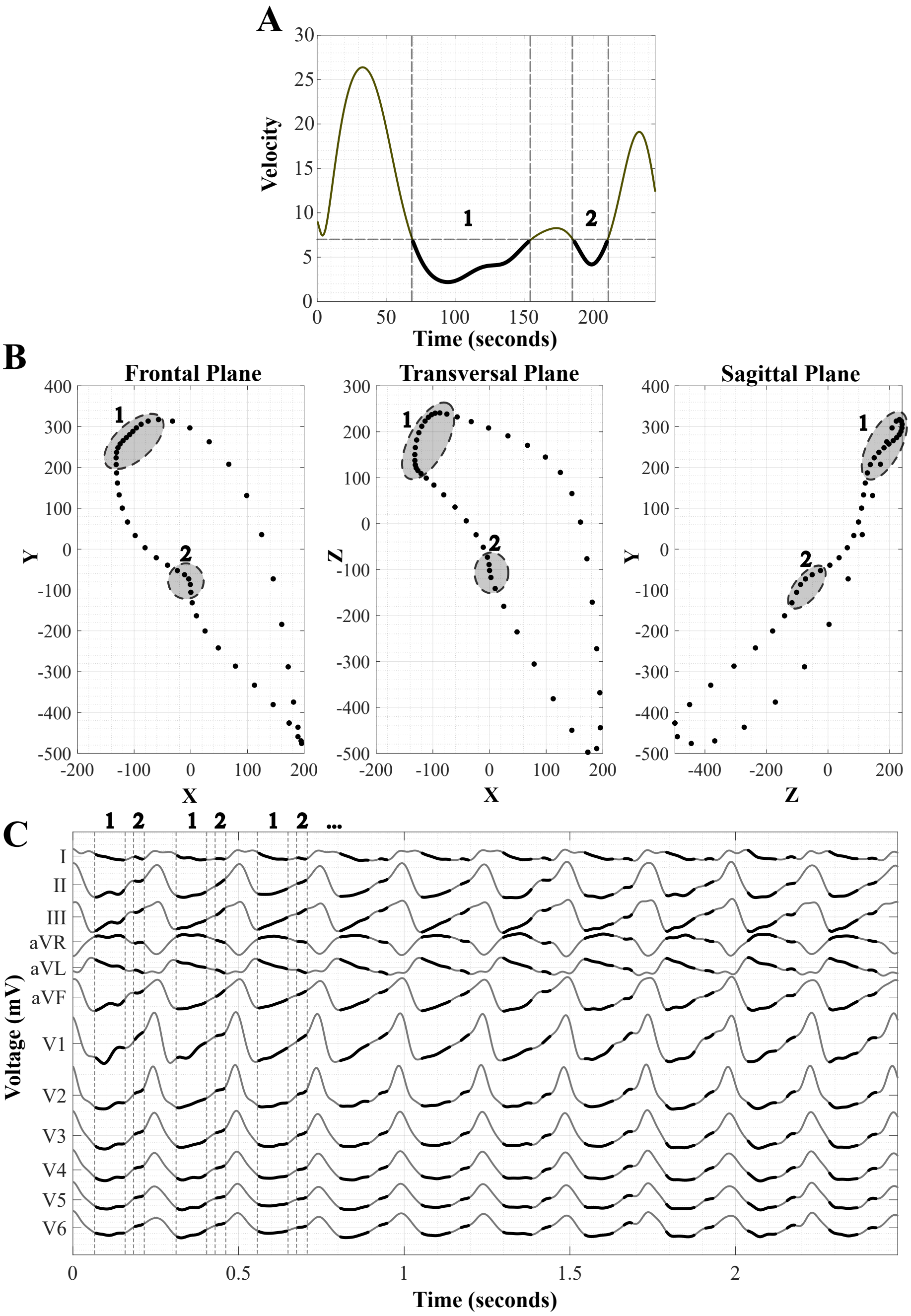

Figure 3.4: **A.** Primary and secondary slow velocity intervals, labelled as 1 and 2, respectively, are detected in a Perimitral CCW MRAT. **B.** Slow velocity regions are highlighted in VCG projections. C. Highlight of slow velocity intervals on the atrial ECG signal. These intervals correspond with segments with smoother slope. 10 atrial waves are represented (from which the average VCG loop in B is created). First three waves are labelled with the two slow conduction region - 1 is the slowest.

in one second it would complete 4 entire loops, or 1.4 deg/ms. This angular velocity is likely to increase with shorter cycle lengths and/or bending traces.

Complexity of the pathway: quantification of bending traces

This parameter intends to capture local variations in order to evaluate the complexity of the trajectory. The rationale of this parameter is that, the further the pathway bends, with more meanders and direction changes, the higher the complexity of the pathway. Therefore, the complexity can be regarded as the accumulation of the instantaneous angle variation Θ_i, which for the i-th sample is computed as:

$$\Theta_i = \arccos\left(\frac{\left(\mathbf{x}_i - \mathbf{x}_{i-1}\right)^T\left(\mathbf{x}_{i+1} - \mathbf{x}_i\right)}{\|\mathbf{x}_i - \mathbf{x}_{i-1}\|\,\|\mathbf{x}_{i+1} - \mathbf{x}_i\|}\right) \tag{3.5}$$

The accumulation of all angle variations Θ_i along the full pathway is lower bounded by 2π rad, which is the value obtained in the simplest case (i.e. the direction vector makes a complete turn). However, since there is no upper boundary for this parameter and, in order to keep a parameter within a reasonable range, we define the complexity C as:

$$C = 1 - \frac{2\pi}{\sum_i \Theta_i}, \tag{3.6}$$

which is lower bounded by 0 (the simplest pathway, with no local oscillations) and upper bounded by 1 (in case of an infinitely complex trajectory).

3.4.4 Statistical analysis

Synthetic VCGs

A one-way analysis of variance (ANOVA) was calculated on ~~participants'~~ synthetic VCGs. Snedecor's F distribution is in analyzing variance to see if three or more samples come from populations with the same mean values. The F-ratio and the associated probability value (p-value) are reported. If the p-value associated with the F is less than 0.05, the null hypothesis will be rejected and a multiple comparison test will be carried out. In these cases, post-hoc tests allows us to examine mean comparisons, which can be thought of a subset of possible contrasts between the means. The Bonferroni method is used for general tests of possible contrasts.

The AUROC curves were computed for each of the synthetic groups, contrasting sensibility and specificity in a binary classification system. Two sets of data were evaluated, one for each direction. In each of the sets, the cases of the group being evaluated (1000 synthetic VCGs) where contrasted to the other groups (3000 synthetic VCGs). The AUROC was used as the measure to quantify a good classifier to distinguish between each AFL archetype for each group from the rest of the groups.

Real data

As the patients database represents different distributions, and given the low number of cases, the non-parametric Kruskal-Wallis test was applied - used for more than two independent samples. It is roughly equivalent to a parametric one way ANOVA with the data replaced by their ranks. If the p-value is less than 0.05, the null hypothesis will be rejected.

3.5 Results

3.5.1 Synthetic data

Comparison between groups

The similarity parameters were tested for VCG comparison between groups. The ANOVA test shows statistical significance for all the cases for all groups. The F-parameter for each group ranged from $F(3,3996) = 959.20$, $p < 0.001$ to $F(3,3996) = 1456.28$, $p < 0.001$. Thus, although overlapping between groups occurs, statistical tests show differences between the types from the evaluation of the correlation parameter. Furthermore, when evaluating through multiple comparisons using Bonferroni's correction, all groups are found to show high statistical significance when compared to any other ($p < 0.001$ for all of them). Figure 3.5 shows the boxplot results of the simulation analysis from the set of data of 8000 synthetic cases (i.e. 1000 per group for each of the 8 groups) taken from the database created as described in section 3.3.1 using the tools proposed in section 3.4.3 - only groups I-IV are represented as groups V-VIII show the same behaviour, since they are described by the same loops rotating in the opposite direction.

The results of the AUROC for each AUROC curve computed from both direction (see figure 3.6) is displayed in table 3.2.

Table 3.2: AUROC for synthetic patients

	Type I	Type II	Type III	Type IV	Type V	Type VI	Type VII	Type VIII
AUROC	0.899	0.902	0.863	0.923	0.895	0.899	0.872	0.926

Influence of the slow regions

Over a controlled synthetic VCG with the slow region at one end of the major semi-axis and the fast on the opposite, rotation around the major semi-axis (slowest and fastest regions remain fixed) presents a decrease in similarity to a value as low as 0.8. On the other side, when rotating with respect to the minor semi-axis (semi-slow regions are fixed and slowest and fastest move), the similarity decreases to 0.3.

Complexity

Over a controlled synthetic VCG, the amplitude of the frequency modulating functions are progressively increasing (beginning with zero amplitude, i.e. as a 'perfect ellipse). Complexity measurements from these simulations increase from 0 up to 0.8.

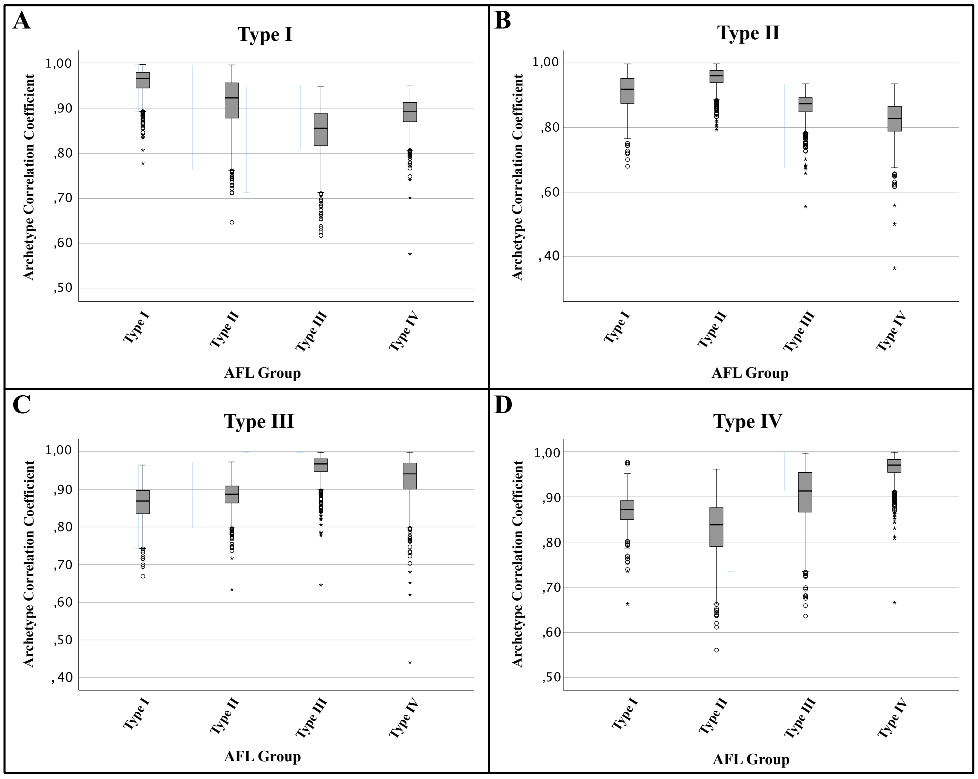

Figure 3.5: Box plot of the correlation coefficient of types I to IV with their representative archetypes (A to D correspondingly). Each subfigure represents the correlation of one archetype (created from the training synthetic cases) with all the patients from groups I to IV (the testing synthetic cases).

3.5.2 Real data

Intra-patient consistence

Consistence values were over 0.85 in all cases, with an average of 0.95±0.04. A patient registered a consistence value of 0.55 and therefore, was excluded from the analysis. Figure 3.3.B shows the superposition of 10 consecutive VCGs for a typical CCW AFL, with the averaged VCG represented by a thick dashed line.

Similarity with archetypes

Archetypes for each group are shown in Figure 3.7. The results from the average similarity of individual VCGs with group archetypes (computed according to a LOO algorithm) are detailed in table 3.3. For all groups, the highest average similarity corresponded to the archetype of its own group. In all groups, the similarity with their respective archetype was at least 0.85 on average, with a SD of less than 0.05 (see an example of perimitral VCGs in figure 3.8). The statistical results from the Kruskal-Wallis test were as follows: except for perimitral CW MRAT (p = 0.062), the results for the other groups were statistically significant. Figure 3.8 shows three examples of CCW Perimitral MRAT.

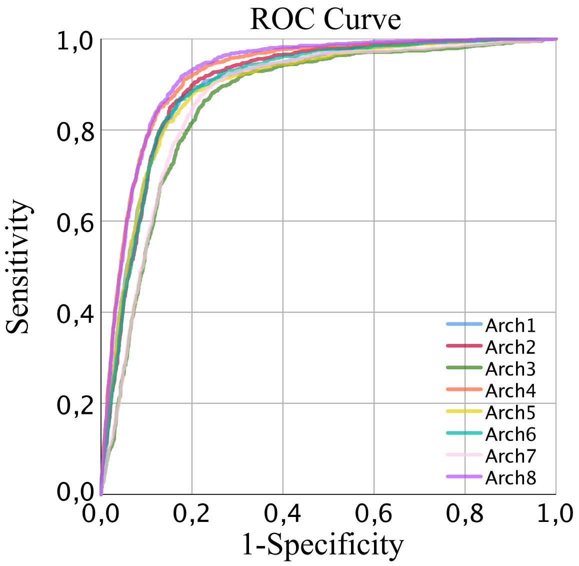

Figure 3.6: AUROC curves for all patients corresponding to each of the groups when taking into account all the 8000 synthetic patients (A) or the first 4000 in one subgroup (with types I-IV) and the rest in the other (types V-VIII).

Table 3.3: Results of correlation of archetypes with patients from MRAT groups.

	Typical CCW	**Typical CW**	**Perimitral CCW**	**Perimitral CW**	**Other types**
Typ.CCW Arch.	**0.85±0.03**	0.67±0.11	0.77±0.05	0.73±0.12	0.68±0.14
Typ.CW Arch.	0.68±0.05	**0.95±0.03**	0.66±0.13	0.75±0.04	0.58±0.13
P.CCW Arch.	0.78±0.09	0.63±0.11	**0.87±0.04**	0.68±0.12	0.62±0.18
P.CW Arch.	0.76±0.08	0.75±0.01	0.70±0.12	**0.91±0.02**	0.65±0.17
p-value	0.014	<0.01	<0.01	0.62	N.A.

Analysis of slow regions

The detection of low velocity intervals and how they can be projected to VCG and atrial signal plots is illustrated in figure 3.9. The results for the time and distance fractions during low velocity periods (TF_{LV} and DF_{LV}, respectively), as well as the ratio between these two parameters (TDR_{LV}) are summarised in table 3.4.

The non-parametric Kruskal-Wallis test over these parameters provide a statistical significance for TF_{LV} ($p = 0.047$) but no statistical significance for DF_{LV} ($p = 0.146$) or TDF_{LV} ($p = 0.698$). Note that the threshold as one fourth of the maximum velocity shows statistical significance among groups ($p = 0.025$).

Loop complexity

Complexity values for each group are shown in Table 3.5. The VCG loop described by perimitral MRAT presented higher complexity and longer periods than typical

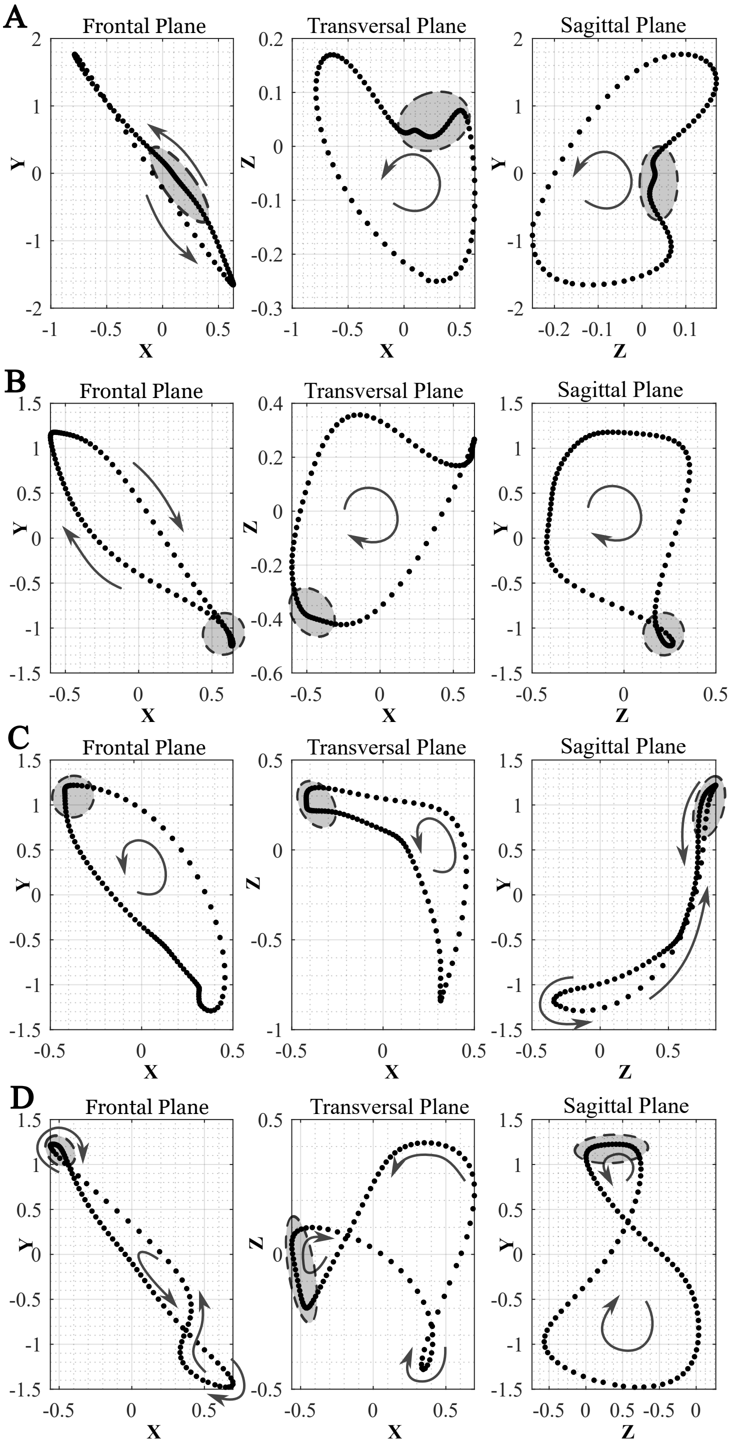

Figure 3.7: VCG archetypes for different MRAT group (principal slow velocity region and rotation sense are indicated). **A.** Typical CCW; **B.** Typical CW; **C.** Perimitral CCW; **D.** Perimitral CW.

Table 3.4: Results of $\mathbf{TF_{LV}}$, $\mathbf{DF_{LV}}$, $\mathbf{TDR_{LV}}$ and ratio between maximum and minimum velocities $V_{\max}/V_{\min}$.
*An outlier case with an unusually slow minimum velocity (which led to a $V_{\max}/V_{\min}$ ratio as high as 267.0) was excluded from the analysis.

	Typ.CCW	**Typ.CW**	**P.CCW**	**P.CW**	**Other**	**Overall**
$\mathbf{TF_{LV}}$	0.41±0.04	0.18±0.12	0.30±0.14	0.21±0.19	0.43±0.18	0.32±0.16
$\mathbf{DF_{LV}}$	0.18±0.03	0.08±0.06	0.12±0.06	0.10±0.14	0.17±0.06	0.14±0.07
$\mathbf{TDR_{LV}}$	2.24±0.30	2.30±0.26	2.47±0.37	3.23±1.54	2.46±0.40	2.47±0.59
$\mathbf{V_{max}/V_{min}}$	25.80±20.99	7.876±2.64	15.03±5.57	11.92±2.47	19.01±12.68	16.64±12.61

AFL. Moreover, complexity differences between CCW and CW variants from the same MRAT type were also found. Complexity was even higher in the miscellaneous group and in patients with anatomical deformities —a patient with typical AFL and a thoracic malformation (severe pectus excavatum) presented a complexity of 0.68. This patient was discarded from the analysis.

When performing the non-parametric Kruskal-Wallis test over the set of patients grouped as previously described, statistical significance is obtained with a p-value of $p = 0.035$ for the complexity parameter. Thus, the null hypothesis is rejected.

The complexity of the VCG loop was mildly correlated with the atrial cycle length under adenosine effects, with a correlation value of 0.62. These values are also provided in Table 3.5.

Table 3.5: Results of arc parameter for all MRAT groups.

	Typ.CCW	**Typ.CW**	**P.CCW**	**P.CW**	**Other**	**Overall**
Complexity	0.24±0.05	0.36±0.12	0.45±0.17	0.39±0.11	0.54±0.18	0.43±0.17
Period (ms)	215.50±7.79	245.20±7.37	250.13±12.79	219.00±11.85	275.89±23.01	249.28±8.85

3.6 Discussion

MRAT may be caused by different macroreentrant circuits which require different ablation approaches. Since there is no current reliable identification of the MRAT type from the analysis of the ECG, advances on this issue previous to the ablation procedure would be valuable [230]. In this study, a methodology based on the analysis of the atrial VCG loop is proposed, which can be derived from the ECG by means of the Inverse Dower's Transform.

The synthetic VCG generator model strengthens the hypothesis of the importance of slow regions when characterising. Although some overlapping occurs when correlating synthetic VCGs to different archetypes, the high significance and discrimination capacity unveiled by the statistical methods allows us to conclude the importance of the slow regions, as the only parameter unique to each group. Furthermore, controlled tests such as correlating around semi-axes shows how correlation highly depends on whether the slow region is fixed or being displaced in the space, entailing a significant decrease in this parameter. Also AUCs demonstrate this discriminating capacity between groups I-IV and V-VIII, without the bias of the noticeable difference between the two directions of rotation.

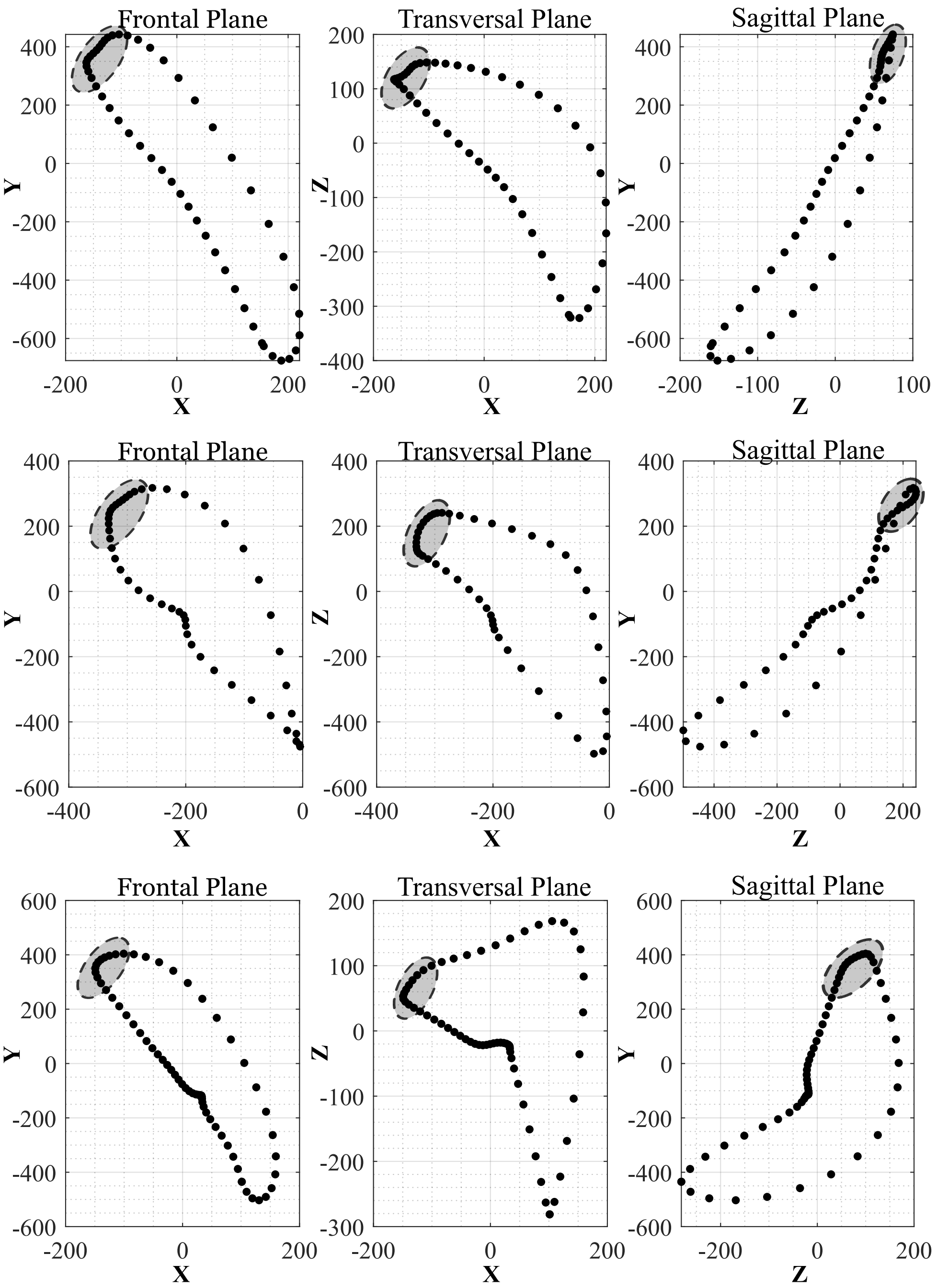

Figure 3.8: Examples of VCGs corresponding to CCW Perimitral MRAT (main slow velocity regions are highlighted). Notice the high coincidence with the CCW Perimitral MRAT in figure 3.7.C.

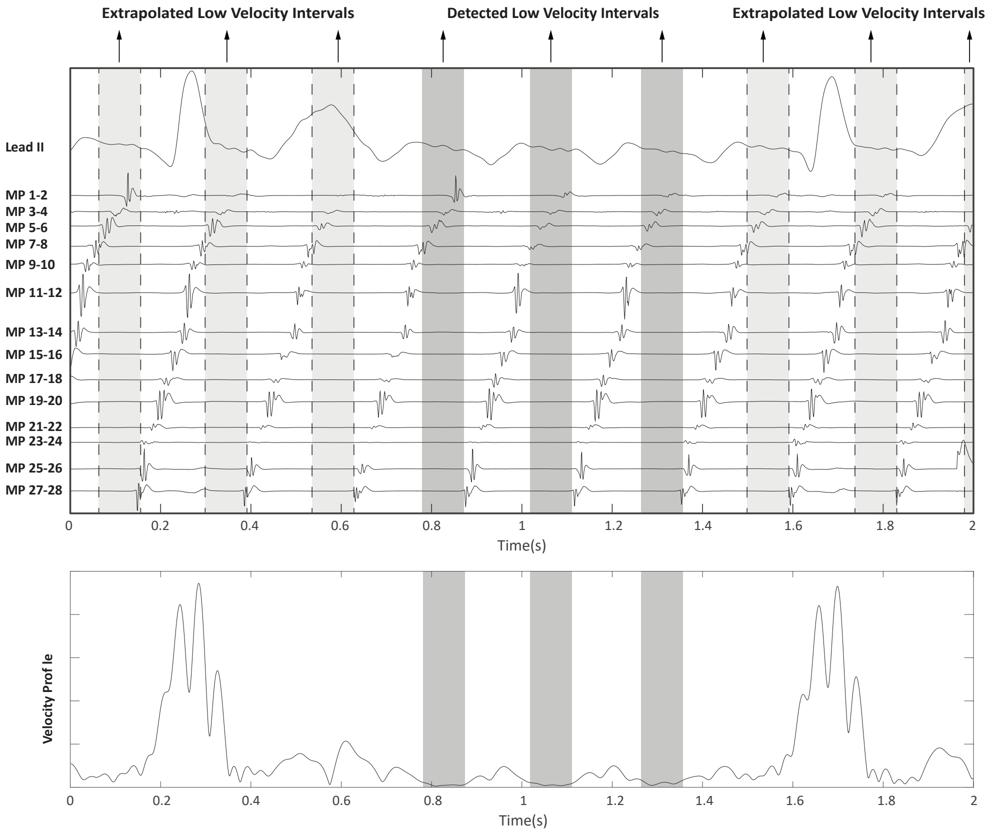

Figure 3.9: Slow velocity intervals detected from the velocity profile of a typical AFL (bottom) are highlighted on the temporal EGM sequence (dark gray), and extrapolated to segments with ventricular activity (light gray). These intervals matched with the activation timing at the electrodes located on the CTI (MP 1-2,3-4 and 5-6).

In the real cases, the proposed methodology enables us to find differences between different MRAT types, even between CCW and CW variants of the same MRAT type. This suggests that loops with CCW and CW rotation directions should be treated independently as different groups. Moreover, there was a high similarity between patients belonging to the same MRAT group, with SDs below 0.04 in this parameter. These results outline a promising capability for the identification of the MRAT type. This approach is based on the comparison of the VCG loop with a collection of archetypes corresponding to each MRAT variant. To increase the utility of this method, a universal and publicly available dataset of archetypes would be an asset, so that each health centre did not have to recruit a large number of patients to initiate the study. To proceed with the comparison of VCG loops, it should be remarked that a normalisation of the same number of samples per atrial cycle is required. Furthermore, loops should be time-aligned. Although in this conceptual study, the brute force was carried out for this alignment, since the cost function would not show local maxima, a simple maximisation approach such as the steepest descent method could be used instead to save computational load. This is not, however, a critical issue, as the number of computations to be run is feasible.

Interestingly, a discretised plot of MRAT VCG loops showed regions with higher density of samples, consistent with the slow-conduction regions responsible for the perpetuation of the macroreentrant circuit. This property of the atrial VCGs has not been reported hitherto. In addition, this may play a key role for the identification of the MRAT type. The velocity profile described by the surface VCG loop showed significant differences along the pathway, with a median of 12.93 for ratios between the fastest and slowest velocity, ranging between 4.55 and 256.95, which confirms the systematic presence of a low velocity region. In those periods with lower velocity, a much longer time is required to cover a similar arc portion in contrast to other instants with higher velocity. In addition to velocity definition measured as voltage increment per cycle unit, the angular velocity would also be of interest, as it may highlight direction changes in sites close to the VCG centre, i.e. with short turning radius, as if an obstacle is surrounded. Whether this is related to an anatomical or physiological feature is still to be explored.

An important application of this method is the identification of the slow conduction intervals. This would allow a real-time projection to highlight these segments on the signal registered by an exploratory catheter (e.g. the ablation catheter), which would be useful for monitoring whether it is approaching or moving away from the slow conduction region. This would help find the target ablation sites more efficiently. Figure 3.9 illustrates an example of a typical AFL, with the 1-2, 3-4 and 5-6 electrode pairs of the multipolar catheter placed on the cavo-tricuspid isthmus. As shown in this figure, once the slow conduction intervals are identified, and due to the periodicity and regularity of the macroreentry mechanisms, these can also be extrapolated to segments where the atrial signal is masked by ventricular components. This is also applicable to patients with q consistent 2:1 AV conduction ratio, where the atrial wave is no longer visible during long periods, which brings tremendous potential to guide the electrophysiologic exploration.

Unexpectedly, there were important differences in time and distance fractions during low velocity between CCW and CW variants of the same MRAT type. This raises new questions regarding asymmetries in the conduction properties depending on the rotation direction, which should be answered by electrophysiologic studies.

Regarding the complexity of the atrial loop, perimitral MRAT presented more complex patterns, which suggests a longer and winding pathway to close the loop. This property is even magnified in MRATs with anatomical deformities.

In order to apply this method successfully, the unequivocal atrial signal —i.e. with no ventricular activity— is required. However, the atrioventricular (AV) conduction ratio is often as short as 2:1. Therefore, the atrial signal is overlapped by either the QRS complex or the T wave. Due to the high consistency of atrial loops, even one single loop could be sufficient, which could be captured if longer RR intervals were available. Otherwise, adenosine administration or carotid massage could facilitate obtaining the atrial signal. Nevertheless, specific approaches to retrieve the atrial signal from the ECG would be valuable. Although several approaches have been proposed for AF, they are likely to fail in the case of AFL. Regarding algorithms based on QRS-T cancellation [231, 210], as long as the atrial cycles are coupled with the ventricular activity, the atrial signal will be removed as well. On the other hand, methods based on Blind Source Separation [212] are able to extract one projection consistent with the atrial source. However, a single component is still insufficient to project back the VCG, as three (or at least 2) components would be required, rendering those methods useless. Therefore, improved algorithms exploiting either the spatial or temporal properties of the signals —such as projective filtering methods [232] or Periodic Component Analysis (πCA) [233]— worth to be developed. In addition to that, another strategy based on the estimation and removal of the T-wave in MRAT has been recently proposed [214], which would also be of high interest if could robustly retrieve a complete atrial cycle in patients with stable AV conduction ratio of 2:1.

3.6.1 Study limitations

We are aware of the low number of patients per group involved in this study. Nonetheless, statistically significant results were obtained, which are expected to improve by adding new data, e.g. with further multicentric studies.

Regarding our simulation model, we employed a geometrical approach, as decribed above. Although this allows us full control of the parameters involved and a thorough evaluation of the properties of the methods, it does not arise from a physiological phenomenon. Further studies with in-silico 3D models of atrial activations according to Courtemanche modelling of ionic mechanisms and numerical computation of the VCG by means of the forward problem could provide different patterns associated with different macroreentrant circuits [234]. In turn, the simulated VCG loops could be compared to their corresponding archetypes obtained from real data.

Finally, we are also constrained to the inherent limitations of the system for signal acquisition and cardiac mapping (CARTO®3, Biosense Webster). Novel high density acquisition systems such as the Advisor™HD Grid Mapping Catheter (Abbott Laboratories) or RHYTHMIA HDx™(Boston Scientific) are able to collect, display and analyze data with higher resolution. These techniques arise as very promising alternatives for a better and more accurate characterization of the EP substrate and, hence, to provide improved and clinically meaningful information for the management of MRATs [235, 236].

3.7 Conclusions

A non-invasive methodology is proposed to characterise different MRAT circuits from ECG recordings. The proposed method is based on the VCG, and more precisely, on the evaluation of the loop trajectory. This study shows how different VCG loops present some similarities between the same MRAT group. Moreover, this tool reflects sites with slow velocity, consistent with slow conduction regions, prominent in the macroreentrant circuit. The proposed approach can help to better identify the MRAT type in a non-invasive way. Having this information prior to the ablation procedure would be valuable in order to improve planning and management of medical interventions.

Chapter 4

Performance Assessment of Electrode Configurations for the Estimation of Omnipolar Electrograms from High Density Arrays

---

Abstract

Objective: The aim of this study is to propose a method to reduce the sensitivity of the estimated omnipolar EGM (oEGM) with respect to the angle of the propagation wavefront. **Methods**: A novel configuration of cliques taking into account all four electrodes of a squared cell is proposed. To test this approach, simulations of HD grids of cardiac activations at different propagation angles, CVs, interelectrode distance and EGM waveforms are considered. **Results**: The proposed approach successfully provided narrower loops (essentially a straight line) of the electrical field described by the bipole pair with respect to the conventional approach. Estimation of the direction of propagation was improved. Additionally, estimated oEGMs presented larger amplitude, and estimations of the LATs were more accurate. **Conclusions**: A novel method to improve the estimation of oEGMs in HD grid of electrodes is proposed. This approach is superior to the existing methods and avoids pitfalls not yet resolved. **Relevance**: Robust tools for quantifying the cardiac substrate are crucial to determine with accuracy target ablation sites during an EP procedure.

This chapter is based on the publication: F. Castells*, S. Ruipérez-Campillo*, et al. (2023). Performance assessment of electrode configurations for the estimation of omnipolar EGMs from high density arrays. *Computers in Biology and Medicine*, 154, 106604. [237]

* denotes co-first authorship

4.1 Introduction

Accurate characterization of the electrophysiologic substrate is crucial in identifying regions responsible for some cardiac arrhythmias and other cardiac disorders such as VT [238], Brugada Syndrome [9] and AF [10], among others. In the case of VT with a reentry mechanism, regions of fibrosis with surviving myocyte bundles create fixed or functional conduction blocks in addition to slow conduction. In this scenario, stable circuits can be mapped with high density mapping catheters and later modelled accordingly. Accurate mapping of the substrate is essential in determining the degree of conduction delay and the critical isthmus. Moreover, remodeling of the myocardium following an infarction contributes to the formation of channels and regions in which conduction time is prolonged, facilitating the initiation of a reentry [239]. In the case of AF, the substrate for AF relates to left atrial (LA) dilation and fibrosis with subsequent LA dysfunction and delay in electromechanical conduction. Regions with anomalous conduction such as fibrotic tissue are associated to arrhythmogenic substrates in AF [35] and, therefore, may become target ablation sites [240].Indeed, previous studies have shown that areas with fibrosis —detected with late gadolium enhanced magnetic resonance imaging— are correlated to lower voltage EGMs and slower CV [241]. Therefore, accurate mapping of these regions would undoubtedly provide important information that can be used for substrate modification during an EP procedure.

However, despite the importance of quantitative EGM biomarkers —such as amplitude and degree of fractionation— for identifying candidate target ablation sites, discrepancies in the detection of low-voltage regions between different electroanatomic mapping systems as yet remain unresolved [242]. Additionally, accurate detection of LATs is required to quantify parameters related to the propagation of the activation wavefront, such as CV. There are two main modes to obtain intracardiac EGMs. One of which is whereby unipolar EGMs (uEGMs) are recorded from the differential potential between an exploring electrode and a distant electrode. On the other hand, bipolar EGMs (bEGMS) are obtained from the differential potential between a pair of closely spaced electrodes (with interelectrode distance of few millimeters). Whereas uEGMs present some problems related to electric far-field interference [11], bEGMs are sensitive to the orientation of the bipole pair with respect to the direction of the propagation wavefront [243] and catheter contact angle, among other factors [244]. In order to overcome these limitations, an ingenious way to obtain an oriented-independent bEGM from high-density multielectrode arrays —denoted as omnipolar EGM (oEGM)— has been recently proposed [245]. This method, also referred to as orientation-independent sensing (OIS), requires a grid of regularly arranged unipolar electrodes. Using this concept, the Advisor™HD Grid Mapping Catheter (Abbott Laboratories, Illinois, US) was developed [17] for a better characterization of the EP substrate [16]. This catheter consists of a 4 × 4 grid of unipolar electrodes regularly arranged with an interelectrode distance of 4mm, which allows a thorough exploration of the local cardiac tissue (see Figure 4.1.A) [15]. This catheter has been successfully used for substrate exploration, e.g. for scar detection [246], characterization of conduction gaps [20], atrial disorders such as AF [247] or VT [22], amongst others.

To estimate an oEGM, at least three unipolar electrodes arranged as the vertices of a triangle are required. The group of electrodes involved to estimate the oEGM has

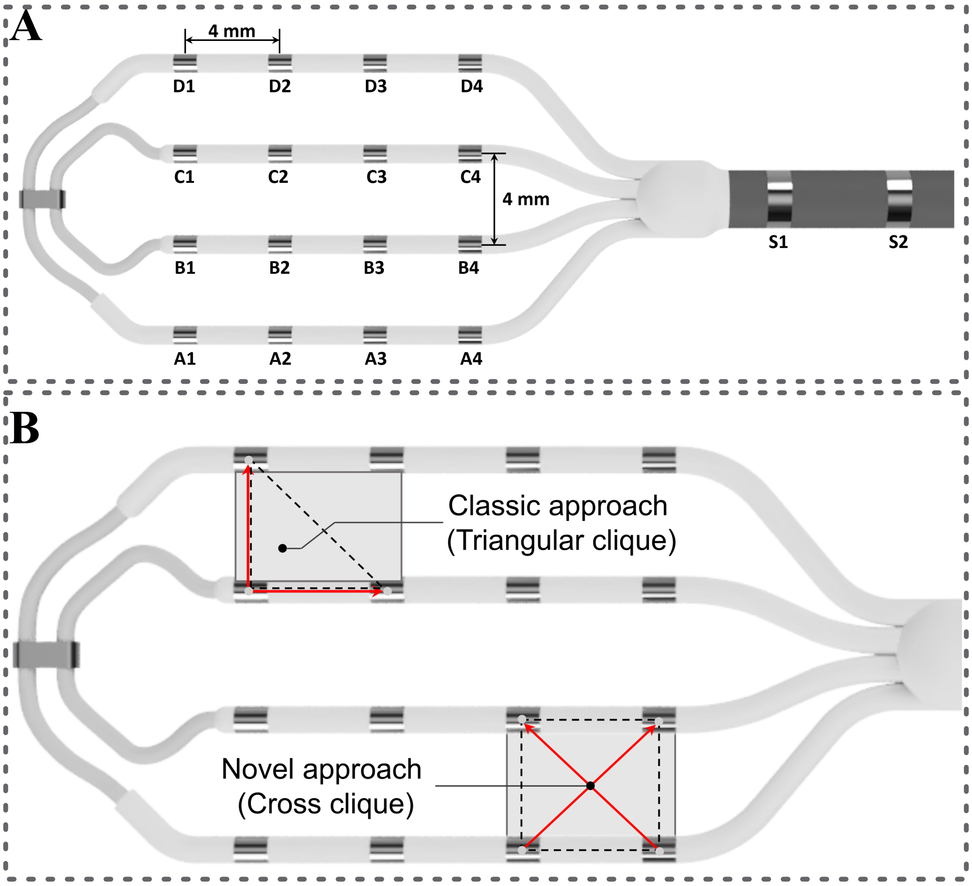

Figure 4.1: Representation of the geometry of the Advisor™HD Grid Mapping Catheter (Abbott Laboratories, Illinois, US). **A.** Geometry and position of the electrodes in a model of the device (not to scale, see measuring marks). **B.** Illustration of the classic approach of a triangluar clique on one of the four-electrode configurations (upper left) and the novel approach described in this work, that is, the cross clique (lower right).

been denoted as a clique [15]. Furthermore, a close proximity between electrodes is required to satisfy the assumption of a locally plane and homogeneous propagation within the clique. Using a configuration based on an isosceles right angled triangle, two orthogonal bEGMs are obtained from the electrodes at the short sides (notice that the unipolar electrode corresponding with the vertex at the right angle is used twice). The representation of the electrical field from a pair of orthogonal bEGMs describes a loop with maximal modulus in the direction of propagation [16]. Subsequently, the oEGM can be computed as the orthogonal transformation that maximizes the amplitude of the activation (i.e. a geometric rotation of the raw data). Accordingly, oEGMs can be regarded as virtual representations of bEGMs as if they were captured from an electrode pair matching the direction of the propagation wavefront. This provides a more meaningful measure of the real amplitude of the activation in comparison to uEGMs and bEGMs, hence, allowing a more robust detection of low-voltage areas [248]. Additionally, it also allows an estimation of the direction of propagation and higher accuracy in the detection of LATs.

Applying this concept to a cell of 2×2 electrodes, 4 triangular cliques can be defined according to the triad of electrodes considered. For each of those cliques, the oEGM can be derived. When extrapolating it to a 4×4 grid of unipolar electrodes (i.e. 3×3 cells), this technique provides an array of 6×6 cliques, with 2×2 cliques arranged per cell [249]. Furthermore, the estimation of such a high-density oEGMs matrix allows other measurements such as CV or heterogeneity of the propagation.

Although claimed as orientation-independent EGM, a recent study has shown significant sensitivity in the reconstruction of the oEGM with respect to the direction of propagation [23]. Additionally, it concluded that the cause for errors in the estimation of oEGMs were temporal misalignments between bipolar activations. This limitation reveals an important research gap regarding the OIS approach, since the electrode configurations and settings under which the orientation independence condition is satisfied remain to be unexplored.

In this study we aim to address that research gap, by evaluating the performance of different clique configurations and interelectrode distances. For this, we considered the conventional triangular clique employed in clinical practice as well as square and cross-oriented cliques using the four electrodes of a 2×2 cell. Whereas the square clique obtains average bipole pairs by averaging the two horizontal and two vertical bipoles of the square, respectively, the cross-oriented clique employs the diagonal bipoles pairs. We hypothesize that misalignments ocurring with triangular cliques can be reduced with other clique configurations and hence, providing oEGMs less sensitive to the direction of the propagation wavefront. Additionally, the effect of interelectrode distance is explored.To test our hypothesis, we explored the sensitivity to angle orientation of different clique configurations using controlled simulations. Specifically, we analyzed the dependence of the performance as a function of the following parameters: CV, morphology of the signal and interelectrode distance.

This manuscript is organized as follows: section 4.2 elaborates on the methods, describing the simulations, clique configurations, procedure to estimate the oEGM and the parameters for performance assessment. Section 4.3 shows an objective comparison of performance using different clique configurations and electrode spacing, which are discussed in-depth in section 4.4. Finally, section 4.5 concludes this work with the main remarks and outcomes of the study.

4.2 Methods

The purpose of synthetic signals is to quantify the influence of the angle orientation in the estimation of oEGMs. With that objective, simulated clique activations with known propagation directions and CV are generated. Considering the waveform of real uEGM activations sampled from intracardiac clinical data, we replicated delayed versions according to the direction of the propagation wavefront and the position of each electrode within the multielectrode grid. Figure 4.1.A illustrates the multielectrode arrangement, with A-D and 1-4 denoting rows and columns, respectively. Montecarlo simulations were carried out considering randomized propagation angles, CV within physiological range (from 0.5m/s to 1m/s) and random selection of atrial uEGMs among 5 different patterns taken from clinical recordings at different atrial sites. Furthermore, we considered different distances from 1mm to 4mm, in steps of 1mm. For each interelectrode distance, 100 simulations were undertaken in accordance with the aforementioned variables.

4.2.1 Configurations of bEGMs within a clique

Given a cell with 2×2 electrodes, up to 6 bEGMs can be computed: the four side bEGMs $b_{\mathrm{A2-A1}}$, $b_{\mathrm{B2-B1}}$, $b_{\mathrm{A1-B1}}$ and $b_{\mathrm{A2-B2}}$, plus the diagonal bEGMs $b_{\mathrm{A2-B1}}$ and $b_{\mathrm{A1-B2}}$. Being b_x and b_y the bEGMs corresponding to x and y axes, respectively, the conventional triangular clique configurations are defined as [23]:

- Top left triangle: $b_x(t) = b_{\mathrm{B2-B1}}(\mathrm{t})$ and $b_y(t) = b_{\mathrm{B1-A1}}(t)$
- Top right triangle: $b_x(t) = b_{\mathrm{B2-B1}}(t)$ and $b_y(t) = b_{\mathrm{B2-A2}}(t)$
- Bottom left triangle: $b_x(t) = b_{\mathrm{A2-A1}}(t)$ and $b_y(t) = b_{\mathrm{B1-A1}}(t)$ (see Figure 4.1.B, Triangular clique)
- Bottom right triangle: $b_x(t) = b_{\mathrm{A2-A1}}(t)$ and $b_y(t) = b_{\mathrm{B2-A2}}(t)$

Notice that the geometrical center of each of the bEGMs involved in the clique, regardless of the triangle configuration, are coincidental (see geometry in Figure 1.B, Triangular clique). This is a major drawback when combining EGMs that are not spatially —and hence, neither temporally— aligned. Notice also that, in the case of triangular configurations, there is always an electrode that is used twice (in both horizontal and vertical bEGMs), whereas there is always an electrode that lays unused. Apart from the classical triangular cliques, two alternative configurations that make use of the four electrodes of the square cell can be defined as:

- Square:

$$b_x(t) = \frac{1}{2}\left(b_{\mathrm{A2-A1}}(t) + b_{\mathrm{B2-B1}}(t)\right) \tag{4.1}$$

  and

$$b_y(t) = \frac{1}{2}\left(b_{\mathrm{B1-A1}}(t) + b_{\mathrm{B2-A2}}(t)\right) \tag{4.2}$$

- Cross:

$$b_{d_1}(t) = b_{\mathrm{B2-A1}}(t) \tag{4.3}$$

  and

$$b_{d_2}(t) = b_{\mathrm{B1-A2}}(t) \tag{4.4}$$

Notice that the diagonal bipoles of the square cell are utilized for the cross-oriented clique (see Figure 4.1.B, Cross clique), which imposes a coincident center for both bipoles. Regardless of the configuration considered, we can define the vector $\mathbf{b}(t)$ containing the orthogonal bipole pair, with $\mathbf{b}(t) = [b_x(t) \;\; b_y(t)]^{\mathrm{T}}$. In the case of the cross-oriented configuration, the unique correction left to be done to determine $\mathbf{b}(t)$ is a simple counterclockwise rotation of $\frac{\pi}{4}$rad:

$$\mathbf{b}(t) = \begin{bmatrix} \cos\frac{\pi}{4} & -\sin\frac{\pi}{4} \\ \sin\frac{\pi}{4} & \cos\frac{\pi}{4} \end{bmatrix} \mathbf{d}(t) = \frac{1}{\sqrt{2}} \begin{bmatrix} 1 & -1 \\ 1 & 1 \end{bmatrix} \mathbf{d}(t), \tag{4.5}$$

where $\mathbf{d}(t) = [b_{\mathrm{B2-A1}}(t) \;\; b_{\mathrm{B1-A2}}(t)]^{\mathrm{T}}$ is the pair of diagonal bEGMs. Therefore, after this orthogonal transformation, the problem to solve remains the same as using the configurations previously mentioned. Despite the fact that square and cross-oriented cliques arise from different definitions, it can be proven that both yield to an equivalent $\mathbf{b}(t)$ vector up to a scaling factor. By breaking down the notation of bEGMs as uEGMs difference (e.g. $b_{\mathrm{A2-A1}}(t) = u_{\mathrm{A2}}(t) - u_{\mathrm{A1}}(t)$):

$$\begin{aligned}\mathbf{b}_{\text{cross}}(t) &= \frac{1}{\sqrt{2}}\begin{bmatrix}1 & -1\\ 1 & 1\end{bmatrix}\begin{bmatrix}u_{\mathrm{B2}}(t) - u_{\mathrm{A1}}(t)\\ u_{\mathrm{B1}}(t) - u_{\mathrm{A2}}(t)\end{bmatrix}\\ &= \frac{1}{\sqrt{2}}\begin{bmatrix}(u_{\mathrm{B2}}(t) - u_{\mathrm{B1}}(t)) + (u_{\mathrm{A2}}(t) - u_{\mathrm{A1}}(t))\\ (u_{\mathrm{B2}}(t) - u_{\mathrm{A2}}(t)) + (u_{\mathrm{A1}}(t) - u_{\mathrm{B1}}(t))\end{bmatrix} = \sqrt{2}\mathbf{b}_{\text{square}}(t)\end{aligned} \tag{4.6}$$

Accordingly, we will unify both square and cross-oriented configurations and refer to them in the following as the square clique.

4.2.2 Estimation of oEGMs

When representing the local electrical field in a clique from a pair of orthogonal bEGMs, it describes a loop that points to the direction of propagation. In the case of a plane and homogeneous wavefront —as it should be fulfilled with HD grids—, the loop should become narrow enough to almost fit a straight line. As long as oEGMs are defined as the projections of orthogonal bEGM pairs on the direction of wavefront propagation, this transformation ideally exhibits maximal peak amplitude of the activation. In addition, the projection on a perpendicular axis would provide a residual signal with low amplitude. In accordance with this, the oEGM is computed as the projection that maximizes the ratio of the oEGM peak amplitude to the peak amplitude of the residue:

$$\hat{\theta} = \underset{\theta}{\operatorname{argmax}}\left[\frac{\max\left(\begin{bmatrix}\cos\theta & -\sin\theta\end{bmatrix}\mathbf{b}(t)\right)}{\max\left|\begin{bmatrix}\sin\theta & \cos\theta\end{bmatrix}\mathbf{b}(t)\right|}\right] \tag{4.7}$$

$$\mathbf{o}(t) = \begin{bmatrix}\cos\hat{\theta} & -\sin\hat{\theta}\\ \sin\hat{\theta} & \cos\hat{\theta}\end{bmatrix}\mathbf{b}(t) \tag{4.8}$$

where $\mathbf{o}(t) = \begin{bmatrix}o(t) & o_{\perp}(t)\end{bmatrix}$, being $o(t)$ the estimated oEGM and $o_{\perp}(t)$ the residual bipolar signal resulting from the projection on the orthogonal axis to the direction of the propagation wavefront. The direction of the wavefront can be estimated as $\Psi = -\hat{\theta}$.

4.2.3 Assessement of oEGM estimation

The quality of oEGM estimations from simulations of perfectly plane and homogeneous wavefront propagations will be assessed from the peak amplitudes of the pulses retrieved from vector $\mathbf{o}(t)$: $p_o = \max(o(t))$ and $p_{o_\perp} = \max\left(|o_{\perp}(t)|\right)$, as well as the peak ratio $r = p_o/p_{o_\perp}$. In order to assess top performance limits for each configuration, true propagation directions will be employed to compute $\mathbf{o}(t)$. Best fits to the real oEGM would exhibit higher p_o, lower $p_{o_\perp}$ and, therefore, higher r values.

With respect to the accuracy in the detection of LATs, these are estimated as the instant at peak amplitude of the oEGM signal [250]. Estimated LATs will then be compared to the ground truth, defined as the instant at maximum negative slope of the unipolar signal as it passes through the center of the clique.

For the analysis of performance dependence with respect to CV, interelectrode distance and uEGM morphology, a simulation is designed. Regarding morphology, uEGMs with slower/faster deflections (i.e. with smoother or sharper transitions) are considered. For each setting, the consistency of the morphology of the estimated bEGM will be evaluated. This will allow us to assess the robustness of the method as well as its limitations.

4.2.4 Statistical Analysis

Results are provided as mean ± standard deviation (SD), or median and interquartile range (IQR) if required. For data exploration, the distribution of the independent variables was evaluated using Kolmogorov-Smirnov and Mann-Whitney-Wilcoxon tests. A *p-value* of <0.05 was considered statistically significant throughout.

4.3 Results

Figure 4.2 shows bidimensional loops decribed by orthogonal bEGMs for different bipole configurations, including all triangular orientations and the square clique. For the sake of simplicity, propagation directions $\Psi = 0^\circ, 15^\circ, 30^\circ, 45^\circ and -45^\circ$ were considered. It can be observed that all configurations display a straight line for horizontal propagation (i.e. $\Psi = 0^\circ$ or $\Psi = 180^\circ$). Although not shown, analogous behavior was obtained for exact vertical propagations (i.e. $\Psi = 90^\circ$ and $\Psi = -90^\circ$). For other propagation directions there was at least one configuration that displayed a bidimensional loop.

Widest loops were obtained with triangular configurations at propagation directions perpendicular to the bisector formed by the bEGMs involved. In those cases, the delay between both bipole centers was maximal. As can be observed in Figure 4.2, triangular configurations 1 and 4 showed the same pattern although rotated and mirrored. The same occurs with triangular configurations 2 and 3. This can be explained by the fact that the wavefront activates b_x earlier than b_y, or vice versa, depending on the triade of electrodes considered for the clique. As well as this, triangular configurations showed a straight line at propagation directions that matched the bisector of the bEGMs. For example, for $\Psi = 45^\circ$, configurations 2 and 3 displayed a straight line, whereas configurations 1 and 4 displayed a wide loop. Analogous behaviour is shown for $\Psi = -45^\circ$, with exchanged roles of the cliques involved. In all cases, the square clique showed consistently narrower loops regardless of the incidence angle. The amplitude of the residual signal at its perpendicular direction was also minimal for the square clique, regardless of the propagation direction (see Figure 4.3). Moreover, triangular configurations estimated angle and LATs with higher error and provided oEGMs with lower amplitude and peak ratio.

Figure 4.4 shows boxplots comparisons among triangular and square cliques for the following parameters: angle errors, oEGM amplitude, amplitude ratios r and LATs errors. In this figure, an interelectrode distance of 1mm was considered. In addition, Table 4.1 shows the numerical results for this and other interelectrode distances. For all parameters, the null hypothesis of the Kolmogorov-Smirnov test of normality was rejected. Accordingly, the Mann-Whitney-Wilcoxon test was performed.

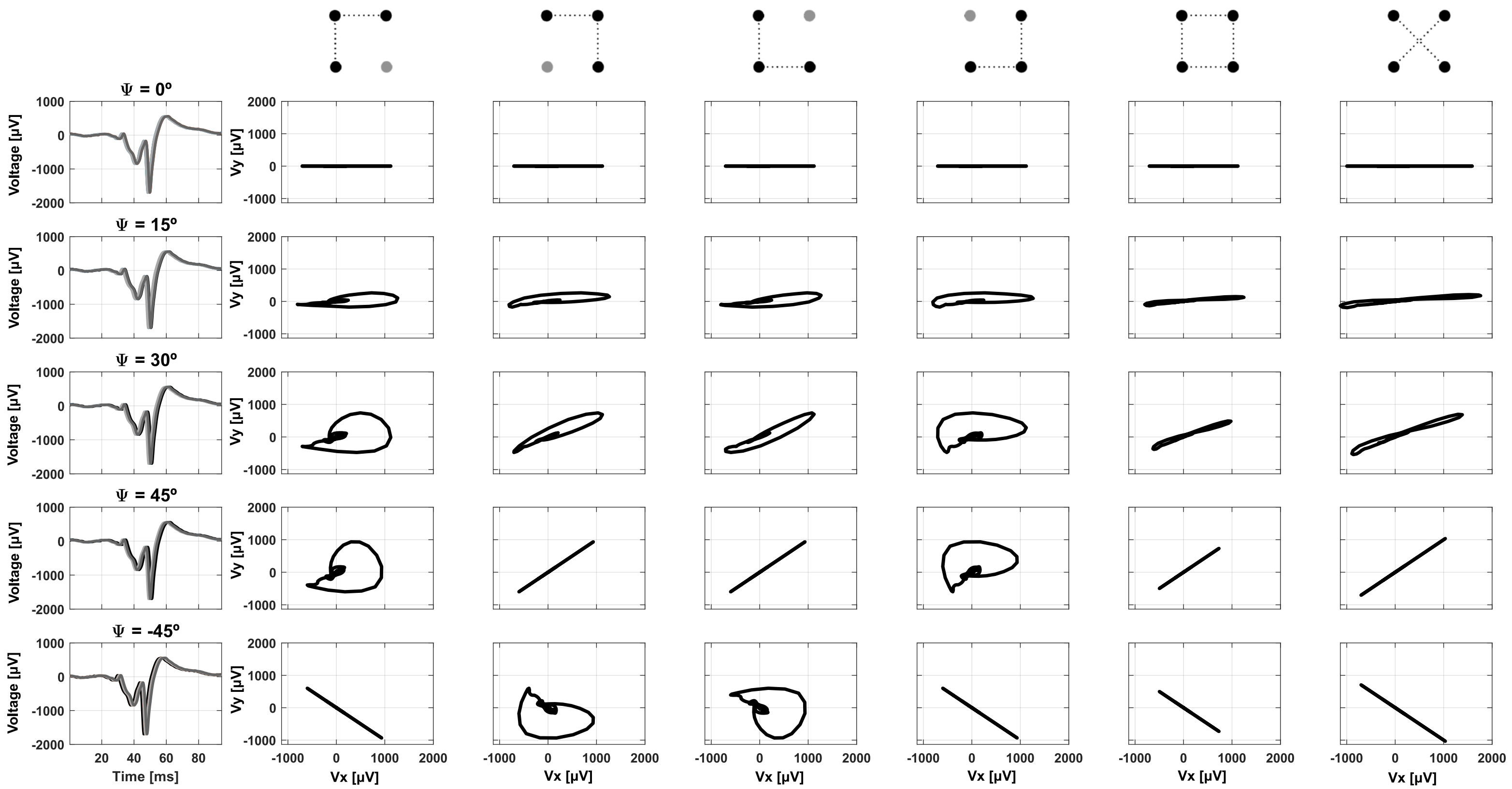

Figure 4.2: Bidimensional loops described by orthogonal bEGMs for triangular, square and cross-oriented configurations and propagation directions $\Psi = 0^\circ, 15^\circ, 30^\circ, 45^\circ and - 45^\circ$.

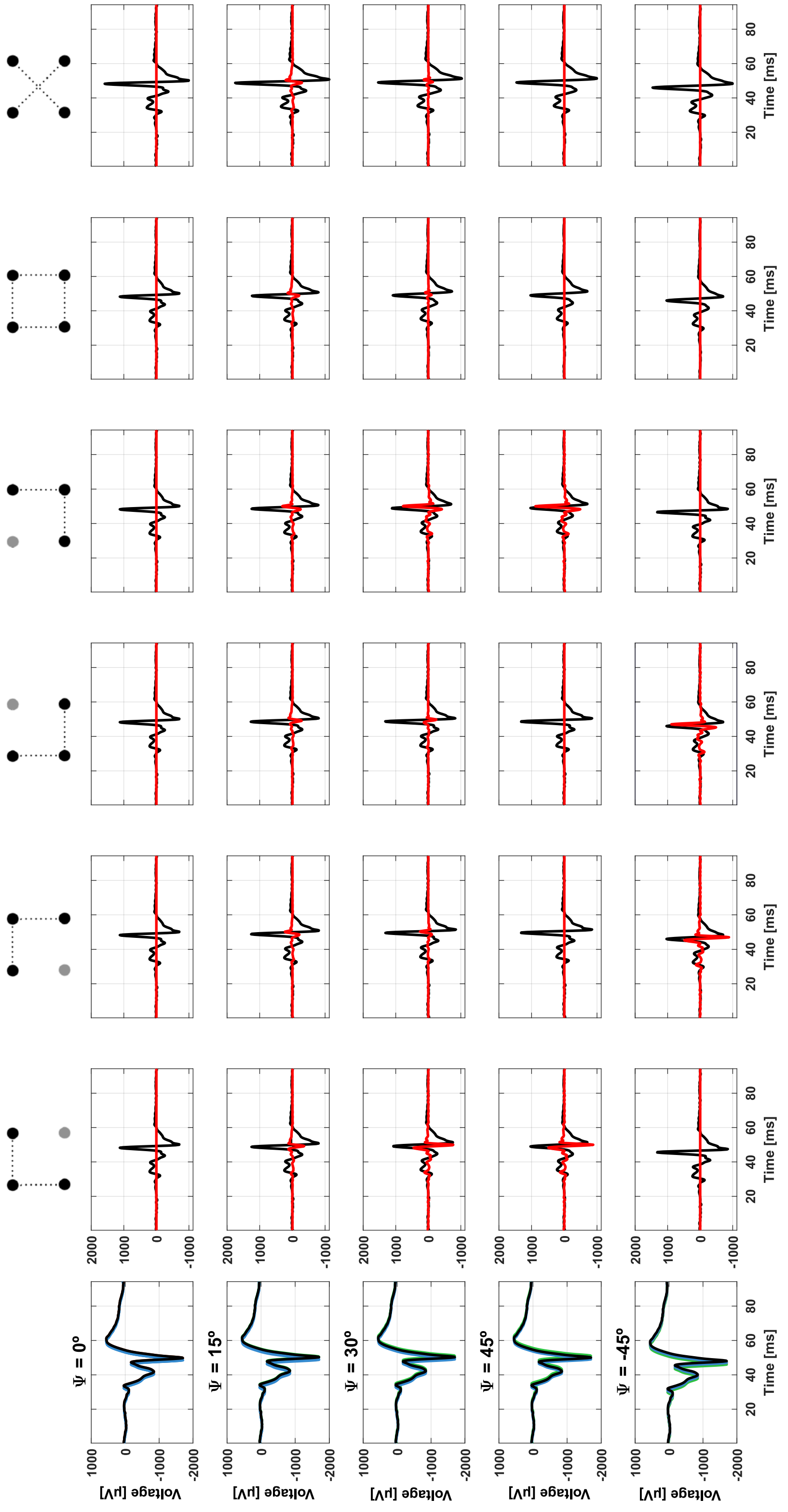

Figure 4.3: Omnipolar EGMs (black) and the residual signal $o_\perp(t)$ (red) retrieved propagation directions and bipole configurations of Figure 4.2.

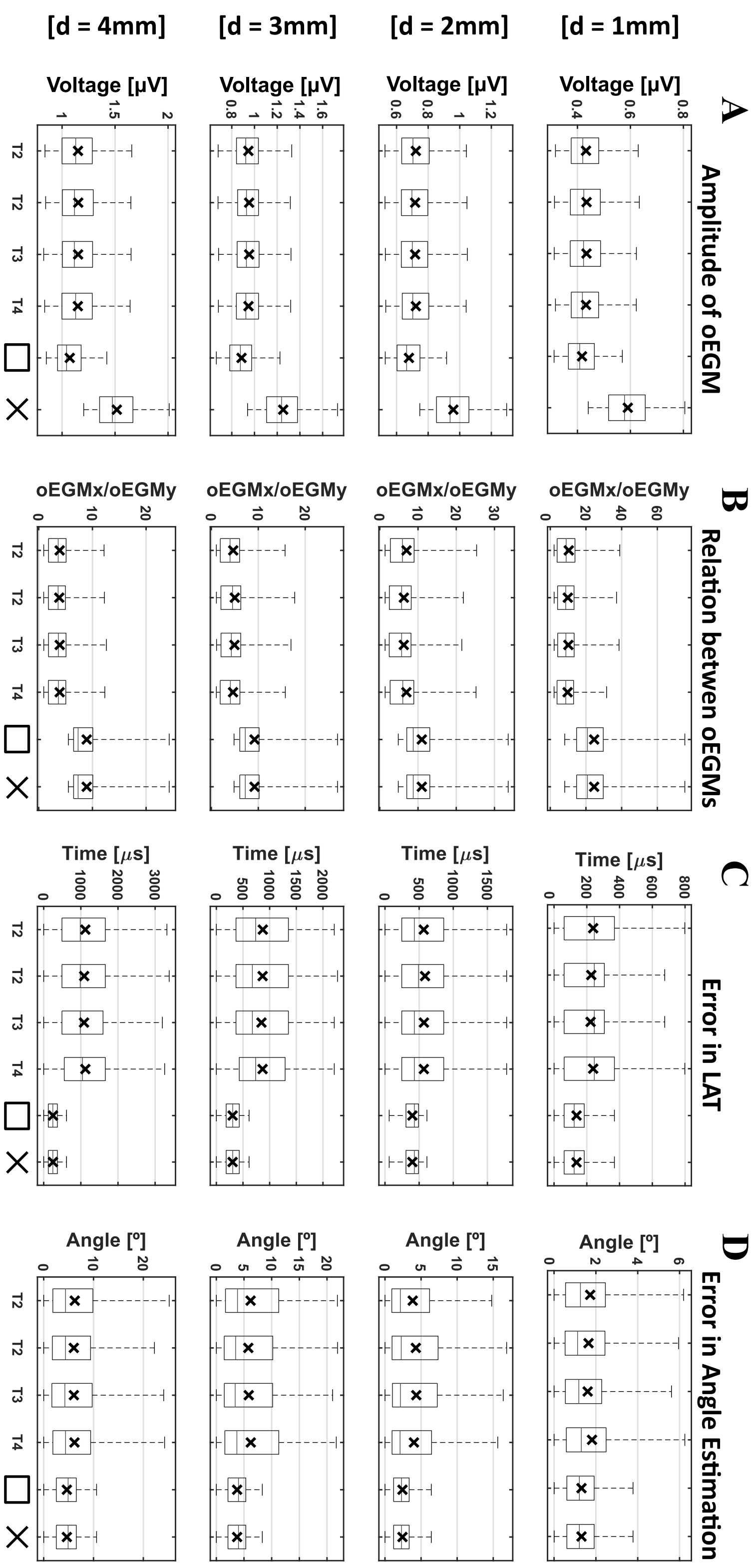

Figure 4.4: Boxplot of different variables to compare the bipoles and the triangular and square configuration, namely: **A.** Amplitude oEGM, **B.** Relation between oEGMs, **C.** Error in LAT and **D**: Error in Angle Estimation.

Table 4.1: Statistical values of results for simulations.

		Triangle	Square
1mm	Angle error	1.81 ± 1.56°	1.20 ± 0.83°
	Amplitude	360.17 ± 88.55μV	345.56 ± 84.45μV
	Peak ratios*	5.98 [2.03. . . ∞]	10.48 [6.10. . . ∞]
	LAT error	168.94 ± 148.78μs	87.18 ± 81.46μs
2mm	Angle error	3.37 ± 3.75°	1.94 ± 1.38°
	Amplitude	595.84 ± 139.01μV	566.04 ± 126.65μV
	Peak ratios*	5.65 [1.40. . . ∞]	9.01 [4.86. . . ∞]
	LAT error	437.56 ± 334.48μs	296.00 ± 152.12μs
3mm	Angle error	4.58 ± 4.46°	2.87 ± 1.81°
	Amplitude	976.34 ± 183.33μV	752.27 ± 162.31μV
	Peak ratios*	5.20 [1.12. . . ∞]	8.14 [4.84. . . ∞]
	LAT error	677.13 ± 504.07μs	365.94 ± 150.67μs
4mm	Angle error	5.92 ± 6.02°	3.82 ± 2.20°
	Amplitude	976.34 ± 213.53μV	911.43 ± 189.64μV
	Peak ratios*	4.76 [0.94. . . ∞]	7.55 [4.87. . . ∞]
	LAT error	929.50 ± 651.50μs	339.88 ± 172.05μs

*Median and range values are shown for this parameter.

Statistical values for interelectrode distances of 1mm, 2mm, 3mm and 4mm are shown in Table 4.1. By increasing the interelectrode distance, the following effects were observed: angle estimation errors increased, oEGM amplitude increased, peak ratios decreased and LAT deviations increased.

Morphologies of bEGMs exhibited dependency on several factors, as depicted in Figure 4.5. In panel A, a uEGM with slow deflections (i.e. smoother slopes) was employed. On the other hand, in panel B, a sharper uEGM morphologies was considered.

In each panel, two simulations were carried out. The first simulation consists of a parametric analysis with respect to CV, while keeping the interelectrode distance unchanged. The second simulation is performed with increasing interelectrode distance, while keeping CV constant (1m/s). Either by decreasing CV or increasing interelectrode distance, the delay between the activations captured by the electrode pair is increased. As can be observed, the larger the delay, the wider the bEGM morphology. In addition, above a certain delay threshold, bEGMs became notched, thus corrupting the bEGM morphology.

For the first simulation and setting the interelectrode distance to 4mm, bEGMs became notched with CV thresholds of 0.28m/s and 1m/s for the smoother and sharper uEGM, respectively. For the second simulation and setting the CV to 1m/s, notch bEGMs were obtained from interelectrode distance thresholds of 14.4 mm and 3.9 mm for the smoother and sharper uEGM, respectively. These results indicate a higher sensitivity for the uEGM waveforms.

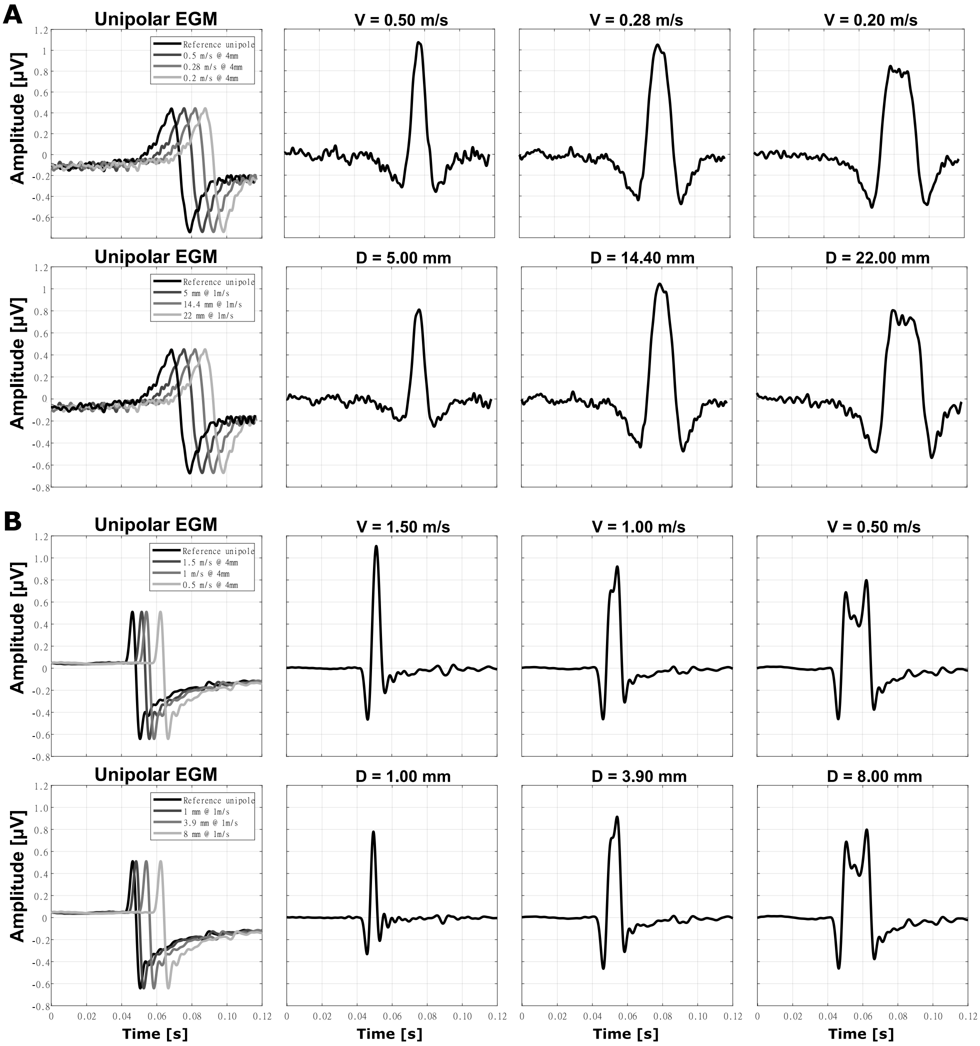

Figure 4.5: Illustration of the dependence of the bipolar morphology from with respect to the delay between unipolar signals and uEGM morphologies. Panel **A** and **B** use different uEGM morphologies, with slow and fast deflections, respectively. For rows 1 and 3, an interelectrode distance of 4mm is fixed. For rows 2 and 4, CV of 1m/s is fixed. The leftmost panel represents the reference unipole in black, and the three delayed unipoles utilized for the construction of the bipoles, in gray scale. The three rightmost columns represent therefore, the bipoles for each of the parameters according to the first column, being the first of those a valid bipole, the central the illustration of the threshold point at which the notch appears, and the rightmost a non-desired outcome with a clearly visible delay effect.

4.4 Discussion

High-density multielectrode arrays have been widely employed in experimental cardiac EP, such as patch-clamp experimentation [251], Lagendorff perfused isolated hearts from animal models [252] and in-vivo animals [253]. However, it was not until development of the Advisor™HD Grid Mapping Catheter (Abbott Laboratories, Illinois, US) [15] when became of greater interest in clinical practice. An advantage of this catheter is that it copes with the problem of directional sensitivity of bEGMs. As a result, orientation-independent bipoles are obtained from an algebraic rotation of an orthogonal bipole pair. An oEGM should be regarded as a virtual bipole as if it were captured from a bipole whose electrodes can be dynamically oriented in the direction of the propagation wavefront.

Nevertheless, some problems related to omnipolar catheters still need to be addressed. By definition, geometric centers of the bEGMs involved in a triangular clique are not coincident. This makes the activation wavefront pass through these sites at different time instants, hence causing temporal misalignments among bEGM activations and being a major cause for errors in oEGM estimation. In this work, we demonstrate that incorrect oEGM estimates may occur even with perfectly plane and homogeneous propagation wavefronts. To mitigate this problem, a temporal alignment of activations has already been proposed [23]. However, after temporally shifting bEGM activations, a reliable time reference would no longer be available and thus, hindering reliable LAT detection and CV measurement. Alternatively, we propose to estimate oEGMs from the diagonal bEGMs of the clique, so that both bEGM centers are spatially coincident with the clique center. Therefore, time alignment of activations is no longer required. To the authors' knowledge, this approach has not been proposed yet. With such configuration, thinner loops of the electrical field are described in comparison to triangular cliques. However, amplitude using the square configuration is slightly underestimated. This result is consistent from a theoretical perspective, as it is well-known that the average of delayed pulses results in a wider pulse with lower amplitude [254]. Nevertheless, this is not a real limitation, as it was shown that the equivalent cross-orientation provides larger amplitude oEGMs (scaled by a factor of $\sqrt{2}$). Finally, LAT estimation with the square clique was also more accurate than using triangular configurations. This is an important result, as accuracy in detection of LATs is essential to estimate delays related to wavefront propagation [255]. In general, it can be stated that estimation of oEGMs from squared cliques overperformed triangular configurations.

Effects of interelectrode distance was also explored. By increasing interelectrode distance, loops became wider (lower values between $o(t)$ and $o_{\perp}(t)$ amplitudes) and errors in the estimation of LATs and propagation directions increased. The unique apparent benefit of increasing interelectrode distance is an increase of the oEGM amplitude. This can be well explained as the amplitude difference of delayed versions of unipolar activations increase with the delay. Another important limitation of increasing interelectrode distance is that a notch may appear at the center of the positive pulse of the bEGM morphology —and thus, the oEGM as well. Indeed, the problem of fractionation in bEGMs computed from spaced uEGMs has been already described [256]. This effect would compromise accuracy in LAT estimation as defined as the instant at which the bEGM amplitude is maximum. Whether this undesirable effect appears or not, not only depends on interelectrode distance, but also on CV and sharpness of unipolar activations. Whereas the interelectrode distance relies on technology, the other constraints depend on the specific patient's EP. The assessment of slow conduction regions would be specially challenging, e.g. as it occurs with the macroreentrant circuit of AFL [193]. Nevertheless, from an engineering perspective, technology should be designed to work properly regardless of a patient's condition.

The main limitation of the square clique configuration is that activation delays are increased by a factor of $\sqrt{2}$, which are equivalent to an increase of $\sqrt{2}$ of the interelectrode distance, hence resulting in a poorer spatial resolution. As a consequence of that, oEGM estimation can be affected by limitations due to notch deflections in greater extent. Consequently, reducing interelectrode space in future HD catheter designs would be an asset. Additionally, with higher electrode density, the assumption of a plane and homogeneous wavefront propagation would be more easily fulfilled. Nevertheless, some questions ought to be taken into account with reduced interelectrode distances. Firstly, LAT precision under millisecond scale should be required. This could be important to further analyze conduction parameters using the full electrode grid, such as CV and heterogeneity of propagation directions, among others. To achieve such time precision, oversampling of the signals should be considered. Moreover, as lower amplitude oEGMs are obtained, equipment with improved resolution in the acquisition and digitization of the signals could be required to keep similar signal-to-noise ratio levels. Apart from reducing interelectrode distance, other solutions could also be explored, such as staggered multielectrode pattern —to avoid the increasing $\sqrt{2}$ factor aforementioned—, or develop improved signal processing algorithms to enhance oEGM estimation.

4.5 Conclusions

This paper analyzes limitations of clique configurations for oEGM estimation in orientation-independent sensing from a simulation perspective. The two main conclusions of the study are: firstly, the square clique provides a more robust estimate of omnipolar EGMs. With this approach, pitfalls associated to temporal misalignments are avoided. This approach resolves the still remaining directional sensitivity of these catheters and provides an efficient solution to problems related to the amplitude of bEGMs. Secondly, as long as electrodes are spaced close enough to avoid notch effects in the resulting bEGMs, estimation of wavefront directions and LATs are consistently improved, which are key factors to obtain high-density CV maps. To better cope with that, interelectrode spacing should be reduced as much as technology allows. Moreover, for multielectrode settings where interelectrode distance is not short enough, the square clique would be less convenient due to a loss of spatial resolution.

Future scope of this work should involve testing in experimental and clinical settings in order to validate and support our conclusions in a more realistic scenario. Studies reporting the limitations and constraints in oEGM estimation are valuable for guiding the design and implementation of future generation catheters and mapping software.

Supplementary material: code

The code written for this manuscript can be found in the following GitHub link: GitHub Repository

Chapter 5

Evaluation and Assessment of Clique Arrangements for the Estimation of Omnipolar Electrograms in High Density Electrode Arrays

An Experimental Animal Model Study

Abstract

Background and Objectives: High-density catheters combined with Orientation Independent Sensing (OIS) methods have emerged as a groundbreaking technology for cardiac substrate characterisation. In this study, we aim to assess the arrangements and constraints to reliably estimate the so-called omnipolar EGM (oEGM). Performance was evaluated using an experimental animal model. **Methods:** Thirty-eight recordings from nine retrospective experiments on isolated perfused rabbit hearts with an epicardial HD multielectrode were used. We estimated oEGMs according to the classic triangular clique (4 possible orientations) and a novel cross-orientation clique arrangement. Furthermore, we tested the effects of interelectrode spacing from 1 mm to 4 mm. Performance was evaluated by means of several parameters that measured amplitude rejection ratios, electric field loop area, activation pulse width and morphology distortion. **Results:** Most reliable oEGM estimations were obtained with cross-configurations and interelectrode spacings ≤ 2 mm. Estimations from triangular cliques resulted in wider electric field loops and unreliable detection of the direction of the propagation wavefront. Moreover, increasing interelectrode distance resulted in increased pulse width and morphology distortion. **Conclusions:** The results prove that current oEGM estimation techniques are insufficiently accurate. This study opens a new standpoint for the design of new-generation HD catheters and mapping software.

This chapter is based on the publication: S. Ruipérez-Campillo et al. (2023). Evaluation and assessment of clique arrangements for the estimation of omnipolar EGMs in high density electrode arrays: an experimental animal model study. *Physical and Engineering Sciences in Medicine*, 46(3) [257].

5.1 Introduction

Local examination of the cardiac tissue is crucial for the characterisation of the EP substrate [258], found to be key to better understand the mechanisms that trigger and sustain cardiac arrhythmias such as AF [259], atrial tachycardia (AT) [260], ventricular tachyarrhythmias [261, 9] and other arrhythmias [262]. Arrhythmogenic substrates usually involve fibrotic regions with anomalous conduction that cause meandering and inhomogeneous routes of the electrical activation [263, 35]. Accurate EP mapping is then required to identify sites responsible for the arrhythmia, and hence pinpoint candidates for ablation procedures [264, 240].

In order to accurately characterise the EP substrate, catheters with high-density (HD) arrays of equispaced electrodes are gaining great interest in the field [15]. These electrodes are able to provide an HD activation map of the local tissue, and hence are appropriate to estimate CV and other features related to inhomogeneities in the propagation of the electrical wavefront [16, 249]. In fact, they have already been introduced to the clinical practice involving successful substrate exploration for the detection of atrial and ventricular disorders [22, 20, 265].

Such multielectrode arrays are also referred to as omnipolar electrodes, due to their capability to derive an omnipolar EGM (oEGM), which is a virtual representation of the bipolar EGM (bEGM), recreating the hypothetical signal obtained from a pair of electrodes arranged in the direction of wavefront propagation. The interest of this operation mode is to overcome the sensitivity of bEGMs to the orientation of the electrode pair with respect to the wavefront [245]. Due to this limitation of bEGMs, the low-amplitude and fragmented activations recorded in the case of wavefronts arriving orthogonally to the electrode pair [243, 246] could lead to misinterpretations, such as mistakenly assuming impaired tissue to be the cause of an abnormal signal [248, 256].

Although omnipolar electrodes are claimed to provide an orientation-independent oEGM [15, 266, 267], some orientation dependencies have been reported [23, 268], which may lead to pitfalls in oEGM estimation at some incidence angles. To overcome this limitation, two alternative methods for oEGM estimation have been recently proposed. The first one consists of a prior alignment of the bEGM pair to minimise delay between activations [23]. Yet, ex-vivo animal experiments are a way, according to the authors, to establish if the simulation-proved superior performance of their modified omnipolar EGM translates to clinical counterpart of their simulation-based study [23]. The second one refers to a cross-orientation method by choosing the diagonal bEGMs of the square clique, as opposed to the conventional triangular configuration. This method is proposed as a way to impose coincident bipole centres [268], and hence avoid delays between bEGMs. Although the latter method showed promising results towards overcomingthe aforementioned limitations and presenting a more robust approach against propagation angle, this was only tested with simulations based on ideal propagation wavefronts presented as homogeneous and plane waves, which differ from the non-ideal propagation patterns intrinsic to the EP environment [15]. Thus, there was not enough evidence that this method could work well in a realistic scenario, considering the complexities of cardiac EP. Therefore, this technique requires further validation in more realistic settings.

Animal models are widely used to test and validate techniques in real biological scenarios [269]. Among them, the isolated perfused heart according to the Langendorff technique is a broadly used ex-vivo model in cardiac EP research [270].

In this paper, we present a study on the performance of the cross-orientation method for oEGM estimation using experimental data. For this, a retrospective dataset of isolated perfused rabbit hearts was employed. These experiments have many conditioning factors derived from the physiological environment where this methodology is meant to be used, including recordings of real epicardial activations, variability among the samples or electrode limitations in a clinical environment, among others. The signals were obtained with an HD multielectrode array containing 128 unipolar electrodes with 1 mm spacing. Objective features such as activation amplitude, pulse duration and loop width are analysed. Furthermore, the effects of interelectrode distance can be assessed given the configuration of the electrode array designed for this experiment (figure 5.1.A).

5.2 Materials

Thirty-eight recordings from 9 retrospective experiments performed on isolated perfused rabbit hearts according to the Langendorff technique were used [271]. Two recordings per heart were used, stimulated at 4 and 6 Hz, and three series were selected per recording. Those with lower quality, noise, or artifacts were discarded. In each experiment, a self-manufactured multielectrode consisting of 128 stainless steel electrodes (interelectrode distance 1 mm; diameter 0.125 mm) [272] was positioned on the epicardial surface of the anterior wall of the left ventricle. A bipolar epicardial stimulating electrode was used (diameter, 0.125 mm; interelectrode distance, 1 mm), always positioned at the same location, proximally to the external lateral side of the recording electrode (figure 5.1) and connected to a GRASS S88 stimulator equipped with a stimulus isolation unit. Signals from several series (epicardial temperature 37 ºC) with ventricular pacing (4 Hz and 6 Hz) were used for this research. Stimuli were applied via a train of 2 ms pulses with voltage of twice the diastolic threshold. Electrogram recordings were obtained through a cardiac electrical activity mapping system (MAPTECH; Waalre, The Netherlands). The reference electrode consisted of a 4 x 6 mm silver plate located over the cannulated aorta. All signals were amplified with a gain of 100–300, bandwidth filtered (1 Hz-400 Hz), multiplexed, and digitised (resolution, 12 bits). The sampling rate was 1000 Hz per channel. Experiments were performed at the Laboratory of Experimental Cardiac Electrophysiology at the Department of Physiology of the University of València, Valencia, Spain. The protocol for the experiments was previously approved by the University of València Local Committee.

5.3 Methods

5.3.1 Clique configurations

Considering the electrode location as the pair (i, j), where i and j are alphabetic and numeric ordinal indices, respectively, the unipolar EGM (uEGM) in a particular electrode will be referred to as $u_{ij}(t)$ (e.g. $u_{\mathrm{A}2}(t)$). From the subtraction of unipole pairs, it is possible to derive a bipolar EGM bEGMs). From a cubicle arranging 2×2 electrodes, a clique is defined as a pair of orthogonal bEGMs, as depicted in figure 5.2. Depending on the bEGM arrangement, several configurations can be considered,

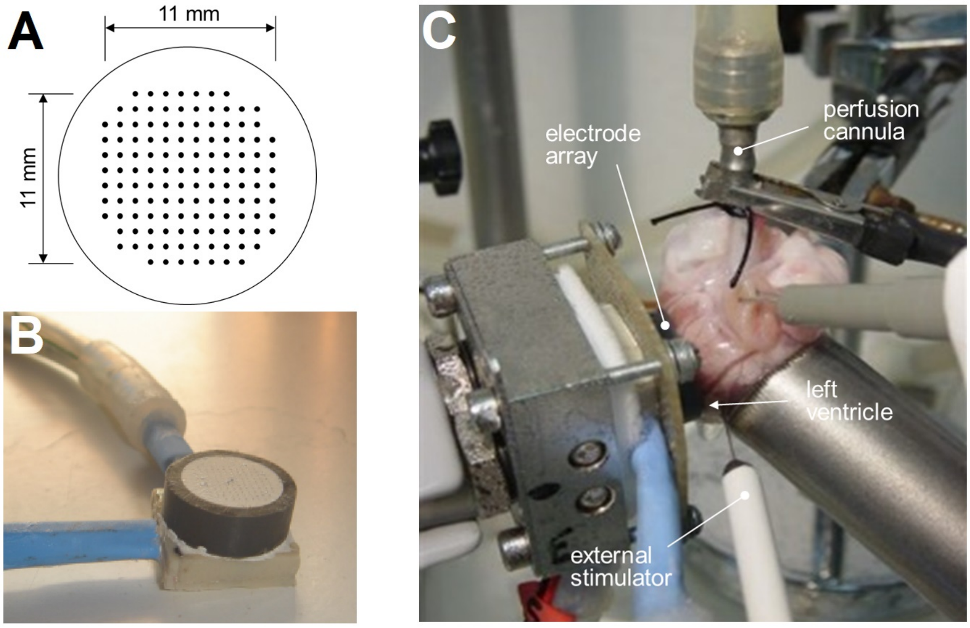

Figure 5.1: **A.** Arrangement of the multielectrode array. **B.** Picture of the self-manufactured multielectrode. **C.** Experimental setting.

such as triangular (with 4 different orientations: ◺, ◿, ◸and ◹) or cross cliques. For the sake of clarity, let us denote different clique configurations as $C_{◺}$, $C_{◿}$, $C_{◸}$, $C_{◹}$ and $C_{\times}$, respectively. Considering a 2×2 cell with electrodes A1, A2, B1 and B2, bipole pairs for each different clique configuration are defined as follows (see figure 5.2):

- For a lower left triangular clique $C_{◺}$:

$$b_x(t) = u_{\mathrm{B2}}(t) - u_{\mathrm{B1}}(t)$$
$$b_y(t) = u_{\mathrm{A1}}(t) - u_{\mathrm{B1}}(t)$$

- For a lower right triangular clique $C_{◿}$:

$$b_x(t) = u_{\mathrm{B2}}(t) - u_{\mathrm{B1}}(t)$$
$$b_y(t) = u_{\mathrm{A2}}(t) - u_{\mathrm{B2}}(t)$$

- For an upper left triangular clique $C_{◸}$:

$$b_x(t) = u_{\mathrm{A2}}(t) - u_{\mathrm{A1}}(t)$$
$$b_y(t) = u_{\mathrm{A1}}(t) - u_{\mathrm{B1}}(t)$$

- For an upper right triangular clique $C_{◹}$:

$$b_x(t) = u_{\mathrm{A2}}(t) - u_{\mathrm{A1}}(t)$$
$$b_y(t) = u_{\mathrm{A2}}(t) - u_{\mathrm{B2}}(t)$$

- For a cross clique $C_{\times}$:

$$b_1(t) = u_{\mathrm{A2}}(t) - u_{\mathrm{B1}}(t)$$
$$b_2(t) = u_{\mathrm{A1}}(t) - u_{\mathrm{B2}}(t)$$

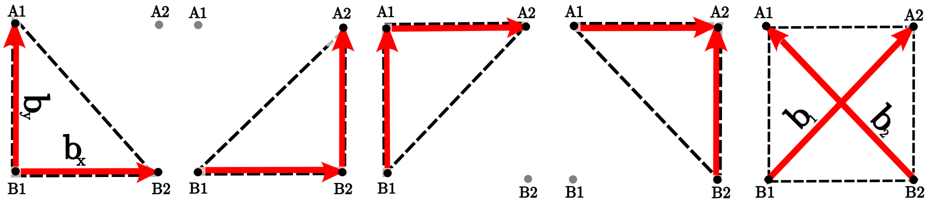

Figure 5.2: Configurations of a clique of electrodes $C_{\text{◺}}$, $C_{\text{◿}}$, $C_{\text{◸}}$, $C_{\text{◹}}$, and $C_{\times}$.

Notice that for the cross clique $C_{\times}$, a correction to align the coordinate system with the bipole orientation, and hence retrieve $b_x(t)$ and $b_y(t)$, is required. That alignment is achieved by means of a counterclockwise $\frac{\pi}{4}$ *rad* rotation:

$$\mathbf{b}(t) = \begin{bmatrix} \cos\left(\frac{\pi}{4}\right) & -\sin\left(\frac{\pi}{4}\right) \\ \sin\left(\frac{\pi}{4}\right) & \cos\left(\frac{\pi}{4}\right) \end{bmatrix} \cdot \begin{bmatrix} b_1(t) \\ b_2(t) \end{bmatrix}, \tag{5.1}$$

where $\mathbf{b}(t) = [b_x(t) \quad b_y(t)]^{\mathrm{T}}$ is the cartesian bipole pair, which applies regardless of the clique configuration.

5.3.2 oEGM estimation

The oEGM is defined as a virtual bEGM reproducing a hypothetical recording by an electrode pair oriented in the direction of the wavefront propagation. Although the oEGM cannot be directly measured from the multielectrode grid, it can be estimated from a mathematical transformation of the bipole pair $\mathbf{b}(t)$. From its orthogonal components, the electric field generated by the cardiac electrical activation can be represented as a loop pointing in the direction of propagation. Under the conditions of planar and homogeneous wavefronts (more likely to apply in small-size cliques), it can be stated that the narrower the loop, the more precise the description of the electric field [23, 268].

The omnipole $o(t)$ can be estimated from the projection of $\mathbf{b}(t)$ along the direction of the wavefront propagation. Ideally, this transformation yields a signal exhibiting an activation with maximal amplitude. Equally, a projection onto a perpendicular axis provides a residual signal $r(t)$ with low amplitude. In this line of thinking, the oEGM is computed from the projection that maximises the ratio of the omnipolar peak amplitude to the peak amplitude of the residual. With Ψ_{w} denoting the direction of the wavefront, a rotation angle that maximises the ratio between the amplitude peak of the projected signal and the peak of the orthogonal projection can be computed by solving the following optimisation problem:

$$\theta_o = \underset{\theta}{\operatorname{argmax}} \left[\frac{\max\left([\cos\theta \;\; -\sin\theta]\, \mathbf{b}(t)\right)}{\max\left|[\sin\theta \;\; \cos\theta]\, \mathbf{b}(t)\right|} \right], \tag{5.2}$$

where θ_o is the angle that retrieves the projection yielding an estimation of the oEGM $\hat{o}(t)$:

$$\begin{bmatrix} \hat{o}(t) \\ r(t) \end{bmatrix} = \begin{bmatrix} \cos(\theta_o) & -\sin(\theta_o) \\ sin(\theta_o) & \cos(\theta_o) \end{bmatrix} \cdot \mathbf{b}(t) \tag{5.3}$$

As shown in equation 5.3, the residual signal $r(t)$ is naturally derived as well.

5.3.3 Assessment of oEGM reliability

As suggested from previous simulations [268], the reliability of oEGM estimations depends on several factors. Some of them are inherent to physiological properties, such as CV and the morphology of the unipolar signal. In addition, the orientation of the multielectrode with respect to the propagation wavefront also plays a role. All these factors are extrinsic to the technique for oEGM estimation as described above. Furthermore, depending on the clique configuration and interelectrode distance, different versions of the estimated omnipole $\hat{o}(t)$ can be obtained. As long as results are not coincident, it can be inferred that a retrieved oEMG cannot be considered the true omnipole but rather an approximation. Therefore, assessing and understanding the limitations of technical issues involved in oEGM reconstruction arises as a key factor when proposing and using reliable settings.

Several measurements to assess the reliability of oEGM estimations are proposed:

- oEGM-to-residuum ratio (ORR): Ratio between peak amplitudes of $\hat{o}(t)$ and $r(t)$ activations:

  $$\text{ORR} = \frac{\max(\hat{o}(t))}{\max|r(t)|} \tag{5.4}$$

  The higher this ratio, the better the oEGM estimation.
- Normalised loop area (NLA): Area of the electric field loop described by normalised bipoles that make up the electrical field loop. The rationale for this parameter is that, assuming a planar wave propagating within a small-sized cell, the electric field loop should reflect a straight line. With this assumption, the thinner the loop, the better the estimation and accordingly, lower NLA values suggest more reliable oEGMs. To compute this parameter, the bipoles $b_x(t)$ and $b_y(t)$ are previously normalised to the peak oEGM amplitude. Such normalisation removes amplitude biases in order to reflect a more representative value of the loop shape. The NLA parameter is defined as the surface constrained by the contour of the bipole loop L. Parameterising the spatial coordinates according to ϱ and ξ, the equation to solve is the surface integral over the magnitude of the cross product of the partial derivatives of the surface element $s(\varrho, \xi)$ in the plane $\varrho - \xi$ within the limits defined by the curve L:

  $$\text{NLA} = \iint_L \left\| \frac{\partial \mathbf{s}}{\partial \varrho} \times \frac{\partial \mathbf{s}}{\partial \xi} \right\| \mathrm{d}\varrho \, \mathrm{d}\xi \tag{5.5}$$

The surface elements are approximated by using an adaptation of the trapezoidal rule, thus avoiding problematic edge cases of triangulation methods such as silver triangles [273].

- Pulse width (PW): The PW is a measure of the elapsed time between the leading and trailing edges of a single pulse (see figure 5.3). The rationale behind this parameter is also related to that of the morphology distortion, as the subtractions of delayed activations will result in an increasing pulse width. From this perspective, the shorter the PW, the better the oEGM estimation.
- Morphology distortion (MD) of $\hat{o}(t)$: The rationale for this is the distortion caused by interelectrode spacing sampling. This may occur when the interelectrode distance is not short enough to consider the bipoles $b_x(t)$ and $b_y(t)$ as if they were obtained from infinitesimally close sites. Instead, there can be a significant delay between the activations, so that the bipoles can be regarded as subtractions of delayed versions of the unipole rather than its gradient. Generalising unipolar activations at any site location within a 2D grid, we could define unipolar EGMs as $u(t, x, y)$. While being the omnipole $o(t)$ the gradient of $u(t, x, y)$ in the direction of propagation, and considering identical unipolar waveforms in infinitesimally close sites, we estimate the true oEGM at a given site $o(t, x, y)$ as the negative time derivative of the unipole:

  $$o(t, x, y) = -\frac{\partial}{\partial t} u(t, x, y) \tag{5.6}$$

  Particularising at the electrodes of the multielectrode array,

  $$o_{ij}(t) = -\frac{du_{ij}(t)}{dt} \tag{5.7}$$

  As long as there are several unipoles involved within a clique, we estimate a reference oEGM $o_{\text{ref}}(t)$ after alignment and average all $o_{ij}(t)$ from the electrodes forming the clique. An additional advantage of this averaging is the reduction of common interference and other noise components. The resulting $o_{\text{ref}}(t)$ will be then compared to the estimated $\hat{o}(t)$ to assess distortion. After amplitude normalisation, MD is measured from root mean squared error (RMSE) between the normalised $\hat{o}(t)$ and $o_{\text{ref}}(t)$ signals.

A graphical description of some of these parameters is presented in figure 5.3. For each experiment in the dataset, oEGM estimates $\hat{o}(t)$ for different clique configurations ($C_{\text{◺}}$, $C_{\text{◿}}$, $C_{\text{◸}}$, $C_{\text{◹}}$ and $C_{\times}$) and interelectrode distances ranging from 1 to 4 mm were obtained. For all cases, performance of oEGM estimation was assessed by means of the parameters described above (i.e. ORR, NLA, PW and MD).

5.3.4 Statistical analysis

Results are provided as mean ± SD, or median and IQR, if required. For data exploration, the distribution of the independent variables was evaluated using Kolmogorov-Smirnov and Mann-Whitney-Wilcoxon tests.

Two linear mixed models were fit to the data, with the computed metrics (NLA, ORR, PW and MD) as the dependent variable, and configuration and distance, as well as their interaction *(configuration * distance)*, as independent variables. Due to the repeated measures on the same rabbit heart origins, a random intercept for the

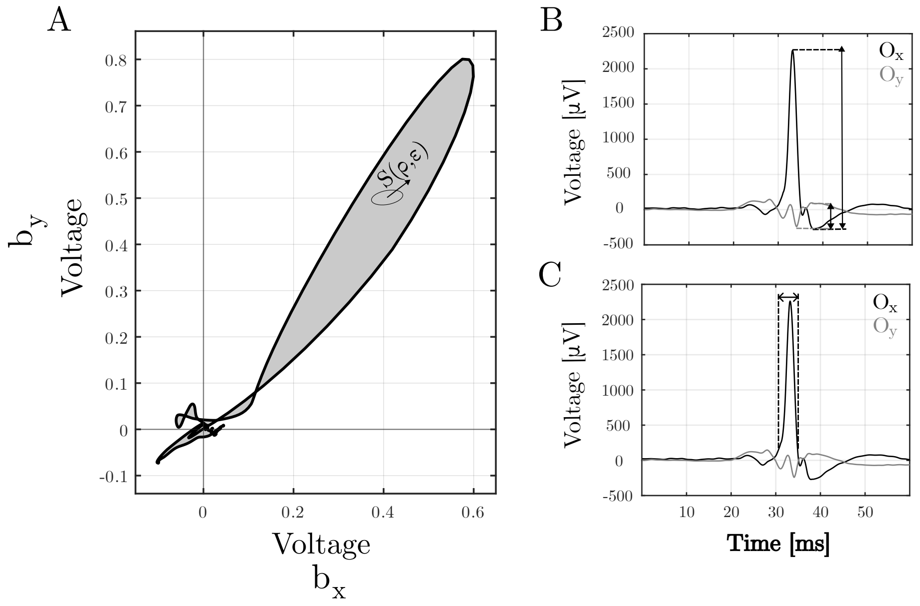

Figure 5.3: Graphical description of some of the metrics assessed: **A.** NLA; **B.** ORR; **C.** PW

heart origin was included. In both models, the right-skewed dependent variables were *log* transformed.

The first model was fit to the raw data, including an additional random intercept for the subsamples within each combination of rabbit heart origin, configuration and distance. The second model was fit to the aggregated subsamples. The latter was chosen due to its intrinsic simplicity compared to the former, and the similar values obtained for the statistics.

To evaluate the model assumptions, Gaussianity and homoscedasticity of the residuals were studied (see quantile-quantile (QQ) plots and the residual diagnostics for hierarchical multi-level regression models (DHARMa) in *Supplementary Material*).

P-values of model coefficients were obtained using the Satterthwaite's degrees of freedom method, applying the package *lmerTest*. We performed a post-hoc pairwise testing with *p-value* adjustment for correction of multiple comparisons following the Tukey method. Multiple comparisons between each configuration were performed separately for each distance, as were their corrections. A *p-value* of <0.05 was considered statistically significant throughout. The statistical model and comparison tests were designed and run in RStudio.

5.4 Results

Figure 5.4 represents an example of electric field loops created from an experiment and considering different clique configurations and interelectrode distances from 1 mm to 4 mm. As can be appreciated, different loop patterns were obtained. At closer inspection, the similarity in the morphology of the bEGM loops generated by complementary triangular cliques (for instance $C_{◺}$ vs $C_{◹}$ on the one hand and $C_{◿}$ vs $C_{◸}$ on the other hand) can be noted. Whereas cliques $C_{◺}$ and $C_{◹}$ reconstruct narrower loops pointing at a consistent direction, cliques $C_{◿}$ and $C_{◸}$ obtain wider loops with no precise pointing. As a result, triangular configurations $C_{◿}$ and $C_{◸}$ fail to accurately detect the direction of propagation. In addition to the triangular cliques, the loop pattern created by the cross clique $C_{\times}$ is also consistent with the loop patterns of triangles $C_{◺}$ and $C_{◹}$, i.e. a narrow loop pointing in the same direction. The reasons for such similarities and differences among patterns will be further discussed in the next section. Moreover, considering the effects of interelectrode distance, it can be observed that with shorter distances, loops become narrower and lower in magnitude.

From the bEGMs that make up the electric field loops in figure 5.4, and after the corresponding algebraic rotation according to equation 5.3, the oEGM estimates $\hat{o}(t)$ and the orthogonal residual signal $r(t)$ are computed. These results are depicted in figure 5.5. As can be observed in the 1 mm setting, configurations $C_{◺}$, $C_{◹}$ and $C_{\times}$ provide estimates with lower amplitude of the residual signal $r(t)$ (in red). As interelectrode distance increases from 1 to 4 mm, so does the amplitude of the oEGM. Moreover, the residual signal in the direction perpendicular to the wavefront propagation increases to an even larger extent, proportionally to the interelectrode distance. Cliques that provided a wider loop (i.e. $C_{◿}$ and $C_{◹}$) provided a $r(t)$ signal displaying a significant residue of the electrical activation.

Beyond the results of a single experiment illustrated in figures 5.4 and 5.5, we performed a quantitative analysis by computing parameters ORR, A_{EFL}, MD and PW for all the experiments in the dataset. Numerical values are provided in Table 5.1, and boxplots are depicted in figure 5.6. Subsequently, we carried out the statistical analyses as described in section 5.3.4. The resulting p-values considering correction for multiple comparisons are given in Table 5.2.

For close interelectrode spacing (1 mm), the cross configuration $C_{\times}$ led to equivalent results to the triangular cliques that detected the angle of propagation direction more accurately ($C_{◺}$ and $C_{◹}$), resulting therefore in non-significant p-values for amplitude ratio (ORR) and loop area (NLA). However, this similarity was no longer applicable when comparing the results of $C_{\times}$ to $C_{◿}$ and $C_{◸}$. For this comparison, the $C_{\times}$ clique led to significantly higher OOR and lower NLA values. By increasing interelectrode distance, such differences were reduced, becoming non-significant for spacing ≥ 3 mm.

Regarding parameters related to pulse morphology PW and MD, comparison among clique configurations provided non-significant results. However, both PW and MD significantly increased with interelectrode distance, especially noticeable for spacing ≥ 3 mm (see Tables 5.1 and 5.3). This effect is reflected in changes in the oEGM morphology (see Figure 5.7.B). As can be observed, the oEGM becomes progressively wider in comparison to the reference oEGM $o_{\mathrm{ref}}(t)$ (Figure 5.7.B). Moreover, in addition to these morphological worsening, NLA and ORR worsened with increased interelectrode distances as well.

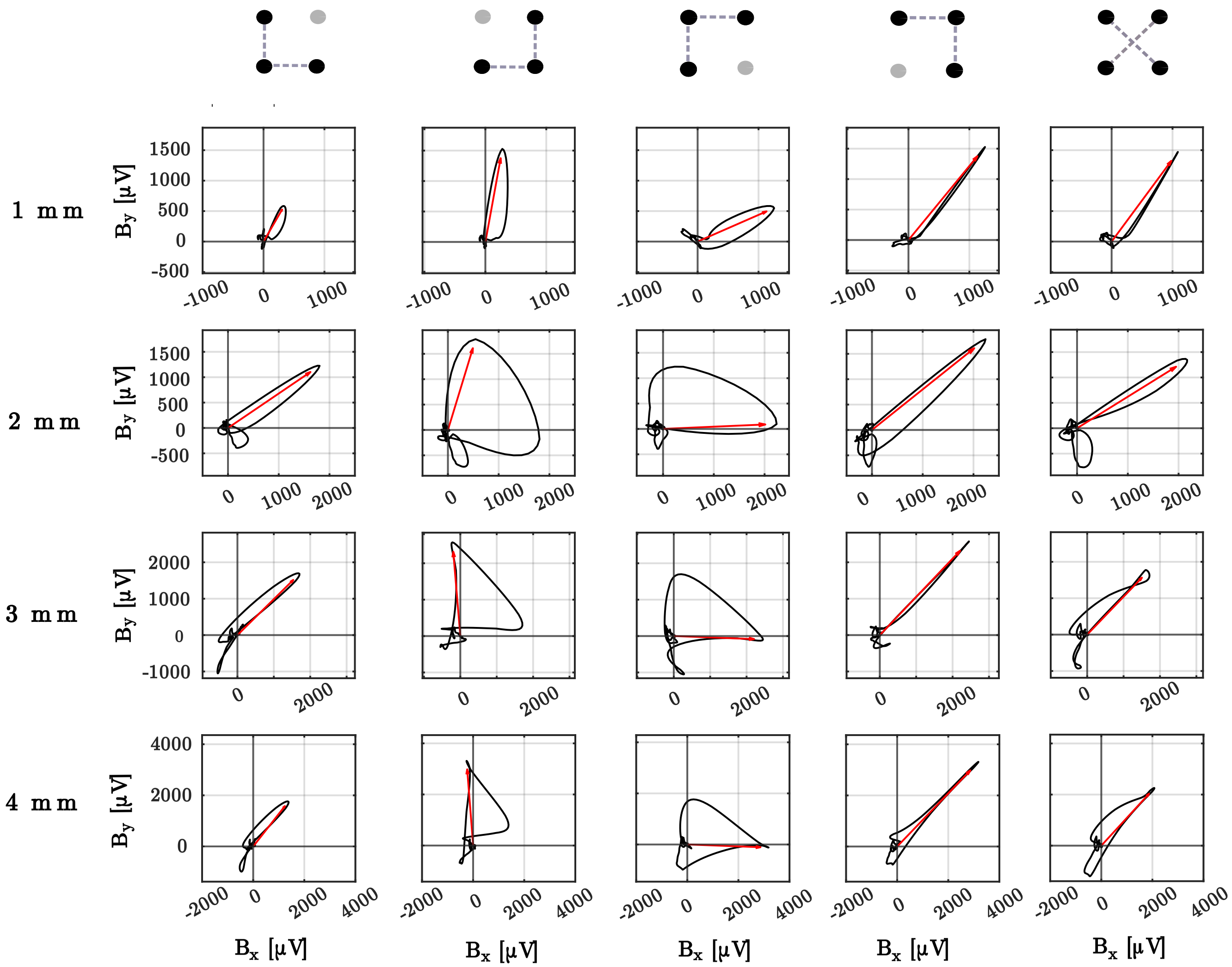

Figure 5.4: Examples of the bipolar loops (in black) and the corresponding propagation direction (in red) generated by triangular and cross-oriented configurations on the same clique along interelectrode distances 1-4 mm

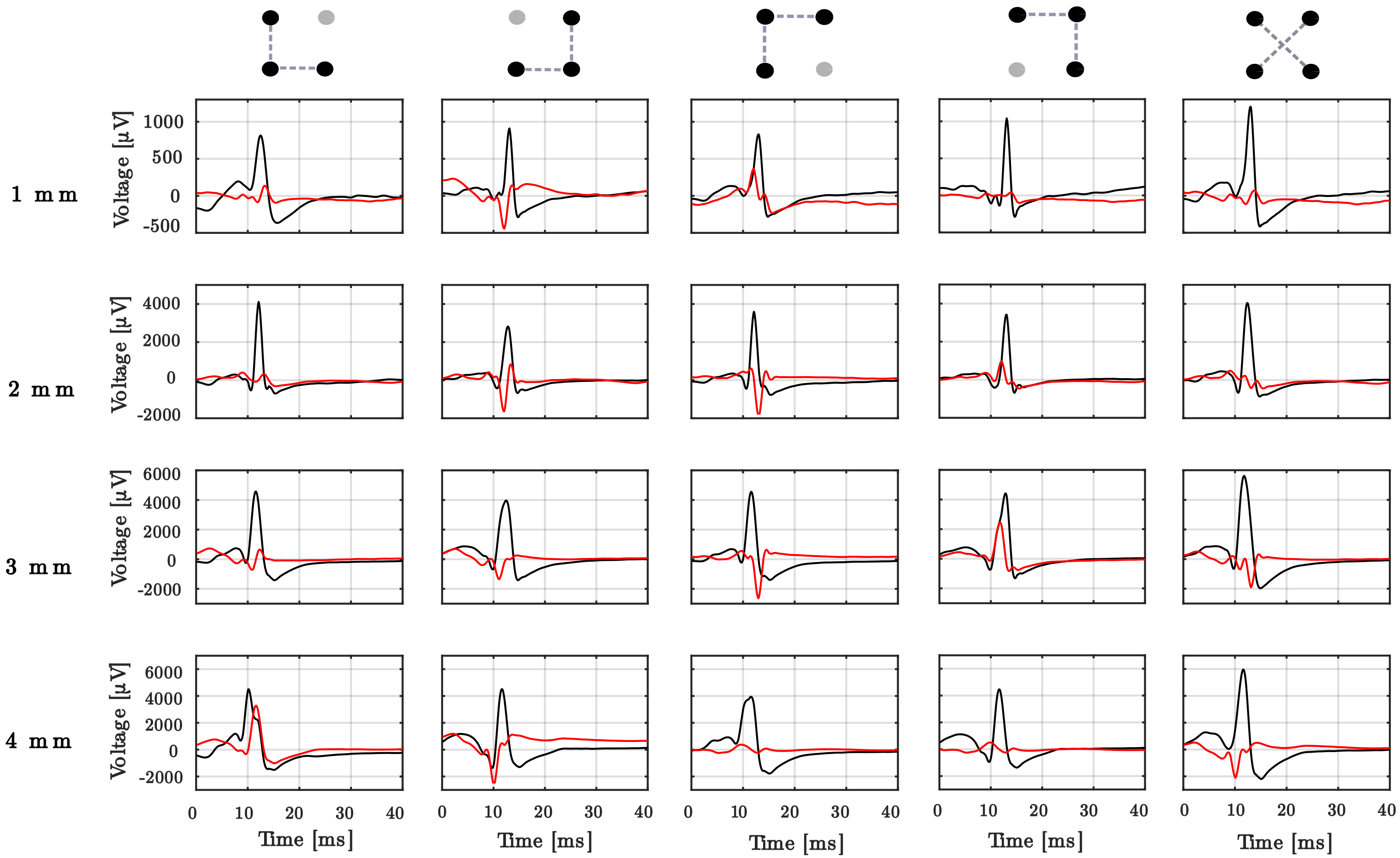

Figure 5.5: Examples of the omnipoles on the same clique reconstructed by triangular and cross-oriented configurations, with horizontal component of oEGM in black and vertical component in red, along interelectrode distances 1-4 mm

Table 5.1: Results for the different metrics

		$\{C_{\text{◺}}$ & $C_{\text{◹}}\}$	$\{C_{\text{◿}}$ & $C_{\text{◸}}\}$	$\{C_{\times}\}$
1 mm	NLA	0.130±0.011	0.265±0.032	0.114±0.014
	ORR	5.258±0.335	3.722±0.378	5.204±0.339
	PW [ms]	5.950±0.441	4.200±0.428	4.324±0.486
	MD [μV]	0.106±0.006	0.086±0.005	0.089±0.006
2 mm	NLA	0.252±0.026	0.359±0.029	0.161±0.022
	ORR	3.695±0.347	2.387±0.128	3.491±0.284
	PW [ms]	5.458±0.753	4.618±0.549	5.863±0.493
	MD [μV]	0.105±0.007	0.111±0.008	0.114±0.007
3 mm	NLA	0.258±0.025	0.308±0.028	0.231±0.033
	ORR	3.274±0.226	2.498±0.168	3.133±0.249
	PW[ms]	5.378±0.489	5.201±0.538	6.258±0.567
	MD [μV]	0.114±0.006	0.132±0.007	0.133±0.008
4 mm	NLA	0.284±0.029	0.281±0.019	0.216±0.023
	ORR	2.914±0.201	2.745±0.179	2.769±0.148
	PW [ms]	6.083±0.380	6.168±0.365	6.732±0.534
	MD [μV]	0.114±0.005	0.136±0.006	0.133±0.008

Table 5.2: *p-values* derived from post-hoc tests comparing coefficients of configurations, stratified by metrics and distances

	$C_{\times}$ - $C_{\text{◺}}$	$C_{\times}$ - $C_{\text{◿}}$	$C_{\text{◺}}$ - $C_{\text{◿}}$	$C_{\times}$ - $C_{\text{◺}}$	$C_{\times}$ - $C_{\text{◿}}$	$C_{\text{◺}}$ - $C_{\text{◿}}$
		NLA			ORR	
1 mm	0.921	< 0.001	< 0.01	0.897	< 0.01	< 0.001
2 mm	0.391	< 0.05	0.335	0.525	0.117	< 0.01
3 mm	0.994	0.505	0.442	0.711	0.419	0.105
4 mm	0.933	0.491	0.712	0.899	0.905	0.664
		PW			MD	
1 mm	0.605	0.911	0.361	0.536	0.689	0.147
2 mm	0.795	0.299	0.675	0.622	0.941	0.822
3 mm	0.380	0.266	0.971	0.463	0.999	0.464
4 mm	0.669	0.882	0.924	0.467	0.997	0.426

5.5 Discussion

Orientation-independent sensing (also referred as OIS) [17] for the estimation of bipolar EGMs is receiving great attention [267]. This technique overcomes the main limitation of bEGMs, which are highly dependent on bipole orientation, hence providing a low amplitude and fractionated signal when the wavefront arrives almost perpendicularly to the electrode pair [248]. Such a limitation is crucial, as low amplitude and identification of Complex Fractionated Atrial Electrograms (CFAEs)

Table 5.3: *p-values* derived from post-hoc tests comparing coefficients of distances, stratified by metrics and configurations

		$C_{\times}$				$C_{◺}$ & $C_{◹}$				$C_{◿}$ & $C_{◸}$			
		1 mm	2 mm	3 mm	4 mm	1 mm	2 mm	3 mm	4 mm	1 mm	2 mm	3 mm	4 mm
NLA	1 mm	1	-	-	-	1	-	-	-	1	-	-	-
	2 mm	0.378	1	-	-	0.061	1	-	-	0.987	1	-	-
	3 mm	< 0.05	0.588	1	-	0.088	0.999	1	-	1	0.985	1	-
	4 mm	< 0.05	0.529	0.999	1	< 0.05	0.979	0.946	1	0.999	0.995	0.999	1
ORR	1 mm	1	-	-	-	1	-	-	-	1	-	-	-
	2 mm	< 0.05	1	-	-	0.066	1	-	-	0.256	1	-	-
	3 mm	< 0.01	0.962	1	-	< 0.01	0.861	1	-	0.383	0.994	1	-
	4 mm	< 0.01	0.877	0.994	1	< 0.01	0.505	0.928	1	0.737	0.84	0.938	1
PW	1 mm	1	-	-	-	1	-	-	-	1	-	-	-
	2 mm	0.159	1	-	-	0.956	1	-	-	0.73	1	-	-
	3 mm	< 0.05	0.791	1	-	0.876	0.995	1	-	0.239	0.827	1	-
	4 mm	< 0.01	0.464	0.95	1	0.297	0.594	0.741	1	< 0.01	0.07	0.371	1
MD	1 mm	1	-	-	-	1	-	-	-	1	-	-	-
	2 mm	0.119	1	-	-	0.995	1	-	-	< 0.05	1	-	-
	3 mm	< 0.01	0.725	1	-	0.76	0.882	1	-	< 0.001	0.548	1	-
	4 mm	< 0.05	0.865	0.993	1	0.868	0.952	0.997	1	< 0.01	0.639	0.999	1

are key features in determining regions with anomalous conduction [274, 275].

Although claimed to be orientation-independent, it has been shown that some orientation dependency still applies [23]. Indeed, it has been proven that state-of-the-art oEGM reconstruction methods based on triangular cliques result in inaccurate estimations of the omnipole, even in perfectly homogeneous and plane propagation wavefronts [268]. As previously reported in a simulation study, oEGM estimation from the diagonal bEGMs of the clique corrects the temporal misalignments, hence improving oEGM estimation.

With this study, we aim to assess performance and limitations of OIS methods for oEGM estimation in a real scenario, employing a series of retrospective experiments with animal models. Several technical issues are tested, such as clique configuration and interelectrode distance. Parameters based on the form factor of the electric field loop and rejection to residual signal resulting from perpendicular electrode arrangement are considered. In addition, morphology distortion caused by increasing spacing between electrodes is analysed.

The fact that the stimulation electrode was placed in approximately the same location in all experiments forced a similar direction of the propagation wavefront, regardless of the experiment under study. As long as the accuracy of the electrical field loop reconstruction with the triangular clique strongly depends on the wavefront incidence angle, loop patterns were dissimilar for different triangle orientations. More specifically, equivalent loops were obtained from pairs of complementary triangles ($C_{◺} - C_{◹}$ and $C_{◿} - C_{◸}$), whereas clearly different loops were obtained when comparing non-complementary triangles. This orientation-dependent property of the triangular clique, together with the specific arrangement of the experimental setting, caused one pair of complementary triangles to be consistently more accurate than the other. As a result, by using triangular cliques, correct oEGM estimations coexist with incorrect oEGM estimations. On the other hand, the cross-oriented configuration, being more robust to the wavefront direction, provided results as accurate as the best complementary triangle pair, and better in any case than the

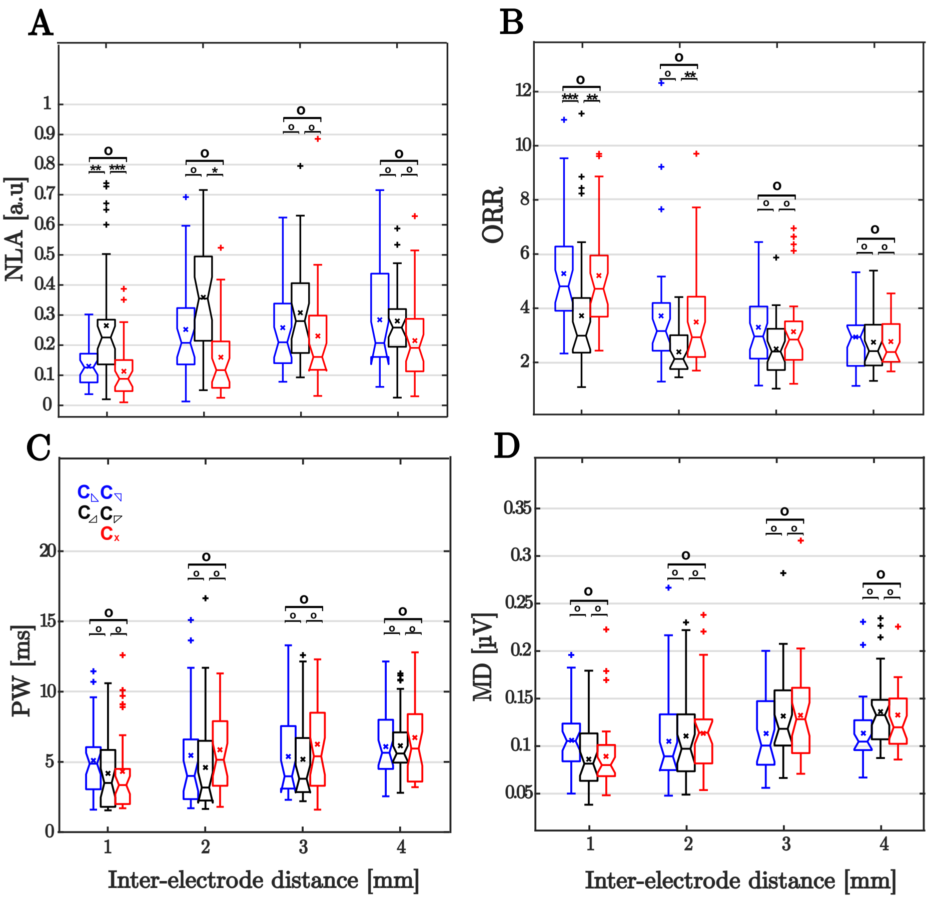

Figure 5.6: Comparison of the triangular and cross-oriented configurations for the different parameters under study. 3A Normalised loop areas. 3B Omnipolar ratios. 3C Morphology distortion of omnipoles. 3D Pulse Width.

worst complementary triangle pair. This is an important benefit of the cross-oriented clique, as in clinical practice the wavefront can arrive randomly from any possible direction (even changing from activation to activation as the catheter moves).

According to our results, the aforementioned benefits of the cross-oriented configuration are obtained with close interelectrode spacing (≤ 2 mm). In fact, it was found that increasing the interelectrode distance is another major performance limiting factor of oEGM estimation. For distances $\geq 3mm$, activation delays between neighbours become more noticeable, thus widening the bipolar pulse and changing its morphology waveform. Indeed, notched or fractionated pulses may be retrieved resulting from excessively delayed activations even in the case of a healthy cardiac tissue. In those cases, the cross-oriented configuration is negatively affected to a greater extent, as the interelectrode distance is scaled at a $\sqrt{2}$ factor with respect to triangular cliques. To tackle this hindrance, higher density catheters shall be designed. Moreover, by reducing interelectrode spacing, the resulting propagation wavefront would be better approximated by a planar and homogeneous wave within

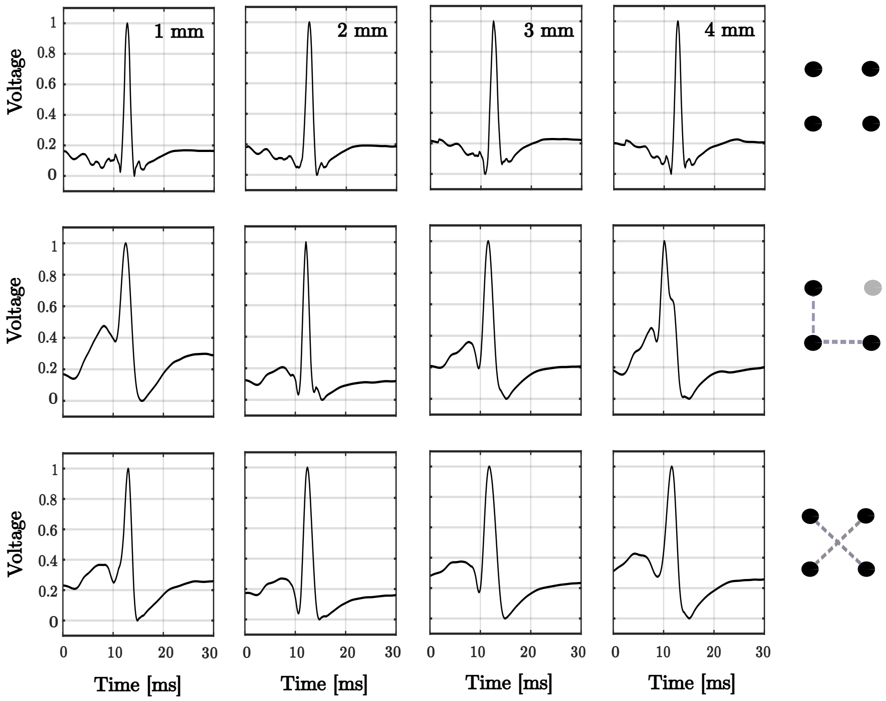

Figure 5.7: Morphology analysis of oEGMs. Top row: reference oEGM $o_{\text{ref}}(t)$ computed from the gradient of the mean uEGM; Central row: estimated oEGM $\hat{o}(t)$ for triangular clique $C_{\triangle}$; Bottom row: estimated oEGM for clique $C_{\times}$. The voltage amplitude has been normalised.

the dimensions of a clique. These findings are consistent with the recent work of *Letchumy* et al., which, aiming to characterise the effect of electrode number and interelectrode distance in the omnipole through an *in silico* set-up, concluded that 2*mm* is an ideal interelectrode distance, and distances above 4*mm* were less effective at characterising the underlying domain [276].

5.5.1 Study limitations

Although experimental animal studies combine the control of experimental settings and the physiological behaviour, the isolated rabbit heart is certainly a limitation for the generalisation to human EP signals. The main question is to what extent the scaling factor of heart dimensions can affect the conclusions, especially those related to interelectrode distance. Nevertheless, it should be taken into account that CV of rabbit and human hearts are around the same order of magnitude. In our opinion, as long as the CV is more relevant than the heart size at local analyses, the conclusions may be extrapolated to a great extent.

Another limitation is that the stimulations were applied roughly in the same location for all experiments (obviously, with some random variations due to experimental settings and handling). Although this proved that the triangular clique arrangement failed consistently at certain angle orientations, it would have been interesting to test the robustness of the cross-orientation at all angles with an additional battery of experiments by placing the stimulation electrode at different sites. Nonetheless, this aspect is not sufficiently grounded to carry out a new series of experiments with animals. In any case, the cross-orientation was proven consistent along the complete experiment series as well as in previous simulation studies [268]. Future work shall be performed on endocavitary signals, given that the current has been performed on epicardial.

5.6 Conclusions

In this paper, performance of orientation-independent sensing methods for cardiac signals are explored. For this, signals recorded from a high-density multielectrode during a retrospective experimental series of isolated perfused heart were employed. Electrical field loop reconstruction and orientation-independent bipolar activations for different technical configurations were compared. Several parameters based on loop shape, rejection ratio to the orthogonal residual signal and pulse morphology were defined. Our results concluded that interelectrode spacing not larger than 2 mm should be employed for accurate oEGM estimation. Moreover, if this condition is satisfied, a cross-orientation clique configuration is preferred over the triangular clique currently employed in clinical practice. This study opens a new standpoint on the reconstruction of oEGMs from high density multielectrode catheters, and a new vision towards the design of new devices and post-processing methods with improved features and performance.

Chapter 6

Vector Field Heterogeneity for the Assessment of Locally Disorganised Cardiac Electrical Propagation Wavefronts from High-Density Multielectrodes

Abstract

Background and Objectives: High-density multielectrode catheters are becoming increasingly popular in cardiac EP for advanced characterisation of the cardiac tissue, due to their potential to identify impaired sites. These are often characterised by abnormal electrical conduction, which may cause locally disorganised propagation wavefronts. **Methods**: To quantify it, a novel heterogeneity parameter based on vector field analysis is proposed, utilising finite differences to measure direction changes between adjacent cliques. The proposed Vector Field Heterogeneity (VFH) metric has been evaluated on a set of simulations with controlled levels of organisation in vector maps, and a variety of grid sizes. Furthermore, it has been tested on animal experimental models of isolated Langendorff-perfused rabbit hearts. **Results**: The proposed parameter exhibited superior capturing ability of heterogeneous propagation wavefronts compared to the classical Spatial Inhomogeneity (SI) index, and simulations proved that the metric effectively captures gradual increments in disorganisation in propagation patterns. Notably, it yielded robust and consistent outcomes for 4×4 grid sizes, underscoring its suitability for the latest generation of orientation-independent cardiac catheters. **Conclusions**: The VFH metric offers a more precise and reliable measure of heterogeneous propagation wavefronts, making it a valuable tool for characterising cardiac tissue using high-density multielectrode catheters.

This chapter is based on the publication: L. Pancorbo*, S. Ruipérez-Campillo*, et al. (2023). Vector Field Heterogeneity for the Assessment of Locally Disorganised Cardiac Electrical Propagation Wavefronts from High-density Multielectrodes. *IEEE Open Journal of Engineering in Medicine and Biology* [277]. (* denotes co-first authorship)

6.1 Introduction

High density grid catheters have been recently proposed for accurate characterisation of local properties of the cardiac EP substrate [278]. This grid arrangement of the electrodes allows the representation of the electrical field loop within a clique which, in turn, allows the reconstruction of orientation-independent EGMs, also known as omnipolar EGMs (oEGMs). This technology, claimed to be orientation-independent, has been introduced to overcome some of the limitations of unipolar and bipolar EGMs [15, 279, 13]. It offers robust signals and can determine the direction of the propagation wavefront in real time, even in complex propagation patterns [280, 18]. Since the release of the Advisor HD Grid Mapping Catheter in 2016, this technology has been receiving significant attention for its use in EP explorations [22].

Examining the propagation of electrical signals within the heart provides valuable insights that can assist cardiologists in identifying conduction abnormalities and, consequently, potential catheter ablation sites [281]. In fact, the electrical propagation in healthy tissue can be locally assumed to be more homogeneous than in scarred tissue, or in arrhythmias, where disorganisation of the electrical propagation may happen. That being a key clinical concern, we propose a novel metric to assess the heterogeneity of the propagation wavefront, by obtaining the direction of propagation in all cliques of the grid arrangement. We test it on a set of *ad-hoc* simulations of the wavefront propagation and on an animal-model with stimulated and non-stimulated propagation patterns, which allow us to analyse the behaviour of the metric on a physiological controlled environment.

Several metrics to quantify the complexity of cardiac propagation based on different properties of the signals have been proposed hitherto. For instance, entropy focuses on the complexity of EGM morphology [282] and has been used in several applications, such as to predict AF recurrence after pulmonary vein ablation [283], to detect complex fractionated atrial EGMs (CFAEs) [284] and rotors [285] or to discriminate paroxysmal vs. persistent AF [286], among others. Alternatively, coherence [287] and cross-correlation [288] were introduced to determine the similarity between pairs of signals, providing information on the synchronicity and coordination among different locations within the heart, which is an indicator of propagation organisation [289, 290]. The frequency spectrum of the signals has also been studied for this purpose. An example is the Organisation Index, which is based on the observation that wavelets sustaining an arrhythmia introduce additional frequency components to the spectrum [291]. This parameter was successful in guiding ablation in clinical studies [292].

Other metrics are directly applied to conduction velocities. In particular, the Anisotropy Ratio is based on the effect of impaired tissue on disrupting the normal anisotropy in conduction [293]. In addition to all these indicators, the most widely employed measurement of heterogeneity is the SI index, described by Lammers in 1990 [294]. This metric, based on conduction delays across the tissue, has been applied to high-density multielectrode recordings to evaluate arrhythmogenicity [295, 296, 297].

Most of these methods require a mapping system with a high number of points to provide robust and consistent measurements. Therefore, there is a need for a reliable parameter applicable to small grids, such as the 4×4 array of the Advisor HD Grid. To address this, we propose in this study the VFH metric, based on vector field analysis. Indeed, vector field operators such as divergence and curl have been already proposed for the analysis of propagation patterns [298]. However, it should be noted that these parameters do not measure the heterogeneity of propagation itself. Rather, they are used to identify specific patterns of interest within the maps, such as ectopic foci, wavefront collisions, or reentry circuits [299, 300].

In this paper, we present the derivation of the novel VFH metric and its validation on omnipolar-derived vector maps obtained with HD grid electrode configurations. Maps for both stimulated and non-stimulated tissue are created from an experiment involving Langendorff-perfused rabbit hearts. Under the assumption that stimulation aligns the propagation vectors resulting in more organised maps, the performance of the VFH metric is based on its ability to differentiate between the two groups. Additionally, a simulation model is created to test the metric performance for different catheter sizes and levels of disorganisation under controlled conditions. Finally, the SI index is replicated to assess the VFH metric's potential as compared to a well-established and recognised metric.

6.2 Materials

6.2.1 Simulated data

Simulated propagation maps are generated to study the behaviour of the VFH metric for different grid sizes and heterogeneity levels under controlled conditions. Notably, the model does not create synthetic signals. Instead, vector maps are directly generated by assigning an angle, within a range of values with respect to a reference, to each clique in a randomised manner. That value represents the angle between that vector of propagation and the horizontal bipole with the east direction —the reference. The level of heterogeneity is therefore given by the possible angular range, which constrains the vector directions that can be generated by the model. For instance, a narrow range of $[-1^\circ, 1^\circ]$ implies a highly organised vector field, which will entail small heterogeneity in the map. Conversely, a broader range of $[-180^\circ, 180^\circ]$ allows any direction and thus implies the possibility of completely disorganised vector fields, associated with higher heterogeneity.

For a general grid, we have N vectors in a $p \times q$ clique arrangement, p being the number of cliques in a row and q the number of cliques in a column. Due to the random nature of the simulation and to avoid similar directions by coincidence, despite highly heterogeneous settings, the specified angle interval $[-\theta_{lim}, \theta_{lim}]$ is divided into N subintervals of equal length, N being the total number of cliques. Subsequently, a random angle is selected from the continuous uniform distribution contained within each subinterval and is assigned to a clique within the grid. The designation of each vector to a clique is also performed at random, which reduces the likelihood of adjacent vectors originating from contiguous subintervals.

With this model, propagation maps of different disorganisation levels were generated by increasing the value of $|\theta_{lim}|$ starting at 1° and from 5° to 180° in steps of 5°. For each level, 100 maps are generated with a fixed random seed for the sake of replicability, to evaluate the global heterogeneity of the maps. Additionally, another set of 100,000 simulated maps is created to examine the trend of the heterogeneity metric in each of the steps.

6.2.2 Experimental data

Recordings taken from Langendorff-perfused rabbit hearts have been selected for the analysis, comprising both non-stimulated (basal) and stimulated signals recorded at 37°C, as previously described by Guill *et al.* [271]. Namely, an ad-hoc multielectrode mapping catheter was placed over the posterolateral wall of the left ventricular epicardium. The electrode grid consisted of 128 electrodes with 1 mm of interelectrode distance. EGMs were collected using the MapTech© system at a sampling frequency of 1 kHz, following the established protocol. The cardiac tissue was stimulated at a point proximal to the left edge of the mapping catheter using a bipolar electrode connected to a GRASS S88 stimulator. To create the propagation maps, an interval containing the activation is selected from each set of EGMs. This process results in a total of 29 propagation maps generated from basal recordings, 21 from recordings with stimulation at 4 Hz, and 18 with stimulation at 6 Hz. The protocol for the experiments was previously approved by the Ethics Committee of Universitat de València.

Initially, we considered a 4×4 subset of the electrode array from its central part, following the scheme of the Advisor HD Grid Catheter. Subsequently, we extended the grid size to investigate the metric's behaviour on various plausible electrode designs. For consistency, all grids are taken from the centre of the catheter, as the acquisition of the outermost electrodes may be less trustworthy due to possible inadequate contact with the epicardium.

6.3 Methods

Non-stimulated recordings have a more heterogeneous activation pattern than stimulated recordings, given a forced alignment of the propagation vectors in the stimulated case. Therefore, we set out to establish that a metric based on vector field finite differences can effectively capture differences between groups.

6.3.1 Creation of propagation maps

The omnipole enables the immediate determination of the propagation direction [249]. During depolarisation, the electric field formed by the perpendicular bipoles within a clique $\mathbf{b}_x - \mathbf{b}_y$ creates the so-called bipolar loop. The loop's greatest magnitude corresponds to the direction of propagation of the wavefront [15], and is indicated by a unitary vector located at the clique's centre (see fig. 6.1).

The cross-clique configuration for the omnipolar reconstruction of signals was implemented, as described in [237] and validated in an animal experimental model in [257]. From a 4×4 electrode grid and according to the definition of a clique, a 3×3 vector map is generated that displays the propagation of the wave under the catheter. The propagation angle θ is determined by the angle between each vector and the horizontal bipole $\mathbf{b}_x$. Therefore, for a specific moment in time on a matrix of $m \times n$ electrodes $G(t) \in \mathbb{R}^{m \times n} (t = c,$ for any constant $c)$, we define a matrix Φ that contains the propagation angles for each clique as:

$$\Phi \in \mathbb{R}^{p \times q} : p = m - 1, q = n - 1 \tag{6.1}$$

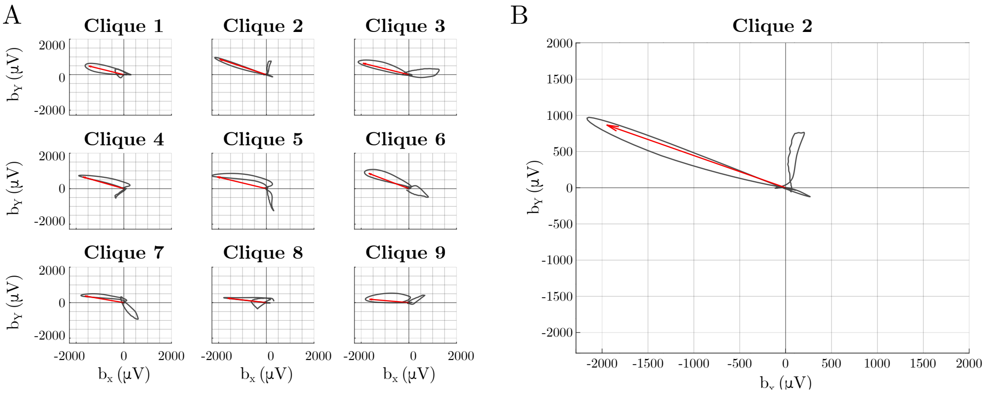

Figure 6.1: Representation of the bipolar loop in a recording on the epicardium of a Langendorff rabbit heart at 37°C and under stimulation of 4 Hz; **A**. Loop traced by each bipole in its corresponding clique; **B**. Closer look at the loop traced by the orthogonal bipoles in clique 2, with a vector indicating the estimated propagation direction for that clique.

$$\theta_{i,j} : 1 \le i \le p, 1 \le j \le q \tag{6.2}$$

$$\Phi := \begin{bmatrix} \theta_{1,1} & \cdots & \theta_{1,q} \\ \vdots & \ddots & \vdots \\ \theta_{p,1} & \cdots & \theta_{p,q} \end{bmatrix} \tag{6.3}$$

Where the variables m and n denote the number of rows and columns in the matrix G, whereas p and q indicate the number of rows and columns in the matrix Φ. The indices i and j specify the position of an element within the angular matrix. Consequently, the propagation is illustrated through a map of unitary vectors that contain elements $\mathbf{u}_{i,j} = \left(\cos\theta_{i,j}, \sin\theta_{i,j}\right)$.

6.3.2 Vector Field Heterogeneity

In this section we describe the proposed VFH metric, based on vector field analysis. Firstly, we create the 2-dimensional vector map that represents the electrical propagation, which can be split into its horizontal and vertical vector components Γ_x and Γ_y, respectively:

$$(\Gamma_x)_{i,j} = \cos\theta_{i,j}; \left(\Gamma_y\right)_{i,j} = \sin\theta_{i,j} \tag{6.4}$$

Where $(*)_{i,j}$ represents the element in the i-th row and j-th column of a given $p \times q$ matrix, such that $1 \le i \le p, 1 \le j \le q$.

Finite differences were used to approximate the partial derivatives of the vector field, by calculating differences between neighbouring vectors in the field. Specifically, $\Delta\Gamma_x/\Delta x$ and $\Delta\Gamma_y/\Delta x$ were used to measure how the horizontal and vertical components vary with respect to their neighbouring points in the horizontal direction. Analogously, $\Delta\Gamma_x/\Delta y$ and $\Delta\Gamma_y/\Delta y$ were used to estimate the variation of the components with their neighbouring points in the vertical direction. Additionally,

$\Delta\Gamma_x/\Delta d_1$, $\Delta\Gamma_y/\Delta d_1$ and $\Delta\Gamma_x/\Delta d_2$, $\Delta\Gamma_y/\Delta d_2$ represent the finite differences with the adjacent diagonal elements across both positive (i.e. northeast, d_1) and negative (i.e. northwest, d_2) diagonals. For the diagonal elements, a scaling factor of $\sqrt{2}$ is used to account for the spatial separation of the cliques. Forward differences of a vector field involve approximating the derivative of the field at a certain position by calculating the difference between the vector components at that point and its adjacent position at a higher index. Similarly, backward differences compute the difference between the vector components at a specific point and its neighbouring point at a lower index.

The metric derivation is based on the computation of forward and/or backward differences, depending on the point. For interior elements, that is, those which do not lie on the corner of the vector field or in the first/last row/column, the mean of the absolute forward and backward differences is computed. For edge elements, the absolute value of either the forward or backward difference is computed, depending on the edge at which the element is located. For all computations, the referred element is constrained to be within the matrix domain.

Videlicet, for a central element $(\Gamma_x)_{i,j}$:

$$\left(\frac{\Delta\Gamma_x}{\Delta x}\right)_{i,j} = \frac{\left|(\Gamma_x)_{i,j+1} - (\Gamma_x)_{i,j}\right| + \left|(\Gamma_x)_{i,j} - (\Gamma_x)_{i,j-1}\right|}{2} \tag{6.5}$$

$$\left(\frac{\Delta\Gamma_x}{\Delta y}\right)_{i,j} = \frac{\left|(\Gamma_x)_{i+1,j} - (\Gamma_x)_{i,j}\right| + \left|(\Gamma_x)_{i,j} - (\Gamma_x)_{i-1,j}\right|}{2} \tag{6.6}$$

$$\left(\frac{\Delta\Gamma_x}{\Delta d_1}\right)_{i,j} = \frac{\left|(\Gamma_x)_{i-1,j+1} - (\Gamma_x)_{i,j}\right| + \left|(\Gamma_x)_{i,j} - (\Gamma_x)_{i+1,j-1}\right|}{2\sqrt{2}} \tag{6.7}$$

$$\left(\frac{\Delta\Gamma_x}{\Delta d_2}\right)_{i,j} = \frac{\left|(\Gamma_x)_{i,j} - (\Gamma_x)_{i-1,j-1}\right| + \left|(\Gamma_x)_{i+1,j+1} - (\Gamma_x)_{i,j}\right|}{2\sqrt{2}} \tag{6.8}$$

The calculations are analogous for the matrix Γ_y. Then, the magnitude of the variations in each direction is computed to take into account both contributions Γ_x and Γ_y. Note that the magnitude variations of the vector field are scalar fields representing how each vector varies from its horizontal, vertical, and diagonal neighbours respectively, that is:

$$\left(\frac{\Delta\mathbf{\Gamma}}{\Delta x}\right)_{i,j} = \sqrt{\left(\frac{\Delta\Gamma_x}{\Delta x}\right)_{i,j}^2 + \left(\frac{\Delta\Gamma_y}{\Delta x}\right)_{i,j}^2} \tag{6.9}$$

$$\left(\frac{\Delta\mathbf{\Gamma}}{\Delta y}\right)_{i,j} = \sqrt{\left(\frac{\Delta\Gamma_x}{\Delta y}\right)_{i,j}^2 + \left(\frac{\Delta\Gamma_y}{\Delta y}\right)_{i,j}^2} \tag{6.10}$$

$$\left(\frac{\Delta\mathbf{\Gamma}}{\Delta d_1}\right)_{i,j} = \sqrt{\left(\frac{\Delta\Gamma_x}{\Delta d_1}\right)_{i,j}^2 + \left(\frac{\Delta\Gamma_y}{\Delta d_1}\right)_{i,j}^2} \tag{6.11}$$

$$\left(\frac{\Delta \boldsymbol{\Gamma}}{\Delta d_2}\right)_{i,j} = \sqrt{\left(\frac{\Delta \Gamma_x}{\Delta d_2}\right)^2_{i,j} + \left(\frac{\Delta \Gamma_y}{\Delta d_2}\right)^2_{i,j}} \tag{6.12}$$

The heterogeneity score matrix Ψ is computed by adding the four magnitude matrices. To normalise the values, each resulting element is divided by its corresponding upper bound.

$$(\Psi)_{i,j} = \frac{\left(\frac{\Delta \boldsymbol{\Gamma}}{\Delta x}\right)_{i,j} + \left(\frac{\Delta \boldsymbol{\Gamma}}{\Delta y}\right)_{i,j} + \left(\frac{\Delta \boldsymbol{\Gamma}}{\Delta d_1}\right)_{i,j} + \left(\frac{\Delta \boldsymbol{\Gamma}}{\Delta d_2}\right)_{i,j}}{(\xi)_{i,j}}, \quad 0 \leq (\Psi)_{i,j} \leq 1 \tag{6.13}$$

The normalisation constant ξ of size $p \times q$ contains the upper bounds of each element, which are the same for all positions except for the vertices:

$$(\xi)_{i,j} = \begin{cases} 4 + \sqrt{2} & i \in \{1, p\} \text{ and } j \in \{1, q\} \\ 4 + 2\sqrt{2} & \text{elsewhere} \end{cases} \tag{6.14}$$

$(\Psi)_{i,j}$ is assigned to the corresponding propagation map element, indicating how dissimilar that vector is from the surrounding vectors (see fig. 6.2). Finally, all elements are averaged to obtain the heterogeneity value VFH, which is assigned to the whole local map:

$$\text{VFH} = \frac{\sum_{i=1}^{p} \sum_{j=1}^{q} (\Psi)_{i,j}}{p \cdot q} : 0 \leq \text{VFH} < 1 \tag{6.15}$$

Note that VFH is not meant to reach 1 because that would imply that all the elements $(\Psi)_{i,j}$ are equal to 1. According to the definition, an element of the map has a value of 1 when all its adjacent vectors point in the opposite direction, which in turn prevents them from having the maximum score of 1 when analysing other adjacent pairs.

6.3.3 Metric comparison with the widely accepted Spatial Inhomogeneity index

The proposed VFH metric is compared to the widely adopted SI index [294], commonly used in the literature. This index was introduced more than three decades ago to quantify cardiac conduction disorders using activation maps derived from high-density recordings. To replicate the methodology, LATs were mapped to each electrode position by timing the $-dV/dT_{max}$ of the unipolar EGMs [12]. A phase difference, also known as activation time-delay, is defined as the temporal variation between activation times and is measured in *ms* [301]. To create a phase map, phase differences were calculated between each pair of electrodes forming a clique and the largest value was assigned to that position. The resulting map represents the spatial distribution of conduction inconsistencies. Finally, local phase differences were represented in a histogram. The total range of differences, computed as $P_{95} - P_5$,

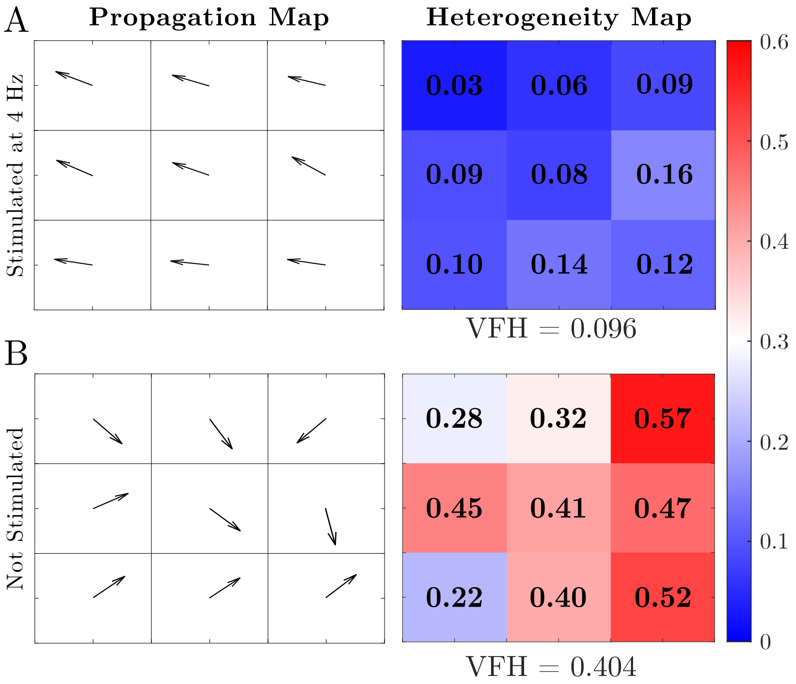

Figure 6.2: Illustration of heterogeneity depicting the heterogeneity scores of each clique $(\Psi)_{i,j}$ and the VFH value assigned to the map; **A.** Results for a recording stimulated at 4 Hz, with the propagation vector map (left) and the heterogeneity map (right), illustrating an organised region of propagation; **B.** Idem for a basal recording where the propagation map is found to be more disorganised.

is the absolute inhomogeneity. This parameter might increase due to a global decrease in conduction velocities, so the SI index $(P_{95} - P_5)/P_{50}$ is used to represent inhomogeneities in conduction independent of the velocities.

To assess this metric's performance and compare it to the proposed one, inhomogeneity indexes were computed for recordings in the experimental data set (see fig. 6.3). The ability of the index to distinguish between basal and stimulated groups is studied. Observe that the mapping catheter possesses a unit interelectrode distance with phase differences calculated solely between adjacent electrodes, excluding the diagonal elements. Consequently, their values are inherently normalised to 1mm.

6.3.4 Statistical analysis

The ability of the proposed metric to distinguish between populations based on stimulation type was evaluated to reveal its potential as a heterogeneity metric. The resulting VFH values are tested for statistical differences across the three groups: basal, stimulation at 4 Hz, and stimulation at 6 Hz. The same analysis is performed on the SI index to provide an objective comparison between the two metrics.

The Wilcoxon rank-sum test (5% significance level) was applied to perform multiple comparisons on the resulting heterogeneity distributions (see fig. 6.5 and 6.7). The Wilcoxon rank-sum test is a non-parametric alternative to the Analysis of Variance

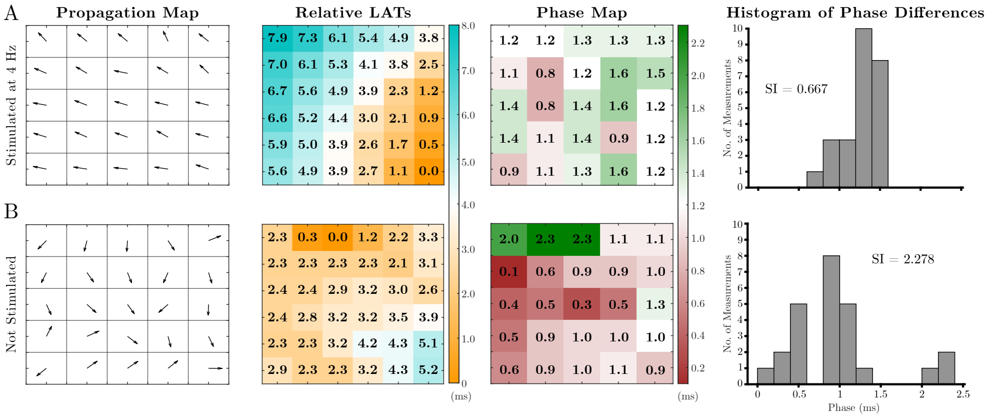

Figure 6.3: Calculation of the SI index, proposed by Lammers *et al.*, for a 6×6 grid of recordings depicted in fig. 6.2; **A.** Results for a recording stimulated at 4 Hz, with the propagation vector map (first column), LAT relative to the earliest LAT of the map, for representation purposes (second column), the corresponding phase map (third column), and the phase differences histogram (last column); **B.** Idem for a basal recording.

(ANOVA) test. Typically, one-way ANOVA would be employed to assess differences in the means of heterogeneity values across the groups, with the type of stimulation being the independent variable. However, due to the limited number of samples in the experimental dataset, the assumption of normality required by ANOVA is not satisfied. This was verified through the Shapiro-Wilk test and examination of the QQ plots (see Appendix A). A similar analysis was conducted to study the effect of the catheter size on the metric's performance. In this case, the independent variable was the size, and multiple comparisons between consecutive grid sizes were performed. In order to account for multiple testing, the Bonferroni correction was applied to adapt the p-values based on the number of comparisons. The values for VFH and SI are summarised in the medians and IQR arising from the Wilcoxon test.

The Receiver Operating Characteristic (ROC) curves were generated for both metrics to compare their effectiveness in distinguishing between basal and stimulated cases. The Area Under the Curve (AUC) was provided to measure the overall performance of the classifiers. For this analysis, stimulated at 4 Hz and 6 Hz results were grouped, resulting in an imbalanced set -29 basal; 39 stimulated. For this reason, Precision-Recall (PR) curves and their respective AUCs were also examined, as they may provide more meaningful insights in the presence of class imbalance.

6.4 Results

6.4.1 Simulations

The VFH metric's behaviour for a 4×4 electrode grid —which leads to a 3×3 clique grid— is studied by computing the VFH value of simulated maps of increasing heterogeneity (fig. 6.4.a). It can be observed that widening the angle interval results in higher VFH values, which are representative of greater disorganisation of the vectors (see fig. 6.4.b). Running 100,000 simulations provides a close approximation of the trend of the metric (dashed line). It shows a linear behaviour until 45° with a slope of 0.0315, computed through linear regression. After that point, the progression curves and smooths out until VFH reaches a value around 0.7 for a completely random set-up. Note that while 0.7 represents the average value for highly disorganised maps, it is not the maximum achievable value. The highest recorded VFH value from among the 100,000 simulations at 180° is 0.7933, which represents an empirical upper bound of the metric.

Simulated maps of different sizes were generated to study the impact of increasing the number of data points on the metric's behaviour (fig. 6.4.c). The VFH values obtained for different catheter sizes are displayed together, comparing the previous results with those obtained from 7 × 7 and 10 × 10 grid sizes. It can be appreciated that using larger grids leads to a decrease in the SD. The three trends have similar shapes, following a linear behaviour for the first points and then reaching a plateau (fig. 6.4.d). However, some differences can be observed for the larger grids. The initial linear trend has a lower slope and they converge to a lower value of VFH = 0.62, approximately. The maximum values recorded at 180° are 0.7262 and 0.6911 for 7 × 7 and 10 × 10 grids, respectively.

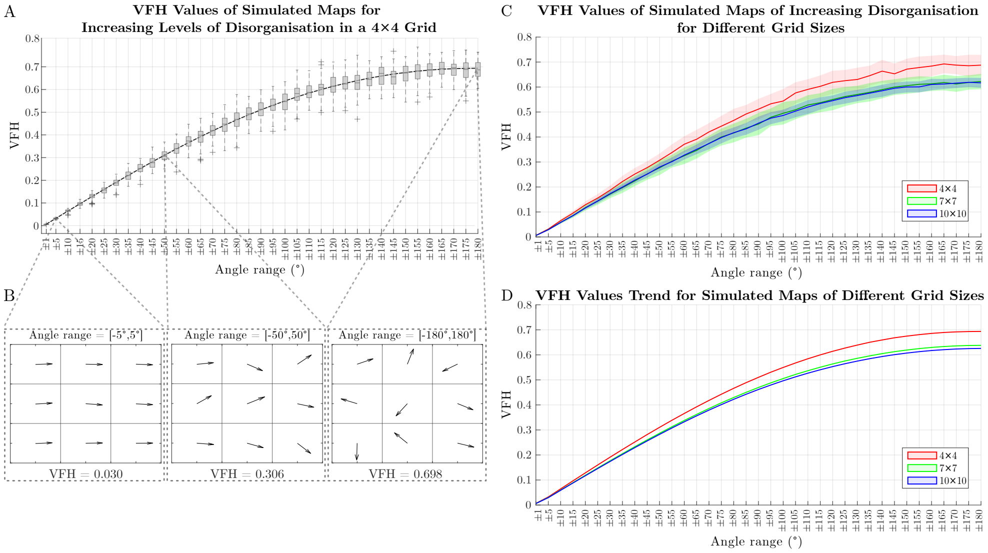

Figure 6.4: A. Box and whisker plot of the VFH values of simulated propagation maps of increasing disorganisation. For each angle range, 100 simulations were performed corresponding to a 4 × 4 catheter grid. The trend of the VFH metric (dashed line) is calculated by running 100,000 simulations for each interval and plotting the mean VFH value; **B.** Propagation maps representative of three distinct angle ranges; **C.** Comparison of the VFH values from simulated propagation maps of different catheter sizes. The shaded region corresponds to the SD and the line is the mean VFH value for the 100 simulations. The decrease in SD from 4 × 4 to 10 × 10 is to be highlighted; **D.** Trends are calculated by taking the mean VFH value from 100,000 simulations for each angle range.

Table 6.1: VFH values for different grid sizes according to the stimulation type

	Basal		Stim. 4 Hz		Stim. 6 Hz	
Size	Median	IQR	Median	IQR	Median	IQR
3×3	0.341	0.334	0.058	0.065	0.065	0.064
4×4	0.323	0.228	0.090	0.071	0.096	0.063
5×5	0.355	0.126	0.085	0.062	0.085	0.056
6×6	0.375	0.102	0.107	0.043	0.114	0.048
7×7	0.370	0.092	0.138	0.049	0.145	0.078

6.4.2 Experimental data

Fig. 6.5 illustrates the distribution of VFH values for different stimulation types using electrode grids of increasing size. Table 6.1 collects the median and IQR values for each case. For a 4×4 grid, the VFH value tends to be approximately 0.35 without stimulation. Conversely, when the heart was stimulated, the value decreased to 0.11 on average. Significant differences are observed between the results of the basal group and both stimulated groups. However, there is no statistical difference between stimulations at 4 Hz and 6 Hz. This is consistent for all catheter sizes (see table 6.2). For a total of 3 comparisons and applying the Bonferroni correction, the null hypothesis, describing lack of difference among results, is rejected for $p < 0.0167$.

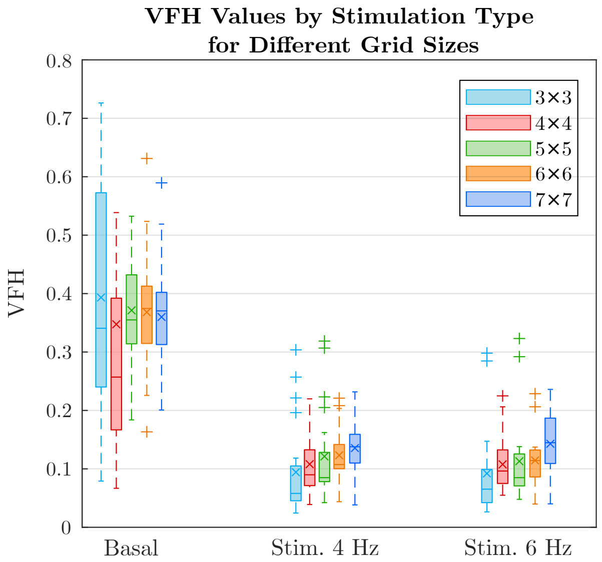

Figure 6.5: Box and whisker plots of the VFH values according to the type of stimulation. Results for different catheter sizes are shown.

When expanding the analysis to include more electrodes, we observe that the mean VFH value remains constant for the basal groups, whereas there is a slight increase in the stimulated cases. Furthermore, as the grid size is increased, the SD of the VFH value decreases for the basal group, but is maintained for stimulation at 4 Hz

Table 6.2: P-values of Wilcoxon rank-sum test for comparing VFH values according to stimulation type

Catheter Size	Basal - Stim. 4 Hz	Basal - Stim. 6 Hz	Stim. 4 Hz - Stim. 6 Hz
3×3	2.8938e-07*	1.0024e-06*	0.8547
4×4	1.6878e-08*	4.7571e-08*	0.8547
5×5	1.6878e-08*	6.8712e-08*	0.7037
6×6	3.7057e-09*	1.7482e-08*	0.5447
7×7	3.7057e-09*	1.9845e-08*	0.5447

∗ *p-values < 0.0167*

Table 6.3: P-values of Wilcoxon rank-sum test for comparing VFH values according to catheter size

Catheter Size	3×3 - 4×4	4×4 - 5×5	5×5 - 6×6	6×6 - 7×7
Basal	0.3924	0.4010	0.9010	0.5650
Stim. 4 Hz	0.0826	0.9198	0.2177	0.0826
Stim. 6 Hz	0.0847	0.6693	0.2750	0.0642

∗ *p-values < 0.0125*

and 6 Hz.

The statistical analysis reveals there is no significant difference in the VFH values when increasing the electrode grid in one unit (i.e. from 3×3 to 4×4). Table 6.3 shows the p-values obtained from applying the Wilcoxon Rank-Sum test on the 4 comparisons. The null hypothesis is rejected when the p-value is lower than the significance level after the Bonferroni correction (p-value < 0.0125).

An example of a propagation map acquired by an 8×8 electrode grid is shown in fig. 6.6. The map shows local differences in heterogeneity which are quantified using a 4×4 grid (fig. 6.6.a). A value of VFH = 0.64 is found for the disorganised region, compared to VFH = 0.07 in the homogeneous area. This local evaluation using a smaller grid is compared to a global quantification of the whole map that results in a value of VFH = 0.23 (fig. 6.6.b).

6.4.3 Metric comparison

Fig. 6.7 shows the resulting SI index values for different stimulation types and for electrode grids of increasing size. Table 6.4 collects the median and IQR values for each case. In the case of a 4×4 catheter size, the resulting index has a mean value of 1.46 for basal recordings. When there is stimulation, this value decreases to an average of 0.87 for both frequencies. Similarly to the VFH values, the SI indexes obtained for the basal groups are statistically different to those from stimulated groups. Additionally, no significant difference exists between stimulation at 4 and 6 Hz. This relationship is maintained for different grid sizes (see table 6.5).

When comparing the results between different catheter sizes, there were only significant differences (p-value ≤ 0.0125) found between 3×3 - 4×4, and 4×4 - 5×5 for

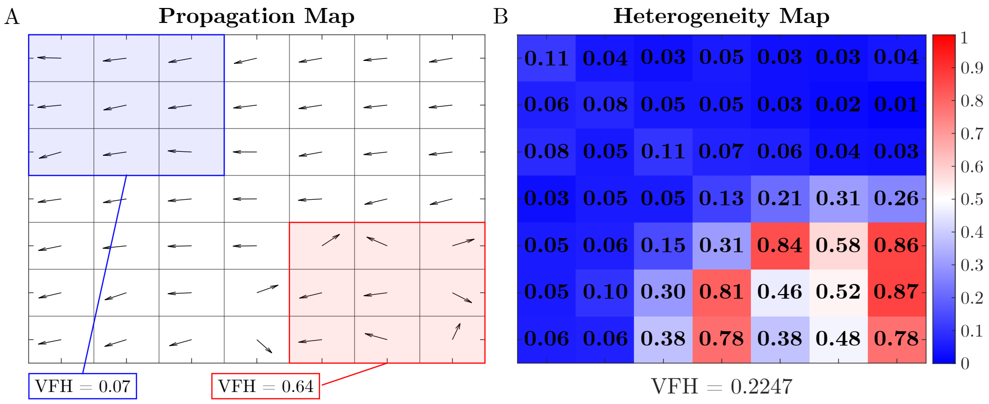

0.11	0.04	0.03	0.05	0.03	0.03	0.04
0.06	0.08	0.05	0.05	0.03	0.02	0.01
0.08	0.05	0.11	0.07	0.06	0.04	0.03
0.03	0.05	0.05	0.13	0.21	0.31	0.26
0.05	0.06	0.15	0.31	0.84	0.58	0.86
0.05	0.10	0.30	0.81	0.46	0.52	0.87
0.06	0.06	0.38	0.78	0.38	0.48	0.78

Figure 6.6: Example of heterogeneity analysis for an 8×8 catheter grid; **A**. Vector map representing propagation under the catheter. The VFH values that a 4×4 grid would obtain are displayed; **B**. Heterogeneity Map displaying the heterogeneity values assigned to each vector $(\Psi)_{i,j}$ and the global VFH value of the whole map.

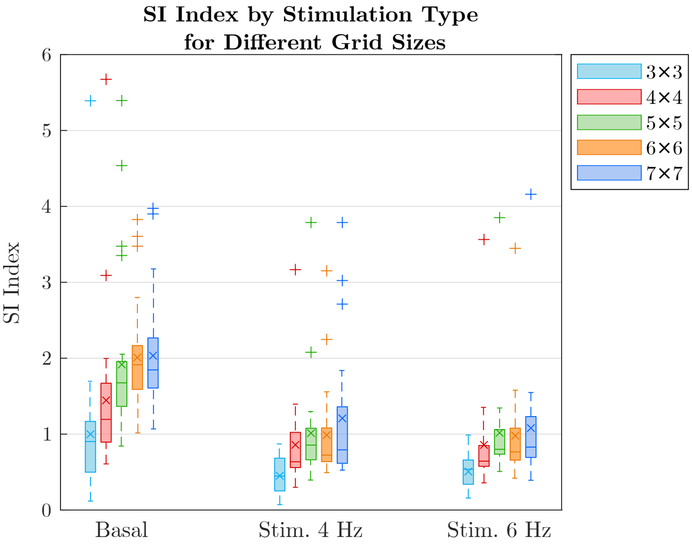

Figure 6.7: Box and whisker plots of the SI index values according to the type of stimulation. Results for different catheter sizes are shown.

the basal cases, and between 3 × 3 - 4 × 4 for stimulation at 4 Hz (see table 6.6).

Given the lack of statistical difference between stimulation at 4 Hz and at 6 Hz revealed by the previous analysis, both groups were merged and the effectiveness of the metrics as binary classifiers basal/stimulated was compared. As depicted in fig. 6.8.a, the ROC curve for the VFH metric is further away from the diagonal than the ROC curve obtained for the SI index. This results in a higher AUC value for the proposed metric for all catheter sizes (see table 6.7, upper panel).

Furthermore, a PR curve is computed to address possible inaccuracies from the imbalanced data set. The PR curves show similar behaviour to the ROC analysis

Table 6.4: SI values for different grid sizes according to the stimulation type

	Basal		Stim. 4 Hz		Stim. 6 Hz	
Size	Median	IQR	Median	IQR	Median	IQR
3 × 3	0.909	0.705	0.455	0.455	0.545	0.336
4 × 4	1.200	0.783	0.643	0.515	0.652	0.296
5 × 5	1.680	0.634	0.862	0.460	0.807	0.368
6 × 6	1.917	0.648	0.731	0.522	0.773	0.457
7 × 7	1.850	0.684	0.800	0.779	0.836	0.560

Table 6.5: Wilcoxon rank-sum test p-values for comparing SI indexes by stimulation type

Catheter Size	Basal - Stim. 4 Hz	Basal - Stim. 6 Hz	Stim. 4 Hz - Stim. 6 Hz
3 × 3	9.5733e-04*	0.0078*	0.4302
4 × 4	2.0249e-04*	5.3850e-05*	0.8546
5 × 5	7.4016e-06*	3.6776e-06*	0.7247
6 × 6	2.8853e-06*	1.5517e-06*	0.6829
7 × 7	5.5782e-05*	1.7295e-06*	0.9663

∗ *p-values < 0.0167*

Table 6.6: P-values of Wilcoxon rank-sum test for comparing SI indexes according to catheter size

Catheter Size	3 × 3 - 4 × 4	4 × 4 - 5 × 5	5 × 5 - 6 × 6	6 × 6 - 7 × 7
Basal	0.0025*	0.0025*	0.0885	0.9690
Stim. 4 Hz	0.0028*	0.1703	0.6966	0.6060
Stim. 6 Hz	0.0176	0.0598	0.7637	0.5797

∗ *p-values < 0.0125*

(see fig. 6.8.B), with higher AUC values for the proposed metric despite the catheter size. These values are displayed in table 6.7 (bottom pannel) and the curves for all sizes are shown in Appendix A.

6.5 Discussion

In this study, we propose the VFH, a heterogeneity metric based on vector field analysis to characterise the local EP substrate. This parameter is computed from omnipolar-derived vector maps obtained with HD grid electrodes. Although it has been designed to provide robust results in small-size arrays, it can be easily adapted to catheters of any size and even to other electrode arrangements through simple parameter adjustments.

The properties of the VFH metric were first explored on simulated maps with progressively higher levels of disorganisation. This allows for objective assessment under controlled conditions. In this case, the success of the VFH parameter is proven

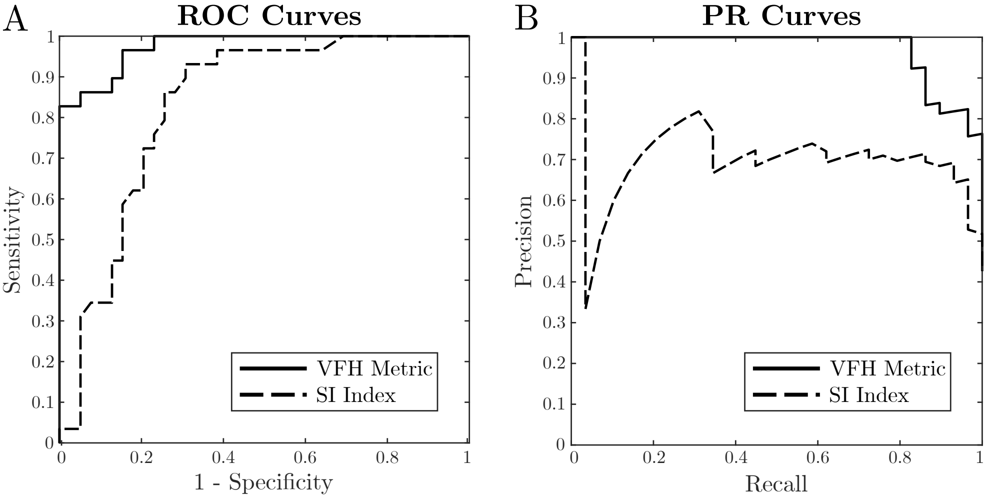

Figure 6.8: A. ROC curves comparison between the VFH metric proposed in this study (solid line) and the SI index (dashed line) for the case of a 4×4 electrode grid; **B.** Same comparison for the PR curves.

Table 6.7: AUC values for the ROC and PR curves

ROC Curves		
Catheter Size	VFH Metric	SI Index
3×3	0.9293	0.7569
4×4	0.9752	0.8311
5×5	0.9726	0.8895
6×6	0.9938	0.9054
7×7	0.9929	0.8753
PR Curves		
Catheter Size	VFH Metric	SI Index
3×3	0.9165	0.7903
4×4	0.9709	0.7014
5×5	0.9640	0.7764
6×6	0.9928	0.8088
7×7	0.9914	0.7024

by its ability to reflect the increasing disorganisation of simulated maps. The curve evolution as well as the SD ranges allow us to obtain a deep understanding of the metric. Furthermore, the asymptotic behaviour at high complexity lets us assign an empirical upper bound for this parameter, which is rather unpractical to derive as a closed-form solution. In contrast, the SI index is not upper-bounded, which may lead to outliers that could bias statistical results, as can be appreciated in fig. 6.7. Moreover, the performance of the VFH metric with different grid sizes was explored. Interestingly, the VFH maintained its robustness when applied to small maps as compared to larger grid sizes, as can be appreciated in fig. 6.4. Nevertheless, there is some decrease in the VFH values when increasing the grid size to 7×7 due to an averaging effect with a higher number of vectors. Accordingly, comparison of VFH values obtained with different grid sizes should be avoided.

The validation of the metric on the experimental data depends on its ability to distinguish between basal (not organised) and stimulated (organised) maps. Both the VFH metric and the SI index provide significant differences between the two groups. However, this distinction is less noticeable in the SI, as can be inferred from the p-values (tables 6.2 and 6.5) and a higher overlapping of the box and whiskers plots between basal and stimulated groups. The ROC analysis confirms the superiority of VFH, obtaining greater AUC values than the SI index for all sizes. An equivalent conclusion is obtained from the PR curves, which support the previous results despite class imbalance. Moreover, the SI index has larger SDs (and outliers, as aforementioned) than the VFH, which implies a less accurate and more inconsistent characterisation of propagation. Moreover, SI values were also dependent on catheter size (tables 6.3 and 6.6).

The caveats of the SI index could be understood by the fact that it is derived from LAT maps [294]. A disadvantage of this methodology is that in the case of complex EGMs, LATs might be difficult to define [301], hence introducing high variability with different LAT detection methods. It might be questioned whether the reported differences between the VFH and the SI index are primarily driven by inconsistencies in LAT determination. To investigate this hypothesis, VFH values were computed using LAT-derived vector maps. As observed in Appendix B, these differences persist, even upon negating the impact of LAT errors. This suggests that the enhanced performance of the VFH metric relative to the established SI index is intrinsic to its properties, thus solidifying its validation.

Other studies have been primarily focused on measuring the complexity of EGM morphology by means of entropy measurements [302]. However, further research is needed to better understand the origins of CFAEs [303]. Alternative metrics, like Coherence or Cross-Correlation [304, 288], compare simultaneous recordings from separate points of the cavity. Nevertheless, this requires the use of larger grids, which may be a limiting factor. On the other hand, CV metrics, such as the Anisotropy Ratio [293], require mapping a high amount of data points [305, 306].

This analysis of heterogeneity in propagation is of great interest in clinical settings. A main focus could be the detection of impaired areas such as fibrotic tissue, given the fact that fibrosis disrupts the uniform propagation of the signals [262], thus causing an arrhythmogenic substrate. Its potential to identify arrhythmia drivers and therefore offer assistance in planning ablation procedures, is also a major clinical problem where this method could be useful.

Furthermore, major works have been recently proposed to understand and characterise the organisation of wavefront propagation based on intracardiac recordings. In particular, the study by Ganesan *et al.* [307] defines a novel metric coined as REACT to evaluate the size of the areas containing synchronised EGMs, shown to be predictive of ablation outcomes. Shortly afterwards, a similar analysis proposes Repetitive Atrial Activation Patterns (RAAPs), found to be associated with arrhythmia drivers [308]. This increasing interest in developing metrics to quantify cardiac organisation

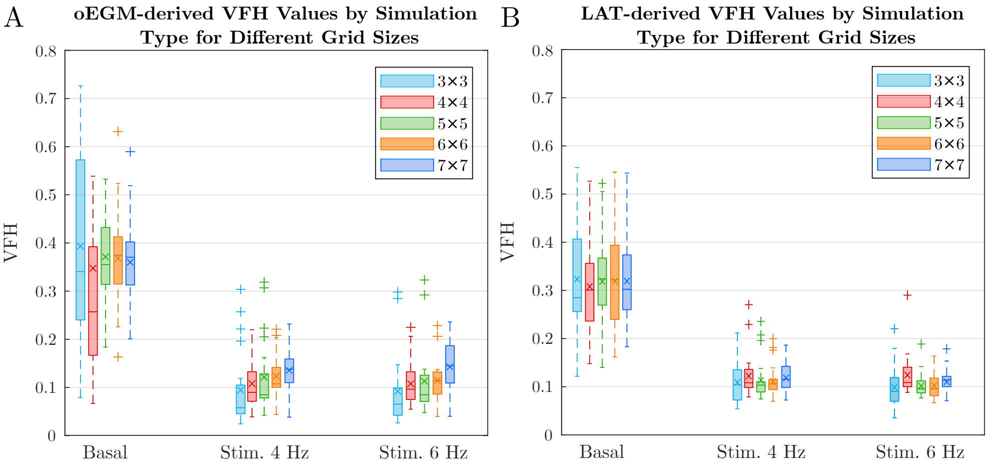

Figure 6.9: Box and whisker plots of the VFH values according to the type of stimulation. Results for different catheter sizes are shown; **A.** Application of VFH metric to omnipolar-derived vector maps; **B.** Application of the metric to LAT-derived vector maps.

highlights the relevance of prior tissue characterisation for better planning and guidance of cardiac interventions.

6.5.1 Limitations and future work

The retrospective nature of the experiment, together with the quality selection of the recordings, has resulted in a restricted sample size for the experimental data set. Additionally, epicardial signals may fail to capture the EP reality of intracardiac propagation. Nevertheless, the statistical analysis produced encouraging results which will likely improve by expanding the data set, preferably using intracardiac signals from larger animal species that better resemble the physiological characteristics of the human heart.

With respect to the simulation model, its design focuses on generating propagation maps specifically for the VFH metric, thereby limiting the ability to test alternative metrics that are not defined on vector maps. A more complex model, capable of producing propagation patterns based on activation times or synthetic EGMs, would enable the evaluation of the SI index using simulated data. By employing this alternative model, it would be possible to compare the behaviours and trends of both metrics, providing a more comprehensive analysis for validation purposes.

The success of the VFH to quantify disorganised patterns in this specific application suggests that this metric could be valuable in other applications related to vector fields. Indeed, vector field analysis has been applied not only to the characterisation of bio-electrical field patterns but also to problems related to magnetic flux [309], wave propagation and fluid flow [310, 311], among others. Whereas the most common parameters employed in vector field analysis involve divergence and curl, which aim to find organised patterns such as whirls [298] and focal sources [155] or sinks [312], the proposed parameter could well be proposed as a complementary metric that intends to detect disorganised and chaotic behaviours. Therefore, and for the sake of generalisability, future work focusing on the development of a theoretical framework of the VFH metric would be valuable. This should include its definition in a continuous form and its subsequent discretisation in an N-dimensional space. Additionally, its properties could be thoroughly contrasted with those of the well-established parameters divergence and curl to highlight their differences as well as their similarities, concluding with suggestions and indications of typical scenarios where to exploit the potential of VFH.

Future work could take the direction of implementing a versatile tool for quantifying heterogeneity in a wider range of vector field-related problems. We could then explore the potential applications of the VFH metric, such as its ability to differentiate between fibrotic and healthy tissue on the surface or through the cavities' wall.

An additional approach would be to explore the implementation of the metric beyond grid arrays. Since there exists a wide variety of catheters, incorporating the metric to the most commonly used types would enhance its applicability and potential. Thus, it is important to define the necessary adjustments and determine if comparable results are achieved.

6.6 Conclusions

Measuring the disorganisation of propagation vector maps presents a promising method for cardiac tissue characterisation. This study introduces the VFH metric to quantify such disorganisation. The success of the metric is demonstrated through its ability to discriminate between stimulated and non-stimulated epicardial tissue, as well as the characterisation of the progressive disorganisation observed in simulated maps. Furthermore, results indicate the superiority of the VFH metric to the SI index, a widely recognised heterogeneity metric from the literature. Ultimately, the proposed metric emerges as a reliable heterogeneity parameter suitable for its application on small HD grids to locally assess fibrotic or impaired cardiac tissue.

Software availability

The online version contains supplementary material available at `https://github.com/SamuelRuiperezCampillo/L_Pancorbo_S_Ruiperez-Campillo_et_al_IEEE-OJEMB_2024_HVF`

Chapter 7

Identification of Potential Ablation Targets for Ventricular Tachycardia Using a Novel Omnipolar-based Propagation Organization Metric

Abstract

Background and Objectives: The optimal approach to identify sites to target with ablation during ventricular substrate mapping for VT remains debated. Our study aims to evaluate the diagnostic utility of a novel propagation organization metric, the omnipolar-based local VFH, to differentiate functionally critical sites from bystander areas during ventricular substrate mapping to inform ablation strategy. **Methods**: We compared VT isthmus sites, low-voltage bystander areas (LVAs), and NVAs. The substrate maps from nine patients were segmented by domain-experts according to these sites, and the VFH metric was calculated for each region. **Results**: We performed statistical analyses of VFH values across the three sites, identifying statistically significant differences between each pair of regions ($p < 0.001$). The VFH mapping revealed a statistically significant increase in electrical heterogeneity at critical isthmus sites compared to LVAs and NVAs. **Conclusions**: The VFH metric is a promising new substrate mapping strategy to identify targets for catheter ablation in scar-related ventricular tachycardias.

This chapter is based on the publication: S. Ruipérez-Campillo et al. (2024). Identification of Potential Ablation Targets for Ventricular Tachycardia Using a Novel Omnipolar-based Propagation Organization Metric. *IEEE Computing in Cardiology Conference*.

An extension of this chapter was published following the completion of this thesis: J. Tonko*, S. Ruipérez-Campillo*, et al. (2024) Vector Field Heterogeneity as a Novel Omnipolar Mapping Metric for Functional Substrate Characterisation in Scar-related Ventricular Tachycardias. *Heart Rhythm* [313]. (* denotes co-first authorship)

7.1 Introduction

VT in patients with structural heart disease can be life-threatening and is most commonly secondary to a reentry mechanism [314]. Percutaneous catheter ablation is an established treatment modality to reduce the risk of VT recurrence and ICD shocks and has been proven to be more effective than medical therapy alone for this purpose [315].

Traditionally, activation and entrainment mapping of induced VTs have been proposed to identify critical sites to target with ablation. Yet, these approaches are frequently hampered by hemodynamic intolerance, unstable and/or changing VTs or non-inducibility [86].

Substrate mapping has emerged as an important alternative approach to characterize areas likely to support reentry based on EP characteristics that can be determined during stable sinus or paced rhythm. In previous studies, it has been suggested that this approach allows for the elimination of VT, irrespective of inducibility or hemodynamic tolerance. Some studies conclude that even for hemodynamically stable VTs, substrate mapping can be used to limit activation mapping or entrainment to a region of interest [174].

Detailed substrate characterization has been facilitated by widespread use and availability of high-density mapping technologies employing dedicated multipolar mapping catheters. Among these, the 16-pole HD Grid catheter has the advantage to offer a fixed electrode arrangement enabling uniform spatial sampling as well as the reconstruction of orientation-independent omnipolar EGMs (oEGMS), that have been reported to address some limitations of unipolar and bipolar EGMs [249]. Here we propose to apply recently developed heterogeneity metric based on intracardiac oEGMs to quantify and characterize abnormal propagation patterns and evaluate its clinical use during ventricular substrate mapping to identify targets for ablation.

7.2 Materials and methods

Study cohort

A cohort of 9 patients (64±18 years) with scar related VT who underwent clinically indicated catheter ablation involving substrate and VT activation mapping was considered. 77.8% had an ischemic etiology. The average left ventricular ejection fraction (LVEF) was 33% (±10). On average, 4.3 VTs (range: 1-8) were induced per case.

Contact mapping

A 16-pole grid catheter with a 4x4 arrangement of 1-mm equidistant electrodes and 3-mm interelectrode spacing was used alongside the EnSite NavX system. This system enabled acquisition of high-density substrate maps and VT activation maps from the patients with scar-related VT. Critical sites were identified based on VT activation maps and confirmed by either entrainment or VT termination with RF ablation. Subsequently, the corresponding substrate maps were segmented into isthmus-site, low voltage bystander areas (LVA, omnipolar voltage <1.5mV), and normal voltage areas (NVA, >1.5mV). The mean substrate map point count was 3825 ± 3190.

Pre-processing and activation window selection

Because unipolar EGMs can be very noisy due to common interferences such as far field, electromagnetic coupling, catheter handling and other interferences, a robust detection of the activation pulse is required. For this purpose, we employed a modified version of the so-called Botteron preprocessing steps, which firstly reduces noise outside the activation intervals by means of a Butterworth bandpass filter (6^{th} order, [40 Hz to 250 Hz]), followed by a rectification and low-pass filter (6th order Butterworth, cut-off 20 Hz) acting as an envelope detector. This processing sequence significantly reduces signal dynamics, highlighting the energy of the activation amidst other interferences [6,7]. The window of interest is selected based on intervals of maximal energy across all 16 electrode recordings.

Propagation wavefront vector

The direction of the propagation wavefront is estimated at clique level from the representation of the electrical field loop. Considering each clique as a square 2x2 electrode arrangement, a pair of orthogonal bipolar EGMs (bEGMs) $\mathbf{b}_1$ and $\mathbf{b}_2$ is derived according to a cross-configuration scheme of the clique. Following this approach, the bEGMs are computed from the subtraction of the unfiltered uEGM activations from the electrode pairs corresponding to the diagonals of the clique. This configuration satisfies the condition of spatial coincidence of the bipole pair, hence avoiding time misalignments of the activations, which are prone to occur when using a triangular clique [257]. To project the signals onto the $x - y$ coordinate system, a $\pi/4$ *rad* clockwise rotation is then applied to the diagonal bipoles:

$$\mathbf{b}(t) = \begin{bmatrix} \cos\left(\frac{\pi}{4}\right) & -\sin\left(\frac{\pi}{4}\right) \\ \sin\left(\frac{\pi}{4}\right) & \cos\left(\frac{\pi}{4}\right) \end{bmatrix} \cdot \begin{bmatrix} b_1(t) \\ b_2(t) \end{bmatrix} = \begin{bmatrix} b_x(t) \\ b_y(t) \end{bmatrix} \tag{7.1}$$

Over the course of a depolarization, the local E-field, formed by the perpendicular bipoles, $\mathbf{b}_x - \mathbf{b}_y$, creates the so-called bipolar loop. The loop's greatest magnitude corresponds to the direction of wavefront propagation [237] and is indicated by a unitary vector Γ located at the clique's centre. This vector

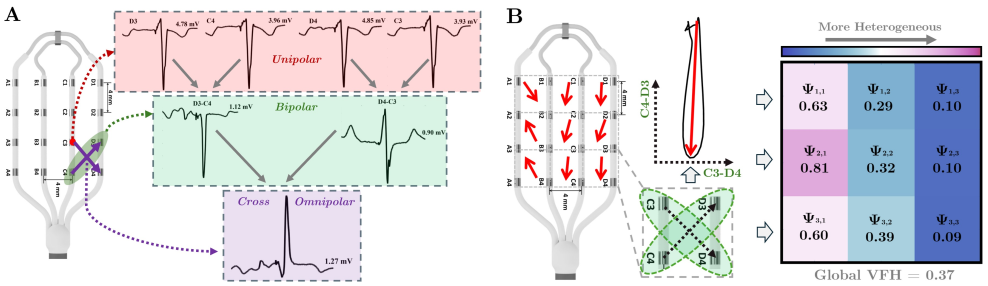

Figure 7.1: Cross omnipolar reconstruction. **A.** Illustration of a cross-omnipole from unipoles in the voltage domain. **B.** Example of the propagation direction estimation from oEGMs and VFH map reconstruction.

conforms an angle θ_o respect to the $x-$axis that is estimated according to the optimization function:

$$\theta_o = \arg\max_{\theta} \left[\frac{\max\left([\cos\theta \quad -\sin\theta]\,\mathbf{b}(t)\right)}{\max|[\sin\theta \quad \cos\theta]\,\mathbf{b}(t)|} \right] \tag{7.2}$$

The omnipolar EGM (oEGM) is then defined as the virtual bipole that would be obtained as if it would have been picked up from a pair of electrodes oriented in the direction of the propagation wavefront(see fig. 7.1). Accordingly, the oEGM es estimated as the projection of the E-field on the axis defined by the unitary vector Γ. The rotation that retrieves the oEGM $o(t)$ is:

$$\begin{bmatrix} o(t) \\ r(t) \end{bmatrix} = \begin{bmatrix} \cos(\theta_o) & -\sin(\theta_o) \\ \sin(\theta_o) & \cos(\theta_o) \end{bmatrix} \mathbf{b}(t) \tag{7.3}$$

with $r(t)$ being the residual component corresponding to the projection of the loop on an axis that is perpendicular to the direction of the propagation wavefront.

Vector Field Heterogeneity

For a 4×4 electrode grid and according to the definition of a clique, a 3×3 vector map is generated, displaying the propagation angle θ_o of the propagation wave on the tissue in contact with the catheter [277]. For each clique (i, j) the local VFH $\Psi_{i,j}$ was defined from the approximated partial derivatives which, in a discrete form, was defined from the finite differences between its propagation vector $\mathbf{u}_p$ and the propagation vectors at its neighboring cliques:

$$(\Psi)_{i,j} = \frac{\left(\frac{\Delta\Gamma}{\Delta x}\right)_{i,j} + \left(\frac{\Delta\Gamma}{\Delta y}\right)_{i,j} + \frac{1}{\sqrt{2}}\left[\left(\frac{\Delta\Gamma}{\Delta d_1}\right)_{i,j} + \left(\frac{\Delta\Gamma}{\Delta d_2}\right)_{i,j}\right]}{(\xi)_{i,j}} \tag{7.4}$$

where $0 \leq (\Psi)_{i,j} \leq 1$, which includes the finite differences not only from the horizontal and vertical axis, but also the diagonals d_1 (at $\pi/4$ rad) and d_2 (at $3\pi/4$ rad). Notice a reduced weighting factor for the diagonal components as the diagonal neighbors are more distant. Moreover, also notice the scaling factor $\xi_{i,j}$ to correct boundary effects at the edges of the multielectrode since fewer neighboring cliques are available. Finally, the VFH at the multielectrode level is computed as an average of the heterogeneity at all cliques:

$$\mathrm{VFH} = \frac{\sum_{i=1}^{p} \sum_{j=1}^{q} (\Psi)_{i,j}}{p \cdot q} : 0 \leq \mathrm{VFH} < 1 \tag{7.5}$$

Statistical analysis

To evaluate the performance of the VFH metric in the segmented regions, firstly we conducted pairwise comparisons using Welch's t-test, also known as the unequal variance t-test. The null hypothesis proposed that the VFH means between two regions are equal. Additionally, to control the Family Wise Error Rate (FWER), we applied the step-down Bonferroni procedure of Holm, correcting for multiple comparisons and providing multiplicity-adjusted values for significance. In addition, we employed Welch's alternative to one-way analysis of variance (ANOVA) to assess the equality of population means across the three different groups (isthmus, LVA, and NVA regions). Area under ROC curves (AUROC) were used to compare the VFH between regions. Data are presented as mean±SD unless stated otherwise.

7.3 Results

The value for the local VFH metrics were 0.56 ± 0.22 at sites corresponding to VT isthmus regions, 0.47 ± 0.26 at LVA, and 0.30 ± 0.25 at NVA. VFH at isthmus sites showed significantly higher values, indicating more disorganization, compared to LVA bystander sites ($p < 0.001$). Conversely, VFH was significantly lower in NVA, indicating more organization, compared to both isthmus and LVA sites ($p < 0.001$). These results are depicted in Table 1 and illustrated in fig. 7.2 (upper panels). Additionally, the Welch's F test shows that the associated probability is < 0.001, supporting the means to not be equal.

Further, we evaluated the ability of the local VFH metric to discern between the isthmus vs NVA, and LVA vs NVA. For isthmus vs NVA regions, the VFH metric achieved an AUROC of 0.78 and an accuracy of 0.71 for the optimal threshold. In the task of delineating LVA from NVA, the AUROC was 0.68, and the accuracy was 0.65. Additionally, qualitative examples of isthmus, NVAs and LVAs heterogeneity maps and their corresponding vector map for the cross-configuration are depicted in fig. 7.2 (lower panel), alongside with

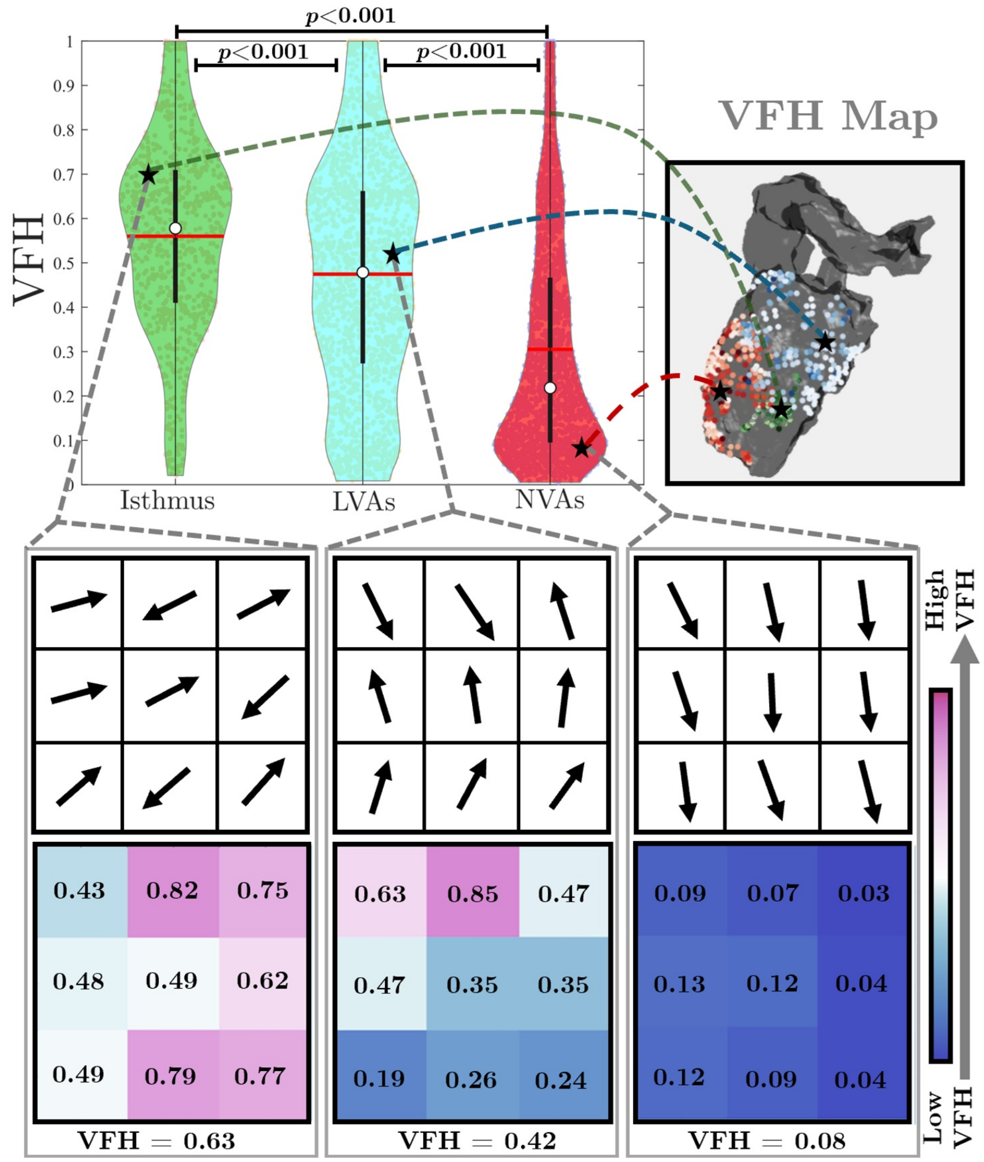

Figure 7.2: Upper panels: summary statistics and data distribution boxplots for local VFH by region of interest in N=9 VT patient recordings. The shape of the box illustrates the density data distribution. The red line indicates the mean value of local VFH for each category. Black bold lines indicate the interquartile range and white dots represent the median of the distribution. Lower Panels: Illustration of a patient in VT. Local heterogeneity and vector maps for: NVA isthmus site (right), LVA (center), isthmus sites (left) alongside the corresponding VT activation maps.

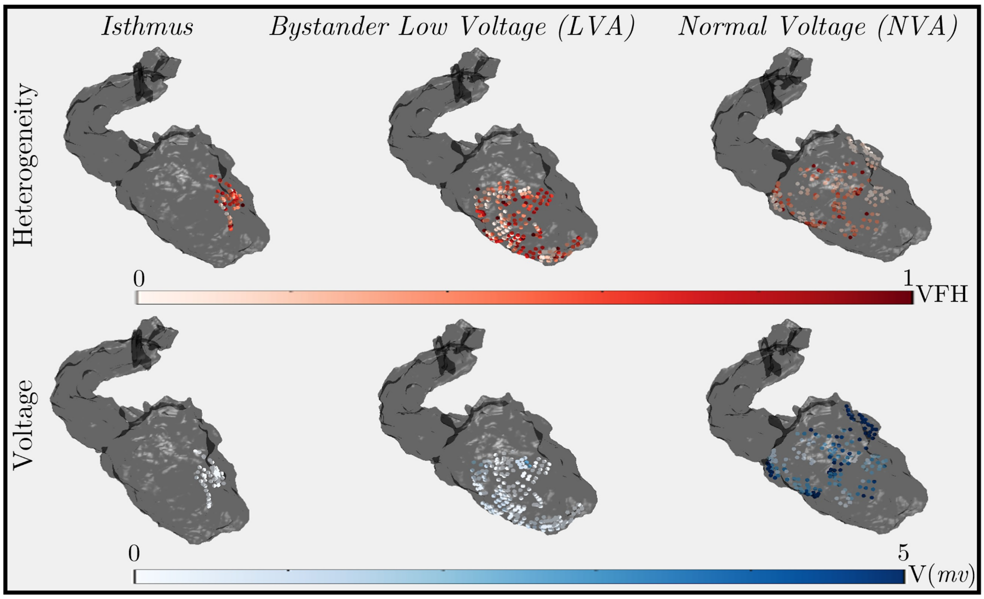

Figure 7.3: Illustration of VFH maps together with voltage maps for a patient with VT (male 64 y.o., ICM, LVEF 25%)

a 3D VFH map for that case. Further, fig. 7.3 depicts the local VFH values for the isthmus regions, LVA and NVA, along with the voltage maps for these regions in a VT patient (male, LVEF 25%).

Table 7.1: Summary of mean and SD of VFH values across different regions.

Region	**Mean ± St. Dev**	**Median [IQR]**
Isthmus	0.56 ± 0.22	0.58[0.30]
LVA	0.47 ± 0.26	0.48[0.39]
NVA	0.31 ± 0.25	0.22[0.25]

7.4 Discussion

In this study, we propose, in the context of a clinically relevant scenario, the validation of the local VFH, a heterogeneity metric based on vector field analysis to characterize the local EP substrate. Applying this approach to a clinical intracardiac mapping dataset acquired during routine clinical catheter ablation procedures for scar related VT using standard multipolar grid catheters, we were able to demonstrate a statistically significant increase in electrical heterogeneity at sites corresponding to the critical isthmus of the VT compared to bystander sites in ventricular substate maps. This supports the clinical value of VFH as a novel mapping strategy to identify critical sites to target with ablation. The VFH metric parameter is computed from omnipolar-derived vector could easily be translated and integrated into commercial mapping systems and complement existing approaches. While there are works aiming to characterize the organization of wavefront propagation based on intracardiac recordings (e.g. REACT [307], RAAPs [308]), we proposed the first approach based on vector field theory generalizable intracardiac recordings on grid catheters. Other possible clinical applications of the VFH metric, could be the identification of focal or rotational patterns, training further algorithms that relate VFH values to propagation patterns.

As any diagnostic tool, the accuracy is fundamentally linked to the quality of the data and presence of confounders. Initial in-silico validation of computational advanced mapping approaches often relies on idealized conditions. Yet, electro anatomical mapping data acquired in the context of clinical VT ablation procedures, that need to prioritize safe and time-efficient delivery of ablation therapy, often deviates substantially. Besides the clinical condition of the patient, sequential contact mapping technology itself is inherently affected by numerous confounders: Catheter movement as well as insufficient electrode-tissue coupling (“poor contact”), far-field signals, iatrogenic extra beats and electrical noise and artefacts all can interfere with the acquisition of in vivo cardiac signals. On the epicardial surface, presence of epicardial adipose tissue may further impact the EGM morphology. Lastly, the restriction to surface mapping does not allow to estimate the true complexity of the ventricular activation wavefronts in structurally abnormal hearts. On top of these, there are technical challenges such as the lack of ground truth to detect activation intervals in intracardiac signals, which may affect the computation of bipolar loops and the propagation direction estimation. Interpretating the diagnostic accuracy of the VFH metric for ventricular substrate mapping needs to take all the above limitations into account.

7.5 Conclusions

In this study, we introduced the VFH as an innovative approach for the analysis of intracardiac signal propagation using matrix-like catheters and vector field theory. Our application of VFH in the context of scar-related VTs demonstrates its potential in enhancing the accuracy of identifying critical isthmus sites for catheter ablation. The mapping outcomes have shown a statistically significant increase in propagation heterogeneity at these sites compared to LVAs and NVAs, suggesting that VFH could be used for targeting ablation sites without the necessity of inducing VT. Looking ahead, further research will focus on integrating VFH into existing intracardiac mapping systems and assessing its applicability to other cardiac conditions, such as AF.

Chapter 8

Quantifying a Spectrum of Clinical Response in Atrial Tachyarrhythmias Using Spatiotemporal Synchronization of Electrograms

Abstract

Background and Objectives: There is a clinical spectrum for atrial tachyarrhythmias wherein most patients with AT and some with AF respond to ablation, while others do not. It is undefined if this clinical spectrum has pathophysiological signatures. This study aims to test the hypothesis that the size of spatial regions showing repetitive synchronized EGM shapes over time reveals a spectrum from AT, to AF patients who respond acutely to ablation, to AF patients without acute response. **Methods**: We studied $n = 160$ patients (35% women, 65.0 ± 10.4 years) of whom (i) $n = 75$ had AF terminated by ablation propensity matched to (ii) $n = 75$ without AF termination and (iii) $n = 10$ with AT. All patients had mapping by 64-pole baskets to identify areas of repetitive activity (REACT) to correlate unipolar EGMs in shape over time. **Results**: Synchronized regions (REACT) were largest in AT, smaller in AF termination, and smallest in non-termination cohorts (0.63 ± 0.15, 0.37 ± 0.22, and 0.22 ± 0.18, $P < 0.001$). Area under the curve for predicting AF termination in hold-out cohorts was 0.72 ± 0.03. Simulations showed that lower REACT represented greater variability in clinical EGM timing and shape. Unsupervised machine learning of REACT and extensive (50) clinical variables yielded four clusters of increasing risk for AF termination ($P < 0.01$, χ^2), which were more predictive than clinical profiles alone ($P < 0.001$). **Conclusions**: The area of synchronized EGMs within the atrium reveals a spectrum of clinical response in atrial tachyarrhythmias. These fundamental EGM properties, which do not reflect any predetermined mechanism or mapping technology, predict outcome and offer a platform to compare mapping tools and mechanisms between AF patient groups.

This chapter is based on the publication: P. Ganesan, B. Deb, R. Feng, M. Rodrigo, S. Ruipérez-Campillo et al. (2023). Quantifying a spectrum of clinical response in atrial tachyarrhythmias using spatiotemporal synchronization of electrograms. *Europace*, 25(5), euad055. [307]. Requests, citations, or recognition should be directed to the first and last authors of this publication.

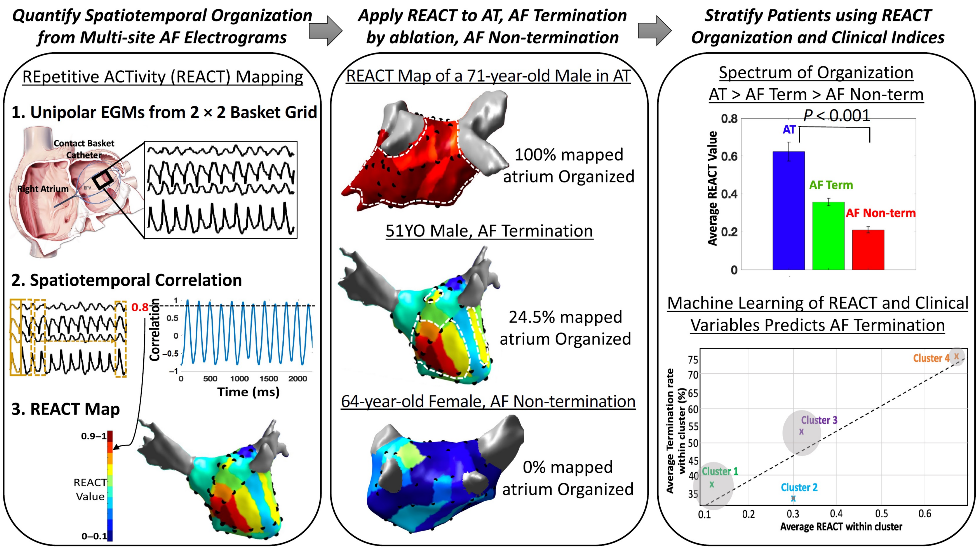

Figure 8.1: Abstract figure of the REACT metric and the current chapter.

8.1 Introduction

AF is the most common arrhythmia that affects about 30 million people globally and may cause hospitalization, heart failure, or stroke [316]. Early rhythm control of AF reduces morbidity and mortality compared to rate control. Nevertheless, the success of several approaches to ablation is ~50–70%, and it remains unclear which AF patients are more or less likely to respond or how to quantify differences in AF between patients.

It is observed that patients with AF may interconvert to organized AT [317], which is often easier to ablate, that some AF patients are easier to treat than others, and that they may have more organized AF [318]. Physiologically, patients with earlier AF not only show higher success from ablation than those with later stage AF [316] but also show less disorganized AF with fewer wavelets and lower spectral DF than later stage AF [316].

We asked whether (i) there is a pathophysiological spectrum of organization underlying both AF and AT and (ii) if this spectrum may improve upon clinical data to identify response to ablation. Several mapping studies to quantify AF organization have been reported, but produce controversial results and are difficult to verify clinically as they use complex mathematical constructs such as Fourier analysis or phase reconstruction [33]. These indices reflect specific mechanisms such as localized drivers [29], areas with high propensity to conduction block [319], or rapid sites (DF) [33], which also may not operate in all patients.

We reasoned that quantifying AF organization in an intuitive fashion that is not tied to a specific mechanism may improve its clinical utility. We hypothesized that atrial regions within which EGMs show similar shapes and are synchronized in time may be larger in AF patients with acute termination from ablation than those with poor acute response and may occupy most of the atrium in AT. This hypothesis provides a three-dimensional extension of concepts of repetitive EGMs in AF at one or two sites.[320, 321, 322]. We tested our hypothesis by developing an approach to map repetitive activity (REACT) areas, which we developed in patients with AT then applied to propensity-matched AF patients with and without acute termination by ablation. We then used machine learning (ML) to assess the additive value of this approach to predict ablation response over bedside features.

8.2 Methods

De-identified data used for this study will be made available from the authors upon reasonable request.

8.2.1 Patient recruitment and clinical electrophysiology study

The study was approved by our Institutional Review Committee, and all subjects gave written informed consent. We identified n = 219 consecutive AF patients (29% women, 64.2 ± 11.0 years) refractory to one or more Class I/III anti-arrhythmic drugs and n = 10 patients with AT (60% women, 59.7 ± 9.7 years) in the following groups:

1. n = 120 patients had acute AF termination by ablation ('term' group).
2. n = 99 in whom ablation did not terminate AF ('non-term' group).
3. n = 10 patients with AT and a prior history of AF, in whom ablation terminated AT.

Patients in Groups 1 and 2 were propensity matched 1:1 based on age, sex, and type of AF (paroxysmal and non-paroxysmal) yielding n = 75 patients per group. Of patients in the term group, n = 7 underwent only pulmonary vein isolation (PVI) and the rest had PVI and ablation of sites identified by a commercial mapping system (Focal Impulse Rotor Modulation or FIRM). All patients in the non-term group had PVI and targeted ablation. Differences before and after matching are reported in Supplementary material, table E.1 S1.

For robust validation, AF patients were divided into training and test sets in a five-fold cross-validation approach that maintained 1:1 propensity matching.

8.2.2 Electrogram recording and pre-processing

Electroanatomic mapping was performed using NavX (St. Jude Medical, MN) that incorporated data from 64-pole multipolar (basket) catheters (Abbott, IL). Basket catheters offer a practical approach for global mapping despite their limitations, and several groups report ~75–80% coverage of the atrium with contemporary designs [323]. Signals were recorded on Bard or Pruka recording systems and bandpass filtered 4-s segments of 1-min recordings of EGMs from the left atrium (LA). We used a 60 Hz notch filter, subtracted a mean QRS complex, and filtered high frequency noise using a fourth order Butterworth bandpass filter (2.5–250 Hz).

8.2.3 Identification of regions of repetitive activity

Our premise was to characterize spatial zones in which EGMs showing REACT synchronized 1:1 in shape over time (REACT). We sampled EGMs in 2×2 electrode grids corresponding to atrial areas of ~ 0.5 cm^2 (fig. 8.2.A) then determined the cycle length (CL) of these four EGMs using the interval between autocorrelation peaks corresponding to the 0th and 1st lag. We defined a one-beat template that spanned this spatial group of four electrodes, duration t_0 = 90% median CL (red boxes in fig. 8.2.B and C), which we slid from 0 ms every 1 ms until its right edge reached 4000 ms. The Pearson function was used to generate a time series of correlations pooled across four electrodes.

Next, we identified consecutively repetitive segments and assigned this as a REACT score (0–1). This process was repeated for all 2×2 sites and all 4-s segments within 1 min. The 4-s map with the highest median REACT was selected and compared to the mean REACT across the minute as summarized in fig. 8.4.C. Figure 8.2.D shows persistent AF in a 51-year-old Caucasian man, in whom higher colour-coded REACT values indicate greater repetition in EGM shape and timing (spatiotemporal similarity or synchronization). We converted 2D median REACT maps to 3D using (x, y, z) coordinates of each electrode from NavX (fig. 8.2.D).

We applied this approach to our cohort of three patient groups. We systematically assessed:

1. Global organization: by averaging the REACT value of the entire map.
2. Regional organization: defined as the total area of atrial islands with REACT equal or higher than average of AF cases (0.6), as % mapping field of 2D approximation of 3D basket.

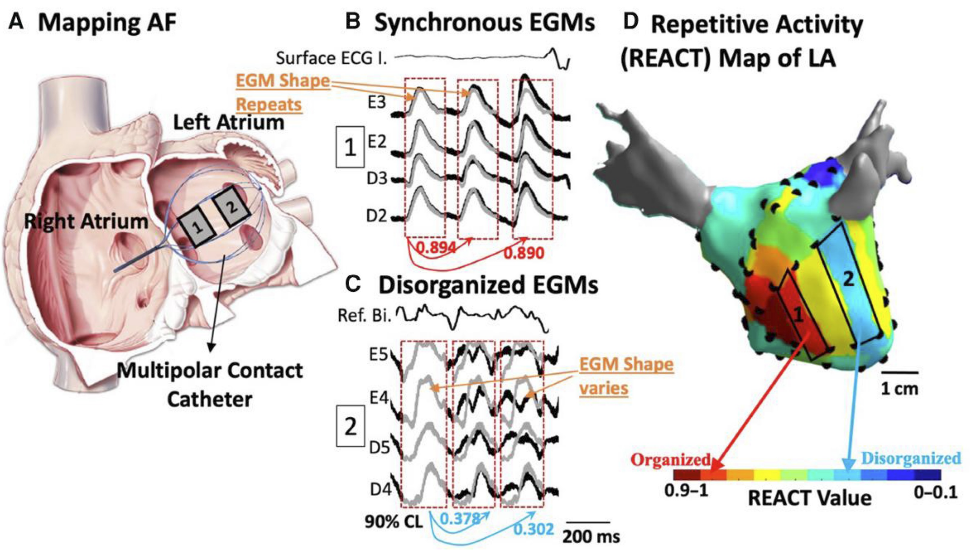

Figure 8.2: Quantifying EGM synchronization by REACT mapping: **A.** mapping in LA using 64-pole contact basket catheter, labels '1' and '2' indicate 2 × 2 electrode groups; **B.** EGMs from 2 × 2 electrode region '1' shows template (grey) repeating synchronously for consecutive cycles (black); **C.** disorganized EGMs where template (grey) does not repeat in successive cycles (black); **D.** 3D visualization of REACT map showing colours matching the correlation value. AF, atrial fibrillation; CL, cycle length; ECGI, electrographic imaging; EGM, electrogram; LA, left atrium; REACT, repetitive activity.

8.2.4 Identifying physiological variations underlying repetitive activity values

We started with 1:1 organization from paced rhythm, selected to avoid subtle biological variations, at cycle length 650 ms to avoid rate-dependent slowing or EGM fractionation. To this REACT map (1.0 at all sites), we introduced calibrated variations in EGM shape (% difference) or timing (in milliseconds).

Electrogram shape was varied by adding random white Gaussian noise of increasing root mean square (RMS) value. Variation was quantified as the Pearson correlation between noisy and original EGMs. Timing was varied by shifting each activation by a random time interval sampled from a 0 mean Gaussian distribution, with SD increasing from 0 to 80 ms (selected to ensure that no 2 activations overlap). Repetitive activity values for each instance of simulated variations was repeated for 100 trials, and their mean used to create a nomogram calibrating REACT to EGM variability.

The fully automated REACT code is available for researchers to analyse their data and as a platform to compare AF metrics `https://github.com/NarayanLab/REACT_Mapping`.

8.2.5 Unsupervised machine learning of repetitive activity and clinical variables

We used unsupervised ML to study if REACT added to clinical data in predicting AF ablation response. We applied k-means clustering on 50 clinical characteristics (see Supplementary material, table E.2) plus global REACT in the n = 150 AF patients. Dimensionality reduction with factor analysis of mixed data algorithm was done prior to using k-means. The optimal value of k was determined automatically using the elbow method [322]. We assessed (i) the quality of cluster using the Silhouette index [322] and (ii) average REACT vs. the termination rate of patients within each cluster.

8.2.6 Statistical analysis

Continuous data are represented as mean ± SD unless otherwise indicated. For validation of the ability of REACT to predict clinical events, we randomly divided the 75 propensity-matched pairs of AF patients into 5 sets of 15 pairs (30 patients). Logistic regression was repeated five times, once for each of the five holdout test sets and the area under the ROC curve (AUROC) was reported for each run, and as a mean across the five sets. Quantified results among the three patient groups were compared using chi-squared test, analysis of variance (ANOVA), and Kruskal-Wallis test if not normally distributed. Chi-squared test was used to distinguish between patient clusters identified by unsupervised ML of REACT and clinical variables.

8.3 Results

8.3.1 Patient demographics

Table 8.1 summarizes baseline characteristics in Groups I (AT), II (AF term), or III (AF non-term). Groups did not differ significantly in any characteristic. Patient characteristics before and after propensity matching are provided in Supplementary material, table E.1.

8.3.2 Islands of electrogram similarity

Figure 8.3.A shows the LA during typical right AFL in a 71-year-old man. Repetitive activity maps show high organization throughout the LA as expected. At multiple sites, REACT values vary from 0.84 to 0.99 with all sites showing REACT ≥ 0.84 indicating high EGM similarity (maximum REACT = 0.96 for the 2 is illustrated). The average REACT in AT cases (0.63 ± 0.15) was to guide a cut point of 0.6 to separate regional AT-like organized islands from disorganized activity during AF. Ablation at the right atrial tricuspid

Table 8.1: Baseline characteristics

Variable	AT (n = 10)	AF termination (n = 75)	AF non-termin. (n = 75)	*P* value
Age, years	59.7 ± 9.7	65.5 ± 10.4	65.1 ± 10.3	0.224
Gender, female, % (n)	60 (6)	34.7 (26)	32 (24)	0.218
+AF duration, years	N/A	4.5 (6.6)	3.1 (5.5)	0.153
Non-paroxysmal AF, % (n)	N/A	69.3 (52)	69.3 (52)	1.000
Persistent, % (n)	N/A	62.7 (47)	65.3 (49)	
Long-standing persistent, % (n)	N/A	6.7 (5)	4.0 (3)	
Previous AF ablation, % (n)	30 (3)	48 (36)	33.3 (25)	0.149
LVEF, %	59.6 ± 8.4	56.8 ± 9.8	55.9 ± 9.4	0.527
LA size, mm	41.9 ± 4.6	40.5 ± 5.7	41.5 ± 6.5	0.555
*Myocardial infarct, % (n)	0 (0)	2.7 (2)	4 (3)	0.649
Hypertension, % (n)	50 (5)	77.3 (58)	71.2 (56)	0.177
*Diabetes Mellitus, % (n)	0 (0)	20 (15)	18.7 (14)	0.836
*CAD, % (n)	0 (0)	14.7 (11)	17.3 (13)	0.656
TIA/stroke, % (n)	20 (2)	8 (6)	10.67 (8)	0.477
CHAD2SVASC	1.9 ± 1.6	2.6 ± 1.5	2.6 ± 1.6	0.330

isthmus successfully terminated flutter. This patient is free of arrhythmias at > 1 year.

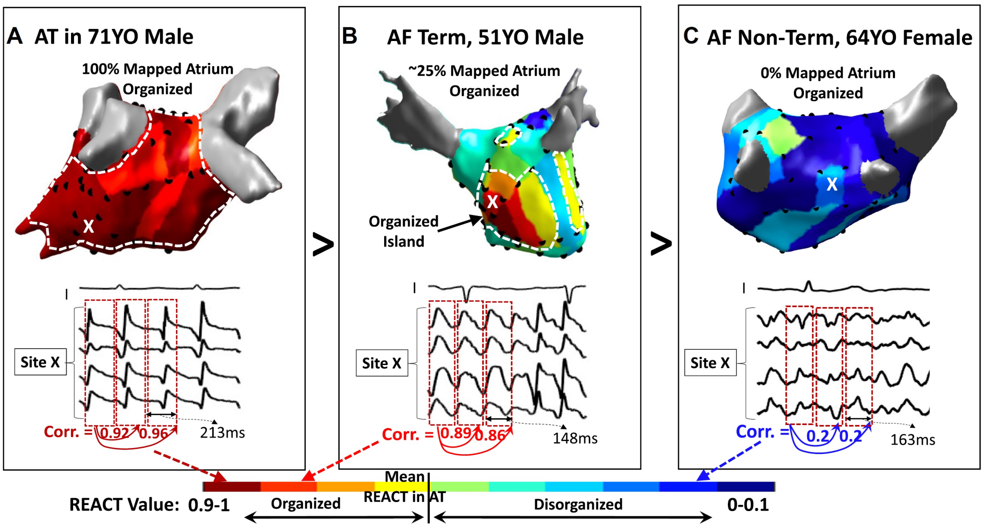

Figure 8.3: Atrial arrhythmias fall along a REACT spectrum that indicates treatment response: REACT falls progressively from a patient with AT (**A**), to a patient with AF in whom ablation was acutely successful (**B**), to a patient with AF who required cardioversion to restore sinus rhythm after ablation (**C**). AF, atrial fibrillation; AT, atrial tachycardia; REACT, repetitive activity.

Figure 8.3.B shows a 51-year-old man with persistent AF for 21.7 months despite amiodarone and cardioversions, at index ablation. There is an organized island of high REACT value (≥ 0.6) spanning 12% of mapped atrium, surrounded by moderately organized regions (0.6 < REACT ≤ 0.8). Using a median of REACT ≥ 0.6, this patient's EGM islands occupy 24.5% of the LA. Ablation at the posterior inferior wall terminated AF.

8.3.3 Islands of electrogram similarity: global and regional

Figure 8.4 summarizes global EGM similarity (REACT) for all $n = 160$ patients. A spectrum is revealed from AT patients with the highest EGM synchronization, followed by AF term and then non-term (fig. 8.4.A, 0.63 ± 0.15, 0.37 ± 0.22, and 0.22 ± 0.18, $P < 0.001$, ANOVA).

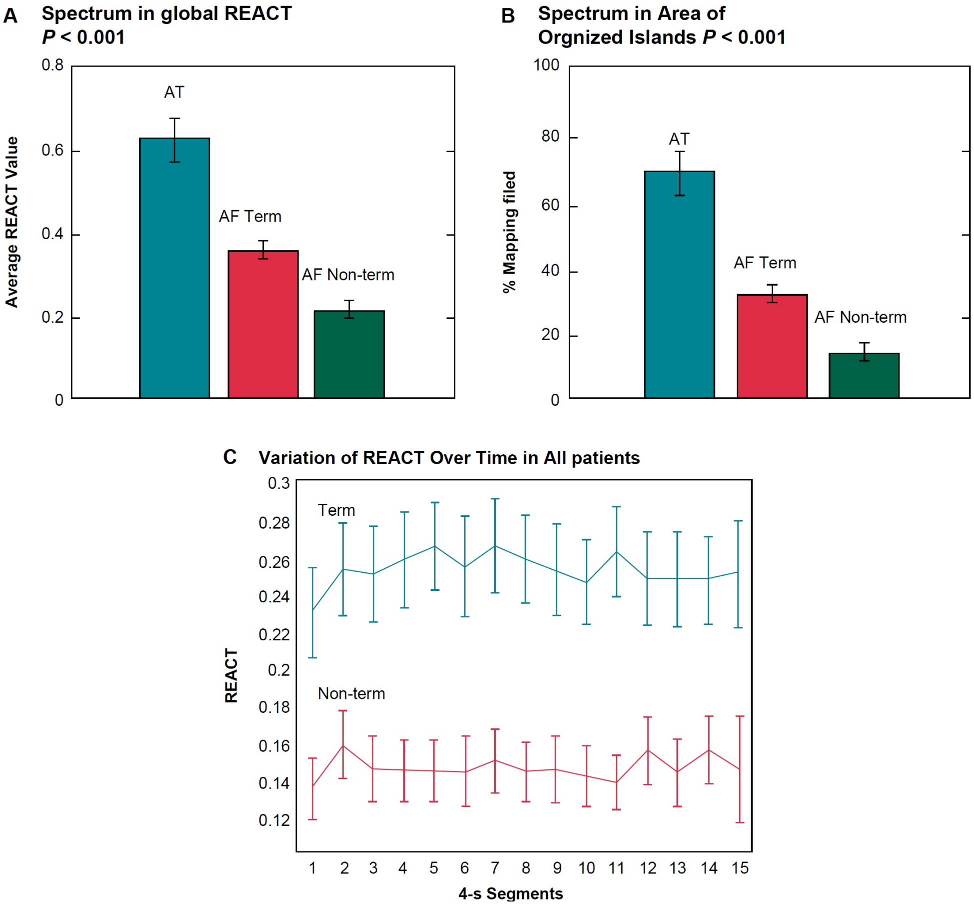

Figure 8.4: Spectrum in organization and temporal analysis: decreasing organization between patients with AT, AF termination, and AF nontermination both (**A**) globally and (**B**) regionally, indicating a spectrum in phenotypes of arrhythmia type and treatment response. Error bars indicate standard error. (**C**) Variations in global REACT over 1 min in all $n = 150$ AF patients; REACT was significantly higher for patients with term than nonterm at all timepoints over a minute ($P < 0.001$). Thus, REACT measured globally across the entire atrium for any one 4-s interval reflects variations over 1 min and robustly separates response to AF ablation. AF, atrial fibrillation; AT, atrial tachycardia; REACT, repetitive activity.

A spectrum was also observed in regional organization (islands with REACT ≥ 0.6). Patients in AT had the largest area of organized islands (e.g. fig. 8.3.A), followed by patients with AF that terminated by ablation (labelled in fig. 8.3.B), then those with AF who did not terminate (labelled in fig. 8.3.C;

in fig. 8.4.B: 68.7 ± 23.2%, 31.5 ± 32.0%, and 14.2 ± 22.1%, $P < 0.001$).

The maximum REACT value of a 4-s EGM segment in each patient was highly correlated with the arithmetic mean of REACT over the entire 1 min of AF ($R^2 = 0.83$, $P < 0.001$). Over 1 min, mean and SD of REACT (i.e. 15× 4-s segments) were 0.25 ± 0.009 and 0.15 ± 0.007 for term and non-term groups, respectively (fig. 8.4.C). Thus, REACT measured globally across the atria is robust to the changes observed over time and separates groups.

8.3.4 Clinical phenotypes based on islands of electrogram similarity

Global REACT values were higher in AF patients with vs. without termination (0.37 ± 0.22 vs. 0.22 ± 0.18, $P < 0.001$). Figure 8.5 presents ROC of global REACT values for predicting AF termination, with an AUROC of 0.72 ± 0.03, positive predictive value of 0.67 ± 0.08, sensitivity of 0.59 ± 0.13, specificity of 0.71 ± 0.12, and F_1 score of 0.62 ± 0.08. The AUROC was higher for patients with non-paroxysmal AF ($n = 52$ term, $n = 51$ non-term) than paroxysmal AF (0.72 vs. 0.64, Supplementary material online, fig. E.2), but this difference was not significant.

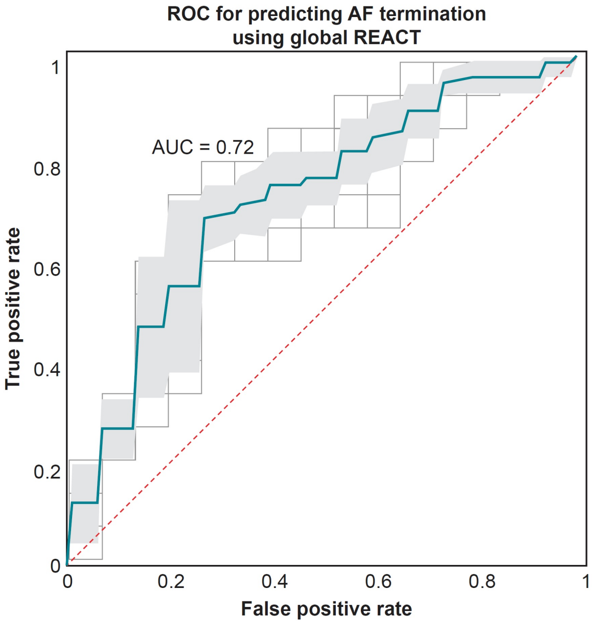

Figure 8.5: Receiver Operating Curve (ROC) of REACT organization for predicting AF termination: figure indicates ROC curves five-fold cross-validation of global organization values obtained using REACT. Mean AUROC was 0.72 indicated by the solid blue line, the grey lines are each cross-validation ROC, the grey shaded area indicates confidence intervals, and the red dotted line indicates a reference of AUROC = 0.5. AF, atrial fibrillation; AT, atrial tachycardia; AUROC, area under the curve; REACT, repetitive activity; ROC, receiver operating characteristics.

8.3.5 Calibrating repetitive activity value to physiological electrogram variations

Figure 8.6 calibrates REACT to variations in EGM shape and timing. Decreasing values of REACT ($P < 0.05$) represent increasing variability in EGM timing (variability 10, 30, and 35 ms) and shape (variability 0.2, 0.2, and 0.3) for patients with AT (black 'X'), AF termination (white 'X'), and non-termination (white '+'), although this did not reach significance. Thus, while REACT separated groups based on variable EGM shape and timing, other factors may operate clinically.

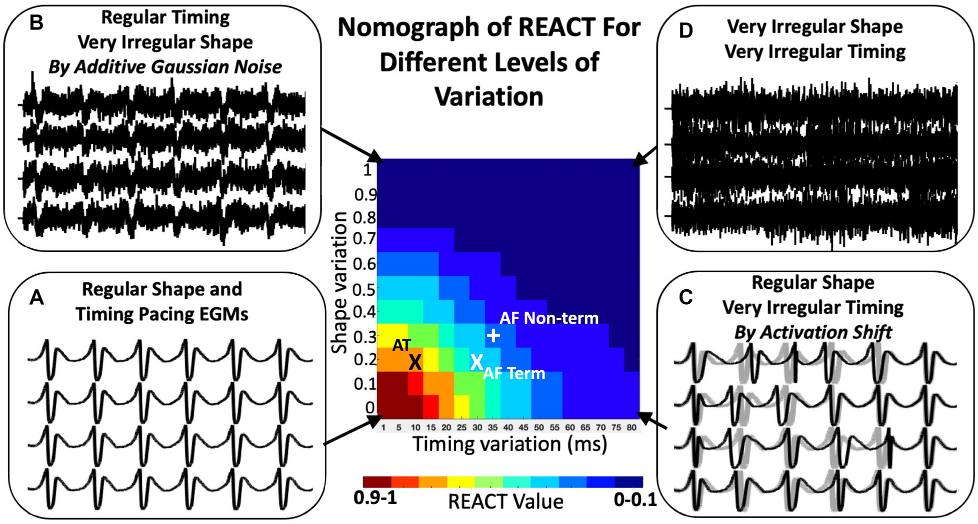

Figure 8.6: Physiology nomograph of REACT: to perfectly regular (**A**) pacing EGMs, variations in (**B**) shape and (**C**) timing were introduced, and REACT value was calculated as average of 100 random variations in (**D**) each shape and timing combination to obtain the nomograph (centre panel). EGM, electrogram; REACT, repetitive activity.

8.3.6 Clinical phenotypes identified by machine learning

We studied if combining REACT with clinical data would better separate AF ablation response. Unsupervised k-means clustering of REACT and 50 clinical variables (listed in Supplementary material, table E.2 resulted in an optimal value of $k = 4$. The clusters from 51-dimensional datapoint projections onto the first two principal components are illustrated in fig. 8.7.A. The cluster silhouette index was 0.41 (range −1 to 1), indicating good cluster quality. $n = 100$ patients with random initializations showed that REACT with clinical variables was more predictive than clinical variables alone (Silhouette index 0.411 ± 0.001 vs. 0.336 ± 0.003, $P < 0.001$). Rates of AF termination were significantly different between clusters ($P < 0.01$, χ^2; fig. 8.7.B) and directly proportional to REACT in three out of four clusters.

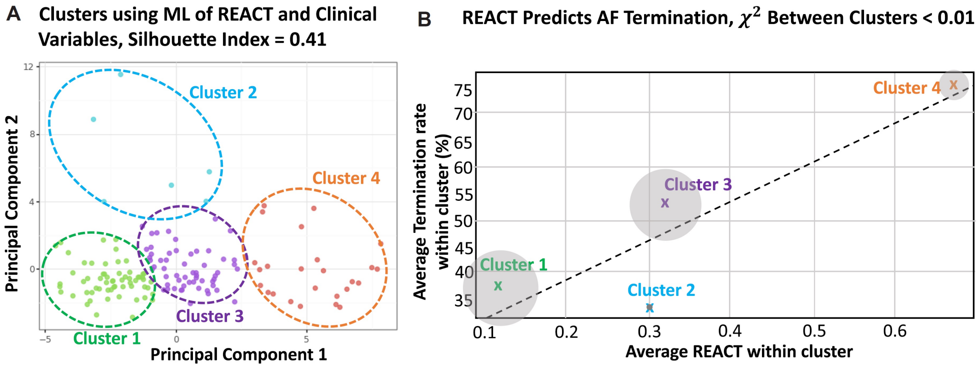

Figure 8.7: Unsupervised ML of REACT and clinical variables: **A.** four clusters found using ML of REACT, and **B.** clinical variables showed a trend for predicting termination rate. The size of grey circles in **B** is proportional to the size of samples within the cluster. AF, atrial fibrillation; ML, machine learning; REACT, repetitive activity.

8.4 Discussion

In this global mapping study of patients with AF, the spatial area within which EGMs were synchronized in shape over time revealed a therapeutic spectrum for atrial arrhythmias. Electrograms in AT were synchronized across the entire atria, as expected. In patients with AF, areas showing synchronized EGMs were larger in patients with termination by ablation than in those without AF termination. We show that REACT fell monotonically with increasing variability in EGM timing (in milliseconds) or shape, providing a physiological calibration for our findings. Finally, ML of REACT and clinical data predicted ablation response better than clinical data alone. Thus, this approach revealed fundamental EGMs properties in atrial arrhythmias independent of any specific mechanism that separated AF patient types by ablation response and may enable comparison of different AF mapping tools.

8.4.1 Metrics of atrial fibrillation organization and disorganization

Repetitive activity features AF organization beat-to-beat by millisecond timing in EGMs and changes in EGM shape, as shown in our nomograph (fig. 8.6). Temporal AF organization has previously been reported as consistent rate, spectral DF, or narrowness of the DF peak (indicating greater organization) [33]. Spatial AF organization has been studied by spatial dispersion of EGMs indicating driver regions [324] or by direct mapping of organized rotational and focal drivers [29]. Spatial disorganization in AF has been reported in the multiple wavelet hypothesis [325], endo-epi dissociation [319], fractionated EGMs [325, 326], and stochastic modelling using renewal theory.

While the mathematical approach to these prior tools varies, our approach uses a simple 'similarity' measure that is visually apparent and combines both spatial and temporal components.

8.4.2 Mechanisms for synchronized sites

Repetitive activity avoided any specific definition of AF sites of block, [319] breakthrough [325], rotational or focal drivers [29], organization around scar, or other mechanisms, which are difficult to verify in patients, may differ between AF patients, and are thus controversial [327]. Accordingly, our approach may provide a platform to compare or even calibrate multiple AF mapping tools such as those reported by Ablacon Inc., Wheat Ridge, CO, USA; CardioNXT, Westminster, CO, USA; Cartofinder, Biosense Webster, Irvine, CA, USA; and Acutus Medical Inc., Carlsbad, CA, USA, to identify features that may or may not support a driver [12].

The slightly higher AUROC for non-paroxysmal vs. paroxysmal AF patients may indicate that EGM features in the left atrial body are more indicative of phenotype for non-paroxysmal AF, while for paroxysmal AF, the most critical features could lie within PVs. This in turn could reflect differences in stability of organized regions, the presence of endomysial fibrosis that, rather than overall connective tissue content, is the main determinant of conduction disturbances in human AF [328] and other features of structural remodelling.

8.4.3 Previous reports of repetitive activations in atrial fibrillation

The present study spatially extends prior studies that examined repetitive activation in small regions (1–2 EGMs sites) and may not have linked those analyses to treatment response.

Zeemering et al. [329] reported repetitive activation in a goat model of AF using a high-density narrow field-of-view approach and showed greater organization in early AF (3 weeks) than late AF (22 weeks). Interestingly, while REACT differed between patients with and without ablation response, they did not reflect AF duration (similar for patients with and without termination in table 8.1). Spatial organization may thus represent a marker for disease progression distinct from AF duration. Lin et al. [321] recently reported recurrence plots of AF EGMs, with higher ablation success when targeting sites identified by single sites of EGM similarity. Our results extend this approach by considering four spatially contiguous channels and by identifying consecutive repetitions. Others studied repeating EGMs in AF at one [320] to two [322] sites and apply unsupervised ML [322] to classify EGMs with similar patterns.

Our group (Bhatia et al. [330]) previously identified consistent vectorial regions in patients with persistent AF, where we detected 1:1 repetitive spatial areas with rotational and focal patterns. Ablation in larger areas terminated AF. The concept of large areas of repetitive patterns is consistent with this study, although REACT indicates fundamental EGM properties that do not assume definitions of rotational or focal patterns. We are working on studies to overlay REACT and vectorial analyses and identify concordance and differences.

8.4.4 Prior studies linking atrial tachycardia and atrial fibrillation

Multiple groups have shown overlap of critical sites between AF and AT. Spatial concordance was recently shown using spatiotemporal EGM dispersion between AT locations and AF driver sites [331]. Previously, Baykaner et al. [317] using basket recordings, and Yamashita et al. [318] using electrographic imaging (ECGI), showed that AT in patients with AF arose at sites that also had harboured ablation termination sites for AF. Our study further advances this concept by revealing how AT-like regions in AF may affect AF treatment response.

8.4.5 Clinical utility of repetitive activity

The computational approach to calculate REACT is fully automated. This could be extended a priori to predict poor responders to ablation by applying it to non-invasive ECGI. As a proof of concept, we have recently shown spatial and temporal concordance in AF indices mapped by ECGI and AF maps acquired inside the heart [332]. Another potential utility of our study is to improve ablation outcomes by determining if sites show organization akin to these 'AT islands', which may respond to additional ablation. Repetitive activity could also be used to distinguish sites with features supporting a driver or passive sites identified by existing mapping approaches such as electrographic flow [325], FIRM (focal impulse and rotor mapping), or spatiotemporal dispersion [324].

8.4.6 Limitations

Our approach focuses only ~ 0.5 cm^2 regions (2×2 electrode), and we are exploring the sensitivity and specificity of larger areas (e.g. 3×3 electrodes). Functional features such as entrainment were not assessed and indeed may not be possible in AF. Area of organized islands was calculated in 2D then scaled to 3D that could introduce small errors, although the organization spectrum was also seen globally (fig. 8.4.A). Our nomogram of shape and timing variations (fig. 8.6) assumes Gaussian distributions that may not reflect clinical variations in AF EGMs but does support the physiological basis of REACT. We have not used these maps prospectively, nor to guide ablation. Such studies are planned and are made possible by others using our freely available code. Ongoing studies will examine potential mechanisms for organized regions including focal or rotational sites or repetitive activations of other spatial patterns representing active or passive activation from other AF mechanisms [325]. We will answer a key question, that is, whether mechanisms differ between patients and whether this could be identified by ML that includes clinical features.

8.5 Conclusions

We developed tools to identify an intuitive signature of organized activity in AF, indicating islands that show similar EGM shapes over time. This approach revealed global organization in patients with AT, large islands in patients with AF and good response to ablation, and small regions in patients with AF and poor response. Using ML, these features better predicted ablation response than existing clinical metrics. This approach, which does not rely upon a specific mechanism, may provide a platform to compare the results of different AF mapping tools and may help guide ablation.

Data availability

De-identified data used for this study will be made available from the authors upon reasonable request. The fully automated REACT code is available online (`https://github.com/NarayanLab/REACT_Mapping`).

Chapter 9

Discussion

This Chapter discusses the outcomes of the research of this doctoral thesis, reflecting on how the objectives have been met and the initial hypotheses addressed. We delve into a comparison between non-invasive and intracardiac measurements, and explores the role of ECGi as a bridging technology. The discussion also critically examines intracardiac recordings, the advantages of omnipolar technology, and validation of the cross-omnipole in both animal and clinical studies, while offering insights into electrode configurations for array catheters. Finally, it highlights the clinical implications of omnipolar technology in detecting local electrical disarray and closes with a discussion on conduction patterns, limitations, and future research directions.

9.1 Achievement of thesis objectives

In reference to the objectives outlined in section 1.2, we can assert that the overarching goal of exploring the potential of high-density catheters combined with advanced signal processing techniques to better characterize arrhythmogenic tissue has been successfully addressed. Below, we evaluate the extent to which each specific objective has been achieved.

Regarding the first objective, the limitations of multielectrode catheters for omnipolar estimation have been thoroughly investigated. This is demonstrated in chapter 4, where all current triangular-clique configurations were assessed theoretically in controlled simulation environments. Additionally, chapter 5 explores these configurations' limitations for omnipolar reconstruction in an animal model, providing further validation. A comprehensive analysis of the impact of interelectrode distance on multielectrode catheter performance was also conducted in chapter 5, with findings contextualized against the existing literature.

Objective two, focused on proposing improved configurations for omnipolar EGM estimation, is achieved in chapter 4. This chapter introduces the cross-clique configuration, a novel approach that reconceives the omnipolar EGM as a virtual bipolar EGM aligned with the direction of propagation. This new configuration demonstrates superior performance compared to the triangular-clique configurations prevalent in current practice. The mathematical underpinnings of this approach were established and validated in simulation studies in chapter 4, with further validation on EP signals from animal models detailed in chapter 5.

Building on the foundation laid by objectives one and two, objective three is addressed in chapter 6, where a novel metric for quantifying conduction heterogeneity in propagation maps is developed and rigorously characterized.

For objective four, which aimed to investigate conduction patterns from a global perspective, chapter 3 provides the groundwork, while the metric derived in chapter 8 is used to examine spatio-temporal electrical disarray through global mapping techniques.

Finally, the translation of these methodologies into clinical practice, corresponding to objective five, is fulfilled in both chapter 8 and chapter 7. These chapters demonstrate the application of local and global heterogeneity metrics (developed in objectives three and four, based on the concepts from objectives one and two) in clinical settings. Specifically, chapter 8 assesses the spectrum of organizational patterns in patients with AF and correlates these patterns with clinical outcomes. In chapter 7, the local propagation heterogeneity metrics are employed to identify areas of interest for ablation planning in patients with VT.

The thesis objectives have, therefore, been fulfilled to a broad extent, with some inherent limitations, which will be discussed later in this chapter.

9.2 Answering the initial hypotheses

In this section, we reflect on the hypotheses posed on section 1.3 at the outset of this dissertation, and evaluate the extent to which they have been confirmed or refined based on the findings of the research.

The first hypothesis stated that recordings from four electrodes arranged in a 2x2 square in high-density multi-electrode catheters could be used to reconstruct omnipolar signals, overcoming the limitations of current triangular omnipoles, bipoles, and unipoles, particularly in terms of orientation independence. This hypothesis has been confirmed through the results presented in chapter 4. Both theoretical and simulation studies demonstrated that the cross-clique configuration provides orientation-independent signals and performs better than traditional configurations. Experimental validation in an animal model, as shown in chapter 5, further supports the superiority of this configuration in omnipolar EGM reconstruction.

The second hypothesis posited that robust omnipolar signal representations could be used to create accurate propagation maps and design biomarkers to quantify the heterogeneity of electrical propagation patterns in patients with arrhythmias, with potential for substrate mapping in clinical settings. This hypothesis has been validated in part. The development of propagation maps based on the proposed omnipolar reconstruction successfully quantified local conduction heterogeneity and identified regions of interest chapter 6. Early clinical studies (chapter 7) have shown promise in correlating these metrics with regions of interest for ablation treatment in VT patients, though further work is needed to refine these biomarkers for broader clinical application.

The third hypothesis suggested that raw unipolar signals from global mapping catheters could be used to analyze spatio-temporal heterogeneity of propagation patterns, helping to identify clinical responses in patients with atrial or ventricular arrhythmias. This hypothesis has been supported by the findings in chapter 8, where spatio-temporal heterogeneity metrics were able to characterize the degree of disorganization in AF patients and correlate to clinical outcomes of interest. These results demonstrate that spatio-temporal heterogeneity may serve as a valuable tool for understanding the underlying mechanisms of arrhythmias and guiding clinical interventions.

In conclusion, the hypotheses proposed at the start of this thesis have largely been confirmed by the research findings. While hypothesis one was fully validated, hypotheses two and three may require further clinical validation to maximize their translational potential.

9.3 Non-invasive vs intracardiac measurements: can we do without one?

Arrhythmias and EP heart conditions are often diagnosed through non-invasive recordings. These are typically sufficient for diagnosis and initial treatment planning, particularly when the treatment involves only medication. However, non-invasive methods may not always be effective, necessitating further invasive procedures. In some cases, detailed mapping becomes essential to plan invasive treatments like ablation.

Despite extensive and frequently updated guidelines, significant variability remains in treatment approaches across the medical community. For instance, ablation procedures for AF vary widely between medical centers and even among clinicians within the same institution. In the study presented in chapter 3, we focused on AFL, a condition with somewhat more consensus within the scientific community. Although AFL can be caused by different macroreentrant circuits requiring varied ablation approaches, there is agreement on the most effective strategies for known circuits.

Many studies highlight the importance of non-invasive diagnosis using ECGs to identify the specific type of arrhythmia [ref]. In chapter 3, we propose a non-invasive identification method for subtypes of AFL, which can help target invasive treatments more precisely to the area of interest. Moreover, our study demonstrated differences in VCG morphology, as well as in time and distance fractions during low CV between CCW and CW variants of the same MRAT type. These findings suggest that these variants should be treated as distinct groups, raising further questions about the asymmetry of conduction patterns in macroreentry circuits, which warrant additional study in an EP setting. However, these findings should be considered cautiously, as accurately identifying atrial signals from non-invasive recordings can be challenging, especially when the atrioventricular conduction ratio is short (e.g., 2:1). While a single loop may suffice for analysis in patients with AFL due to the high consistency among loops, adenosine administration or carotid massage was often required to facilitate the recording of several contiguous loops of atrial activity. Nevertheless, the near-field precision of intracardiac recordings cannot be matched by non-invasive techniques.

Various methods have been proposed for non-invasively removing the ventricular component in AF, but they often fail with AFL. For instance, QRS-T cancellation algorithms [210, 231] may inadvertently remove atrial signals when they are coupled with ventricular activity. While Blind Source Separation methods [212] can isolate an atrial source, they fall short in reconstructing the VCG, as more than one component is needed. Other approaches, such as estimating and removing the T-wave in MRAT [214], have been proposed but have only been tested on synthetic signals and lack clinical validation. Improved algorithms, such as those utilizing spatial or temporal signal properties—like projective filtering [232] or Periodic Component Analysis (πCA) [233]—may be required.

All in all, while non-invasive recordings are crucial for preliminary diagnoses and treatment planning, they are insufficient even in well-defined arrhythmias like AFL. The EP community still relies on high-density invasive mapping to accurately determine arrhythmia patterns and plan ablation strategies. However, the valuable insights gained from non-invasive recordings should not be overlooked. With advanced signal processing techniques, as proposed in chapter 3, non-invasive methods can focus attention on critical regions of interest, potentially saving time and effort and aiding in the identification of key slow conduction areas in complex cases.

9.4 ECGi as a promising bridge

While traditional non-invasive methods such as surface ECGs provide important initial insights, they often fall short in the nuances of electrical conduction patterns on the tissue. This is where Electrocardiographic Imaging (ECGi) offers a significant advancement, narrowing the gap between non-invasive diagnostics and a higher precision required for invasive EP studies by mapping electrical activity on the heart's epicardial surface. This technique integrates multi-electrode body surface recordings with geometrical data from CT or MRI scans, enabling the non-invasive reconstruction of electrical potentials, EGMs, activation sequences, and repolarization patterns [333].

ECGi has proven particularly useful in mapping the cardiac substrate in various conditions with relatively high spatial resolution. For example, in hereditary arrhythmogenic syndromes such as Long QT syndrome (LQTS) and Brugada syndrome (BrS), ECGi has been able to identify abnormal substrates that are undetectable with conventional surface ECGs [334, 335]. In LQTS, it revealed prolonged and heterogeneous repolarization times, indicating a substrate for reentrant arrhythmias [336]. In BrS, ECGi differentiated between malignant and benign forms by mapping structurally-based abnormal conduction confined to the right ventricular outflow tract (RVOT) [335]. Moreover, ECGi has been effectively employed to map the electrical substrate of post-myocardial infarction scars, particularly in relation to VT. It identified critical features such as low EGM voltage and scar heterogeneity, which are key in differentiating patients with and without VT [337, 338].

However, despite its potential, ECGi is not without limitations. Its accuracy depends heavily on the quality of the body surface recordings and the geometrical data from imaging modalities, which can be influenced by patient-specific factors such as body habitus and the presence of structural heart disease. While ECGi provides valuable non-invasive insights, it cannot replace the precision of invasive intracardiac mapping, particularly in complex cases [333]. Additionally, further validation through larger clinical studies and technological advancements are needed before it can become a standard tool in cardiac EP [339, 340].

9.5 Intracardiac recordings: not all that glitters is gold

Intracardiac signal acquisition, though critical for guiding ablation and other interventions in the EP lab, is not without significant challenges. The environment is inherently noisy, with a multitude of devices such as ECG machines, pulse oximeters, and defibrillators contributing to leakage currents that interfere with both extracardiac and intracardiac signals. Additionally, patients themselves can act as antennas, picking up electromagnetic noise from surrounding equipment and wiring, further compounding the interference [341, 342]. These disturbances, along with motion artifacts from muscular and cardiac activity, create a highly complex setting for accurate signal acquisition [343]. Even though analog amplification and noise reduction techniques help in improving signal quality, they do not entirely eliminate the noise that complicates the interpretation of real-time recordings [344].

Moreover, the process of converting these analog signals into digital form introduces additional distortions. Quantization noise, aliasing issues due to inadequate sampling rates, and thermal noise arising from analog-to-digital conversion all degrade the fidelity of the recorded signals [345]. Despite advancements in both analog and digital signal processing, these persistent sources of noise often obscure critical details in the intracardiac recordings, making it difficult for electrophysiologists to extract meaningful insights during procedures [345]. As a result, achieving a high signal-to-noise ratio remains a significant technical challenge, particularly when the goal is to distinguish between true cardiac signals and unwanted artifacts. Thus, while intracardiac recordings provide invaluable insights, the development of new technologies, like those proposed in this dissertation, is crucial to overcome some of these limitations and enhance clarity during the EP procedures.

9.6 Omnipolar technology and the advantage of the cross clique

Proposed by Deno et al., the omnipolar EGM emerged as a novel method to characterize propagation patterns in the myocardium, offering a catheter-orientation insensitive approach for real-time high-density recordings [15]. This technique has shown promise in producing accurate voltage maps in complex AF patterns [18] and in successfully delineating infarcted areas both in vivo [22] and ex vivo [192] during ventricular mapping. These capabilities address the limitations of traditional bipolar and unipolar mapping methods. However, Riccio et al. [23] identified a key limitation in the triangular configuration proposed by Deno et al. [15, 17], revealing dependencies on wavefront propagation orientation that can affect voltage and velocity estimations, as well as tasks such as fibrosis detection.

In light of these limitations, chapter 4 introduces an alternative configuration to the triangular omnipolar approach: the cross omnipole. In the conventional triangular configuration, the geometric centers of bipolar EGM signals do not coincide, resulting in the propagation wavefront passing through these points at different times. This misalignment leads to significant errors in estimating the theoretical omnipole, even under idealized conditions with homogeneous and planar propagation patterns. While Riccio et al. [23] suggested that temporal alignment could mitigate these errors, challenges such as the lack of a reliable time reference may affect the accuracy of LAT and CV estimations.

The cross-clique configuration inherently avoids the need for temporal alignment, as the bipolar EGM centers are spatially aligned. This results in more precise and thinner bipolar loops, leading to more robust conduction propagation measurements compared to the traditional triangular approach. This finding aligns with the observation that averaging delayed pulses results in a wider pulse with lower amplitude [254]. Additionally, as demonstrated in chapter 4, the cross-configuration yields more accurate LAT estimations in our simulation study, which is crucial for accurately detecting delays in electrical wavefront propagation [255].

9.7 Validation of the cross-omnipole in animal and clinical studies

Chapter 4 provided a methodological introduction to the cross-omnipole, testing it within a simulation environment under unphysiological conditions, such as plane wavefront propagation. However, its direct translational value to physiological conditions was limited. Chapter 5 extends this work by testing and evaluating the performance of the cross-omnipole in an animal study, comparing it to other triangular-clique configurations [15] under controlled conditions. In particular, we retrospectively assessed the cross-oEGM estimation in a Langendorff heart model, which allowed us to better understand the strengths and limitations of these so-called orientation-independent sensing (OIS [17]) methods.

One advantage of the animal study was the consistent placement of the stimulation electrode in the rabbit Langendorff model, ensuring a uniform propagation direction of the wavefront. This consistency enabled reliable comparisons across complementary, mirrored triangular-clique configurations, given a steady catheter placement. As anticipated, results from chapter 5, which were obtained under controlled conditions, demonstrated a high degree of consistency between complementary mirrored triangles. In contrast, non-complementary configurations showed varied performance. This led to the coexistence of both accurate and inaccurate omnipolar EGM estimations, depending on the chosen configuration. These findings support Riccio et al.'s [23] assertion that triangular clique configurations are dependent on the orientation of the propagation wavefront to reliably reconstruct the omnipole.

The cross-oriented configuration proposed in Chapter 4, however, proved to be at least as accurate as the best-performing complementary triangular pairs. This highlights the cross-clique's advantages in clinical practice, where its independence from catheter orientation and movement—both of which are notoriously difficult to control—offers a more robust and reliable approach for oEGM reconstruction. While further validation in clinical settings is necessary, the successful application of this technique as the foundation for VFH analysis in animal studies (chapter 6) and clinical environments (chapter 7) demonstrates its robustness and potential for clinical translation. A comparative study similar to the one presented in chapter 5 but in a clinical scenario, would be a valuable contribution to the literature.

9.8 Insights on the inter-electrode distance for array catheters

The choice of catheter and its interelectrode distance is critical for effective arrhythmia mapping. Standard catheters, with a 3.5-mm distal electrode and 4.75-mm center-to-center spacing, record bipolar EGMs from tissue areas between 3.5 and 7.5 mm, depending on the catheter's angle. In contrast, catheters with 1-mm electrodes and 3-mm center-to-center spacing capture signals from a smaller tissue range of 1 to 4 mm [ref]. This smaller inter-electrode distance improves mapping resolution, enabling more accurate detection of heterogeneity in low-voltage areas and viable tissue channels. Additionally, closer spacing minimizes signal averaging, producing clearer EGMs with higher bipolar voltage and shorter duration, while requiring lower output for pacing due to increased electric density. This enhanced precision is particularly valuable in mapping scar-related arrhythmias.

Anter et al. (2015) [346] compared the standard linear catheter (Thermocool) with a 3.5-mm distal electrode and 4.75-mm center-to-center spacing to a multielectrode catheter (Pentaray) with 1-mm electrodes and 3-mm center-to-center spacing. The study, conducted under general anesthesia with jet ventilation using the Carto 3 mapping system, showed that catheters with smaller electrodes and tighter interelectrode spacing offer superior resolution in mapping atrial scar. In a subset of 10 patients, mapping with both catheters confirmed that the multielectrode catheter's closer spacing provided greater clarity in detecting scar heterogeneity, facilitating more accurate ablation of scar-related atrial tachycardias. This highlights the significant advantage of using smaller electrodes and closer interelectrode spacing for scar mapping and ablation.

Letchumy et al. [276] investigated the impact of electrode configuration and spacing on EGM morphology, concluding that an interelectrode distance of 2-3 mm provides the optimal balance between minimizing signal cancellation and enhancing activation localization. Distances exceeding 4 mm were less effective due to multiple minima in the EGMs, which reduced the ability to differentiate between healthy and scar tissue. Conversely, distances under 2 mm resulted in low-amplitude signals that were more susceptible to noise. Electrode groupings of three to four electrodes were most effective in capturing localized electrical activity, while larger groupings diminished spatial resolution. Yet, they based their conclusions on an in-silico study which requires of clinical validation.

Consistent with the findings of Anter et al. [346] and aligning with most of the arguments presented by Letchumy et al. [276], chapter 5 emphasizes the importance of electrode spacing below 2 mm for omnipolar-based analyses, as introduced in chapter 4. The interelectrode distance dependency study in chapter 5 particularly illustrates how distances greater than 3 mm lead to activation delays between neighboring unipolar electrodes, which in turn affect the morphology of diagonal bipoles and, consequently, the omnipolar EGM. Even in healthy tissue, fractionated signals may emerge under these clinical conditions. Notably, these effects are more pronounced for diagonal bipoles, which are crucial for spatial alignment and accurate bipolar activation, as they scale the interelectrode distance by a factor of the square root of two. These findings, consistent with prior studies, underscore the need to design and clinically implement catheters with higher electrode density and closer spacing, such as the recently developed Octarray^{TM} Mapping Catheter from Biosense Webster (Jonson&Johnson MedTech).

9.9 From omnipolar technology to quantifying local electrical disarray in clinical settings

Omnipolar technology enables the development of metrics based on orientation-independent catheter recordings, which motivated chapter 6. In this chapter, we propose a novel local heterogeneity metric, termed VFH, to assess local electrical disarray at both the clique and grid levels. The properties of VFH were first validated in simulations with progressively disorganized conduction patterns, showing promising results in characterizing electrical disarray. These findings were further confirmed in an experimental setup using a Langendorff-perfused rabbit heart, similar to the experiments discussed in chapter 5. The experiments demonstrated that the VFH metric successfully distinguished between basal and stimulated patterns, outperforming the SI metric [294], which has notable limitations due to its reliance on LAT maps [294, 12].

Unlike other metrics, VFH provides a unique method for quantifying spatio-temporal electrical disarray. While some studies have quantified the entropy of ECG morphology [302], the underlying causes of complex fractionated atrial EGMs (CFAEs) require further investigation [347]. Other approaches, such as coherence [288] or cross-correlation [304], compare simultaneous recordings from different locations but necessitate larger grids, losing the focus on local tissue dynamics. Similarly, anisotropy ratios [293] and other methods require extensive data points and specific conditions, which are often difficult to obtain in clinical EP studies [305, 306].

Assessing local electrical disarray in propagation patterns may be of particular interest in clinical settings, for example, to understand how fibrotic tissue disrupts uniform propagation [262]. In this case, the VFH could be correlated with impaired tissue regions. Alternatively, VFH could be used to map heterogeneity in arrhythmogenic tissue, as proposed in chapter 7, where its diagnostic value was demonstrated in identifying abnormal propagation in substrate mapping for patients with scar-related VT.

In this study, we observed a statistically significant increase in quantified local electrical disarray at both the clique and grid levels within functional isthmus regions, compared to normal and low-voltage bystander regions in scar-related VT substrate mapping. This finding highlights the clinical potential of the VFH metric in identifying regions of interest where current metrics or methods fall short. For example, recent strategies for functional substrate mapping in VT aim to target the functional isthmus by identifying isochronal late activation areas [348], decremental conduction patterns [349], or mapping repolarization dynamics [350] and multiple wavefronts [351]. However, these methods have limitations, including the need for extended mapping time and additional catheter maneuvers. The VFH metric aims to overcome some of these issues and offer an alternative marker by accounting for dynamic changes in wavefront propagation and increased non-linear anisotropy in the formation of functional isthmuses during VT [352].

Additionally, VFH holds the potential to integrate easily into mapping systems without requiring additional hardware. Unlike other approaches, such as the SI index, VFH is designed to be bounded between 0 and 1, making it a more practical and scalable tool in clinical EP procedures.

9.10 Local and global organization conduction patterns

In understanding local propagation patterns with a high level of detail, the VFH proves useful as it quantifies electrical disarray at the finest scale achievable with current technology, specifically through the use of cliques in multi-array diagnostic catheters. This has been particularly helpful in identifying regions of interest during the mapping of arrhythmias such as VT. However, to gain a broader understanding of temporal and spatial disorganization in complex arrhythmias such as AF, tools that assess global heterogeneity are needed. This motivated the development of the REACT metric in chapter 8, which, in a manner somewhat analogous to the VFH metric, was designed to identify areas of repetitive activity in unipolar EGMs in space and time in the spectrum of atrial tachyarrhythmias.

In this global mapping study of AF patients, as expected, atrial tachycardia rhythms displayed synchronization across the entire atria. Meanwhile, in AF rhythms, patients who terminated after ablation treatment exhibited greater overall synchronization compared to those who did not. The REACT metric showed predictive power for ablation outcomes and characterized AF organization by measuring beat-to-beat timing variations and changes in EGM morphology. Temporal AF organization has been linked to consistent rates, narrow DF peaks, and increased overall organization [33]. Spatial organization has been studied through EGM dispersion to identify driver regions [324], and through the mapping of rotational and focal drivers [29]. In contrast, AF disorganization has been associated with the multiple wavelet hypothesis [325], endo-epicardial dissociation [319], fractionated EGMs [325, 326], and stochastic modeling.

The REACT method integrates spatial and temporal components using a visually intuitive *similarity* measure that represents global heterogeneity across the atrium while offering insights into sub-anatomical spatiotemporal disorganization. Zeemering et al. showed that early AF in a goat model exhibited greater organization than late AF, suggesting that spatial organization could serve as a marker for disease progression independent of AF duration [329]. Lin et al. reported higher ablation success when targeting sites identified by single-site EGM similarity, a method extended by our study through the use of four spatially contiguous channels to capture consecutive repetitions [321]. Prior studies have also shown overlap between critical sites in atrial tachycardia (AT) and AF, with spatial concordance demonstrated between AT locations and AF driver sites [317, 318, 331]. Our findings build on this concept by suggesting that regions resembling AT may affect AF treatment response. The fully automated REACT metric, which is also applicable to non-invasive ECGI, has the potential to improve ablation outcomes by identifying organized sites similar to AT *islands*, facilitating the distinction between driver and passive sites [325, 324].

9.11 Overall limitations and future work

Each of the methods proposed in this thesis, along with their potential clinical applications, carry certain limitations. Rather than restating all of them in detail—since each chapter has a dedicated section addressing these—we will briefly summarize the overarching limitations of the work presented in this dissertation.

Due to the methodological nature of this thesis, the number of patients or animal subjects involved in applying the proposed methods may limit the clinical translation. For instance, in the vectorcardiographic approach to non-invasively diagnose AFL types presented in chapter 3, the sample size for each patient group was relatively small. While the statistical analyses were appropriately adapted and the results were significant, the small sample size for certain peripheral AFL types should be considered, as it reflects the clinical reality of the uneven distribution of these cases.

Similarly, for the cross-omnipolar EGM reconstruction proposed in chapter 4, the limitation lies in its testing solely in controlled simulation settings. However, in chapter 5, this was addressed by comparing cross-clique and triangular clique configurations for omnipole reconstruction in an experimental setting, studying inter-electrode distance. Although the number of recordings and rabbit hearts in the Langendorff-perfused model was sufficient to draw conclusions, translating these findings to clinical settings is limited by the assumptions inherent to animal studies.

The generalization to clinical settings poses a challenge due to the lack of control and absence of ground truth for propagation patterns *in vivo*. This reflects a common limitation between *in vivo* and *in vitro* studies, as well as between animal models and simulations. In chapter 5, we opted for an intermediate step between controlled experiments and realistic physiological conduction patterns by using the rabbit Langendorff model, since key factors such as CV are similar in both rabbit and human hearts.

It is important to note that the success of the cross-omnipolar reconstruction is also linked to the design of the VFH metric, as proposed in chapter 6. The limitations of this chapter are similar, as its clinical translation was also demonstrated in the same animal model settings, with similar motivations as in chapter 5. However, the work was extended in chapter 7, where the clinical potential of the VFH metric was tested in identifying functional isthmuses versus bystander areas in patients with VT during substrate mapping. Although this study could have benefited from a larger patient cohort for more robust conclusions and analysis of diverse etiologies, these concerns do not apply to the study on global spatio-temporal heterogeneity in chapter 8, which was validated with a sufficient number of patients and a well-designed hold-out test cohort.

The technical limitations for each method are discussed in their respective chapters. A common limitation across most methods arises from the inter-electrode distance in high-density multielectrode array catheters. We observed that even in healthy tissue, fractionated signals may appear in diagonal bipoles with current technology. These findings, consistent with previous studies, underscore the need for catheters with a higher electrode density and a closer spacing for more accurate results in clinical applications.

In future work, several avenues of research can build on the methods and findings of this thesis. First, expanding the validation of the proposed methods to larger, more diverse patient cohorts would be crucial for increasing the generalizability of the results. Multi-center collaborations and clinical trials involving different patient populations could offer a more comprehensive understanding of the effectiveness and limitations of each technique across various cardiac arrhythmias and etiologies. Second, translating the cross-omnipolar approach and the VFH metric into real-time systems for use in clinical catheter ablation procedures would be a significant next step. This involves not only optimizing the computational methods for speed and efficiency but also integrating them into existing EP mapping systems to facilitate their adoption in real-world settings. Additionally, further exploration of electrode configuration and density in high-density catheters is warranted. As demonstrated in the current work, electrode spacing plays a critical role in the accuracy of signal reconstruction; hence, developing new hardware designs that support the increasing resolution of these methods will be necessary for future clinical applications. Lastly, extending the methodologies to non-invasive and less-invasive approaches, such as body-surface mapping or wearable technologies, could further enhance early diagnosis and real-time monitoring of arrhythmias, making these innovations more accessible to broader patient populations.

Chapter 10

Conclusions

This doctoral dissertation has explored the integration of high-density catheters and advanced signal processing techniques to enhance the characterization of arrhythmogenic tissue. Through the development of novel methodologies for both local and global analysis of cardiac conduction patterns, this work has made significant strides in improving our tools for understanding electrical propagation patterns in cardiac maps, with a clear focus on clinical applications in atrial and ventricular arrhythmias.

A key achievement of this research was the development of the cross-clique configuration for omnipolar EGM reconstruction, understanding the omnipole as a bipolar EGM aligned with the propagation direction. Addressing the limitations of traditional triangular-clique configurations, this novel approach provided an orientation-independent solution for omnipolar EGM estimation. Through both theoretical simulations and experimental validation in animal models, the cross-clique configuration was shown to outperform existing methods, resolving critical issues such as orientation bias and improving the reliability of EGM reconstruction. This formulation opens new possibilities for more accurate intracardiac mapping, particularly in complex arrhythmias where signal orientation can impact diagnosis.

Another major contribution of this thesis was the development of the VFH metric, designed to quantify local electrical disarray in arrhythmogenic tissue. This metric was rigorously validated in both simulation environments, experimental EP studies, and clinical retrospective studies. The VFH metric has proven to be a robust tool for assessing conduction heterogeneity, offering clinicians a new method for identifying and characterizing arrhythmogenic substrates. Its application in VT substrate mapping demonstrated its clinical potential in guiding ablation therapy by accurately identifying functional isthmuses and other regions of interest.

In addition to local conduction analysis, this dissertation also advanced the understanding of global conduction patterns through the introduction of the REACT metric. This metric, designed to assess spatio-temporal heterogeneity at a broader scale, was shown to be effective in identifying regions of repetitive activity and disarray in patients with AF. The REACT metric provided valuable insights into AF organization, offering a predictive tool for ablation outcomes by identifying areas of higher synchronization in patients who responded positively to treatment. By addressing both local and global conduction patterns, the REACT and VFH metrics together provide a comprehensive approach to arrhythmia mapping, enhancing the diagnostic capabilities for clinicians managing atrial and ventricular arrhythmias.

Crucially, this research demonstrated the translational potential of these novel techniques in clinical settings. The local and global heterogeneity metrics were validated in patients with AF and VT, showing strong clinical relevance. The ability of these metrics to identify regions of interest in substrate mapping underscores their potential to improve patient outcomes, offering a more targeted approach to treating arrhythmias. This work paves the way for further clinical adoption of these techniques, marking a significant step forward in the use of high-density catheters for cardiac EP.

While the objectives of this dissertation have been successfully fulfilled, some areas require further exploration. Future studies will benefit from larger clinical trials to validate the proposed metrics across diverse patient populations and arrhythmia types. Additionally, the integration of these methods with emerging technologies, such as Electrocardiographic Imaging (ECGi), could further enhance their diagnostic accuracy and clinical utility. Such advancements could bridge the gap between non-invasive and invasive diagnostic methods, ultimately refining the way arrhythmias are diagnosed and treated.

All in all, this dissertation has laid a strong foundation for improving the characterization and treatment of arrhythmias through advanced signal processing techniques. The cross-clique configuration for omnipolar signal reconstruction, along with the VFH metric, represent significant innovations in both the theoretical understanding and practical application of high-density catheters in cardiac EP. These contributions have the potential to shape future clinical practices, offering more accurate and reliable tools for diagnosing and treating patients with complex arrhythmogenic substrates.

Appendix A

Scientific Impact of this Dissertation

The scientific impact of this doctoral dissertation is reflected through several channels, including the peer-reviewed scientific publications that emerged from the research, presentations at international and national engineering and clinical conferences, and the awards received for both oral and written contributions. This chapter outlines and quantifies these contributions to the scientific community.

A.1 Scientific journal articles

The following peer-reviewed journal articles are related to the research conducted in this dissertation:

- **Ruipérez-Campillo, S.**, Castrejón, S., Martínez, M., Cervigón, R., Meste, O., Merino, J. L., & Castells, F. (2021). Non-invasive characterization of macroreentrant atrial tachycardia types using a vectorcardiographic approach with the slow conduction region as a key marker. *Computer Methods and Programs in Biomedicine, 200*, 105932. [193]
- Castells, F.*, **Ruipérez-Campillo, S.***, Segarra, I., Cervigón, R., Casado-Arroyo, R., Merino, J. L., & Millet, J. (2023). Performance assessment of electrode configurations for omnipolar electrogram estimation from high-density arrays. *Computers in Biology and Medicine, 154*, 106604. [237]
- **Ruipérez-Campillo, S.**, Crespo, M., Tormos, Á., Guill, A., Cebrián, A., Alberola, A., & Castells, F. (2023). Evaluation and assessment of clique arrangements for omnipolar electrogram estimation in high-density electrode arrays: An experimental animal model study. *Physical and Engineering Sciences in Medicine, 46*(3), 1193-1204. [257]
- Pancorbo, L.*, **Ruipérez-Campillo, S.***, Tormos, Á., Guill, A., Cervigón, R., Alberola, A., & Castells, F. (2023). Vector field heterogeneity for assessing locally disorganized cardiac electrical propagation wavefronts

from high-density multielectrodes. *IEEE Open Journal of Engineering in Medicine and Biology.* [277]

- Ganesan, P., Deb, B., Feng, R., Rodrigo, M., **Ruiperez-Campillo, S.**, Rogers, A. J., & Narayan, S. M. (2023). Quantifying a spectrum of clinical response in atrial tachyarrhythmias using spatiotemporal synchronization of electrograms. *Europace, 25*(5), euad055. [307]
- Tonko, J.*, **Ruipérez-Campillo, S.***, Cabero-Vidal, G., Cabrera-Borrego, E., Roney, C., Jiminez, J., Roig, J. M., Castells-Ramon, F., & Lambiase, P. (2024). Vector field heterogeneity as a novel omnipolar mapping metric for functional substrate characterisation in scar-related ventricular tachycardias. *Heart Rhythm.* [313]

*Note: *Indicates shared first authorship.*

A.2 Awards associated with the research for this thesis

- **2019**: Award for the **Best Poster** at the Annual Congress of the *Spanish Society of General Medicine*. Poster: *A Vectorcardiographic Approach to Discriminate Between Different Atrial Flutter Reentrant Circuits*.
- **2020**: **First Prize José María Ferrero Corral** at the National Congress of the *Spanish Society of Biomedical Engineering* (CASEIB). Talk: *Atrial Vectorcardiogram Parameterization for Characterization of Different Flutter Types*.
- **2023**: Award for the **Best Oral Presentation** at the Annual Congress of the *Spanish Society of General Medicine*. Talk: *Reconstruction and Classification of Human Signals Using Advanced Signal Processing and Artificial Intelligence Techniques*.
- **2024**: **Clinical Needs Translation Award** at the International Conference *Computing in Cardiology*. Talk: *Identification of Potential Ablation Targets for Ventricular Tachycardia Using a Novel Omnipolar-Based Propagation Organization Metric*.

A.3 International engineering conference publications

The following publications were presented at international engineering conferences, further contributing to the dissemination of this research:

- Crespo, M.*, **Ruipérez-Campillo, S.***, Casado-Arroyo, R., Millet, J., & Castells, F. (2023, July). Assessment of the Interelectrode Distance Effect over the Omnipole with High Multielectrode Arrays. In *2023 45th Annual International Conference of the IEEE Engineering in Medicine & Biology Society (EMBC)* (pp. 1-4). IEEE. [353]
- Segarra, I., Cebrián, A., **Ruipérez-Campillo, S.**, Tormos, Á., Chorro, F. J., Castells, F., & Millet, J. (2023, July). Mini Peltier Cell Array System for

the Generation of Controlled Local Epicardial Heterogeneities. In *2023 45th Annual International Conference of the IEEE Engineering in Medicine & Biology Society (EMBC)* (pp. 1-4). IEEE. [354]

- Pancorbo, L., **Ruipérez-Campillo, S.**, Castells, F., & Millet, J. (2023, October). Heterogeneity Quantification of Electrophysiological Signal Propagation in High-Density Multielectrode Recordings. In *2023 Computing in Cardiology (CinC)* (Vol. 50, pp. 1-4). IEEE. [355]
- **Ruipérez-Campillo, S.**, Millet, J., & Castells, F. (2022, September). Classification of Atrial Tachycardia Types Using Dimensional Transforms of ECG Signals and Machine Learning. In *2022 Computing in Cardiology (CinC)* (Vol. 498, pp. 1-4). IEEE. [356]
- Segarra, I., **Ruipérez-Campillo, S.**, Castells, F., & Millet, J. (2022, September). Novel Method for Orientation-Independent Analysis in Equi-Spaced Multi-Electrode Arrays. In *2022 Computing in Cardiology (CinC)* (Vol. 498, pp. 1-4). IEEE. [357]
- **Ruipérez-Campillo, S.**, Castrejón, S., Martínez, M., Cervigón, R., Meste, O., Merino, J. L., & Castells, F. (2020, September). Slow conduction regions as a valuable vectorcardiographic parameter for the non-invasive identification of atrial flutter types. In *2020 Computing in Cardiology (CinC)* (Vol. 496, pp. 1-4). IEEE. [358]

*Note: *Indicates shared first authorship.*

A.4 International medical conference publications

The following publications were presented at international medical conferences, further disseminating the research and its clinical implications:

- **Ruiperez-Campillo, S.**, Pancorbo, L., Ramirez, E., Chorro, F. J., Merino, J. L., Casado-Arroyo, R., & Millet, J. (2024). Quantifying local cardiac substrate heterogeneity from high-density recordings: an experimental study. *Europace, 26* (Supplement_1), euae102-650. [359]
- **Ruiperez-Campillo, S.**, Castells, F., Casado-Arroyo, R., Merino, J. L., & Millet, J. (2023). Improving omnipolar electrogram reconstruction: an animal model study. *European Heart Journal, 44* (Supplement_2), ehad655-290. [360]
- **Ruiperez-Campillo, S.**, Pancorbo, L., Castells, F., Crespo, M., Chorro, F. J., Merino, J. L., & Millet, J. (2023). Quantification of local heterogeneity from activation maps of omnipolar multielectrode recordings. *European Heart Journal, 44* (Supplement_2), ehad655-328. [361]
- **Ruiperez-Campillo, S.**, Castells, F., Segarra, I., Merino, J. L., Casado-Arroyo, R., & Millet, J. (2023). Novel reconstruction technique of omnipolar signals in high-density electrode arrays. *Europace, 25* (Supplement_1), euad122-589. [362]

- **Ruiperez-Campillo, S.**, Castells, F., Crespo, M., Pancorbo, L., Guill, A., Chorro, F. J., & Millet, J. (2023). Study of the omnipolar EGM reconstruction for robustness against wavefront propagation in epicardial signals. *Europace, 25* (Supplement_1), euad122-662. [363]
- Ganesan, P., Deb, B., Feng, R., Rodrigo, M., **Ruiperez-Campillo, S.**, Rogers, A. J., & Narayan, S. M. (2022). Spectrum of clinical response in atrial tachyarrhythmias identified by spatiotemporal synchronization of electrograms. *Circulation, 146* (Suppl_1), A11304-A11304. [364]
- Ganesan, P., Rogers, A. J., Deb, B., Feng, R., Rodrigo, M., **Ruiperez-Campillo, S.**, & Narayan, S. M. (2022). Spatiotemporal signatures of response to atrial fibrillation ablation. *European Heart Journal, 43* (Supplement_2), ehac544-601. [365]
- Ganesan, P., Deb, B., Feng, R., Rodrigo, M., **Ruiperez-Campillo, S.**, Bhatia, N. K., & Narayan, S. M. (2022). Novel detection of atrial tachycardia-like islands during atrial fibrillation predicts response to ablation. *Heart Rhythm, 19*(5), S17-S18. [366]

A.5 National engineering conference publications

The following publications were presented at national engineering conferences, highlighting the dissemination of this research in a local scientific context:

- **Ruipérez-Campillo, S.**, Castells, F., & Millet, J. (2020, November). Parametrización del vectorcardiograma auricular para la caracterización de distintos tipos de flutter. In *Congress of the National Society of Biomedical Engineering (CASEIB)*, ISBN: 978-84-09-25491-0.
- Segarra, I., **Ruipérez-Campillo, S.**, Castells, F., & Millet, J. (2022, November). Nuevo método para el análisis independiente de la orientación de matrices multielectrodo equiespaciadas. In *Congress of the National Society of Biomedical Engineering (CASEIB)*, ISBN: 978-84-09-45972-8, pp. 134-137.
- Pancorbo, L., **Ruipérez-Campillo, S.**, & Millet, J. (2022, November). Cuantificación de la heterogeneidad del sustrato electrofisiológico cardiaco en registros obtenidos mediante multielectrodos de alta densidad. In *Congress of the National Society of Biomedical Engineering (CASEIB)*, ISBN: 978-84-09-45972-8, pp. 150-153.
- Crespo-Aguirre, M., **Ruipérez-Campillo, S.**, & Castells, F. (2022, November). Estudio comparativo con señales epicárdicas de las limitaciones del omnipolo con multielectrodos de alta densidad. In *Congress of the National Society of Biomedical Engineering (CASEIB)*, ISBN: 978-84-09-45972-8, pp. 138-141.
- **Ruipérez-Campillo, S.**, Castells, F., & Millet, J. (2022, November). Metodología robusta basada en los fundamentos del machine learning

para la clasificación de señales biomédicas: Aplicación a 3 desafíos de la ingeniería biomédica. In *Congress of the National Society of Biomedical Engineering (CASEIB)*, ISBN: 978-84-09-45972-8, pp. 31-34.

- Segarra, I., **Ruipérez-Campillo, S.**, & Millet, J. (2022, November). Mini Peltier cell array system for the generation of controlled local epicardial heterogeneities. In *Congress of the National Society of Biomedical Engineering (CASEIB)*, ISBN: 978-84-09-45972-8.

Appendix B

Appendices to Chapter 3

B.1 VCG loop alignment

Defining each individual loop by the triplet $(\mathbf{X}_k, \mathbf{Y}_k, \mathbf{Z}_k)$, where a bold typeface vector is composed of all time samples and $k = 1 \ldots K$, a least square minimisation approach is considered. Unlike the model in [367], each individual loop is simply assumed to be a noisy observation of a time shifted reference loop $(\mathbf{X}^{\{r\}}, \mathbf{Y}^{\{r\}}, \mathbf{Z}^{\{r\}})$. The noise level is assumed to be identical whatever the lead and the patient, providing the simple least square expression:

$$\hat{d}_1, \ldots, \hat{d}_K, \hat{\mathbf{X}}^{\{r\}}, \hat{\mathbf{Y}}^{\{r\}}, \hat{\mathbf{Z}}^{\{r\}} = arg \max_{d_1, \ldots, d_K, \mathbf{X}^{\{r\}}, \mathbf{Y}^{\{r\}}, \mathbf{Z}^{\{r\}}} (J)$$

with

$$\begin{aligned} J &= \sum_k (\| \mathbf{X}_k - \mathbf{X}_{d_k}^{\{r\}} \|^2 + \| \mathbf{Y}_k - \mathbf{Y}_{d_k}^{\{r\}} \|^2 + \| \mathbf{Z}_k - \mathbf{Z}_{d_k}^{\{r\}} \|^2) \\ &= \sum_k \Big(\mathbf{X}_k^T \mathbf{X}_k + \mathbf{Y}_k^T \mathbf{Y}_k + \mathbf{Z}_k^T \mathbf{Z}_k - 2\mathbf{X}_k^T \mathbf{X}_{d_k}^{\{r\}} - 2\mathbf{Y}_k^T \mathbf{Y}_{d_k}^{\{r\}} \\ &\quad -2\mathbf{Z}_k^T \mathbf{Z}_{d_k}^{\{r\}} + \mathbf{X}_{d_k}^{\{r\}T} \mathbf{X}_{d_k}^{\{r\}} + \mathbf{Y}_{d_k}^{\{r\}T} \mathbf{Y}_{d_k}^{\{r\}} + \mathbf{Z}_{d_k}^{\{r\}T} \mathbf{Z}_{d_k}^{\{r\}} \Big) \end{aligned}$$

With this formulation, the shifts d_k's operates on the reference loop. Using the property that each record is a loop, the expression can be replaced and simplified by:

$$\begin{aligned} J &= \sum_k \Big(-2\mathbf{X}_{k,-d_k}^T \mathbf{X}^{\{r\}} - 2\mathbf{Y}_{k,-d_k}^T \mathbf{Y}^{\{r\}} - 2\mathbf{Z}_{k,-d_k}^T \mathbf{Z}^{\{r\}} \\ &\quad + \mathbf{X}^{\{r\}T} \mathbf{X}^{\{r\}} + \mathbf{Y}^{\{r\}T} \mathbf{Y}^{\{r\}} + \mathbf{Z}^{\{r\}T} \mathbf{Z}^{\{r\}} \Big) + C \end{aligned}$$

where C stands for a constant. In order to minimise the criteria J the derivation with respect to each reference loop is given by:

$$\begin{aligned}
\frac{\partial J}{\partial \mathbf{X}^{\{r\}}} &= \sum_k \left(-2\mathbf{X}_{k,-d_k} + 2\mathbf{X}^{\{r\}}\right) \\
\frac{\partial J}{\partial \mathbf{Y}^{\{r\}}} &= \sum_k \left(-2\mathbf{Y}_{k,-d_k} + 2\mathbf{Y}^{\{r\}}\right) \\
\frac{\partial J}{\partial \mathbf{Z}^{\{r\}}} &= \sum_k \left(-2\mathbf{Z}_{k,-d_k} + 2\mathbf{Z}^{\{r\}}\right)
\end{aligned}$$

Zeroing each expression provides the solutions:

$$\begin{aligned}
\hat{\mathbf{X}}^{\{r\}} &= \frac{1}{K}\sum_k \mathbf{X}_{k,-d_k} \\
\hat{\mathbf{Y}}^{\{r\}} &= \frac{1}{K}\sum_k \mathbf{Y}_{k,-d_k} \\
\hat{\mathbf{Z}}^{\{r\}} &= \frac{1}{K}\sum_k \mathbf{Z}_{k,-d_k}
\end{aligned}$$

It can be shown that when replacing these solutions in J we get:

$$\begin{aligned}
J &= C - \hat{\mathbf{X}}^{\{r\}T}\hat{\mathbf{X}}^{\{r\}} - \hat{\mathbf{Y}}^{\{r\}T}\hat{\mathbf{Y}}^{\{r\}} - \hat{\mathbf{Z}}^{\{r\}T}\hat{\mathbf{Z}}^{\{r\}} \\
&= C - ||\hat{\mathbf{X}}^{\{r\}}||^2 - ||\hat{\mathbf{Y}}^{\{r\}}||^2 - ||\hat{\mathbf{Z}}^{\{r\}}||^2
\end{aligned}$$

Meaning that the minimisation of J is equivalent to maximise the sum of the energy of the resynchronised averaged leads. That is:

$$\hat{d}_1, \ldots, \hat{d}_k = arg \max_{d_1,\ldots,d_k} (||\hat{\mathbf{X}}^{\{r\}}||^2 + ||\hat{\mathbf{Y}}^{\{r\}}||^2 + ||\hat{\mathbf{Z}}^{\{r\}}||^2)$$

We propose using an iterative scheme to get the solution of this maximization. The delays d_k's are sequentially selected over an interval corresponding to the length of the loop in order to maximize the criteria. After the selection of the last delay d_k, the global process is repeated until convergence. Note that using the estimated delays, not only is the loop temporally aligned but also the estimated reference loops $\mathbf{X}^{\{r\}}$, $\mathbf{Y}^{\{r\}}$, $\mathbf{Z}^{\{r\}}$.

Appendix C

Appendices to Chapter 5

C.1 Statistical analysis

DHARMa is an R package that aims to facilitate the problematic interpretation of residuals from generalised linear mixed models.

The package uses a simulation-based approach normalising the residuals to a scale 0-1. If the statistical model is correctly defined, its fitted residuals will all follow the same known distribution [368].

The R script lines used for the first model based on a random intercept dependence on the heart origin:

```
model <- lmer (log(metrics) ~ treatment * distance  +
               (1|rabbit) + (1|rabbit:treatment:
                  distance),
              data=dat)
```

where `dat` is the dataframe containing the experimental data, *treatment* refers to the configuration ($C_{\text{◺}}$, $C_{\text{◹}}$ and $C_{\times}$), `metrics` to the variable (NLA, ORR...), and `distance` to the interelectrode distance, describing `rabbit` the rabbit heart origin dependence.

The R script lines from the second model (the one used) built as a mixed model on the aggregated data (aggregation of subsamples of the rabbit heart origin):

```
aggregated_data <- aggregate (metrics ~ treatment +
                              distance + rabbit,
                              data = d, FUN= mean)
model_agg <- lmer(log(metrics) ~ distance * treatment
    +
                  (1|rabbit), data = aggregated_data)
```

A summary table from the regression models was retrieved, as well as the random effect variance of the heart origin, the p-values were computed with Kenward-Roger Approximation for the degrees of freedom.

To calculate the randomised quantile residuals coming from the fitted model defined above and plot the DHARMa residual plot we made use of the following line of R code:

```
simulateResiduals(model_agg,plot=T)
```

Two plots were retrieved. A QQ plot containing added tests for correct distribution, dispersion and outliers, highly useful to detect overall deviations from the expected distribution.

A second figure was equally obtained with the DHARMa simulation, plotting the residuals against the rank transformed model predictions, including quantile regressions to discover trends.

C.2 Code

The code written for this manuscript can be found in the following GitHub link: GitHub Repository.

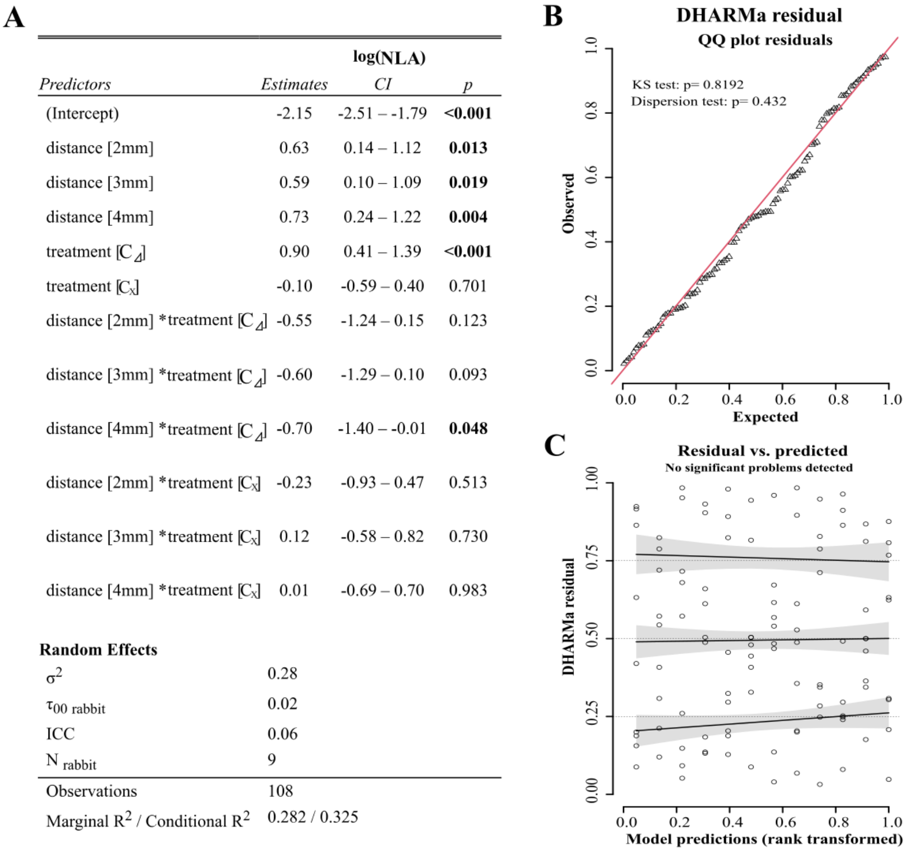

A

	log(NLA)		
Predictors	*Estimates*	*CI*	*p*
(Intercept)	-2.15	-2.51 – -1.79	**<0.001**
distance [2mm]	0.63	0.14 – 1.12	**0.013**
distance [3mm]	0.59	0.10 – 1.09	**0.019**
distance [4mm]	0.73	0.24 – 1.22	**0.004**
treatment [$C_{⊿}$]	0.90	0.41 – 1.39	**<0.001**
treatment [C_{X}]	-0.10	-0.59 – 0.40	0.701
distance [2mm] *treatment [$C_{⊿}$]	-0.55	-1.24 – 0.15	0.123
distance [3mm] *treatment [$C_{⊿}$]	-0.60	-1.29 – 0.10	0.093
distance [4mm] *treatment [$C_{⊿}$]	-0.70	-1.40 – -0.01	**0.048**
distance [2mm] *treatment [C_{X}]	-0.23	-0.93 – 0.47	0.513
distance [3mm] *treatment [C_{X}]	0.12	-0.58 – 0.82	0.730
distance [4mm] *treatment [C_{X}]	0.01	-0.69 – 0.70	0.983
Random Effects			
σ^2	0.28		
$\tau_{00\ \mathrm{rabbit}}$	0.02		
ICC	0.06		
N_{rabbit}	9		
Observations	108		
Marginal R^2 / Conditional R^2	0.282 / 0.325		

Figure C.1: Residual diagnostics for hierarchical regression model in NLA metric. **A.** Regression model table; **B.** Residuals QQ plot; **C.** Residuals plot over their expected value.

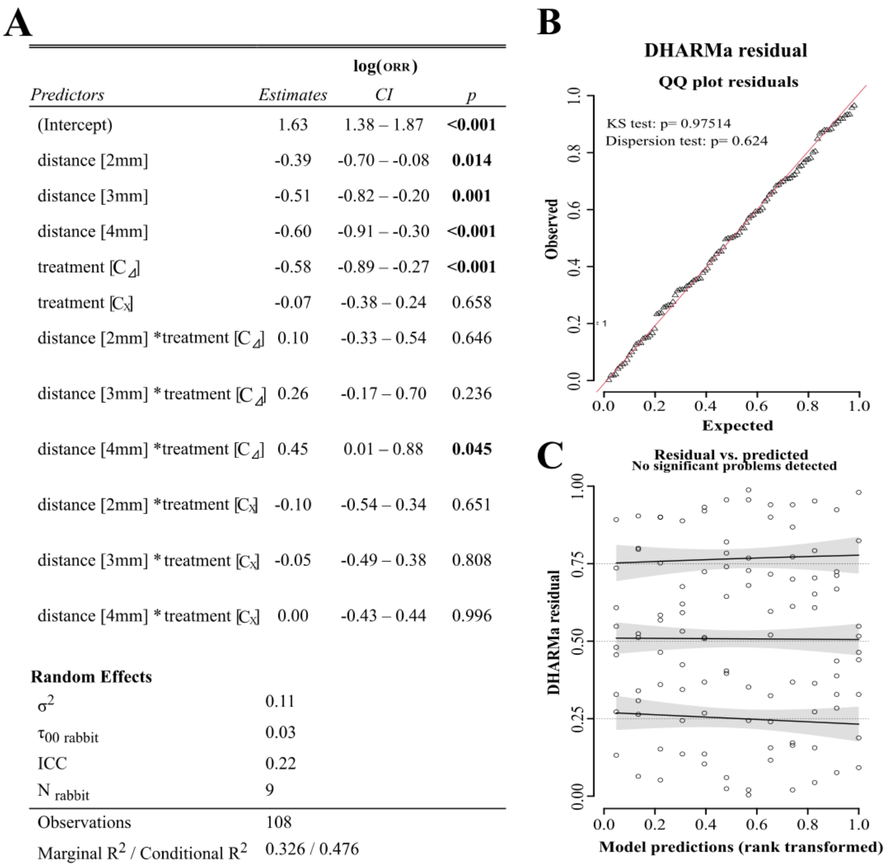

A

	log(ORR)		
Predictors	*Estimates*	*CI*	*p*
(Intercept)	1.63	1.38 – 1.87	**<0.001**
distance [2mm]	-0.39	-0.70 – -0.08	**0.014**
distance [3mm]	-0.51	-0.82 – -0.20	**0.001**
distance [4mm]	-0.60	-0.91 – -0.30	**<0.001**
treatment [C_{Δ}]	-0.58	-0.89 – -0.27	**<0.001**
treatment [C_{x}]	-0.07	-0.38 – 0.24	0.658
distance [2mm] *treatment [C_{Δ}]	0.10	-0.33 – 0.54	0.646
distance [3mm] *treatment [C_{Δ}]	0.26	-0.17 – 0.70	0.236
distance [4mm] *treatment [C_{Δ}]	0.45	0.01 – 0.88	**0.045**
distance [2mm] *treatment [C_{x}]	-0.10	-0.54 – 0.34	0.651
distance [3mm] *treatment [C_{x}]	-0.05	-0.49 – 0.38	0.808
distance [4mm] *treatment [C_{x}]	0.00	-0.43 – 0.44	0.996
Random Effects			
σ^2	0.11		
$\tau_{00\ \text{rabbit}}$	0.03		
ICC	0.22		
N_{rabbit}	9		
Observations	108		
Marginal R^2 / Conditional R^2	0.326 / 0.476		

Figure C.2: Residual diagnostics for hierarchical regression model in ORR metric; **A.** Regression Model table; **B.** Residuals QQ plot; **C.** Residuals over model predictions.

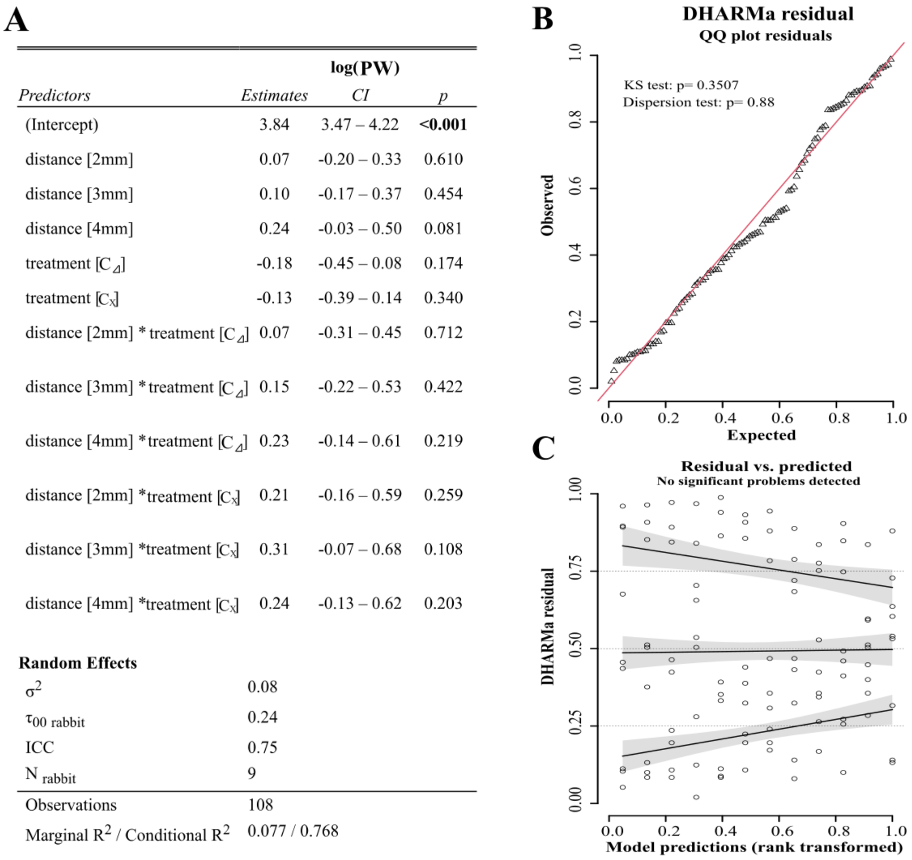

Predictors	Estimates	CI	p
		log(PW)	
(Intercept)	3.84	3.47 – 4.22	**<0.001**
distance [2mm]	0.07	-0.20 – 0.33	0.610
distance [3mm]	0.10	-0.17 – 0.37	0.454
distance [4mm]	0.24	-0.03 – 0.50	0.081
treatment [C_{Δ}]	-0.18	-0.45 – 0.08	0.174
treatment [C_{X}]	-0.13	-0.39 – 0.14	0.340
distance [2mm] * treatment [C_{Δ}]	0.07	-0.31 – 0.45	0.712
distance [3mm] * treatment [C_{Δ}]	0.15	-0.22 – 0.53	0.422
distance [4mm] * treatment [C_{Δ}]	0.23	-0.14 – 0.61	0.219
distance [2mm] * treatment [C_{X}]	0.21	-0.16 – 0.59	0.259
distance [3mm] * treatment [C_{X}]	0.31	-0.07 – 0.68	0.108
distance [4mm] * treatment [C_{X}]	0.24	-0.13 – 0.62	0.203
Random Effects			
σ^2	0.08		
$\tau_{00\ \mathrm{rabbit}}$	0.24		
ICC	0.75		
N $_{\mathrm{rabbit}}$	9		
Observations	108		
Marginal R^2 / Conditional R^2	0.077 / 0.768		

Figure C.3: Residual diagnostics for hierarchical regression model in PW metric; **A.** Regression model table; **B.** Residuals QQ plot; **C.** Residuals over model predictions.

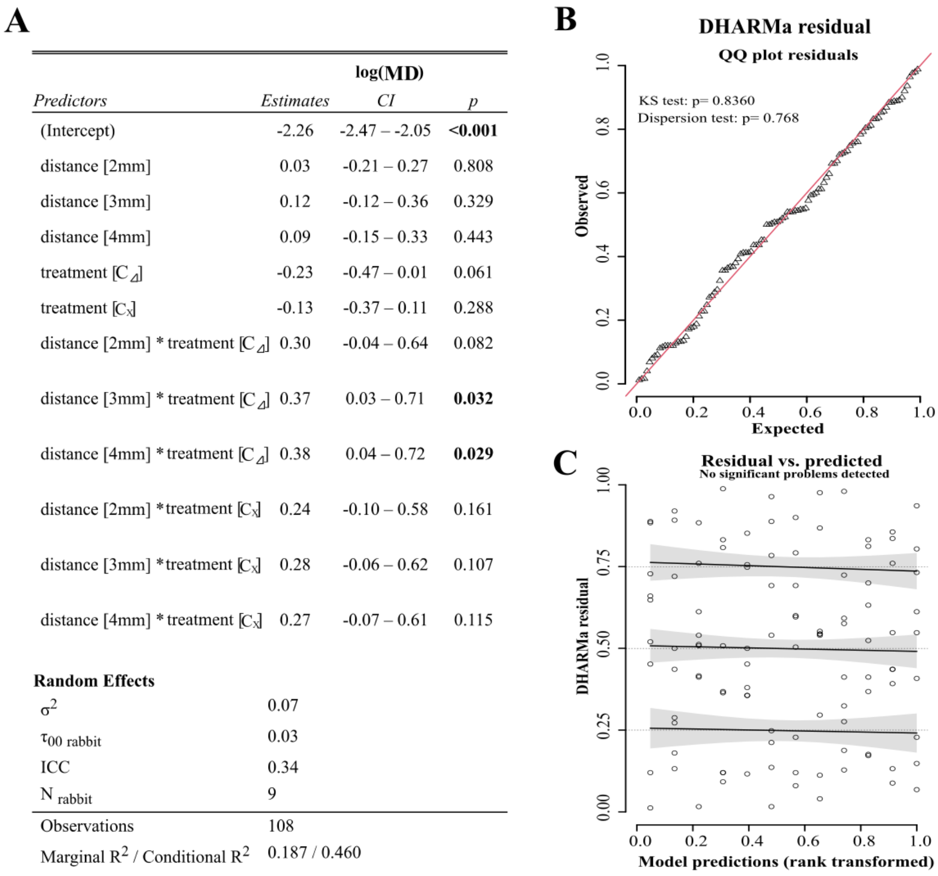

	log(MD)		
Predictors	*Estimates*	*CI*	*p*
(Intercept)	-2.26	-2.47 – -2.05	**<0.001**
distance [2mm]	0.03	-0.21 – 0.27	0.808
distance [3mm]	0.12	-0.12 – 0.36	0.329
distance [4mm]	0.09	-0.15 – 0.33	0.443
treatment [C_{Δ}]	-0.23	-0.47 – 0.01	0.061
treatment [C_X]	-0.13	-0.37 – 0.11	0.288
distance [2mm] * treatment [C_{Δ}]	0.30	-0.04 – 0.64	0.082
distance [3mm] * treatment [C_{Δ}]	0.37	0.03 – 0.71	**0.032**
distance [4mm] * treatment [C_{Δ}]	0.38	0.04 – 0.72	**0.029**
distance [2mm] * treatment [C_X]	0.24	-0.10 – 0.58	0.161
distance [3mm] * treatment [C_X]	0.28	-0.06 – 0.62	0.107
distance [4mm] * treatment [C_X]	0.27	-0.07 – 0.61	0.115
Random Effects			
σ^2	0.07		
$\tau_{00\ \text{rabbit}}$	0.03		
ICC	0.34		
N_{rabbit}	9		
Observations	108		
Marginal R^2 / Conditional R^2	0.187 / 0.460		

Figure C.4: Residual diagnostics for hierarchical regression model in MD metric; **A.** Regression model table; **B.** Residuals QQ plot; **C.** residuals over model predictions.

Appendix D

Appendices to Chapter 6

D.1 Statistical tests results

The decision to use the Wilcoxon Rank-Sum test as a non-parametric alternative to ANOVA lies in the fact that both the VFH and SI values fail to follow a normal distribution. This was proven by the Shapiro-Wilk test and can be visually observed in the QQ plots (fig. D.1.A and D.1.B), where the points deviate from the diagonal line. Moreover, the ROC and PR curves corresponding to the values in table 6.7 are represented in figure D.1.C.

D.2 Computation of VFH from LATs

To eliminate the influence of LAT annotation errors on the superior performance of the proposed metric over the SI, the comparative analysis has been repeated with VFH values resulting from LAT-derived vector maps. The gradient operator is applied to the LAT map and, after normalisation, a vector map representative of the propagation directions is obtained, from which a LAT-derived VFH value is computed. The comparison of these results with the original omnipolar-derived VFH values is displayed in fig. 6.9. The performance of the VFH in distinguishing between stimulated and basal maps remains high, as depicted by the low p-values in table D.1, and the high AUCs in fig. D.2. Additionally, no significant differences are found when comparing results for different catheter sizes (table D.2).

Table D.1: P-values of Wilcoxon rank-sum test for comparing LAT-derived VFH values according to stimulation type

Catheter Size	Basal - Stim. 4 Hz	Basal - Stim. 6 Hz	Stim. 4 Hz - Stim. 6 Hz
3×3	1.1962e-08*	2.8946e-08*	0.3311
4×4	2.3732e-08*	7.7600e-08*	0.7460
5×5	8.4498e-09*	1.9845e-08*	0.5828
6×6	3.7057e-09*	1.3548e-08*	0.3311
7×7	2.5882e-09*	1.1919e-08*	0.5447

$*$ *p-values < 0.0167*

Table D.2: P-values of Wilcoxon rank-sum test for comparing LAT-derived VFH values according to catheter size

Catheter Size	3×3 - 4×4	4×4 - 5×5	5×5 - 6×6	6×6 - 7×7
Basal	0.6632	0.5137	0.9504	0.9380
Stim. 4 Hz	0.3520	0.1824	0.6327	0.3143
Stim. 6 Hz	0.0480	0.0279	0.9370	0.1892

$*$ *p-values < 0.0125*

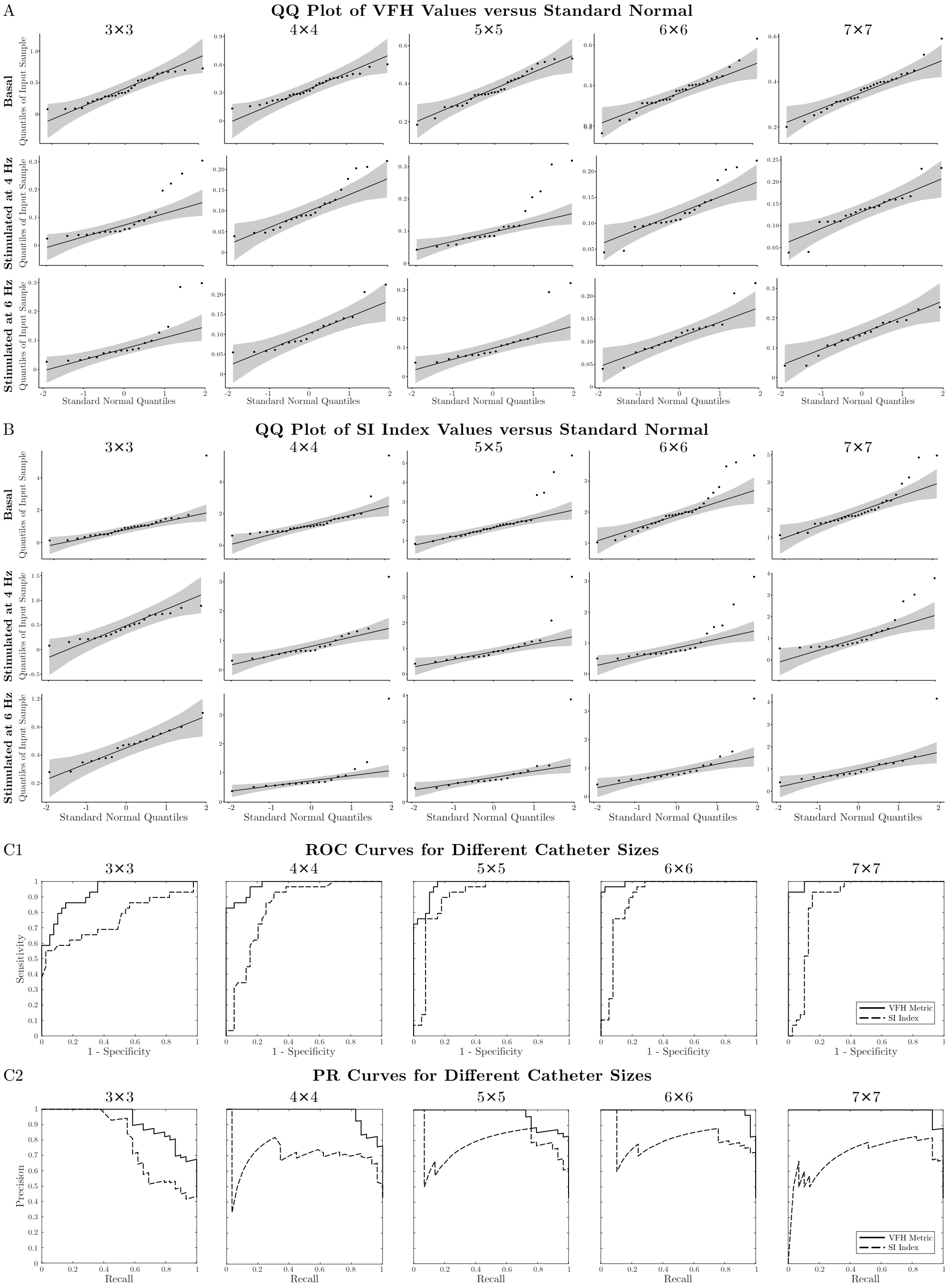
A QQ Plot of VFH Values versus Standard Normal

B QQ Plot of SI Index Values versus Standard Normal

C1 ROC Curves for Different Catheter Sizes

C2 PR Curves for Different Catheter Sizes

Figure D.1: Statistical Test Results; **A.** QQ Plots of the VFH value samples according to stimulation type (rows) and for different catheter sizes (columns). The 95% confidence interval is indicated by the shaded region; **B.** QQ Plots of the SI index samples according to stimulation type (rows) and for different catheter sizes (columns). The 95% confidence interval is indicated by the shaded region; **C.** ROC and Precision-Recall (PR) curves comparison between the VFH metric proposed in this study (solid line) and the SI index (dashed line).

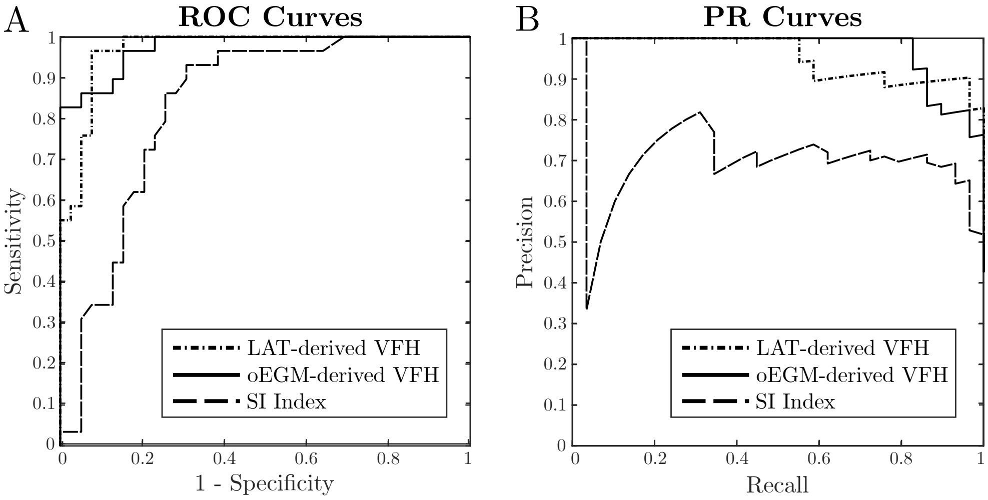

Figure D.2: A. ROC curves comparison between omnipolar-derived and LAT-derived VFH for the case of a 4×4 electrode grid. SI Index results are also displayed; **B.** Same comparison for the PR curves.

Appendix E

Appendices to Chapter 8

E.1 Additional description of the data

Table E.1: Propensity matching characteristics

Variable	Before Matching			After Matching		
	Term	**Non-Term**	**Standardized Difference**	**Term**	**Non-Term**	**Standardized Difference**
Age	63.9 (12.0)	64.6 (9.6)	6.9%	65.5 (10.5)	65.1 (10.3)	4.1%
Male	81 (67.5%)	75 (75.8%)	13.3%	49 (65.3%)	51 (68.0%)	5.6%
Paroxysmal AF	66 (55.0%)	24 (24.2%)		23 (30.7%)	23 (30.7%)	
Persistent AF	48 (40.0%)	65 (65.7%)	61.5%	47 (62.7%)	49 (65.3%)	4.9%
Long-standing Persistent AF	6 (5.0%)	10 (10.1%)		5 (6.7%)	3 (4.0%)	

E.2 Dynamics of AF organization quantified by the REACT algorithm

The REACT approach quantifies organization by varying thresholds for the correlation time-series of electrograms. In this section, we will discuss how altering the threshold for REACT can be used to probe the interaction between organized and disorganized EGM regions.

Supplement fig. E.1.A shows EGM from two 2-by-2 electrode grids (0.5cm^2) in a 71-year-old man. The blue box is a template of width 145ms, selected as 90% of average cycle length across 4 EGMs (163ms here). The correlation time-series indicate that EGMs E1-E4 in fig. 8.2.A show repeating organized patterns. EGMs E5-E8 show a disorganized region lacking such repeating organized patterns (again template in red box). As the correlation cut-point is reduced from 0.8 (for example) to 0, we can probe the relationship of organized-to-disorganized regions.

In fig. 8.2.B, applying a cut-point of 0.8 on the disorganized EGM shows few

Table E.2: List of clinical variables used in clustering

Category	Clinical Variables
Basic Demographics	1. Age 2. Sex 3. Race 4. Ethnicity 5. BMI
Cardiovascular Disease History	6. Congenital heart failure 7. Hypertension 8. Hyperlipidemia 9. TIA/CVA/stroke 10. Coronary artery disease 11. Myocardial infarction 12. Valvular disease 13. Ventricular tachycardia 14. Congenital heart disease 15. Peripheral artery disease 16. Other cardiovascular diseases
Cardiac Procedure History	17. Coronary artery bypass graft 18. Percutaneous coronary intervention 19. Valvular surgery 20. Congenital 21. Pacemaker 22. ICD 23. Maze procedure 24. CRT
Other History	25. History of smoking 26. Chronic Kidney Disease 27. Diabetes Mellitus 28. CHADS2VASc
AF Characteristics	29. AF type 30. AF duration
Presenting Symptoms	31. Syncope 32. Dizziness 33. Palpitations 34. Chest pain 35. Fatigue 36. Shortness of breath
Procedure Characteristics	37. Number of previous DCCV 38. Prior AF ablation 39. AF recurrence
Echo Measurements	40. LA size 41. LVEF
Antiarrhythmic Drugs	42. CCB 43. Digoxin 44. Flecainide 45. Propafenone 46. Amiodarone 47. Dronedarone 48. Sotalol 49. Dofetilide 50. Quinidine

repeating cycles, but this number will increase as the cutpoint is reduced. Thus, EGMs that are repetitive for more cycles will exceed a higher cut-point (REACT score) than those with fewer repeating cycles.

The interactions between organized and disorganized regions can thus be measured by the number of repeating cycles captured in the temporal window (green window in fig. 8.2.B). The REACT algorithm is designed to maximize the width of this temporal window, meaning that shorter repeating cycles during the recording period are ignored.

Spatially, dynamic interaction is handled by the sliding window that extends across electrodes in fig. 8.2.A. In the disorganized EGM example, EGM E5 is visually more organized than the EGMs E6-E8, this reflects in the correlation time series producing higher peaks. Thus, a greater number of spatial electrodes with organized EGMs will produce a higher REACT score.

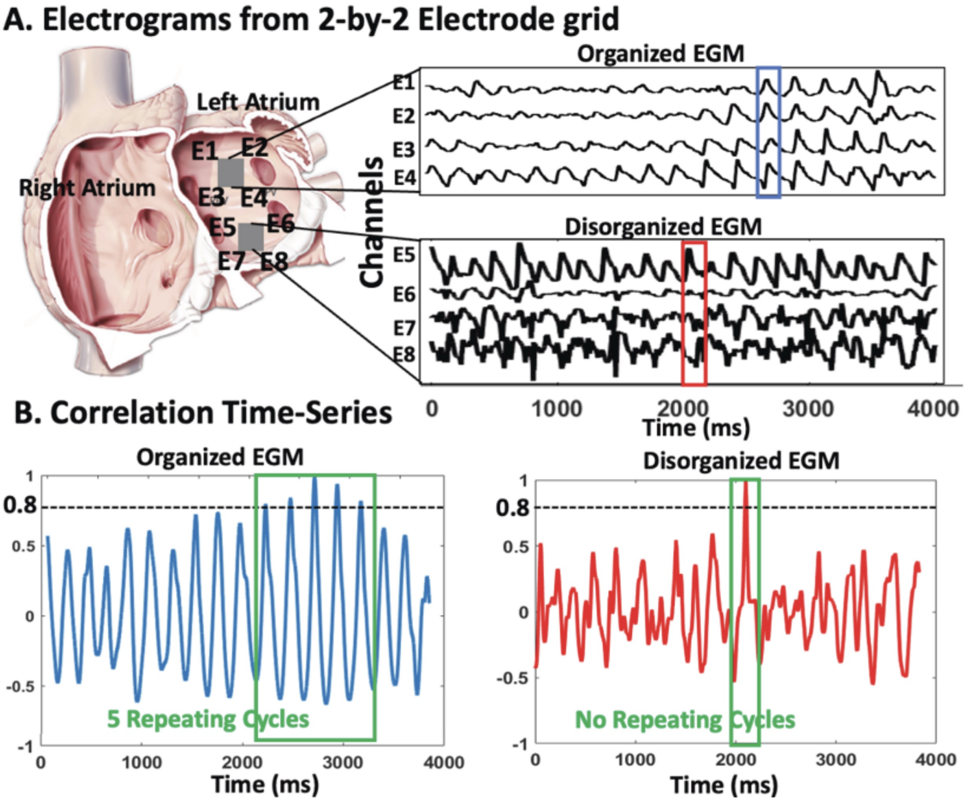

Figure E.1: Electrograms from 2-by-2 electrode grid

E.3 REACT pseudocode

Algorithm 1: REACT algorithm pseudocode

```
for each 2x2 EGM do
    Find CL
    Split EGM into 15 segments, each 4 seconds
    for each 2x2, 4-second EGM do
        Set sliding window width $W = 90\%$ CL
        for $n = 0, 1, 2, \ldots$ do
            Choose template signal: $t = n$ to $t = (n + 1) \times W$
            Find correlation time-series by sliding across 4-second EGM
        end for
        Repeat using all templates and store all correlation time-series
        for each cut-point = 1, 0.9, 0.8, . . . , 0 do
            Find the duration of consecutive peaks in all correlation time-series
            Store the maximum duration of consecutive peaks for each cut-point
        end for
    end for
    Compute REACT Score = Cut-point given a duration
end for
```

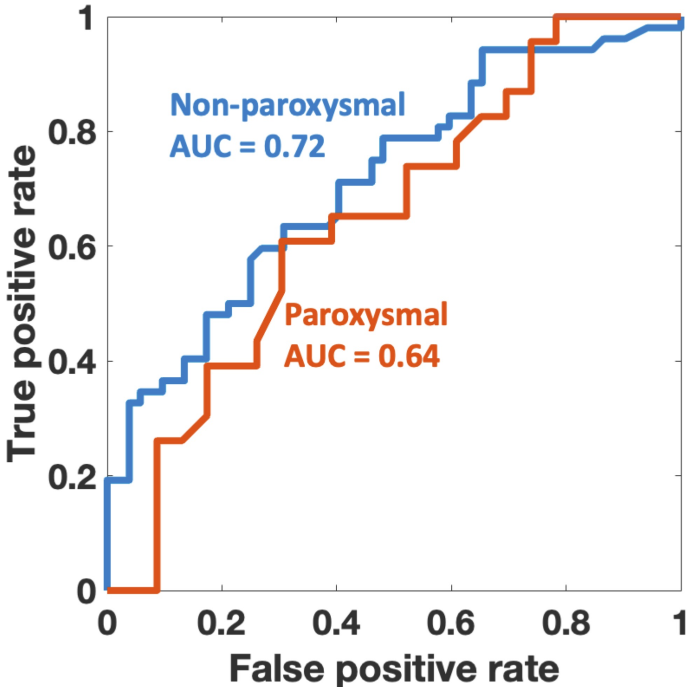

Figure E.2: AUC curves for predicting AF termination in non-paroxysmal and paroxysmal AF patients

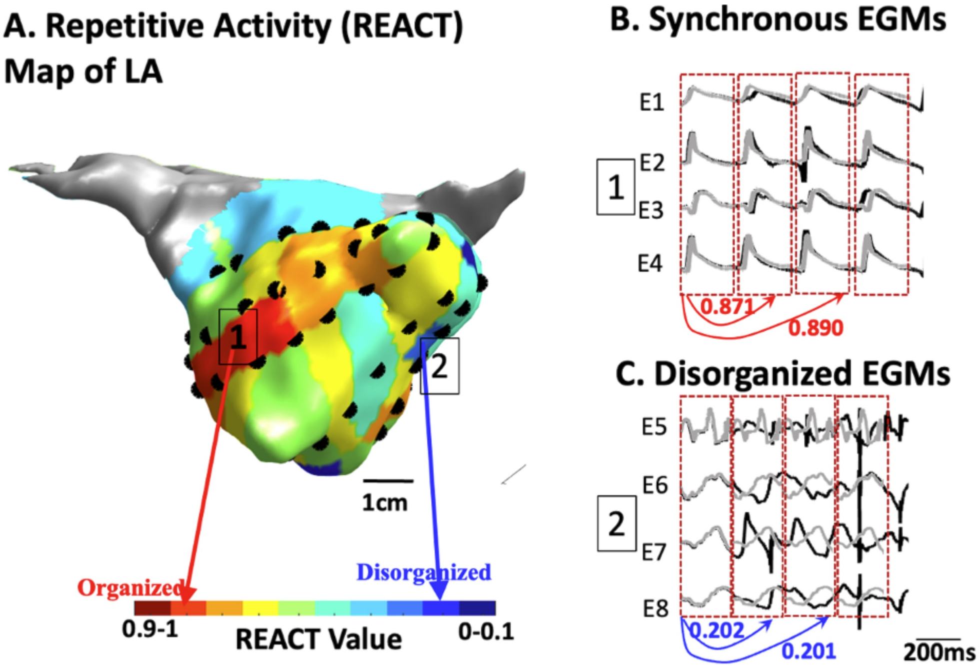

Figure E.3: **A.**: REACT Map of 55 YO Male with AF Termination shows large island (red and orange in color) of synchronous EGMs. Labels '1' and '2' indicate 2x2 electrode groups, 'X' indicates site of ablation where AF terminated; **B.** EGMs from 2x2 electrode region '1' shows template (gray) repeating synchronously for consecutive cycles (black); **C.** Disorganized EGMs where template (gray) does not repeat in successive cycles (black).

Bibliography

[1] Kamakshi Lakshminarayan et al. “Clinical epidemiology of atrial fibrillation and related cerebrovascular events in the United States”. In: *The neurologist* 14.3 (2008), pp. 143–150.

[2] S Adam Strickberger et al. “Relationship between atrial tachyarrhythmias and symptoms”. In: *Heart Rhythm* 2.2 (2005), pp. 125–131.

[3] Edward LC Pritchett. “Management of atrial fibrillation”. In: *New England Journal of Medicine* 326.19 (1992), pp. 1264–1271.

[4] Carl J Wiggers. “The mechanism and nature of ventricular fibrillation”. In: *American Heart Journal* 20.4 (1940), pp. 399–412.

[5] Hein JJ Wellens. “Ventricular tachycardia: diagnosis of broad QRS complex tachycardia”. In: *Heart* 86.5 (2001), pp. 579–585.

[6] BJ Deal et al. “New directions in surgical therapy of arrhythmias”. In: *Pediatric cardiology* 21 (2000), pp. 576–583.

[7] Paul C Zei and Scott Soltys. “Ablative radiotherapy as a noninvasive alternative to catheter ablation for cardiac arrhythmias”. In: *Current cardiology reports* 19 (2017), pp. 1–9.

[8] David A Cesario et al. “Value of high-density endocardial and epicardial mapping for catheter ablation of hemodynamically unstable ventricular tachycardia”. In: *Heart Rhythm* 3.1 (2006), pp. 1–10.

[9] Pier D Lambiase et al. “High-density substrate mapping in Brugada syndrome: combined role of conduction and repolarization heterogeneities in arrhythmogenesis”. In: *Circulation* 120.2 (2009), pp. 106–117.

[10] Thomas Rostock et al. “High-density activation mapping of fractionated electrograms in the atria of patients with paroxysmal atrial fibrillation”. In: *Heart Rhythm* 3.1 (2006), pp. 27–34.

[11] Piotr Podziemski et al. “Far-field effect in unipolar electrograms revisited: High-density mapping of atrial fibrillation in humans”. In: *2015 37th Annual International Conference of the IEEE Engineering in Medicine and Biology Society (EMBC)*. IEEE. 2015, pp. 5680–5683.

[12] Natasja MS De Groot et al. “Critical appraisal of technologies to assess electrical activity during atrial fibrillation: A position paper from the European heart rhythm association and European society of cardiology working group on eCardiology in collaboration with the heart rhythm society, asia pacific heart rhythm society, Latin American heart rhythm society and computing in cardiology”. In: *EP Europace* 24.2 (2022), pp. 313–330.

[13] Stephen Gaeta, Tristram D Bahnson, and Craig Henriquez. “Mechanism and magnitude of bipolar electrogram directional sensitivity: characterizing underlying determinants of bipolar amplitude”. In: *Heart Rhythm* 17.5 (May 2020), pp. 777–785.

[14] Minki Hwang et al. “Multiple factors influence the morphology of the bipolar electrogram: an in silico modeling study”. In: *PLoS computational biology* 15.4 (2019), e1006765.

[15] Don C Deno et al. “Orientation-independent catheter-based characterization of myocardial activation”. In: *IEEE Transactions on Biomedical Engineering* 64.5 (May 2016), pp. 1067–1077.

[16] Karl Magtibay et al. “Reinserting physiology into cardiac mapping using omnipolar electrograms”. In: *Cardiac Electrophysiology Clinics* 11.3 (2019), pp. 525–536.

[17] Don Curtis Deno et al. *Orientation independent sensing, mapping, interface and analysis systems and methods*. US Patent 11,406,312. Aug. 2022.

[18] Shouvik K Haldar et al. “Resolving bipolar electrogram voltages during atrial fibrillation using omnipolar mapping”. In: *Circulation: Arrhythmia and Electrophysiology* 10.9 (2017), e005018.

[19] Masateru Takigawa et al. “Impact of spacing and orientation on the scar threshold with a high-density grid catheter”. In: *Circulation: Arrhythmia and Electrophysiology* 12.9 (2019), e007158.

[20] Jose L Merino et al. “Characterization of conduction gaps at the pulmonary vein antra by omnipolar voltage mapping”. In: *EP Europace* 23.Supplement_3 (2021), euab116–256.

[21] Wen-Han Cheng et al. “Identification of circumferential pulmonary vein isolation gaps and critical atrial substrate from HD grid maps in atrial fibrillation patients: insights from omnipolar technology”. In: *Circulation: Arrhythmia and Electrophysiology* 15.1 (2022), e010424.

[22] Andreu Porta-Sánchez et al. “Omnipolarity applied to equi-spaced electrode array for ventricular tachycardia substrate mapping”. In: *EP Europace* 21.5 (May 2019), pp. 813–821.

[23] Jennifer Riccio et al. “Characterization of Atrial Propagation Patterns and Fibrotic Substrate With a Modified Omnipolar Electrogram Strategy in Multi-Electrode Arrays”. In: *Frontiers in Physiology* 12 (2021).

[24] MJ Davies and Ariela Pomerance. “Pathology of atrial fibrillation in man.” In: *British heart journal* 34.5 (1972), p. 520.

[25] Stanley Nattel, Brett Burstein, and Dobromir Dobrev. “Atrial remodeling and atrial fibrillation: mechanisms and implications”. In: *Circulation: Arrhythmia and Electrophysiology* 1.1 (2008), pp. 62–73.

[26] Koonlawee Nademanee et al. “Catheter ablation of atrial fibrillation guided by complex fractionated atrial electrogram mapping of atrial fibrillation substrate”. In: *Journal of cardiology* 55.1 (2010), pp. 1–12.

[27] Dennis H Lau et al. “Stability of complex fractionated atrial electrograms: a systematic review”. In: *Journal of cardiovascular electrophysiology* 23.9 (2012), pp. 980–987.

[28] Jiaxiong Lin et al. “Autonomic mechanism to explain complex fractionated atrial electrograms (CFAE)”. In: *Journal of cardiovascular electrophysiology* 18.11 (2007), pp. 1197–1205.

[29] Sanjiv M Narayan et al. “Treatment of atrial fibrillation by the ablation of localized sources: CONFIRM (Conventional Ablation for Atrial Fibrillation With or Without Focal Impulse and Rotor Modulation) trial”. In: *Journal of the American College of Cardiology* 60.7 (2012), pp. 628–636.

[30] Sanjiv M Narayan et al. “Ablation of rotor and focal sources reduces late recurrence of atrial fibrillation compared with trigger ablation alone: extended follow-up of the CONFIRM trial (Conventional Ablation for Atrial Fibrillation With or Without Focal Impulse and Rotor Modulation)”. In: *Journal of the American College of Cardiology* 63.17 (2014), pp. 1761–1768.

[31] Eric Buch et al. “Long-term clinical outcomes of focal impulse and rotor modulation for treatment of atrial fibrillation: A multicenter experience”. In: *Heart Rhythm* 13.3 (2016), pp. 636–641.

[32] Laura Martinez-Mateu et al. “Factors affecting basket catheter detection of real and phantom rotors in the atria: a computational study”. In: *PLoS computational biology* 14.3 (2018), e1006017.

[33] Felipe Atienza et al. “Real-time dominant frequency mapping and ablation of dominant frequency sites in atrial fibrillation with left-to-right frequency gradients predicts long-term maintenance of sinus rhythm”. In: *Heart rhythm* 6.1 (2009), pp. 33–40.

[34] Kentaro Yoshida et al. “A critical decrease in dominant frequency and clinical outcome after catheter ablation of persistent atrial fibrillation”. In: *Heart Rhythm* 7.3 (2010), pp. 295–302.

[35] Nassir F Marrouche et al. “Association of atrial tissue fibrosis identified by delayed enhancement MRI and atrial fibrillation catheter ablation: the DECAAF study”. In: *JAMA* 311.5 (Feb. 2014), p. 498.

[36] Eyal Herzog et al. “Pathway for the management of atrial fibrillation and atrial flutter”. In: *Critical pathways in cardiology* 16.2 (2017), pp. 47–52.

[37] Carmelo Butta et al. “Electrocardiographic diagnosis of atrial tachycardia: classification, P-wave morphology, and differential diagnosis with other supraventricular tachycardias”. In: *Annals of Noninvasive Electrocardiology* 20.4 (2015), pp. 314–327.

[38] Alexander JC Mittnacht, Srinivas Dukkipati, and Aman Mahajan. “Ventricular tachycardia ablation: a comprehensive review for anesthesiologists”. In: *Anesthesia & Analgesia* 120.4 (2015), pp. 737–748.

[39] Michael O Sweeney et al. “Differences in effects of electrical therapy type for ventricular arrhythmias on mortality in implantable cardioverter-defibrillator patients”. In: *Heart rhythm* 7.3 (2010), pp. 353–360.

[40] HCM Kamphuis et al. “Implantable cardioverter defibrillator recipients: quality of life in recipients with and without ICD shock delivery: a prospective study”. In: *Ep Europace* 5.4 (2003), pp. 381–389.

[41] Faramarz H Samie and Jose Jalife. “Mechanisms underlying ventricular tachycardia and its transition to ventricular fibrillation in the structurally normal heart”. In: *Cardiovascular research* 50.2 (2001), pp. 242–250.

[42] William G Stevenson. “Ventricular scars and ventricular tachycardia”. In: *Transactions of the American Clinical and Climatological Association* 120 (2009), p. 403.

[43] Edmond M Cronin et al. “2019 HRS/EHRA/APHRS/LAHRS expert consensus statement on catheter ablation of ventricular arrhythmias”. In: *EP Europace* 21.8 (2019), pp. 1143–1144.

[44] Douglas C Eaton and John P Pooler. *Vander’s renal physiology*. Mc Graw Hil Medicall, 2009.

[45] JE Eckenhoff et al. “Cardiac oxygen metabolism and control of the coronary circulation”. In: *American Journal of Physiology-Legacy Content* 149.3 (1947), pp. 634–649.

[46] M Zimmermann. “General principles of regulation”. In: *Human physiology*. Springer, 1989, pp. 324–332.

[47] Paul A Iaizzo. *Handbook of cardiac anatomy, physiology, and devices*. Springer Science & Business Media, 2010.

[48] Valentin Fuster et al. “Hurst S the heart”. In: (2011).

[49] Benson R Wilcox, Andrew C Cook, and Robert H Anderson. *Surgical anatomy of the heart*. Cambridge university press, 2005.

[50] Susan Standring et al. “Gray’s anatomy: the anatomical basis of clinical practice”. In: *American journal of neuroradiology* 26.10 (2005), p. 2703.

[51] Siew Yen Ho, Karen P McCarthy, and Francesco F Faletra. “Anatomy of the left atrium for interventional echocardiography”. In: *European Journal of Echocardiography* 12.10 (2011), pp. i11–i15.

[52] Siew Yen Ho, José Angel Cabrera, and Damian Sanchez-Quintana. “Left atrial anatomy revisited”. In: *Circulation: Arrhythmia and Electrophysiology* 5.1 (2012), pp. 220–228.

[53] Shinelle Whiteman et al. “An anatomical review of the left atrium”. In: *Translational Research in Anatomy* 17 (2019), p. 100052.

[54] Michel Haissaguerre et al. “Spontaneous initiation of atrial fibrillation by ectopic beats originating in the pulmonary veins”. In: *New England Journal of Medicine* 339.10 (1998), pp. 659–666.

[55] Arthur Garson Jr et al. “Supraventricular tachycardia due to multiple atrial ectopic foci: a relatively common problem”. In: *Journal of Cardiovascular Electrophysiology* 1.2 (1990), pp. 132–138.

[56] Frank H Netter. *Atlas of human anatomy, Professional Edition E-Book: including NetterReference. com Access with full downloadable image Bank*. Elsevier health sciences, 2014.

[57] Filippos Triposkiadis et al. "The sympathetic nervous system in heart failure: physiology, pathophysiology, and clinical implications". In: *Journal of the American College of Cardiology* 54.19 (2009), pp. 1747–1762.

[58] WC Randall et al. "Selective vagal innervation of the heart". In: *Annals of Clinical & Laboratory Science* 16.3 (1986), pp. 198–208.

[59] Andrei Brateanu. "Heart rate variability after myocardial infarction: what we know and what we still need to find out". In: *Current medical research and opinion* 31.10 (2015), pp. 1855–1860.

[60] Toshio Nakayama et al. "Action potential and membrane currents of single pacemaker cells of the rabbit heart". In: *Pflügers Archiv* 402 (1984), pp. 248–257.

[61] Gordon M Wahler. "Cardiac action potentials". In: *Cell Physiology Source Book* (2001), pp. 887–898.

[62] Edward Carmeliet. "Intracellular Ca2+ concentration and rate adaptation of the cardiac action potential". In: *Cell Calcium* 35.6 (2004), pp. 557–573.

[63] Jussi T Koivumäki, Topi Korhonen, and Pasi Tavi. "Impact of sarcoplasmic reticulum calcium release on calcium dynamics and action potential morphology in human atrial myocytes: a computational study". In: *PLoS computational biology* 7.1 (2011), e1001067.

[64] Unglaub Silverthorn. "Human Physiology: An Integrated Approach by Dee". In: *San Fransico: Pearson Benjamin Cummings* (2010), pp. 598–601.

[65] Philip De Chazal, Maria O'Dwyer, and Richard B Reilly. "Automatic classification of heartbeats using ECG morphology and heartbeat interval features". In: *IEEE transactions on biomedical engineering* 51.7 (2004), pp. 1196–1206.

[66] William H Barry. *Heart physiology from cell to circulation*. 2004.

[67] JH Coote and RA Chauhan. "The sympathetic innervation of the heart: Important new insights". In: *Autonomic Neuroscience* 199 (2016), pp. 17–23.

[68] Akinori Noma, Martin Morad, and Hiroshi Irisawa. "Does the "pacemaker current" generate the diastolic depolarization in the rabbit SA node cells?" In: *Pflügers Archiv* 397 (1983), pp. 190–194.

[69] Juul Achten and Asker E Jeukendrup. "Heart rate monitoring: applications and limitations". In: *Sports medicine* 33 (2003), pp. 517–538.

[70] Ahmed Faeq Hussein et al. "An automated remote cloud-based heart rate variability monitoring system". In: *IEEE access* 6 (2018), pp. 77055–77064.

[71] N Saoudi et al. "A classification of atrial flutter and regular atrial tachycardia according to electrophysiological mechanisms and anatomical bases. A Statement from a Joint Expert Group from the Working Group of Arrhythmias of the European Society of Cardiology and the North American Society of Pacing and Electrophysiology". In: *European heart journal* 22.14 (2001), pp. 1162–1182.

[72] Francisco G Cosio et al. "Atrial flutter mapping and ablation I: studying atrial flutter mechanisms by mapping and entrainment". In: *Pacing and clinical electrophysiology* 19.5 (1996), pp. 841–853.

[73] Francisco G Cosío et al. "Atrial flutter: an update". In: *Revista Española de Cardiología (English Edition)* 59.8 (2006), pp. 816–831.

[74] Ernest Frank. "The image surface of a homogeneous torso". In: *American Heart Journal* 47.5 (1954), pp. 757–768.

[75] Bethan Freestone, Gregory Lip, and J Godtfredsen. "Epidemiology and costs of cardiac arrhythmias". In: *Cardiac arrhythmias: a clinical approach*. 2003.

[76] Graham Thrall et al. "Quality of life in patients with atrial fibrillation: a systematic review". In: *The American journal of medicine* 119.5 (2006), 448–e1.

[77] Donald M Lloyd-Jones et al. "Lifetime risk for development of atrial fibrillation: the Framingham Heart Study". In: *Circulation* 110.9 (2004), pp. 1042–1046.

[78] Jan Heeringa et al. "Prevalence, incidence and lifetime risk of atrial fibrillation: the Rotterdam study". In: *European heart journal* 27.8 (2006), pp. 949–953.

[79] Valentin Fuster et al. "Acc/aha/esc 2006 guidelines for the management of patients with atrial fibrillation: A report of the american college of cardiology/american heart association task force on practice guidelines and the european society of cardiology committee for practice guidelines (writing committee to revise the 2001 guidelines for the management of patients with atrial fibrillation): Developed in collaboration with the european heart rhythm association and the heart rhythm society". In: *Circulation* 114.7 (2006), e257–e354.

[80] Gregory YH Lip and Hung-Fat Tse. "Management of atrial fibrillation". In: *The Lancet* 370.9587 (2007), pp. 604–618.

[81] Daniel E Singer et al. "Antithrombotic therapy in atrial fibrillation: the Seventh ACCP Conference on Antithrombotic and Thrombolytic Therapy". In: *Chest* 126.3 (2004), 429S–456S.

[82] Hakan Oral et al. "Pulmonary vein isolation for paroxysmal and persistent atrial fibrillation". In: *Circulation* 105.9 (2002), pp. 1077–1081.

[83] Nassir F Marrouche et al. "Phased-array intracardiac echocardiography monitoring during pulmonary vein isolation in patients with atrial fibrillation: impact on outcome and complications". In: *Circulation* 107.21 (2003), pp. 2710–2716.

[84] Bruce A Koplan and William G Stevenson. "Ventricular tachycardia and sudden cardiac death". In: *Mayo clinic proceedings*. Vol. 84. 3. Elsevier. 2009, pp. 289–297.

[85] Ruairidh Martin et al. "Characteristics of scar-related ventricular tachycardia circuits using ultra-high-density mapping: a multi-center study". In: *Circulation: Arrhythmia and Electrophysiology* 11.10 (2018), e006569.

[86] Ruairidh Martin et al. "Ventricular tachycardia isthmus characteristics: insights from high-density mapping". In: *Arrhythmia & Electrophysiology Review* 8.1 (2019), p. 54.

[87] Charles Antzelevitch. “Basic mechanisms of reentrant arrhythmias”. In: *Current opinion in cardiology* 16.1 (2001), pp. 1–7.

[88] William G Stevenson et al. “Identification of reentry circuit sites during catheter mapping and radiofrequency ablation of ventricular tachycardia late after myocardial infarction.” In: *Circulation* 88.4 (1993), pp. 1647–1670.

[89] William G Stevenson et al. “Radiofrequency catheter ablation of ventricular tachycardia after myocardial infarction”. In: *Circulation* 98.4 (1998), pp. 308–314.

[90] Nikolaos Papageorgiou and Neil T Srinivasan. “Dynamic high-density functional substrate mapping improves outcomes in ischaemic ventricular tachycardia ablation: sense protocol functional substrate mapping and other functional mapping techniques”. In: *Arrhythmia & Electrophysiology Review* 10.1 (2021), p. 38.

[91] William G Stevenson et al. “Exploring postinfarction reentrant ventricular tachycardia with entrainment mapping”. In: *Journal of the American College of Cardiology* 29.6 (1997), pp. 1180–1189.

[92] Paula Sanchez-Somonte et al. “Scar conducting channel characterization to predict arrhythmogenicity during ventricular tachycardia ablation”. In: *Europace* 25.3 (2023), pp. 989–999.

[93] Sucharita Mitra, Madhuchhanda Mitra, and Bidyut Baran Chaudhuri. “A rough-set-based inference engine for ECG classification”. In: *IEEE Transactions on instrumentation and measurement* 55.6 (2006), pp. 2198–2206.

[94] S Serge Barold. “Willem Einthoven and the birth of clinical electrocardiography a hundred years ago”. In: *Cardiac electrophysiology review* 7 (2003), pp. 99–104.

[95] Ivan Tomašić and Roman Trobec. “Electrocardiographic systems with reduced numbers of leads—synthesis of the 12-lead ECG”. In: *IEEE reviews in biomedical engineering* 7 (2013), pp. 126–142.

[96] Dewar D Finlay et al. “Eigenleads: ECG leads for maximizing information capture and improving SNR”. In: *IEEE transactions on information technology in biomedicine* 14.1 (2009), pp. 69–78.

[97] Emanuel Goldberger. “A simple, indifferent, electrocardiographic electrode of zero potential and a technique of obtaining augmented, unipolar, extremity leads”. In: *American Heart Journal* 23.4 (1942), pp. 483–492.

[98] Frank N Wilson et al. “The precordial electrocardiogram”. In: *American Heart Journal* 27.1 (1944), pp. 19–85.

[99] Leif Sörnmo and Pablo Laguna. *Bioelectrical signal processing in cardiac and neurological applications*. Academic press, 2005.

[100] Dee Unglaub Silverthorn. *Human physiology*. Jones & Bartlett Publishers, 2015.

[101] Horatio B Williams. “On the cause of the phase difference frequently observed between homonymous peaks of the electrocardiogram”. In: *American Journal of Physiology-Legacy Content* 35.3 (1914), pp. 292–300.

[102] Jaakko Malmivuo and Robert Plonsey. *Bioelectromagnetism: principles and applications of bioelectric and biomagnetic fields*. Oxford University Press, USA, 1995.

[103] HC Burger, AGW Van Brummelen, and G Van Herpen. “Heart-vector and leads”. In: *American Heart Journal* 61.3 (1961), pp. 317–323.

[104] Richard McFee and Amante Parungao. “An orthogonal lead system for clinical electrocardiography”. In: *American Heart Journal* 62.1 (1961), pp. 93–100.

[105] Otto H Schmitt and Ernst Simonson. “Symposium on electrocardiography and vectorcardiography: The present status of vectorcardiography”. In: *AMA archives of internal medicine* 96.5 (1955), pp. 574–590.

[106] Ernest Frank. “An accurate, clinically practical system for spatial vectorcardiography”. In: *circulation* 13.5 (1956), pp. 737–749.

[107] Edward D Frohlich. “Robert P. Grant, MD”. In: *American Journal of Cardiology* 91.5 (2003), pp. 646–648.

[108] C Richard Conti and Mark E Silverman. “J. Willis Hurst—a Man of achievement”. In: *Clinical Cardiology* 20.6 (1997), pp. 584–586.

[109] HC Burger, JB Van Milaan, and W Den Boer. “Comparison of different systems of vectorcardiography”. In: *British Heart Journal* 14.3 (1952), p. 401.

[110] HP Hurd 2nd et al. “Comparative accuracy of electrocardiographic and vectorcardiographic criteria for inferior myocardial infarction.” In: *Circulation* 63.5 (1981), pp. 1025–1029.

[111] JA Kors et al. “Reconstruction of the Frank vectorcardiogram from standard electrocardiographic leads: diagnostic comparison of different methods”. In: *European heart journal* 11.12 (1990), pp. 1083–1092.

[112] Bahareh Abdi et al. “Improved local activation time annotation of fractionated atrial electrograms for atrial mapping”. In: *Computers in Biology and Medicine* 117 (2020), p. 103590.

[113] Robert Plonsey, Roger C Barr, and A Bioelectricity. “Quantitative Approach”. In: *Cham, Switzerland: Springer* (2007).

[114] Marc Courtemanche, Rafael J Ramirez, and Stanley Nattel. “Ionic mechanisms underlying human atrial action potential properties: insights from a mathematical model”. In: *American Journal of Physiology-Heart and Circulatory Physiology* 275.1 (1998), H301–H321.

[115] Bahareh Abdi et al. “A compact matrix model for atrial electrograms for tissue conductivity estimation”. In: *Computers in biology and medicine* 107 (2019), pp. 284–291.

[116] Anatoly G Yagola and Yury M Korolev. “Error estimation in ill-posed problems in special cases”. In: *Applied Inverse Problems: Select Contributions from the First Annual Workshop on Inverse Problems*. Springer. 2013, pp. 155–164.

[117] Richard PM Houben, Natasja MS De Groot, and Maurits A Allessie. “Analysis of fractionated atrial fibrillation electrograms by wavelet decomposition”. In: *IEEE transactions on biomedical engineering* 57.6 (2010), pp. 1388–1398.

[118] Andres Orozco-Duque, John Bustamante, and German Castellanos-Dominguez. “Semi-supervised clustering of fractionated electrograms for electroanatomical atrial mapping”. In: *Biomedical engineering online* 15 (2016), pp. 1–19.

[119] Nicolas Navoret et al. “Detection of complex fractionated atrial electrograms using recurrence quantification analysis”. In: *IEEE Transactions on Biomedical Engineering* 60.7 (2013), pp. 1975–1982.

[120] Tom Goldstein and Stanley Osher. “The split Bregman method for L1-regularized problems”. In: *SIAM journal on imaging sciences* 2.2 (2009), pp. 323–343.

[121] Jian Zou, Haifeng Li, and Guoqi Liu. “Split Bregman algorithm for structured sparse reconstruction”. In: *IEEE Access* 6 (2018), pp. 21560–21569.

[122] Bahareh Abdi et al. “Local activation time annotation in atrial electrogram arrays using deconvolution”. In: *2019 Computing in Cardiology (CinC)*. IEEE. 2019, Page–1.

[123] Alan H Kadish et al. “Vector mapping of myocardial activation.” In: *Circulation* 74.3 (1986), pp. 603–615.

[124] Mauritis A Allessie. “Reentrant mechanism underlying atrial fibrillation”. In: *Cardiac electrophysiology: from cell to bedside* (1995).

[125] Nicholas S Peters et al. “Characteristics of the temporal and spatial excitable gap in anisotropic reentrant circuits causing sustained ventricular tachycardia”. In: *Circulation research* 82.2 (1998), pp. 279–293.

[126] Michael S Hanna et al. “Mechanisms of resetting reentrant circuits in canine ventricular tachycardia”. In: *Circulation* 103.8 (2001), pp. 1148–1156.

[127] YX Tu et al. “Estimation of conduction velocity distribution by regularized-least-squares method”. In: *IFAC Proceedings Volumes* 30.11 (1997), pp. 1253–1258.

[128] Alan R Barnette et al. “Estimation of 3-D conduction velocity vector fields from cardiac mapping data”. In: *IEEE transactions on biomedical engineering* 47.8 (2000), pp. 1027–1035.

[129] Prapa Kanagaratnam et al. “Relative expression of immunolocalized connexins 40 and 43 correlates with human atrial conduction properties”. In: *Journal of the American College of Cardiology* 39.1 (2002), pp. 116–123.

[130] Guido Iaccarino et al. “Ischemic neoangiogenesis enhanced by β2-adrenergic receptor overexpression: a novel role for the endothelial adrenergic system”. In: *Circulation research* 97.11 (2005), pp. 1182–1189.

[131] David E Leaf et al. “Connexin40 imparts conduction heterogeneity to atrial tissue”. In: *Circulation research* 103.9 (2008), pp. 1001–1008.

[132] Anthony WC Chow et al. “Mechanism of pacing-induced ventricular fibrillation in the infarcted human heart”. In: *Circulation* 110.13 (2004), pp. 1725–1730.

[133] Tokuhiro Kawara et al. “Activation delay after premature stimulation in chronically diseased human myocardium relates to the architecture of interstitial fibrosis”. In: *Circulation* 104.25 (2001), pp. 3069–3075.

[134] Edward J Ciaccio et al. “Model of bipolar electrogram fractionation and conduction block associated with activation wavefront direction at infarct border zone lateral isthmus boundaries”. In: *Circulation: Arrhythmia and Electrophysiology* 7.1 (2014), pp. 152–163.

[135] Paramdeep S Dhillon et al. "Relationship Between Connexin Expression and Gap–Junction resistivity in human atrial myocardium". In: *Circulation: Arrhythmia and electrophysiology* 7.2 (2014), pp. 321–329.

[136] Shahnaz Jamil-Copley et al. "Application of ripple mapping to visualize slow conduction channels within the infarct-related left ventricular scar". In: *Circulation: Arrhythmia and Electrophysiology* 8.1 (2015), pp. 76–86.

[137] James H King, Christopher L-H Huang, and James A Fraser. "Determinants of myocardial conduction velocity: implications for arrhythmogenesis". In: *Frontiers in physiology* 4 (2013), p. 154.

[138] Candido Cabo et al. "Wave-front curvature as a cause of slow conduction and block in isolated cardiac muscle." In: *Circulation research* 75.6 (1994), pp. 1014–1028.

[139] Stephen Bruce Knisley and Bruce C Hill. "Effects of bipolar point and line stimulation in anisotropic rabbit epicardium: assessment of the critical radius of curvature for longitudinal block". In: *IEEE transactions on biomedical engineering* 42.10 (1995), pp. 957–966.

[140] Vladimir G Fast and Andre G Kleber. "Role of wavefront curvature in propagation of cardiac impulse". In: *Cardiovascular research* 33.2 (1997), pp. 258–271.

[141] Jan P Kucera, André G Kléber, and Stephan Rohr. "Slow conduction in cardiac tissue, II: effects of branching tissue geometry". In: *Circulation research* 83.8 (1998), pp. 795–805.

[142] Jan P Kucera and Yoram Rudy. "Mechanistic insights into very slow conduction in branching cardiac tissue: a model study". In: *Circulation research* 89.9 (2001), pp. 799–806.

[143] Bruce H Smaill, Jichao Zhao, and Mark L Trew. "Three-dimensional impulse propagation in myocardium: arrhythmogenic mechanisms at the tissue level". In: *Circulation research* 112.5 (2013), pp. 834–848.

[144] Qiao Zheng et al. "3-D consistent and robust segmentation of cardiac images by deep learning with spatial propagation". In: *IEEE transactions on medical imaging* 37.9 (2018), pp. 2137–2148.

[145] Arsenii Dokuchaev, Alexander V Panfilov, and Olga Solovyova. "Myocardial fibrosis in a 3d model: Effect of texture on wave propagation". In: *Mathematics* 8.8 (2020), p. 1352.

[146] Chris D Cantwell et al. "Techniques for automated local activation time annotation and conduction velocity estimation in cardiac mapping". In: *Computers in Biology and Medicine* 65 (Oct. 2015), pp. 229–242.

[147] Pipin Kojodjojo et al. "The effects of carbenoxolone on human myocardial conduction: a tool to investigate the role of gap junctional uncoupling in human arrhythmogenesis". In: *Journal of the American College of Cardiology* 48.6 (2006), pp. 1242–1249.

[148] Pipin Kojodjojo et al. "Age-related changes in human left and right atrial conduction". In: *Journal of cardiovascular electrophysiology* 17.2 (2006), pp. 120–127.

[149] Akira Sawa et al. “Activation patterns and conduction velocity in posterolateral right atrium during typical atrial flutter using an electroanatomic mapping system”. In: *Circulation Journal* 72.3 (2008), pp. 384–391.

[150] Flavia Ravelli et al. “Acute atrial dilatation slows conduction and increases AF vulnerability in the human atrium”. In: *Journal of cardiovascular electrophysiology* 22.4 (2011), pp. 394–401.

[151] B Delaunay. “Sur la sph6re vide: Bull, Acad. Science USSR VII, Clas”. In: *Sci. Mat. Nat* (1934), pp. 793–800.

[152] Roger C Barr, Thomas M Gallie, and Madison S Spach. “Automated production of contour maps for electrophysiology II. Triangulation, verification, and organization of the geometric model”. In: *Computers and Biomedical Research* 13.2 (1980), pp. 154–170.

[153] Rishi Arora et al. “Arrhythmogenic substrate of the pulmonary veins assessed by high-resolution optical mapping”. In: *Circulation* 107.13 (2003), pp. 1816–1821.

[154] Jacob I Laughner et al. “Processing and analysis of cardiac optical mapping data obtained with potentiometric dyes”. In: *American Journal of Physiology-Heart and Circulatory Physiology* 303.7 (2012), H753–H765.

[155] Gregory E Morley et al. “Characterization of conduction in the ventricles of normal and heterozygous Cx43 knockout mice using optical mapping”. In: *Journal of cardiovascular electrophysiology* 10.10 (1999), pp. 1361–1375.

[156] Martin Wolfgang Krüger. *Personalized multi-scale modeling of the atria: heterogeneities, fiber architecture, hemodialysis and ablation therapy*. Vol. 19. KIT Scientific Publishing, 2014.

[157] Tamara N Fitzgerald et al. “Estimation of cardiac conduction velocities using small data sets”. In: *Annals of biomedical engineering* 31 (2003), pp. 250–261.

[158] Qing Lou et al. “Quantitative panoramic imaging of epicardial electrical activity”. In: *Annals of biomedical engineering* 36 (2008), pp. 1649–1658.

[159] Frank M Weber et al. “Wave-direction and conduction-velocity analysis from intracardiac electrograms–a single-shot technique”. In: *IEEE transactions on biomedical engineering* 57.10 (2010), pp. 2394–2401.

[160] Michael Burdumy et al. “Comparing measured and simulated wave directions in the left atrium–a workflow for model personalization and validation”. In: (2012).

[161] Frank M Weber et al. “Conduction velocity restitution of the human atrium—an efficient measurement protocol for clinical electrophysiological studies”. In: *IEEE Transactions on Biomedical Engineering* 58.9 (2011), pp. 2648–2655.

[162] Caroline H Roney et al. “An automated algorithm for determining conduction velocity, wavefront direction and origin of focal cardiac arrhythmias using a multipolar catheter”. In: *2014 36th Annual International Conference of the IEEE Engineering in Medicine and Biology Society*. IEEE. 2014, pp. 1583–1586.

[163] Michela Masè et al. “Velocity field analysis of activation maps in atrial fibrillation a simulation study”. In: *World Congress on Medical Physics and Biomedical Engineering, September 7-12, 2009, Munich, Germany: Vol. 25/4 Image Processing, Biosignal Processing, Modelling and Simulation, Biomechanics*. Springer. 2010, pp. 1014–1017.

[164] CS Chen, YC Hon, and RA Schaback. “Scientific computing with radial basis functions”. In: *Department of Mathematics, University of Southern Mississippi, Hattiesburg, MS* 39406 (2005).

[165] Matthew W Kay and Richard A Gray. “Measuring curvature and velocity vector fields for waves of cardiac excitation in 2-D media”. In: *IEEE transactions on biomedical engineering* 52.1 (2004), pp. 50–63.

[166] Ayman Mourad and Martyn P Nash. “Method for quantifiying conduction velocity during ventricular fibrillation”. In: *Physical Review E—Statistical, Nonlinear, and Soft Matter Physics* 75.1 (2007), p. 011914.

[167] Rémi Dubois et al. “Global and directional activation maps for cardiac mapping in electrophysiology”. In: *2012 Computing in Cardiology*. IEEE. 2012, pp. 349–352.

[168] SM Horner, Z Vespalcova, and MJ Lab. “Electrode for recording direction of activation, conduction velocity, and monophasic action potential of myocardium”. In: *American Journal of Physiology-Heart and Circulatory Physiology* 272.4 (1997), H1917–H1927.

[169] Chris D Cantwell et al. “A software platform for the comparative analysis of electroanatomic and imaging data including conduction velocity mapping”. In: *2014 36th Annual International Conference of the IEEE Engineering in Medicine and Biology Society*. IEEE. 2014, pp. 1591–1594.

[170] Guy Salama, Anthony Kanai, and Igor R Efimov. “Subthreshold stimulation of Purkinje fibers interrupts ventricular tachycardia in intact hearts. Experimental study with voltage-sensitive dyes and imaging techniques.” In: *Circulation research* 74.4 (1994), pp. 604–619.

[171] Derrick Sung, Jeffrey H Omens, and Andrew D McCulloch. “Model-based analysis of optically mapped epicardial activation patterns and conduction velocity”. In: *Annals of biomedical engineering* 28 (2000), pp. 1085–1092.

[172] Michela Masé and F Ravelli. “Automatic reconstruction of activation and velocity maps from electro-anatomic data by radial basis functions”. In: *2010 Annual International Conference of the IEEE Engineering in Medicine and Biology*. IEEE. 2010, pp. 2608–2611.

[173] Chiara Rabotti et al. “Noninvasive estimation of the electrohysterographic action-potential conduction velocity”. In: *IEEE Transactions on Biomedical Engineering* 57.9 (2010), pp. 2178–2187.

[174] Gustavo S Guandalini, Jackson J Liang, and Francis E Marchlinski. “Ventricular tachycardia ablation: past, present, and future perspectives”. In: *JACC: Clinical Electrophysiology* 5.12 (2019), pp. 1363–1383.

[175] Young-Hoon Kim et al. “2019 APHRS expert consensus statement on three-dimensional mapping systems for tachycardia developed in collaboration with HRS, EHRA, and LAHRS”. In: *Journal of arrhythmia* 36.2 (2020), p. 215.

[176] Hugh Calkins. *The 2019 ESC Guidelines for the Management of Patients with Supraventricular Tachycardia: What you need to know about the 2019 ESC Guidelines are discussed by Professor Hugh Calkins, Member of the Guideline Writing Group*. 2019.

[177] Jason G Andrade et al. "Contemporary atrial fibrillation management: a comparison of the current AHA/ACC/HRS, CCS, and ESC guidelines". In: *Canadian Journal of Cardiology* 33.8 (2017), pp. 965–976.

[178] Developed with the Special Contribution of the European Heart Rhythm Association (EHRA) et al. "Guidelines for the management of atrial fibrillation: the Task Force for the Management of Atrial Fibrillation of the European Society of Cardiology (ESC)". In: *European heart journal* 31.19 (2010), pp. 2369–2429.

[179] Hanno U Klemm et al. "Catheter ablation of multiple ventricular tachycardias after myocardial infarction guided by combined contact and noncontact mapping". In: *Circulation* 115.21 (2007), pp. 2697–2704.

[180] Richard J Schilling, Nicholas S Peters, and D Wyn Davies. "Feasibility of a noncontact catheter for endocardial mapping of human ventricular tachycardia". In: *Circulation* 99.19 (1999), pp. 2543–2552.

[181] Hugh Calkins et al. "HRS/EHRA/ECAS Expert Consensus Statement on Catheter and Surgical Ablation of Atrial Fibrillation: Recommendations for Personnel, Policy, Procedures and Follow-Up: A report of the Heart Rhythm Society (HRS) Task Force on Catheter and Surgical Ablation of Atrial Fibrillation Developed in partnership with the European Heart Rhythm Association (EHRA) and the European Cardiac Arrhythmia Society (ECAS); in collaboration with the American College of Cardiology (ACC), American Heart Association (AHA), and the Society of Thoracic Surgeons (STS). Endorsed and Approved by the governing bodies of the American College of Cardiology, the American Heart Association, the European Cardiac Arrhythmia Society, the European Heart Rhythm Association, the Society of Thoracic Surgeons, and the Heart Rhythm Society." In: *Europace* 9.6 (2007), pp. 335–379.

[182] Francis E Marchlinski et al. "Linear ablation lesions for control of unmappable ventricular tachycardia in patients with ischemic and nonischemic cardiomyopathy". In: *Circulation* 101.11 (2000), pp. 1288–1296.

[183] Corinna B Brunckhorst et al. "Identification of the ventricular tachycardia isthmus after infarction by pace mapping". In: *Circulation* 110.6 (2004), pp. 652–659.

[184] Christian Knackstedt, Patrick Schauerte, and Paulus Kirchhof. "Electroanatomic mapping systems in arrhythmias". In: *Europace* 10.suppl_3 (2008), pp. iii28–iii34.

[185] Laurens F Tops et al. "Fusion of multislice computed tomography imaging with three-dimensional electroanatomic mapping to guide radiofrequency catheter ablation procedures". In: *Heart Rhythm* 2.10 (2005), pp. 1076–1081.

[186] Jun Dong et al. "Integrated electroanatomic mapping with three-dimensional computed tomographic images for real-time guided ablations". In: *Circulation* 113.2 (2006), pp. 186–194.

[187] Hans Kottkamp et al. "Electromagnetic versus fluoroscopic mapping of the inferior isthmus for ablation of typical atrial flutter: a prospective randomized study". In: *Circulation* 102.17 (2000), pp. 2082–2086.

[188] Paulus Kirchhof et al. "A novel nonfluoroscopic catheter visualization system (LocaLisa) to reduce radiation exposure during catheter ablation of supraventricular tachycardias". In: *American Journal of Cardiology* 90.3 (2002), pp. 340–343.

[189] Mark J Earley et al. "Radiofrequency ablation of arrhythmias guided by non-fluoroscopic catheter location: a prospective randomized trial". In: *European heart journal* 27.10 (2006), pp. 1223–1229.

[190] Timm Dickfeld et al. "Anatomic stereotactic catheter ablation on three-dimensional magnetic resonance images in real time". In: *Circulation* 108.19 (2003), pp. 2407–2413.

[191] Saman Nazarian et al. "Feasibility of real-time magnetic resonance imaging for catheter guidance in electrophysiology studies". In: *Circulation* 118.3 (2008), pp. 223–229.

[192] Karl Magtibay et al. "Physiological assessment of ventricular myocardial voltage using omnipolar electrograms". In: *Journal of the American Heart Association* 6.8 (2017), e006447.

[193] Samuel Ruipérez-Campillo et al. "Non-invasive characterisation of macroreentrant atrial tachycardia types from a vectorcardiographic approach with the slow conduction region as a cornerstone". In: *Computer methods and programs in biomedicine* 200 (2021), p. 105932.

[194] William Dresen and Pamela K Mason. "Atrial flutter after surgical maze: incidence, diagnosis, and management". In: *Current opinion in cardiology* 31.1 (2016), pp. 57–63.

[195] Steven M Markowitz et al. "Approach to catheter ablation of left atrial flutters". In: *Journal of Cardiovascular Electrophysiology* 30.12 (2019), pp. 3057–3067.

[196] Francisco G Cosío. "Atrial flutter, typical and atypical: a review". In: *Arrhythmia & electrophysiology review* 6.2 (2017), p. 55.

[197] Chung-Hsing Lin et al. "Novel electrophysiological characteristics of atrioventricular nodal continuous conduction curves in atrioventricular nodal re-entrant tachycardia with concomitant cavotricuspid isthmus-dependent atrial flutter". In: *Ep Europace* 18.8 (2016), pp. 1259–1264.

[198] Vincent Y See. "Organized atrial arrhythmias after cardiac transplantation: The overlooked value of the 12-lead electrocardiogram and cavotricuspid atrial flutter isthmus". In: *The Journal of Heart and Lung Transplantation* 37.2 (2018), pp. 192–194.

[199] Miki Yokokawa et al. "The relationship between the P wave and local atrial electrogram in predicting conduction block during catheter ablation of cavotricuspid isthmus-dependent atrial flutter". In: *Journal of Interventional Cardiac Electrophysiology* 53.2 (2018), pp. 187–193.

[200] Maria Stella Baccillieri et al. “Anatomy of the cavotricuspid isthmus for radiofrequency ablation in typical atrial flutter”. In: *Heart rhythm* 16.11 (2019), pp. 1611–1618.

[201] Serkan Saygi et al. “Impact of cavotricuspid isthmus morphology in CRYO versus radiofrequency ablation of typical atrial flutter”. In: *Scandinavian Cardiovascular Journal* 51.2 (2017), pp. 69–73.

[202] Graham Peigh et al. “Use of the cryoballoon to ablate pulmonary vein-dependent left atrial flutter”. In: *Pacing and Clinical Electrophysiology* 42.12 (2019), pp. 1589–1593.

[203] Sok-Sithikun Bun et al. “Atrial flutter: more than just one of a kind”. In: *European heart journal* 36.35 (2015), pp. 2356–2363.

[204] Yoram Rudy. “Electrocardiographic imaging (ECGI): a new noninvasive imaging modality for cardiac electrophysiology and arrhythmia”. In: *Medical Imaging 2006: Physiology, Function, and Structure from Medical Images*. Vol. 6143. International Society for Optics and Photonics. 2006, p. 614306.

[205] Charulatha Ramanathan et al. “Noninvasive electrocardiographic imaging for cardiac electrophysiology and arrhythmia”. In: *Nature medicine* 10.4 (2004), pp. 422–428.

[206] Jonathan P Piccini. *Clinical Trials in Atrial Fibrillation: Lessons From the Box Score*. 2018.

[207] Claudio Pedrinazzi et al. “Atrial flutter: from ECG to electroanatomical 3D mapping”. In: *Heart international* 2.3-4 (2006), p. 161.

[208] Antonis S Manolis. “Contemporary Diagnosis and Management of Atrial Flutter”. In: *Cardiology in Review* 25.6 (2017), pp. 289–297.

[209] Paul Milliez et al. “Variable electrocardiographic characteristics of isthmus-dependent atrial flutter”. In: *Journal of the American College of Cardiology* 40.6 (2002), pp. 1125–1132.

[210] Francisco Castells et al. “Estimation of atrial fibrillatory wave from single-lead atrial fibrillation electrocardiograms using principal component analysis concepts”. In: *Medical & Biological Engineering & Computing* 43 (2005), pp. 557–560.

[211] E. K. Roonizi and R. Sassi. “An Extended Bayesian Framework for Atrial and Ventricular Activity Separation in Atrial Fibrillation”. In: *IEEE Journal of Biomedical and Health Informatics* 21.6 (2017), pp. 1573–1580.

[212] José Joaquín Rieta et al. “Atrial activity extraction for atrial fibrillation analysis using blind source separation”. In: *IEEE Transactions on Biomedical Engineering* 51.7 (2004), pp. 1176–1186.

[213] Francisco Castells et al. “Spatiotemporal blind source separation approach to atrial activity estimation in atrial tachyarrhythmias”. In: *IEEE Transactions on Biomedical Engineering* 52.2 (2005), pp. 258–267.

[214] Vincent Jacquemet et al. “Extraction and Analysis of T Waves in Electrocardiograms During Atrial Flutter”. In: *IEEE Transactions on Biomedical Engineering* 58.4 (2010), pp. 1104–1112.

[215] Jean-Claude Deharo, Michele Brignole, and Régis Guieu. "Adenosine hypersensitivity and atrioventricular block". In: *Herzschrittmachertherapie+ Elektrophysiologie* 29.2 (2018), pp. 166–170.

[216] Carlos Alberto Pastore et al. "Applicability of the Electro-Vectorcardiogram in Current Clinical Practice". In: *Arquivos brasileiros de cardiologia* 113.1 (2019), pp. 87–99.

[217] Golriz Sedaghat et al. "Quantitative Assessment of Vectorcardiographic Loop Morphology". In: *Journal of Electrocardiology* 49 (Jan. 2016).

[218] Sayantani Choudhuri et al. "Planarity of the spatial QRS loop of vectorcardiogram is a crucial diagnostic and prognostic parameter in acute myocardial infarction". In: *Medical hypotheses* 130 (2019), pp. 109–251.

[219] Drew Oehler et al. "QRS-T angle: a review". In: *Annals of Noninvasive Electrocardiology* 19 (Sept. 2014).

[220] Muhammad Haziq Kamarul Azman et al. "Localizing atrial flutter circuit using variability in the vectorcardiographic loop parameters". In: *2018 Computing in Cardiology Conference (CinC)*. Vol. 45. IEEE. 2018, pp. 1–4.

[221] Jason Ng et al. "A vectorcardiographic approach to understanding the 12-lead electrocardiogram of atrial flutter". In: *Computers in Cardiology, 2004*. IEEE. 2004, pp. 629–632.

[222] Alejandro Alcaine et al. "A multi-variate predictability framework to assess invasive cardiac activity and interactions during atrial fibrillation". In: *IEEE Transactions on Biomedical Engineering* 64.5 (2016), pp. 1157–1168.

[223] Ciprian Doru Giurcăneanu, Ioan Tăbuş, and Şerban Mereuţă. "Using contexts and R–R interval estimation in lossless ECG compression". In: *Computer Methods and Programs in Biomedicine* 67.3 (2002), pp. 177–186.

[224] Mathieu Lemay et al. "Cancellation of ventricular activity in the ECG: evaluation of novel and existing methods". In: *IEEE Transactions on Biomedical Engineering* 54.3 (2007), pp. 542–546.

[225] Deepshikha Acharya et al. "Application of adaptive Savitzky–Golay filter for EEG signal processing". In: *Perspectives in science* 8 (2016), pp. 677–679.

[226] Alfonso Aranda et al. "Performance of Dower's inverse transform and Frank lead system for Identification of Myocardial Infarction". In: *2015 37th Annual International Conference of the IEEE Engineering in Medicine and Biology Society (EMBC)*. IEEE. 2015, pp. 4495–4498.

[227] Rene Jaros, Radek Martinek, and Lukas Danys. "Comparison of different electrocardiography with vectorcardiography transformations". In: *Sensors* 19.14 (2019), p. 3072.

[228] Francisco Castells et al. "Principal component analysis in ECG signal processing". In: *EURASIP Journal on Advances In Signal Processing* (2007).

[229] G. Liu and H. Yang. "Multiscale Adaptive Basis Function Modeling of Spatiotemporal Vectorcardiogram Signals". In: *IEEE Journal of Biomedical and Health Informatics* 17.2 (2013), pp. 484–492.

[230] Muhammad Haziq Bin Kamarul Azman. “Novel pre-interventional atrial flutter localization tool for the improvement of radiofrequency ablation efficacy”. PhD thesis. COMUE Université Côte d’Azur (2015-2019); Universiti Kuala Lumpur (Malaisie), 2019.

[231] Martin Stridh and L Sornmo. “Spatiotemporal QRST cancellation techniques for analysis of atrial fibrillation”. In: *IEEE Transactions on Biomedical Engineering* 48.1 (2001), pp. 105–111.

[232] “On clustering based nonlinear projective filtering of biomedical signals”. In: *Biomedical Signal Processing and Control* 44 (2018), pp. 237–246. ISSN: 1746-8094.

[233] Tobias G Oesterlein et al. “Periodic component analysis to eliminate ventricular far field artifacts in unipolar atrial electrograms of patients suffering from atrial flutter”. In: Oct. 2014, S162–S165.

[234] Giorgio Luongo et al. “Automatic classification of 20 different types of atrial tachycardia using 12-lead ECG signals”. In: *EP Europace* 22.Supplement$_1$ (June 2020). ISSN: 1099-5129.

[235] Daniel Frisch. “Identifying a Gap in a Cavotricuspid Isthmus Flutter Line Using the Advisor™ HD Grid High-Density Mapping Catheter”. In: *Journal of Innovations in Cardiac Rhythm Management* 10 (Dec. 2019), pp. 3919–3922.

[236] Masateru Takigawa et al. “Revisiting anatomic macroreentrant tachycardia after atrial fibrillation ablation using ultrahigh-resolution mapping: Implications for ablation”. In: *Heart Rhythm* 15.3 (2018), pp. 326–333. ISSN: 1547-5271.

[237] Francisco Castells et al. “Performance assessment of electrode configurations for the estimation of omnipolar electrograms from high density arrays”. In: *Computers in Biology and Medicine* 154 (Mar. 2023), p. 106604.

[238] David A Cesario et al. “Value of high-density endocardial and epicardial mapping for catheter ablation of hemodynamically unstable ventricular tachycardia”. en. In: *Heart Rhythm* 3.1 (Jan. 2006), pp. 1–10.

[239] Stephen M Dillon et al. “Influences of anisotropic tissue structure on reentrant circuits in the epicardial border zone of subacute canine infarcts.” In: *Circulation research* 63.1 (1988), pp. 182–206.

[240] Dennis H Lau et al. “Pathophysiology of paroxysmal and persistent atrial fibrillation: Rotors, foci and fibrosis”. In: *Heart Lung Circ.* 26.9 (Sept. 2017), pp. 887–893.

[241] Gala Caixal et al. “Accuracy of left atrial fibrosis detection with cardiac magnetic resonance: correlation of late gadolinium enhancement with endocardial voltage and conduction velocity”. en. In: *Europace* 23.3 (Mar. 2021), pp. 380–388.

[242] Kenichi Kaseno et al. “Discrepancy between CARTO and Rhythmia maps for defining the left atrial low-voltage areas in atrial fibrillation ablation”. en. In: *Heart Vessels* 36.7 (July 2021), pp. 1027–1034.

[243] Stephen Gaeta, Tristram D Bahnson, and Craig Henriquez. “Mechanism and magnitude of bipolar electrogram directional sensitivity: Characterizing underlying determinants of bipolar amplitude”. en. In: *Heart Rhythm* 17.5 Pt A (May 2020), pp. 777–785.

[244] Minki Hwang et al. "Multiple factors influence the morphology of the bipolar electrogram: An in silico modeling study". en. In: *PLoS Comput. Biol.* 15.4 (Apr. 2019), e1006765.

[245] Shouvik Haldar et al. "Resolving Bipolar Electrogram Voltages During Atrial Fibrillation Using Omnipolar Mapping". In: *Circulation: Arrhythmia and Electrophysiology* 10 (Sept. 2017), e005018.

[246] Masateru Takigawa et al. "Impact of spacing and orientation on the scar threshold with a high-density Grid catheter". en. In: *Circ. Arrhythm. Electrophysiol.* 12.9 (Sept. 2019), e007158.

[247] Wen-Han Cheng et al. "Identification of Circumferential Pulmonary Vein Isolation Gaps and Critical Atrial Substrate From HD Grid Maps in Atrial Fibrillation Patients: Insights From Omnipolar Technology". In: *Circulation: Arrhythmia and Electrophysiology* 15.1 (2022), e010424.

[248] Mathijs van Schie et al. "Identification of Low-Voltage Areas: A Unipolar, Bipolar, and Omnipolar Perspective". In: *Circulation Arrhythmia and Electrophysiology* 14 (June 2021), pp. 627–637.

[249] Don C Deno et al. "High-resolution, live, directional mapping". In: *Heart Rhythm* 17.9 (Sept. 2020), pp. 1621–1628.

[250] T Paul et al. "Epicardial mapping: how to measure local activation?" en. In: *Pacing Clin. Electrophysiol.* 13.3 (Mar. 1990), pp. 285–292.

[251] Kurt Pfannkuche et al. "Cardiac myocytes derived from murine reprogrammed fibroblasts: intact hormonal regulation, cardiac ion channel expression and development of contractility". en. In: *Cell. Physiol. Biochem.* 24.1-2 (July 2009), pp. 73–86.

[252] Francisco J Chorro et al. "Modifications in Ventricular Fibrillation and Capture Capacity Induced by a Linear Radiofrequency Lesion". en. In: *Rev. Esp. Cardiol. (Engl. Ed.)* 65.2 (Feb. 2012), pp. 143–151.

[253] Jens Eckstein et al. "Transmural conduction is the predominant mechanism of breakthrough during atrial fibrillation: evidence from simultaneous endo-epicardial high-density activation mapping". en. In: *Circ. Arrhythm. Electrophysiol.* 6.2 (Apr. 2013), pp. 334–341.

[254] Leif Sornmo and Pablo Laguna. *Bioelectrical signal processing in cardiac and neurological applications*. Biomedical Engineering. San Diego, CA: Academic Press, June 2005.

[255] Raquel Cervigón et al. "Propofol effects on atrial fibrillation wavefront delays". en. In: *IEEE Trans. Biomed. Eng.* 57.8 (Aug. 2010), pp. 1877–1885.

[256] Lisette JME van der Does and Natasja MS de Groot. "Inhomogeneity and complexity in defining fractionated electrograms". In: *Heart Rhythm* 14.4 (2017), pp. 616–624.

[257] Samuel Ruipérez-Campillo et al. "Evaluation and assessment of clique arrangements for the estimation of omnipolar electrograms in high density electrode arrays: an experimental animal model study". In: *Physical and Engineering Sciences in Medicine* 46.3 (2023), pp. 1193–1204.

[258] Hiroshi Morita et al. “Isolation of Canine Coronary Sinus Musculature From the Atria by Radiofrequency Catheter Ablation Prevents Induction of Atrial Fibrillation”. In: *Circulation: Arrhythmia and Electrophysiology* 7.6 (2014), pp. 1181–1188.

[259] Nazem Akoum and Nassir Marrouche. “Assessment and impact of cardiac fibrosis on atrial fibrillation”. In: *Current cardiology reports* 16.8 (2014), pp. 1–7.

[260] Weizhu Ju et al. “Idiopathic isolated fibrotic atrial cardiomyopathy underlies unexplained scar-related atrial tachycardia in younger patients”. In: *EP Europace* 20.10 (2018), pp. 1657–1665.

[261] Norishige Morita et al. “Cardiac fibrosis as a determinant of ventricular tachyarrhythmias”. In: *Journal of arrhythmia* 30.6 (2014), pp. 389–394.

[262] Sanne De Jong et al. “Fibrosis and cardiac arrhythmias”. In: *Journal of cardiovascular pharmacology* 57.6 (2011), pp. 630–638.

[263] Jacques MT de Bakker et al. “Slow conduction in the infarcted human heart. 'Zigzag' course of activation.” In: *Circulation* 88.3 (1993), pp. 915–926.

[264] Dennis W den Uijl et al. “Impact of left atrial fibrosis and left atrial size on the outcome of catheter ablation for atrial fibrillation”. en. In: *Heart* 97.22 (Nov. 2011), pp. 1847–1851.

[265] Barbara Bellmann et al. “First epicardial mapping of the left ventricle using the Advisor™ HD Grid catheter”. In: *Journal of Interventional Cardiac Electrophysiology* 53.1 (2018), pp. 103–104.

[266] Jason T Jacobson et al. “Abstract 17013: Voltage Resolution of Standard Bipolar and Omnipolar Ventricular Electrograms”. In: *Circulation* 142.Suppl_3 (2020), A17013–A17013.

[267] Natasja M S de Groot et al. “Critical appraisal of technologies to assess electrical activity during atrial fibrillation: a position paper from the European Heart Rhythm Association and European Society of Cardiology Working Group on eCardiology in collaboration with the Heart Rhythm Society, Asia Pacific Heart Rhythm Society, Latin American Heart Rhythm Society and Computing in Cardiology”. In: *EP Europace* 24.2 (Dec. 2021), pp. 313–330. ISSN: 1099-5129.

[268] Francisco Castells et al. “Performance assessment of electrode configurations for the estimation of omnipolar electrograms from high density arrays”. In: *Computers in Biology and Medicine* (2024).

[269] “Animal Models of Cardiovascular Disease”. In: *Revista Española de Cardiología* 62.1 (2009), pp. 69–84. ISSN: 0300-8932.

[270] P R Beckett. “The isolated perfused heart preparation: two suggested improvements”. In: *Journal of Pharmacy and Pharmacology* 22.11 (), pp. 818–822.

[271] Antonio Guill et al. “QT interval heterogeneities induced through local epicardial warming/cooling. An experimental study.” In: *Revista española de cardiologia* 67.12 (2014), pp. 993–998.

[272] Alvaro Tormos et al. “New epicardial mapping electrode with warming/-cooling function for experimental electrophysiology studies.” In: *Medical engineering & physics* 33.5 (2011), pp. 653–659.

[273] William Kahan. "Miscalculating area and angles of a needle-like triangle". In: *University of California, Berkeley* 94720 (2014).

[274] Michael J. Cutler et al. "Impact of Voltage Mapping to Guide Whether to Perform Ablation of the Posterior Wall in Patients With Persistent Atrial Fibrillation". In: *Journal of Cardiovascular Electrophysiology* 27.1 (2016), pp. 13–21.

[275] "A new approach for catheter ablation of atrial fibrillation: mapping of the electrophysiologic substrate". In: *Journal of the American College of Cardiology* 43.11 (2004), pp. 2044–2053. issn: 0735-1097.

[276] MK Jothi Letchumy et al. "The Effects of Electrode Configuration on Omnipolar Electrograms: An In-Silico Approach". In: *2022 Computing in Cardiology (CinC)*. Vol. 498. IEEE. 2022, pp. 1–4.

[277] Lucía Pancorbo et al. "Vector Field Heterogeneity for the Assessment of Locally Disorganised Cardiac Electrical Propagation Wavefronts from High-density Multielectrodes". In: *IEEE Open Journal of Engineering in Medicine and Biology* (2023).

[278] Ruhong Jiang et al. "High-density grid catheter for detailed mapping of sinus rhythm and scar-related ventricular tachycardia: comparison with a linear duodecapolar catheter". In: *Clinical Electrophysiology* 6.3 (2020), pp. 311–323.

[279] Susan M Blanchard et al. "The effects of distant cardiac electrical events on local activation in unipolar epicardial electrograms". In: *IEEE Transactions on Biomedical Engineering* BME-34.7 (July 1987), pp. 539–546.

[280] Jason T Jacobson et al. "Abstract 17013: Voltage Resolution of Standard Bipolar and Omnipolar Ventricular Electrograms". In: *Circulation* 142.Suppl_3 (Nov. 2020), A17013–A17013.

[281] David Luengo et al. "Hierarchical algorithms for causality retrieval in atrial fibrillation intracavitary electrograms". In: *IEEE Journal of Biomedical and Health Informatics* 23.1 (Jan. 2019), pp. 143–155.

[282] Jason Ng et al. "Measuring the complexity of atrial fibrillation electrograms". In: *Journal of Cardiovascular Electrophysiology* 21.6 (May 2010), pp. 649–655.

[283] Raquel Cervigón et al. "Entropy at the right atrium as a predictor of atrial fibrillation recurrence outcome after pulmonary vein ablation". In: *Biomedical Engineering/Biomedizinische Technik* 61.1 (June 2016), pp. 29–36.

[284] Eva Cirugeda–Roldán et al. "Characterization of complex fractionated atrial electrograms by sample entropy: An international multi-center study". In: *Entropy* 17.11 (Oct. 2015), pp. 7493–7509.

[285] Anand N Ganesan et al. "Bipolar electrogram shannon entropy at sites of rotational activation: implications for ablation of atrial fibrillation". In: *Circulation: Arrhythmia and Electrophysiology* 6.1 (Dec. 2013), pp. 48–57.

[286] Raquel Cervigón et al. "Entropy measurements in paroxysmal and persistent atrial fibrillation". In: *Physiological Measurement* 31.7 (June 2010), p. 1011.

[287] Kristina M Ropella et al. "The coherence spectrum. A quantitative discriminator of fibrillatory and nonfibrillatory cardiac rhythms." In: *Circulation* 80.1 (July 1989), pp. 112–119.

[288] Gregory W Botteron and Joseph M Smith. “A technique for measurement of the extent of spatial organization of atrial activation during atrial fibrillation in the intact human heart”. In: *IEEE Transactions on Biomedical Engineering* 42.6 (June 1995), pp. 579–586.

[289] Lahn Fendelander, Peng-Wei Hsia, and Ralph J Damiano Jr. “Spatial coherence: a new method of quantifying myocardial electrical organization using multichannel epicardial electrograms”. In: *Journal of Electrocardiology* 30.1 (Jan. 1997), pp. 9–19.

[290] Gregory W Botteron and Joseph M Smith. “Quantitative assessment of the spatial organization of atrial fibrillation in the intact human heart”. In: *Circulation* 93.3 (Feb. 1996), pp. 513–518.

[291] Thomas H Everett et al. “Frequency domain algorithm for quantifying atrial fibrillation organization to increase defibrillation efficacy”. In: *IEEE Transactions on Biomedical Engineering* 48.9 (Sept. 2001), pp. 969–978.

[292] Julian WE Jarman et al. “Organizational index mapping to identify focal sources during persistent atrial fibrillation”. In: *Journal of Cardiovascular Electrophysiology* 25.4 (Jan. 2014), pp. 355–363.

[293] Andre G Kléber et al. “Changes in conduction velocity during acute ischemia in ventricular myocardium of the isolated porcine heart.” In: *Circulation* 73.1 (Jan. 1986), pp. 189–198.

[294] WJ Lammers et al. “Quantification of spatial inhomogeneity in conduction and initiation of reentrant atrial arrhythmias”. In: *American Journal of Physiology-Heart and Circulatory Physiology* 259.4 (Oct. 1990), H1254–H1263.

[295] Danshi Li et al. “Promotion of atrial fibrillation by heart failure in dogs: atrial remodeling of a different sort”. In: *Circulation* 100.1 (July 1999), pp. 87–95.

[296] Sander Verheule et al. “Increased vulnerability to atrial fibrillation in transgenic mice with selective atrial fibrosis caused by overexpression of TGF-β1”. In: *Circulation Research* 94.11 (Apr. 2004), pp. 1458–1465.

[297] Xiuming Dong et al. “Heterogeneities in ventricular conduction following treatment with heptanol: a multi-electrode array study in Langendorff-perfused mouse hearts”. In: *Life* 12.7 (May 2022), p. 996.

[298] Tamara N Fitzgerald, Dana H Brooks, and John K Triedman. “Identification of cardiac rhythm features by mathematical analysis of vector fields”. In: *IEEE Transactions on Biomedical Engineering* 52.1 (Jan. 2005), pp. 19–29.

[299] Corentin Dallet et al. “Cardiac propagation pattern mapping with vector field for helping tachyarrhythmias diagnosis with clinical tridimensional electro-anatomical mapping tools”. In: *IEEE Transactions on Biomedical Engineering* 66.2 (Feb. 2019), pp. 373–382.

[300] Michela Masè et al. “A divergence-based approach for the identification of atrial fibrillation focal drivers from multipolar mapping: a computational study”. In: *Frontiers in Physiology* 12 (Dec. 2021), p. 2347.

[301] Chris D Cantwell et al. “Techniques for automated local activation time annotation and conduction velocity estimation in cardiac mapping”. In: *Computers in Biology and Medicine* 65 (Oct. 2015), pp. 229–242.

[302] Juan P Ugarte, Catalina Tobón, and Andrés Orozco-Duque. "Entropy mapping approach for functional reentry detection in atrial fibrillation: an in-silico study". In: *Entropy* 21.2 (Jan. 2019), p. 194.

[303] Amir S Jadidi et al. "Functional nature of electrogram fractionation demonstrated by left atrial high-density mapping". In: *Circulation: Arrhythmia and Electrophysiology* 5.1 (Jan. 2012), pp. 32–42.

[304] Ulrike Richter et al. "A novel approach to propagation pattern analysis in intracardiac atrial fibrillation signals". In: *Annals of Biomedical Engineering* 39 (Aug. 2011), pp. 310–323.

[305] Ashish N Doshi et al. "Feasibility of a semi-automated method for cardiac conduction velocity analysis of high-resolution activation maps". In: *Computers in Biology and Medicine* 65 (Oct. 2015), pp. 177–183.

[306] Caroline H Roney et al. "A technique for measuring anisotropy in atrial conduction to estimate conduction velocity and atrial fibre direction". In: *Computers in Biology and Medicine* 104 (Jan. 2019), pp. 278–290.

[307] Prasanth Ganesan et al. "Quantifying a spectrum of clinical response in atrial tachyarrhythmias using spatiotemporal synchronization of electrograms". In: *EP Europace* 25.5 (May 2023), euad0558.

[308] Ozan Özgül et al. "High-density and high coverage composite mapping of repetitive atrial activation patterns". In: *Computers in Biology and Medicine* 159 (June 2023), p. 106920.

[309] M Enokizono and N Soda. "Direct magnetic loss analysis by FEM considering vector magnetic properties". In: *IEEE transactions on magnetics* 34.5 (1998), pp. 3008–3011.

[310] Yiying Tong et al. "Discrete multiscale vector field decomposition". In: *ACM Transactions on Graphics (TOG)* 22.3 (2003), pp. 445–452.

[311] Chiao-Fe Shu and Ramesh C Jain. "Vector field analysis for oriented patterns". In: *IEEE Transactions on Pattern Analysis and Machine Intelligence* 16.9 (1994), pp. 946–950.

[312] Stéphane Massé et al. "Resolving myocardial activation with novel omnipolar electrograms". In: *Circulation: Arrhythmia and Electrophysiology* 9.7 (2016), e004107.

[313] Johanna Tonko et al. "Vector Field Heterogeneity as a Novel Omnipolar Mapping Metric for Functional Substrate Characterisation in Scar-related Ventricular Tachycardias". In: *Heart Rhythm* (2024).

[314] Milad El Haddad et al. "Novel algorithmic methods in mapping of atrial and ventricular tachycardia". In: *Circulation: Arrhythmia and Electrophysiology* 7.3 (2014), pp. 463–472.

[315] Rohin K Reddy et al. "Catheter Ablation for Ventricular Tachycardia After MI: A Reconstructed Individual Patient Data Meta-analysis of Randomised Controlled Trials". In: *Arrhythmia & Electrophysiology Review* 12 (2023).

[316] Hugh Calkins et al. "2017 HRS/EHRA/ECAS/APHRS/SOLAECE expert consensus statement on catheter and surgical ablation of atrial fibrillation". In: *Ep Europace* 20.1 (2018), e1–e160.

[317] Tina Baykaner et al. “Spatial relationship of sites for atrial fibrillation drivers and atrial tachycardia in patients with both arrhythmias”. In: *International journal of cardiology* 248 (2017), pp. 188–195.

[318] Seigo Yamashita et al. “Atrial tachycardias: cause or effect with ablation of persistent atrial fibrillation?” In: *Journal of Cardiovascular Electrophysiology* 29.2 (2018), pp. 274–283.

[319] Maurits A Allessie et al. “Electropathological substrate of long-standing persistent atrial fibrillation in patients with structural heart disease: longitudinal dissociation”. In: *Circulation: Arrhythmia and Electrophysiology* 3.6 (2010), pp. 606–615.

[320] Jason Ng et al. “Electrogram morphology recurrence patterns during atrial fibrillation”. In: *Heart Rhythm* 11.11 (2014), pp. 2027–2034.

[321] Chin-Yu Lin et al. “Efficacy of patient-specific strategy: catheter ablation strategy of persistent atrial fibrillation based on morphological repetitiveness by periodicity and similarity”. In: *Circulation: Arrhythmia and Electrophysiology* 14.5 (2021), e009719.

[322] Tiago P Almeida et al. “Unsupervised classification of atrial electrograms for electroanatomic mapping of human persistent atrial fibrillation”. In: *Ieee Transactions on Biomedical Engineering* 68.4 (2020), pp. 1131–1141.

[323] Shohreh Honarbakhsh et al. “Panoramic atrial mapping with basket catheters: A quantitative analysis to optimize practice, patient selection, and catheter choice”. In: *Journal of cardiovascular electrophysiology* 28.12 (2017), pp. 1423–1432.

[324] Julien Seitz et al. “AF ablation guided by spatiotemporal electrogram dispersion without pulmonary vein isolation: a wholly patient-tailored approach”. In: *Journal of the American College of Cardiology* 69.3 (2017), pp. 303–321.

[325] Caroline H Roney, Andrew L Wit, and Nicholas S Peters. “Challenges associated with interpreting mechanisms of AF”. In: *Arrhythmia & Electrophysiology Review* 8.4 (2019), p. 273.

[326] Felipe Atienza et al. “Mechanisms of fractionated electrograms formation in the posterior left atrium during paroxysmal atrial fibrillation in humans”. In: *Journal of the American College of Cardiology* 57.9 (2011), pp. 1081–1092.

[327] Prasanth Ganesan and Sanjiv M Narayan. “Re-evaluating the multiple wavelet hypothesis for atrial fibrillation”. In: *Heart rhythm* 17.12 (2020), pp. 2219–2220.

[328] Bart Maesen et al. “Endomysial fibrosis, rather than overall connective tissue content, is the main determinant of conduction disturbances in human atrial fibrillation”. In: *EP Europace* 24.6 (2022), pp. 1015–1024.

[329] Stef Zeemering et al. “A novel tool for the identification and characterization of repetitive patterns in high-density contact mapping of atrial fibrillation”. In: *Frontiers in physiology* 11 (2020), p. 570118.

[330] Neal K Bhatia et al. “Termination of persistent atrial fibrillation by ablating sites that control large atrial areas”. In: *EP Europace* 22.6 (2020), pp. 897–905.

[331] Edouard Gitenay et al. “Localized atrial tachycardia and dispersion regions in atrial fibrillation: evidence of spatial concordance”. In: *Journal of Clinical Medicine* 10.14 (2021), p. 3170.

[332] Miguel Rodrigo et al. “Noninvasive assessment of complexity of atrial fibrillation: correlation with contact mapping and impact of ablation”. In: *Circulation: Arrhythmia and Electrophysiology* 13.3 (2020), e007700.

[333] Yoram Rudy. “Noninvasive ECG imaging (ECGI): Mapping the arrhythmic substrate of the human heart”. In: *International journal of cardiology* 237 (2017), pp. 13–14.

[334] Antonio Bisignani et al. “Atrial abnormalities in Brugada syndrome: evaluation with ECG imaging”. In: *Clinical Electrophysiology* 9.10 (2023), pp. 2096–2105.

[335] Junjie Zhang et al. “Cardiac electrophysiological substrate underlying the ECG phenotype and electrogram abnormalities in Brugada syndrome patients”. In: *Circulation* 131.22 (2015), pp. 1950–1959.

[336] Ramya Vijayakumar et al. “Electrophysiologic substrate in congenital long QT syndrome: noninvasive mapping with electrocardiographic imaging (ECGI)”. In: *Circulation* 130.22 (2014), pp. 1936–1943.

[337] Phillip S Cuculich et al. “The electrophysiological cardiac ventricular substrate in patients after myocardial infarction: noninvasive characterization with electrocardiographic imaging”. In: *Journal of the American College of Cardiology* 58.18 (2011), pp. 1893–1902.

[338] Yoram Rudy. “Noninvasive electrocardiographic imaging of arrhythmogenic substrates in humans”. In: *Circulation research* 112.5 (2013), pp. 863–874.

[339] Josselin Duchateau et al. “Performance and limitations of noninvasive cardiac activation mapping”. In: *Heart rhythm* 16.3 (2019), pp. 435–442.

[340] Laura R Bear et al. “Advantages and pitfalls of noninvasive electrocardiographic imaging”. In: *Journal of electrocardiology* 57 (2019), S15–S20.

[341] KL Venkatachalam, Joel E Herbrandson, and Samuel J Asirvatham. “Signals and signal processing for the electrophysiologist: part I: electrogram acquisition”. In: *Circulation: Arrhythmia and Electrophysiology* 4.6 (2011), pp. 965–973.

[342] International Electrotechnical Commission et al. “Medical electrical equipment-Part 1: General requirements for basic safety and essential performance”. In: *IEC 60601-1: 2005* (2005).

[343] Manish Undavia, Hejmadi Prabhu, and Todd Cohen. “Deceptive intracardiac electrograms during an ICD interrogation. A clinical challenge”. In: *Indian Pacing and Electrophysiology Journal* 16.1 (2016), pp. 32–33.

[344] Roderick Tung. “Challenges and pitfalls of entrainment mapping of ventricular tachycardia: ten illustrative concepts”. In: *Circulation: Arrhythmia and Electrophysiology* 10.4 (2017), e004560.

[345] KL Venkatachalam, Joel E Herbrandson, and Samuel J Asirvatham. “Signals and signal processing for the electrophysiologist: part II: signal processing and artifact”. In: *Circulation: Arrhythmia and Electrophysiology* 4.6 (2011), pp. 974–981.

[346] Elad Anter, Cory M Tschabrunn, and Mark E Josephson. "High-resolution mapping of scar-related atrial arrhythmias using smaller electrodes with closer interelectrode spacing". In: *Circulation: Arrhythmia and Electrophysiology* 8.3 (2015), pp. 537–545.

[347] Amir S Jadidi et al. "Functional nature of electrogram fractionation demonstrated by left atrial high-density mapping". en. In: *Circ. Arrhythm. Electrophysiol.* 5.1 (Feb. 2012), pp. 32–42.

[348] Zaid Aziz et al. "Targeted ablation of ventricular tachycardia guided by wavefront discontinuities during sinus rhythm: a new functional substrate mapping strategy". In: *Circulation* 140.17 (2019), pp. 1383–1397.

[349] Nicholas Jackson et al. "Decrement evoked potential mapping: basis of a mechanistic strategy for ventricular tachycardia ablation". In: *Circulation: Arrhythmia and Electrophysiology* 8.6 (2015), pp. 1433–1442.

[350] Johanna B Tonko et al. "Visualizing Reentry Vulnerable Targets During Scar-Related VT Ablation: A Novel Functional Substrate Mapping Approach Integrating Conduction and Repolarization Metrics". In: *Circulation: Arrhythmia and Electrophysiology* 17.8 (2024), e012915.

[351] Elad Anter et al. "Ablation of reentry-vulnerable zones determined by left ventricular activation from multiple directions: a novel approach for ventricular tachycardia ablation: a multicenter study (PHYSIO-VT)". In: *Circulation: Arrhythmia and Electrophysiology* 13.6 (2020), e008625.

[352] Edward J Ciaccio et al. "Structure and function of the ventricular tachycardia isthmus". In: *Heart Rhythm* 19.1 (2022), pp. 137–153.

[353] Marina Crespo et al. "Assessment of the Interelectrode Distance Effect over the Omnipole with High Multielectrode Arrays". In: *2023 45th Annual International Conference of the IEEE Engineering in Medicine & Biology Society (EMBC)*. IEEE. 2023, pp. 1–4.

[354] Izan Segarra et al. "Mini Peltier Cell Array System for the Generation of Controlled Local Epicardial Heterogeneities". In: *2023 45th Annual International Conference of the IEEE Engineering in Medicine & Biology Society (EMBC)*. IEEE. 2023, pp. 1–4.

[355] Lucía Pancorbo et al. "Heterogeneity Quantification of Electrophysiological Signal Propagation in High-Density Multielectrode Recordings". In: *2023 Computing in Cardiology (CinC)*. Vol. 50. IEEE. 2023, pp. 1–4.

[356] Samuel Ruipérez-Campillo, José Millet, and Francisco Castells. "Classification of Atrial Tachycardia Types Using Dimensional Transforms of ECG Signals and Machine Learning". In: *2022 Computing in Cardiology (CinC)*. Vol. 498. IEEE. 2022, pp. 1–4.

[357] Izan Segarra et al. "Novel Method for Orientation-Independent Analysis in Equi-Spaced Multi-Electrode Arrays". In: *2022 Computing in Cardiology (CinC)*. Vol. 498. IEEE. 2022, pp. 1–4.

[358] Samuel Ruipérez-Campillo et al. "Slow conduction regions as a valuable vectorcardiographic parameter for the non-invasive identification of atrial flutter types". In: *2020 Computing in Cardiology*. IEEE. 2020, pp. 1–4.

[359] Samuel Ruiperez-Campillo et al. "Quantifying local cardiac substrate heterogeneity from high density recordings: an experimental study". In: *Europace* 26.Supplement_1 (2024), euae102–650.

[360] Samuel Ruiperez-Campillo et al. "Improving omnipolar electrogram reconstruction: an animal model study". In: *European Heart Journal* 44.Supplement_2 (2023), ehad655–290.

[361] Samuel Ruiperez-Campillo et al. "Quantification of local heterogeneity from activation maps of omnipolar multielectrode recordings". In: *European Heart Journal* 44.Supplement_2 (2023), ehad655–328.

[362] Samuel Ruiperez-Campillo et al. "Novel reconstruction technique of omnipolar signals in high density electrode arrays". In: *Europace* 25.Supplement_1 (2023), euad122–589.

[363] Samuel Ruiperez-Campillo et al. "Study of the omnipolar EGM reconstruction for robustness against wavefront propagation in epicardial signals". In: *Europace* 25.Supplement_1 (2023), euad122–662.

[364] Prasanth Ganesan et al. "Spectrum of Clinical Response in Atrial Tachyarrhythmias Identified by Spatiotemporal Synchronization of Electrograms". In: *Circulation* 146.Suppl_1 (2022), A11304–A11304.

[365] Prasanth Ganesan et al. "Spatiotemporal signatures of response to atrial fibrillation ablation". In: *European Heart Journal* 43.Supplement_2 (2022), ehac544–601.

[366] Prasanth Ganesan et al. "Novel detection of atrial tachycardia-like islands during atrial fibrillation predicts response to ablation". In: *Heart Rhythm* 19.5 (2022), S17–S18.

[367] Leif Sörnmo. "Vectorcardiographic loop alignment and morphologic beat-to-beat variability". In: *IEEE Transactions on Biomedical Engineering* 45 (1998), pp. 1401–1413.

[368] Florian Hartig. *DHARMa: Residual Diagnostics for Hierarchical (Multi-Level / Mixed) Regression Models*. 2022.